ISAS - INTERNATIONAL SCHOOL
FOR ADVANCED STUDIES

A Unifying View on Blazars

Thesis submitted for the degree of
Doctor Philosophiæ

Astrophysics Sector

CANDIDATE
Giovanni Fossati

SUPERVISORS
Dr. Annalisa Celotti
Prof. Gabriele Ghisellini

October 1998

SISSA - SCUOLA
INTERNAZIONALE
SUPERIORE
STUDI AVANZATI
TRIESTE
Via Beirut 2-4

TRIESTE

SISSA ISAS
SCUOLA INTERNAZIONALE SUPERIORE DI STUDI AVANZATI
INTERNATIONAL SCHOOL FOR ADVANCED STUDIES

A Unifying View on Blazars

Thesis submitted for the degree of
Doctor Philosophiæ

Astrophysics Sector

CANDIDATE
Giovanni Fossati

SUPERVISORS
Dr. Annalisa Celotti
Prof. Gabriele Ghisellini

October 1998

Preface

What blazars are

Blazars are radio–loud Active Galactic Nuclei (AGN) characterized by strong variability, high and variable polarization, and high luminosity. They are core dominated, flat spectrum radio sources. Radio spectra smoothly join the infrared-optical-UV spectra, and in all these bands flux is highly variable and polarized. These extreme properties are successfully interpreted in terms of synchrotron radiation produced in relativistic jets and beamed into our direction due to plasma moving relativistically close to the line of sight (Blandford and Rees 1978; Blandford and Konigl 1979).

This interpretation is strongly supported by direct observations of superluminal motions observed in radio cores in VLBI data (Vermeulen and Cohen 1994), and constitutes the basis for the unified scheme of radio-loud AGN (Urry and Padovani 1995).

As was recently discovered by the Compton Gamma Ray Observatory (*CGRO*), many blazars are strong and variable sources of high energy γ–rays. In a few sources, the spectrum extends up to the TeV energies. The γ–ray radiation forms a separate spectral component, with the luminosity peak located in the MeV–TeV range. Variability of GeV/TeV radiation itself provides evidence for relativistic speeds of radiating plasma (Maraschi et al. 1992).

Why to study blazars ?

Because of their special properties, blazars offer an important probe of the very central region of AGNs and the opportunity to shed light on the mechanisms of energy extraction from the putative central black hole where jets form, a fundamental goal of AGN research. The problem of energy production and jet formation/acceleration can certainly enlighten the physics of (spinning ?) black holes. The first step is to understand which are the fundamental physical parameters and processes at work in these extreme power engines which are supermassive black holes and relativistic jets, able for instance to power extended structures laying at several Mega parsecs distance.

Moreover, in blazars jets most probably strong relativistic shocks occur, whose physics is poorly known. In this respect, it is noteworthy the intriguing possibility that blazars may also be the acceleration sites of exceptionally high energy ($E > 10^{19}$ eV) cosmic rays (Biermann 1995).

The goal of my work was to make progress in the identification of the physical parameters ruling the rich phenomenology of blazars: the investigation of the mutual relationships among them turned out to be especially enlightening.

(Our) Questions on Blazars

For a deeper understanding of the fundamental mechanisms at work in these sources we think it is crucial to address the questions:

① within the blazar phenomenon which is the physical origin of the difference among BL Lac objects and even more broadly between BL Lacs and Flat Spectrum Radio Quasars (FSRQ) ?

② is it possible to identify continuity among them, with a limited number of physical properties determining the observational characteristics of all blazars?

③ γ–ray observations have raised again the question of similarities/differences of in the γ–ray properties of the various blazars subclasses. Understanding this issue is essential to assess the role of different radiative mechanisms and to verify whether the idea of blazars as a unitary class can be maintained.

* * * * *

our approach

In this thesis, we address these issues from both the observational and the theoretical side, following several lines of research, which we are going to illustrate in the following Chapters.

In the introductory Chapter we present the framework in which we will be discussing the problematic of blazars. We will briefly go through the basic phenomenology, illustrate the reasons supporting the study of Spectral Energy Distributions (SED), and discuss the important change in blazars research occurred in the last few years, when we "moved" from the orientation–based unification scheme towards the more complex picture based directly on physical properties. This is the new and main result of the work described in this thesis.

In the Introduction particular emphasis is given to BL Lac objects, because the most important progress, leading to the change of "paradigm" has being done starting from the study of the few complete samples of BL Lacs, available. Current ideas about

the nature of the relation (similarities) between BL Lac objects and FSRQ are then reviewed. In Section 1.1.4 we point out the relevance of the study of the high energy emission, X and γ–ray bands, which constitutes a fundamental tile in the picture that we are going to study.

We then illustrate in Chapter 2 the very basic ingredients of blazars emission models, in particular synchrotron and inverse Compton radiative processes, and the effects of relativistic beaming. We report a handful of equations useful to derive estimates and constraints on physical properties, expressing them in terms of observational SED properties.
In these first two Chapters we anticipate in many instances the new results of our work, in order to present them as part of the general scenario of blazars unification.

In the second part of this thesis (Chapters 3, 4, 5, 6) we enter into the details of the work, which lead to the proposal of our new (physical) unification scenario.

In Chapter 3 we report on the results of Montecarlo simulations of complete samples of BL Lacs, performed to test the new scenarios arising from the remnants of the "orientation paradigm".

In Chapter 4 we focus on a restricted sample of blazars selected on the basis of their γ–ray and soft-X–ray detection, in order to investigate the phenomenology and relationship between high energy properties.

In the last two chapters we concentrate on the full broad band, radio to γ–ray, spectral distributions, with two complementary approaches. A purely observational one based on complete *sub–samples* of blazars (Chapter 5), and a more theoretical approach, by modeling individually the SEDs of all the γ–ray sources with sufficient available data to constrain their physical parameters (Chapter 6). This allows us to derive trends between the physical quantities underlying the correlations between the observed ones.

Finally, we summarize the emerging unifying picture and synthetically discuss a few developments, consequences and perspectives arising in/from this "new" picture of blazars.

Contents

CHAPTER 1

INTRODUCTION

Among AGN blazars represent the most extreme and powerful sources. The fundamental property characterizing blazars is their beamed continuum, due to plasma moving relativistically along the line of sight.

This scenario seems to apply to objects with somewhat different observational properties leading to different classifications/definitions.

- ✘ Objects with significant emission line equivalent widths are usually found as Flat Spectrum Radio Quasars (FSRQ).
- ✘ Objects without emission lines (EW < 5 Å) are classified as BL Lac objects.

Moreover, different "flavours" of BL Lac objects have been found in radio and X-ray surveys, with marked differences in the overall spectral energy distributions, which have been interpreted either as due to orientation, or as intrinsic (Urry and Padovani 1995). Nevertheless, while different blazars sub–classes have different average properties, the actual distinction among them is certainly fuzzy and so far several sources have shown intermediate behaviour. How much the distinction between BL Lacs and FSRQ is due to intrinsic properties or it is a consequence of the classification criteria remains unclear, and it is one of our goals to clarify this point. In fact arguments for a substantial 'continuity' in the continuum spectral properties leading to adopt the blazar denomination as including both, BL Lacs as well as FSRQs, have been recently

re–proposed by Maraschi et al. (1995), Sambruna et al. (1996), and Fossati et al. (1997).

Parent Population

If blazars do indeed have relativistic jets oriented at small angles to the line of sight, there must exist a substantial population of intrinsically identical sources seen at large angles. This large class of objects is called the *parent population*, and its identification constitutes a constraint to the study of blazars. On the other hand the knowledge of their properties provide a source of further insight for the understanding of blazars, imposing constraints on the supposedly isotropic properties.

The strong dependence of several observables on the aspect angle will cause these sources to show a significantly different phenomenology due to the lack of the boosted jet emission. However, they should match blazars in properties expected to be isotropic, such as host galaxies, extended radio emission and its morphology, and cluster environment. The suggested parent population for blazars are the radio galaxies classified as Fanaroff–Riley type I and II (FR I, FR II, Fanaroff and Riley 1974), for BL Lac objects and FSRQ respectively.
We will not further discuss this important topic, which will be only recalled in the last Chapter in the context of consequences and perspectives of the unification scenario that we are proposing for the beamed population.

1.1 Blazars phenomenology

1.1.1 Blazars signatures

Blazars constitute only a tiny fraction of the extragalactic sources, being only a few percent of the Radio–Loud population, which in turn is only a 15–20% of the total, dominated by radio–quiet AGNs. However, blazars can be readily distinguished from other AGNs by a number of properties:

① compact, core-dominated radio sources, which seems to be fundamental to the blazar phenomenon, because searches for radio-quiet examples have been unsuccessful;

② strong millimeter emitters, yielding a flat/inverted radio spectrum,

③ bright at any observable frequency, with in particular comparable radio, optical, and X-ray luminosities. Their optical counterparts dominates any host galaxy;

④ strongly variable in any observed energy band, although for some sources (different classes ?) the nature of these variations requires long term observations for proper classification;

⑤ strong (i.e. $P > 3$ %) and variable optical linear polarization, an important characteristic, because it directly indicates optically thin synchrotron emission;

⑥ strong (i.e. $P > 1 - 2$ %) and variable radio linear polarization,

⑦ superluminal motion of VLBI components;

⑧ strong γ–ray sources.

In particular properties ② and ③ reveals to be of fundamental importance in the "hunt" for blazars providing the most powerful way to look for and select them from large survey samples, where the number of candidates can be very large. In fact cross-correlation of radio and X-ray surveys catalogues is the main and powerful tool driving to the selection and discovery of new blazars, with high efficiency in finding them (expected success rate of $\simeq$ 20–30 per cent) (see e.g. Wolter et al. 1997, Perlman et al. 1998, Laurent-Muehleisen 1996).

It is worth noting that there is growing evidence that at least ②, ④ (especially referring to the optical band), ⑤, ⑥ and possibly ⑧ are basically equivalent, in the sense that are redundant and inseparable traits of a unique "character".
On the other hand there are properties which play an important role in the recognition and classification for other classes of AGNs, that do not help in distinguishing blazars:

❶ presence of strong extended radio emission,

❷ emission line widths are similar to other sources, although emission lines are (sometimes) absent in BL Lacs,

❸ infrared luminosities and colors are not distinct as a population,

❹ optical luminosities and colors are not distinct as a population.

Of these properties, ❶ and ❷ are of fundamental importance in the understanding of the blazar phenomenon, due to their probable connection with physical properties not directly related to the presence of relativistic jets oriented close to the line of sight.

Historically by focusing on one or two properties we have been able to define different types of AGNs, and in turn of blazars, growing a confused variety of classifications, partly overlapping, depending on which of the above characteristic were taken into consideration. For instance for line–emitting blazars there were available at least the names of High Polarization Quasars (HPQ), Optically Violent Variables (OVV),

and Flat Spectrum Radio Quasars (FSRQ). The distinction itself between BL Lacertae and quasar–like objects has grown in a rather confused way, eventually towards a nonsense, mainly pushed and maintained by a restrict community of researchers who progressively lost the goal, concentrating in the maintenance of this sub-classification as if BL Lacs were an endangered species.

We will treat blazars as a class, adopting different naming (like BL Lacs, FSRQ, HBL, LBL) only for sake of simplicity, considering them only as convenient conventions to grossly explain/understand what we are talking about, without ever meaning anything more fundamental.

FSRQ We will refer to quasar–like blazars as FSRQ. Eventually there seems to a reasonable agreement in this sense, that probably developed from the mere fact that from the observational point of view is far easier to recognize (and classify) a source on the basis of its radio spectrum than it is starting from polarization (HPQ) and variability properties (OVV).

BL Lacs Of course we keep the traditional name of BL Lacs for blazars with featureless optical spectrum, and/or with very low equivalent width emission lines, and for their further phenomenological subdivision we will introduce and adopt the Padovani and Giommi's HBL/LBL distinction (§ 1.2.2), having already in mind that the *BL* could eventually stay for *BL*azars. A suggestive and handy nomenclature could be that of *red* and *blue* blazars proposed by Laura Maraschi, where the color is assigned according to the energy range of the synchrotron peak, directly reminding it in a very intuitive way.

1.1.2 Blazars SED properties

In our work we concentrate on the study of the properties of the spectral energy distributions, investigating differences, similarities and, mainly, regularities. Here we just want to give some basic pieces of information, somehow anticipating the content and the results of Chapters 3– 6, in order to provide the basic terminology on which is going to be based part of the discussion of this two first Chapters.

In Fig. 1.1 we show a collection of data sketching the spectral energy distributions of a few representatives BL Lacs and FSRQ. These enable us to illustrate the main properties, namely the presence of two smooth prominent peaks, located at different energies in different sources, but with the X–ray band falling in the middle in most cases, and with the power in the γ–rays equals or exceeding the power in the infrared–optical band. According to the general accepted picture (see Chapter 2) the two broad band components are interpreted respectively as due to synchrotron and inverse Comp-

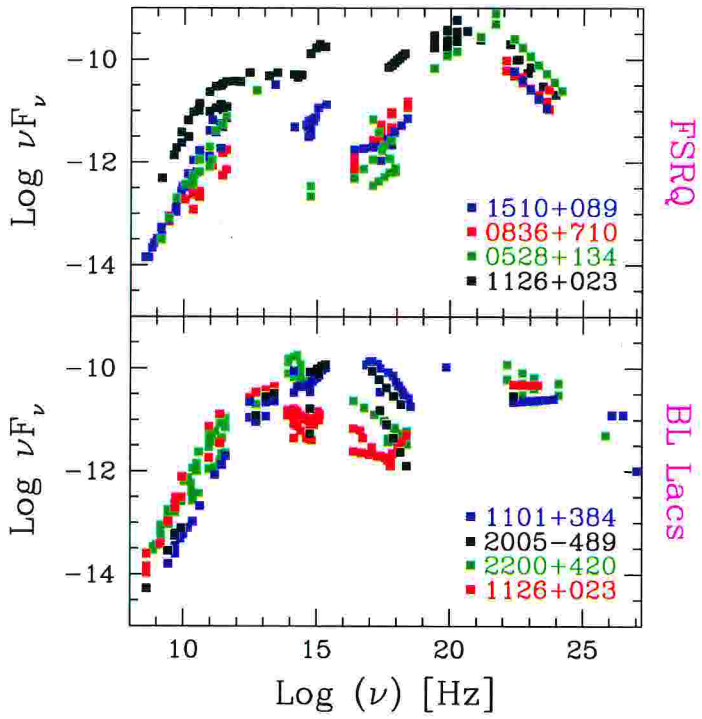

Figure 1.1: Some representatives examples of blazars spectral energy distributions, from radio to TeV γ–rays. In the top panel, FSRQs, and in the lower one BL Lac objects.

ton emission by relativistic electrons.

Why to study SED properties ?

There several reasons/advantages in studying SED:

- ✔ take into account γ–ray information: the recent discoveries of about 60 blazars emitting in the γ–ray band, by the Energetic Gamma Ray Experiment Telescope (EGRET) onboard the Compton Gamma Ray Observatory (Fichtel et al. 1994; Von Montigny et al. 1995; Thompson et al. 1995; Thompson et al. 1996) and of a few BL Lac objects by ground based Cherenkov telescope, Whipple and HEGRA (Weekes et al. 1996; Petry et al. 1996), have revealed that a substantial fraction and in some cases the bulk of their radiative output is emitted in the γ–ray range, thus allowing us to discuss for the first time the characteristics of blazars knowing their total emission output and their entire SED. Any model of high-energy gamma ray emission in blazars needs to explain this basic observational fact.
- ✔ excellent diagnostic tool for emission models. As we will discuss in the following chapters there is a handful of very interesting information that we can get

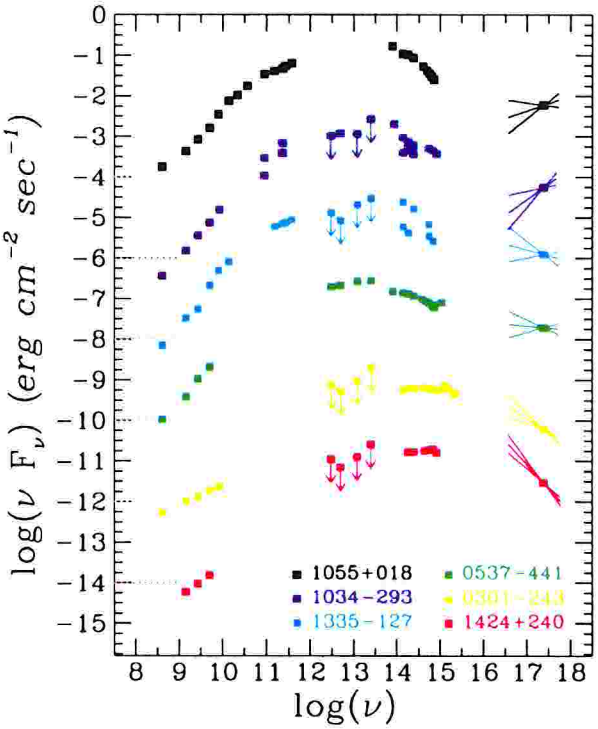

Figure 1.2: Examples of radio–X–ray SED. Sources are ordered in according to their value of α_{RO} , increasing toward the top, fluxes are progressively scaled of one decade each and their reference "zero-level" is marked with a colored segment on the left side (from Maraschi et al. 1995).

from SEDs which are quite directly related with the physical properties of the emission region, such as magnetic field and electron spectrum. As far as variability is concerned, on the one hand detailed emission models are still not good enough to reproduce and predict the observed "narrow band" fast variability features. On the other hand the status of the most critical observations, that would be simultaneous fast "broad band" tracing both the synchrotron and Compton components, is not good enough. The better assessed accessible tool is then the comparison of snapshot spectra.

✔ the striking differences: blazars SEDs show quite a large variety of behaviours, with marked and somewhat striking differences, and it is easy to recognize them only on the basis of a few observational data, thanks to.....

✔ .....the internal coherence, or at least what we see as such, linking the spectral properties in very different spectral bands, and greatly strengthening our insight. Just to give an example, in Fig. 1.2 we show the radio to X–ray SED of a few BL Lacs. They are ordered bottom to top according to the value of the radio–

optical spectral index[1] α_{RO}. It is interesting to note how the overall spectral shape changes smoothly and continuously along the α_{RO} sequence, and the same happens for the X–ray spectrum.
These characteristics and regularities are worth a deeper study, and if proven to hold would enable us to greatly improve our understanding, both because of the need to explain them, and for the fact of being themselves a powerful tool.

- ✔ robustness of the method: to support the idea just illustrated, we can look at Fig. 1.3, where about 200 sources belonging to a few complete samples of blazars are plotted in the α_{RO} *vs.* α_{OX} diagram. Data points clearly follow a pattern. Moreover there is a clear relationship between the position occupied by sources in the diagram and their spectral (but not only) properties, as we are going to argue in many occasions later on. At this stage it is enough to recognize that different samples occupy different parts of the plane. We will "learn" that different observational selections, and in turn different samples tend to select different types of blazars. The same is true also in Fig. 1.4b, where radio and X–ray luminosity are considered: different samples fill different regions.
- ✔ better and larger amount of available data/info: these last examples show a further important point, i.e. the study of SEDs allows us to use larger samples and variety of sources than it is possible, at present, by any other mean. Basically the trivial point is that the only known way to discover and select blazars, is by flux limited surveys at different frequencies and their cross-correlation (§ 1.1.1, § 5.3.2). Any other information will be available on a statistically significant basis only afterwards.

1.1.3 Other general properties

We briefly summarize the more relevant blazars properties which are not directly related to the SED phenomenology.

emission lines By definition the emission line equivalent widths of BL Lac objects are small. Since equivalent width depends both on line and continuum luminosity, a better indicator of the "strength" of the line emission, and of the physics of the source is probably the luminosity. Emission lines in BL Lacs are nearly always an

[1]Broad band spectral indices are defined as:

$$\alpha_{12} \equiv -\frac{\log(L_2/L_1)}{\log(\nu_2/\nu_1)}$$

where L_1 and L_2 are the rest–frame luminosities observed at the frequencies ν_1 and ν_2.

order of magnitude or more less luminous than those in FSRQs, although the line luminosities for a few BL Lacs approach those of FSRQs. For any given optical continuum luminosity there is substantially a continuity of line luminosities (see e.g. Fig. 10 of Scarpa and Falomo 1997). This seems to be simply a selection effect due to the definition criteria, according to which we expect to find that BL Lacs (or better still, *objects classified as BL Lacs*) have smaller line luminosities. A further and not negligible complication is introduced by the emission line variability that can be very large in some cases. This makes the object classification time dependent.

Finally, there seems to be a sequence in emission line properties with at one extreme FSRQ, and at the opposite end HBL, which really appear to have *truly featureless* optical spectra. This could be related with the fact that for these objects the maximum of the synchrotron emission is occurring right in the optical–UV band, and then likely overwhelming the emission line spectrum.

radio properties There are three major topics concerning radio observations:

- ✔ angle of polarization vector with respect to the jet axis,
- ✔ apparent superluminal speeds,
- ✔ morphology of the host galaxy extended emission.

Clear differences have emerged between the polarization properties of the parsec scale jet, observed with VLBI, in FSRQ and BL Lacs: the inferred magnetic field direction in FSRQ tends to be parallel to the local jet direction, whereas in BL Lacs jets tend to be orthogonal to it. It is usually supposed that the longitudinal magnetic fields in FSRQ are due to shear, while perhaps the most natural interpretation of the transverse magnetic field structure observed in BL Lacs is that polarized jet regions are relativistic shocks in which the transverse component of the magnetic field has been enhanced by compression.

It has sometimes been suggested that the relevant distinction is not between BL Lac objects and FSRQs but rather between *low* and *high redshift* objects. The available VLBI polarization information suggests quite strongly that this is not the case, since the transverse magnetic field in BL Lacs have been observed in both low and high redshift sources. In terms of their VLBI polarization structure high z BL Lacs more closely resemble low z BL Lacs than they do with FSRQs.

Recently it has been shown that the apparent speeds in the VLBI jets of BL Lac objects are systematically lower than those of FSRQs, although there is clearly an

overlap between the two distributions (Gabuzda et al. 1994). Again there does not appear to be a distinction between high and low redshift objects, whereas the difference between FSRQ and BL Lacs persists when considering a common restricted redshift interval.

It seems more likely that the observed systematics difference in VLBI components speeds of BL Lacs and FSRQs is associated with systematic differences in their *intrinsic* speed.

Regarding morphology of the extended radio emission, there is a difference which could be summarized by saying that BL Lacs and FSRQ have properties similar to those of Fanaroff–Riley radio galaxies of type I and II, respectively. Analyzing the extended radio structure of BL Lacs, Kollgaard et al. (1992) conclude, however, that the parent population of BL Lacs may include both FR I and FR II. Similar results were also reported by Murphy et al. (1993).

variability Blazars are known to be strongly variable in all spectral bands, from radio, IR, optical, UV, X–rays, up to γ–rays at GeV and TeV energies, and this is maybe their most striking property. The patterns of variability are usually complex, as they cover a wide range of time scales (from hours to years) and depend on the spectral band (see, e.g. Ulrich et al. 1997). Most of the variability data comes from the low energy bands, optical and radio, often spanning tens of years. These data show that, on average, the amplitude of variability is increasing with photon energy, and the same was recently discovered in the high energy spectral components, both in BL Lac objects and FSRQ. In addition to the amplitude/energy dependence within the low energy and the high energy spectral components, there is a clear trend observed in quasars showing higher variability amplitudes in the high energy spectral component than in the low-energy spectral component (see, e.g. Wehrle et al. 1998).
It is interesting to note that the largest variability is usually observed close to or above each of the two peaks and is usually in the sense of a hardening of the spectrum at higher energies.
Furthermore, *spectral* variability properties in the low (synchrotron) and high (Compton) components are more or less the same at, or above, the respective peak frequencies.

evolution it has been so far established that BL Lac objects selected in the radio band show a slight positive evolution, consistent with no evolution at the 2σ level (e.g. Stickel et al. 1991; Wolter et al. 1994). The evidence for samples of X–ray

selected objects is quite different, and again recently Wolter et al. (1994) and Perlman et al. (1996) confirmed the strong negative evolution in the X–ray band: X–ray bright objects are much less luminous or common at high redshifts. FSRQ share the general trend of positive evolution of the quasar population (e.g., for a radio selected sample Impey and Tapia 1990).

1.1.4 High energy emission

The X-ray band

The knowledge of the X–ray properties is of special relevance because in this energy range both the synchrotron and inverse Compton processes can contribute to the emission. The first mechanism is expected to produce a steep continuum in this band while the second one should give rise to a flat component ($\alpha_X \leq 1$, rising in a νF_ν plot) the shape of the X–ray spectrum can give a fundamental hint for disentangling the two components and inferring the respective peak frequencies.

variability

Further constraints on the emission mechanisms can be obtained from the variability pattern and the slope of the X–ray spectrum. As steep X–ray spectrum is expected if the emission is mainly due to the synchrotron process, the X–ray data coupled with the radio to UV spectrum allow the measurements of the peak of the SED and the determination of the physical parameters of the synchrotron emission. Rapid flux and spectral variability is expected in this case. Viceversa, a flat X–ray spectrum, expected if the emission is dominated by the Compton flux, suggests that the same process is producing both the X– and γ–ray components, which therefore should show correlated variability patterns.

X–rays in different sub-classes of blazars indeed have different origins.

- ✔ in most BL Lac objects X–ray spectra are steep ($\alpha_X \simeq 1 - 3$ in the 0.1 – 10 keV band) and variable, and lay on an extrapolation of the UV spectrum, indicating that X–rays in these objects represent high energy tails of the synchrotron component.
- ✔ in FSRQs, the X–ray spectra are usually very hard ($\alpha_X \simeq 0.5 - 0.7$), showing weaker variability than in other spectral bands. These spectra are often interpreted as low energy tails of the γ–ray components; however, one cannot exclude the possibility that they are superposed from two or more components (see § 2.6).
- ✔ then there are intermediate objects where the soft X–rays are dominated (at least occasionally) by the synchrotron component, while higher energy X–rays belong

to the high-energy Compton component (Madejski et al. 1996; Cappi et al. 1994).

The differences in the X–ray spectra seem to follow the general trend where in less luminous blazars, the peaks of the low-energy (synchrotron) component are located at higher energies (Sambruna et al. 1996; Kubo 1997).

Constraints coming from γ–rays

Discovery of strong and variable γ–ray radiation in blazars by CGRO provided an exceptional opportunity to see at work non-thermal processes, and to study the structure, energetics and matter content of jets. Some of the main results and constraints coming from the study of gamma ray emission are for instance:

- ✔ As already mentioned in the previous sections the γ–ray component contains the bulk of the power radiated by blazars jets, and its discovery provided an unprecedented challenge for emission models.
- ✔ Moreover the huge apparent γ–ray luminosities, reaching in some FSRQ $10^{48} - 10^{49}$ erg s^{-1}, show that blazar jets must indeed be very powerful.
- ✔ γ–ray observations have raised again the question as to whether and how the various subclasses differ in their γ–ray properties.
- ✔ γ–ray radiation provides independent evidence that blazar radiation is indeed produced by relativistic jets. This is because the compactness of the source derived from the observed γ- and X–ray luminosities and variability time scales is so high that if it was intrinsic (true) compactness, all γ–rays would be absorbed by $\gamma\gamma$ pair production process. This implies that the true source compactness must be much lower than the observed one, and this is the case if the observed radiation originates from plasma propagating in our direction at relativistic speed (e.g. Maraschi et al. 1992).
- ✔ γ–rays can also be absorbed by external radiation fields, and because the compactness of such fields decreases with distance, this gives the minimum distance from which the γ–rays can escape. This imposes a constraint on the location of the γ–ray emission region, where most of the energy is radiatively dissipated. In the external Compton picture this region should be located far enough from the central source to avoid attenuation of the highest energy γ–rays observed. This in turn imposes a constraint on the allowed means of transport (e.g. Poynting flux, pair dominated jet, cold e–p jet, etc...) of the energy from the very

inner region where the jet is formed. The transport should be efficient (i.e. with negligible dissipation), up to the region where energy is radiated away, since any conversion of energy to relativistic electrons and photons would lead to a catastrophic reprocessing of γ–rays to X–rays, contrary to observations.

1.2 BL Lacs: the change of perspective

In the second part of this introductory Chapter we illustrate the current ideas about the unification of the various "flavours" of blazars, in order to prepare the general framework in which we will be "moving" afterwards. We anticipate some of the original results of our work, that will be the subject detailed in this thesis and which are the basis for the formulation of the unification picture that we are proposing.

For historical reasons, and for simplicity, we first concentrate (§ 1.2.1 to § 1.2.6) on BL Lac objects. In fact, in the last few years, the more lively debate first developed within the restricted area of BL Lac research, whereas little attention has been given to FSRQs. The problem seemed to be well bounded, the available statistically complete samples were (are) a only few, and apparently there was a strong observational dichotomy in several properties, enough to attract some interest on the topic. It is then easier, and more faithful to the actual growth of ideas, to present and discuss the changes that affected the unification paradigm following the progresses as they occurred in BL Lac research field.

In the last section we then go back considering blazars as a whole. We briefly report on the main alternative ideas to relate BL Lacs and FSRQs, and we stress and again anticipate our picture of blazars as a unique phenomenon and some observational findings supporting this belief.

1.2.1 XBL & RBL

BL Lacs have been almost exclusively discovered through radio or X–ray surveys[2]. However the properties of objects selected in the two spectral bands are systematically different, posing a question as to whether there are two "types" of BL Lacs. The first difference to be recognized and perhaps still the most striking is the shape of the SED, in particular the relative intensity of the X–ray and radio emission, as first noted by Ledden and O'Dell (1985) who spoke about *X–ray normal* and *X–ray strong* blazars on the basis of their X–ray/radio flux ratio. The differences show up very clearly using broad band spectral indices and color–color diagrams, e.g. $\alpha_{\rm RO}$ *vs.* $\alpha_{\rm RX}$ (see Fig. 1.3,

[2]Hereinafter, we will refer to BL Lac selected in radio or X–ray as RBL and XBL, respectively.

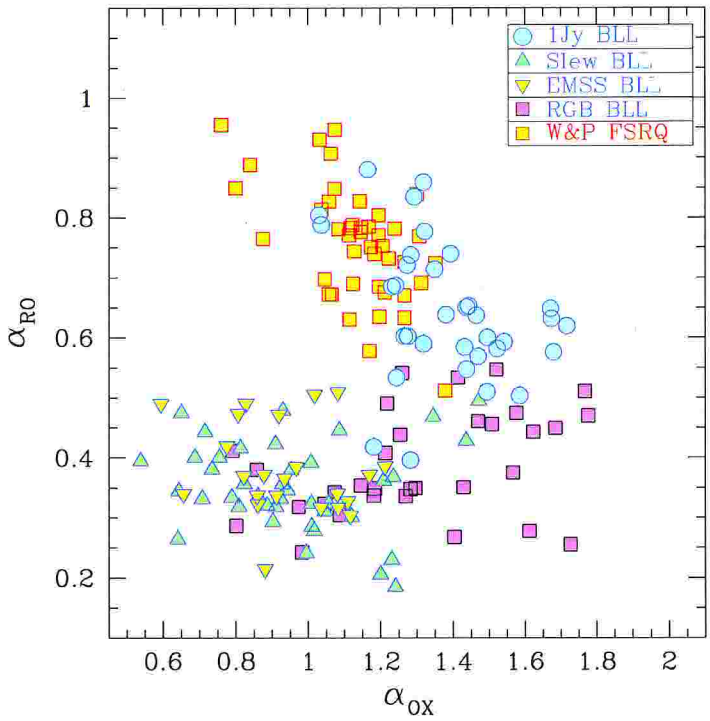

Figure 1.3: The α_{RO} *vs.* α_{OX} plane. We plot the following complete samples: 1 Jy, EMSS, Slew, *ROSAT*–Green Bank (Laurent-Muehleisen 1996) for BL Lacs, and for FSRQ the sample from Padovani and Urry (1992) (all symbols are defined in the inlet).

Ledden and O'Dell 1985; Stocke et al. 1985; Maraschi et al. 1995; Sambruna et al. 1996). Others include optical polarization, variability, presence of (weak) emission lines, radio luminosity, core–dominance, all of which are less conspicuous in X-ray selected objects (e.g. Kollgaard et al. 1992; Perlman and Stocke 1993; Kollgaard et al. 1996; Jannuzi et al. 1994; see Kollgaard 1994 for a recent review).

1.2.2 HBL & LBL

Giommi and Padovani (1994,1995) quantified the differences in SEDs between XBLs and RBLs, and introduced the distinction between "High–energy peak BL Lacs" (HBL) and "Low–energy peak BL Lacs"' (LBL), for objects which emit most of their synchrotron power at high (UV–soft–X) or low (far–IR, near–IR) frequencies, respectively.

Quantitatively a distinction can be done on the basis of the ratio between radio and X-ray fluxes, defining an objective criterion (independent of the selection band) separating two (putative) classes of objects. We define

- ✔ HBLs the objects with $\log(F_{1keV}/F_{5GHz}) \geq -5.5$ and
- ✔ LBLs the objects with a ratio smaller than this dividing value,

where the fluxes are monochromatic and expressed in the same units (see also Wurtz 1994; Giommi and Padovani 1994, for similar definitions[3]). This dividing line corresponds to a value of $\alpha_{RX} \simeq 0.72$. The definition is based on observed fluxes because the number of HBL/LBL in a flux limited sample, depends on the depth of the survey, and then on the flux limit, due to K–correction effects combined with the shape of the blazar SED, flat in radio, and steep in X–ray (for a large fraction of objects, and for the greater part of BL Lacs). Selection acts against HBLs, and we can only meaningfully speak of *detected fraction* of a kind of objects, which in some cases could be not very representative of the intrinsic one.

As can be seen from Fig. 1.4a HBLs (in this figure laying in the upper –left– half) are found mostly but not exclusively in X-ray surveys and the same is true for LBLs with respect to radio surveys.

orientation

The spread in spectral shapes and the smaller/weaker degree of activity of HBLs were originally attributed to orientation effects, namely that the X–ray radiation was less beamed than the radio one and that HBLs were observed at larger inclination to the jet axis (e.g. Stocke et al. 1985; Maraschi et al. 1986; Celotti et al. 1993).

The main support to this idea came from the observational evidence that BL Lacs discovered in radio and X–ray surveys actually show similar X–ray luminosities while the radio luminosities typically differ by two–three orders of magnitude (e.g. Fig. 1.4b). This could be accounted for if X–ray radiation had a wider beaming cone than radio emission: observers would see similar X–ray luminosities over a wide range of angles while the accompanying radio luminosity would be high for a small fraction of objects seen at very small angles and strongly dimmed for the majority, observed at larger angles (e.g. Fig. 5 in Celotti et al. 1993). Consequently the number density ratio between the two "flavours" would be determined by the associated solid angles. Since the X–ray emission is largely isotropic, X–ray surveys are not biased against any of the two classes of objects, and can give the correct number ratio. The different beaming affecting the various bands could be due to an accelerating (Ghisellini and Maraschi 1989) or an increasingly collimated jet (Celotti et al. 1993).

[3]We note that the definition of HBL and LBL by Giommi and Padovani is based on the X–ray flux in the 0.3–3.5 keV *Einstein* IPC band (in erg/cm^2/sec) and the radio flux at 5 GHz (in Jy). According to this different definition, and for average values of spectral index and N_H , the value of -5.5 adopted here corresponds to $\simeq -10.8$

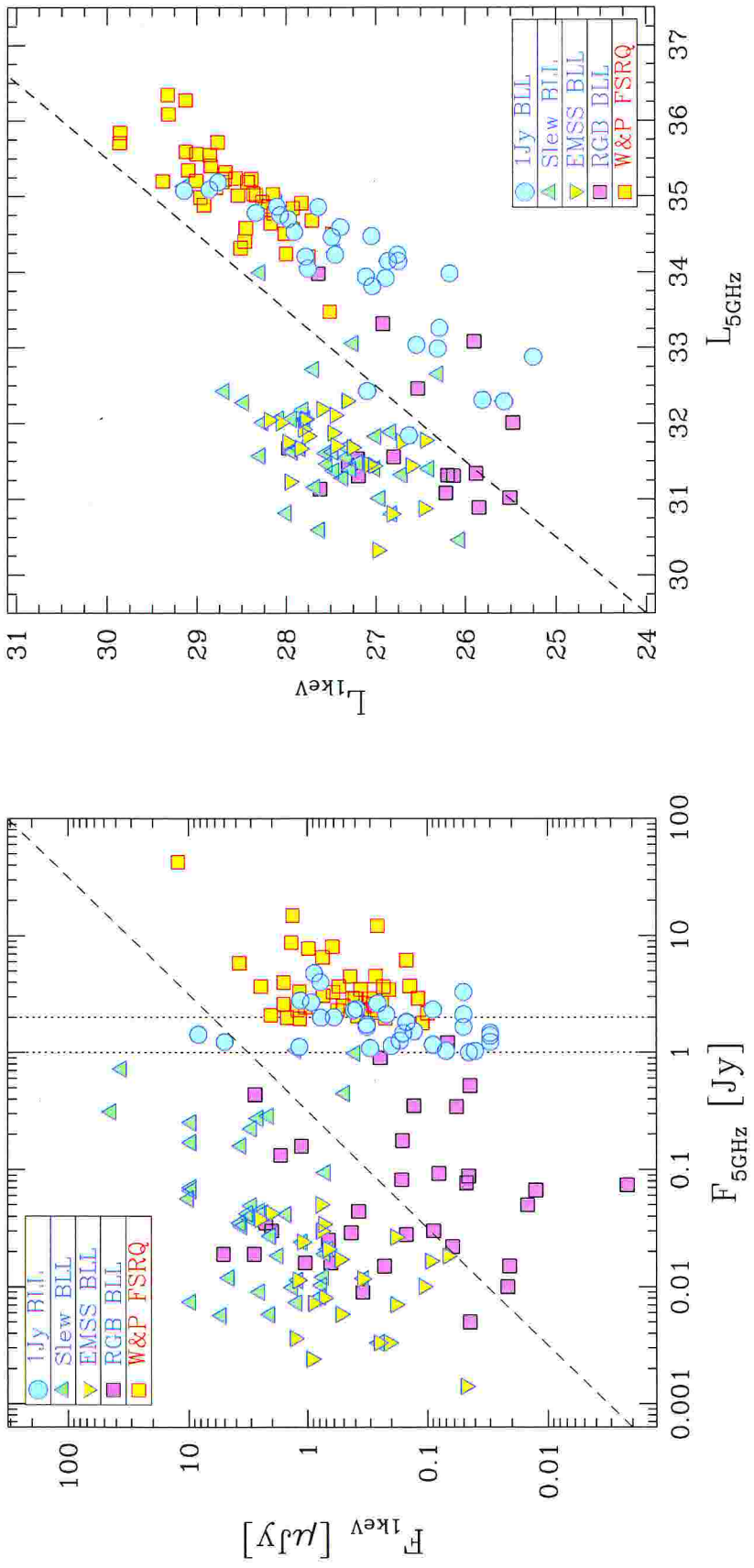

Figure 1.4: (a) The $\log F_{1keV}$ vs. $\log F_{5GHz}$ and L_{1keV} vs. L_{5GHz} plane for different complete samples: 1 Jy, EMSS, Slew, *ROSAT*–Green Bank (Laurent-Muehleisen 1996) BL Lacs, and the FSRQ sample from Padovani and Urry (1992) (all the corresponding symbols are defined in the inlet). The vertical line represents the 1 Jy and 2 Jy flux detection limits, while the dashed line defines the separation between HBL and LBL. (b) Distribution of luminosities for the same source samples. Only objects having at least an estimate of the redshift are plotted. The oblique line indicates the values of L_{1keV}/L_{5GHz} roughly corresponding to the definition of LBL and HBL.

1.2.3 From "different viewing angle" to "different peak energy"

Substantial progress in the data on the SEDs of BL Lac objects has been obtained in recent years, in terms both of sensitivity and statistics, especially in the X-ray band[4], which is particularly insightful (see § 1.1.4).

This lead to a definite and fundamental improvement of our knowledge of the phenomenology of spectral energy distributions which is nowadays quite stably assessed. In terms of the power emitted per decade HBLs display a continuous rise up to the UV and in extreme cases the soft X–ray band, while LBLs are characterized by a spectral turn over in the IR domain. In HBLs the X–ray emission is dominated by a soft spectral component which extrapolates continuously to lower frequencies. In LBLs the X–ray emission is dominated by a separate harder component which at least in some cases extends to the γ–ray domain. A hard GeV to TeV component is present also in HBLs though it does not show up in medium energy X-rays (e.g. Von Montigny et al. 1995, Lin et al. 1997).

"ruling out" viewing angle

Sambruna et al. (1996) then showed that it is difficult to model the detailed transition from an HBL to an LBL SED in terms of orientation only and suggested rather a continuous change in the physical parameters of the jet. If the main role is played by the aspect angle θ of the jet with respect to the observer, the important parameter is the relativistic Doppler factor δ. Energy (and then peak position) goes as $\nu_{\rm peak} \sim \delta$, while luminosity changes as strongly as $\mathrm{L} \sim \delta^{3-4}$ (see Chapter 2, § 2.2 for definition and details). For a jet with a bulk Lorentz factor $\Gamma = 10$, $\delta \simeq 10$ for $\theta \simeq 5°$, and $\delta \simeq 0.4$ for $\theta \simeq 40°$, with a change of only slightly more than one order of magnitude. It is immediate to see that a change of the value of δ by a factor 10, shifts the peak up by one decade, but at the same time luminosity will increase by at least a factor $\gtrsim 1000$. We would end up having a strong trend with most luminous sources peaking at the highest energies, contrary to known phenomenology. Even worse is the fact that in any case it would be very difficult to account for the whole (broad) range of values covered by synchrotron peak frequencies ($10^{13} - 10^{18}$ Hz, see Chapter 5) with only a change in the viewing angle without changing in correlated way any other source property. Summarizing: *angle certainly plays a role, but it cannot be the leading parameter.*

It is then necessary to reconsider the HBL/LBL phenomenology in a new perspective. The two main options are:

[4] e.g. Giommi et al. (1995), Comastri et al. (1995), Comastri et al. (1997), Lamer et al. (1996), Perlman et al. (1996), Perlman et al. (1996), Padovani and Giommi (1996), Urry et al. (1996), Sambruna et al. (1996), and more is coming with the strong observational programs with *Beppo*SAX, covering an unprecedented wide band between 0.1 and $\simeq$ 200 keV.

- ✔ the *nature of the source* is different, there is a real dichotomy, and we are dealing with truly different phenomena, or
- ✔ they are different manifestations of an intrinsically identical phenomenon, but the *physical conditions* of the emitting material are different.

On the basis of the substantial continuity in their properties, strongly contrasting the idea of dichotomy, the fundamental ingredient to carry on a trustworthy "different nature" scenario, we think that HBLs and LBLs are *different representatives of a more complex phenomenology*, based on the variety of physical conditions.

1.2.4 Radio leading scenario

Giommi & Padovani

The first model developed along this line to explain the "statistics" of HBLs and LBLs is the "radio luminosity + different energy cutoff" scenario by Giommi and Padovani (Giommi and Padovani 1994; Padovani and Giommi 1995; hereafter we refer to it as the radio leading scenario) alternative in many ways to the commonly accepted "different viewing angle" model sketched above.

They propose that a single luminosity function in the radio band describes the full BL Lac population. For each radio luminosity X–ray bright BL Lacs (i.e. HBLs) are intrinsically a minority described by a fixed, *luminosity independent* distribution of X–ray to radio flux ratios. In X–ray surveys however selection effects substantially enhance the HBL fraction. According to this approach the intrinsic fraction of the two types of BL Lac (HBL *vs.* LBL) would be objectively reflected in radio surveys. With these hypotheses Giommi and Padovani were able to reproduce the observed X–ray counts, luminosity functions and the distribution of BL Lacs in the $\alpha_{RO} - \alpha_{OX}$ plane (Padovani and Giommi 1995).

The basic radio leading hypothesis (Giommi and Padovani 1994; Padovani and Giommi 1995) is that radio selection would be objective with respect to the intrinsic spread of broad band spectral properties. The underlying idea is that the radio emission is only weakly affected by the properties of the synchrotron component at higher energies, such as the peak frequency. Therefore the radio selection is not expected to suffer of any bias regarding the SED shape properties and sources with different X–ray/radio luminosity ratios are sampled from a common radio luminosity function.

In this approach, the X–ray counts (and X–ray luminosity function) are easily predictable from the radio counts (and radio luminosity function) and the results can be compared with real data coming from surveys. It is worth reminding that there are essentially no free parameters in the model.

According to this scenario, the observational evidence that HBL objects are more numerous, apparently in contradiction with their assumption that HBL sources are intrinsically only 1/10 of the entire population, is due to selection effects. In fact, given their F_{1keV}/F_{5GHz} ratios, HBL have a relatively low radio flux. Therefore, at the same X–ray flux level we are detecting together BL Lacs belonging to different parts of the radio luminosity function, with LBLs coming from a brighter but poorer part of it.

The proposal of this simple, successful idea and its controversial meaning, suggested us to elaborate and investigate other unifying pictures for BL Lac objects, which could eventually include also FSRQ.

1.2.5 X–ray leading scenario

Beside the radio leading model we consider the "symmetric" alternative, assuming that the common property of HBL and LBL is the X–ray luminosity. i.e. that the X–ray luminosity function basically represents the whole BL Lac population. In this case X–ray surveys would give objective results regarding the intrinsic abundance of HBLs and LBLs. This scenario, which we refer to as the X–ray leading model, can be considered as an evolution of the "different viewing angle" scenario, where the X–ray luminosity was the basic property and the population ratio reflected the ratio of solid angles.

As already mentioned, this idea originally comes from the observational evidence that BL Lacs discovered in radio and X–ray surveys show similar X–ray luminosities, while the radio luminosities typically differ by two–three orders of magnitude. This is in general true also if the distinction between the two types of sources is made in terms of the HBL/LBL classification as formally defined in Section 1.2.2 (see also Fig. 1.4a).

1.2.6 Unified bolometric scenario

In Fossati et al. (1997) we proposed a further completely alternative way of facing the HBL/LBL issue, a new unified picture, in which the key feature is a link between the shape of the SEDs, in particular the peak frequency of the synchrotron power distribution, and the bolometric luminosity. In particular, we parameterize the shape of the SED in terms of its synchrotron peak frequency.

We wanted to take into account the properties of the overall observed SED of BL Lacs, as well as recent indication of a possible link, along a continuous sequence, between the SED shape and the source luminosity (e.g. Sambruna et al. 1996; Fossati et al. 1998; Ghisellini et al. 1998).

The fundamental hypothesis of the model is still that HBL and LBL sources are manifestations of the same physical phenomenon. The new ingredient is the idea that HBLs and LBLs are different representatives of a spectral sequence that can be described in terms of a single parameter, which we identify with the *bolometric luminosity of the synchrotron component*, $L_{bol,sync}$. Both "flavours" of BL Lac objects share the same bolometric luminosity function and the SED properties depend *strongly* on this quantity.

The main positive feature of this approach is that it offers a more direct interpretation in terms of the physical properties of the sources. In fact:

① the assumptions are largely independent of the details of the observed statistical samples and moreover they are not based on the choice of a leading spectral band;

② it is based on the relative dependence of two quantities which are strongly related to the physical properties of the emitting plasma, namely the emitted luminosity and the cut–off in the synchrotron spectrum. One can therefore speculate on the physical origin of this dependence.

Moreover the "bolometric" picture can be *naturally extended to include also FSRQ*, as we will discuss in Chapter 3.

* * * * *

A representation of the main features of the presented scenarios is shown in the cartoons of Fig. 1.5a,b,c.

The radio and X–ray leading models (see Fig. 1.5a,b) are symmetric, and differ in the choice of the leading parameter, i.e. the radio and X–ray luminosities, respectively. These scenarios, being purely phenomenological, can be constructed from observed properties, like the probability distribution $\mathcal{P}(L_{1keV}/L_{5GHz})$ of the flux ratios and the luminosity functions, with basically no free parameters.

One important characteristic of these two scenarios is that they assume that the fraction of each HBLs and LBLs is *constant* at any epoch and, even more relevant, for any source luminosity.

The "unified bolometric" model (see Fig. 1.5c), is based too on observational trends, however has the peculiar characteristic to link the bolometric luminosity with the energy of the synchrotron cut–off. It starts directly from a unified description of the BL Lacs spectral energy distribution.

We will see in Chapter 3 that they can all correctly predict a significant number of quantities in agreement with current observations, though they (and in particular the radio leading one) fail to reproduce some of the observed distributions.

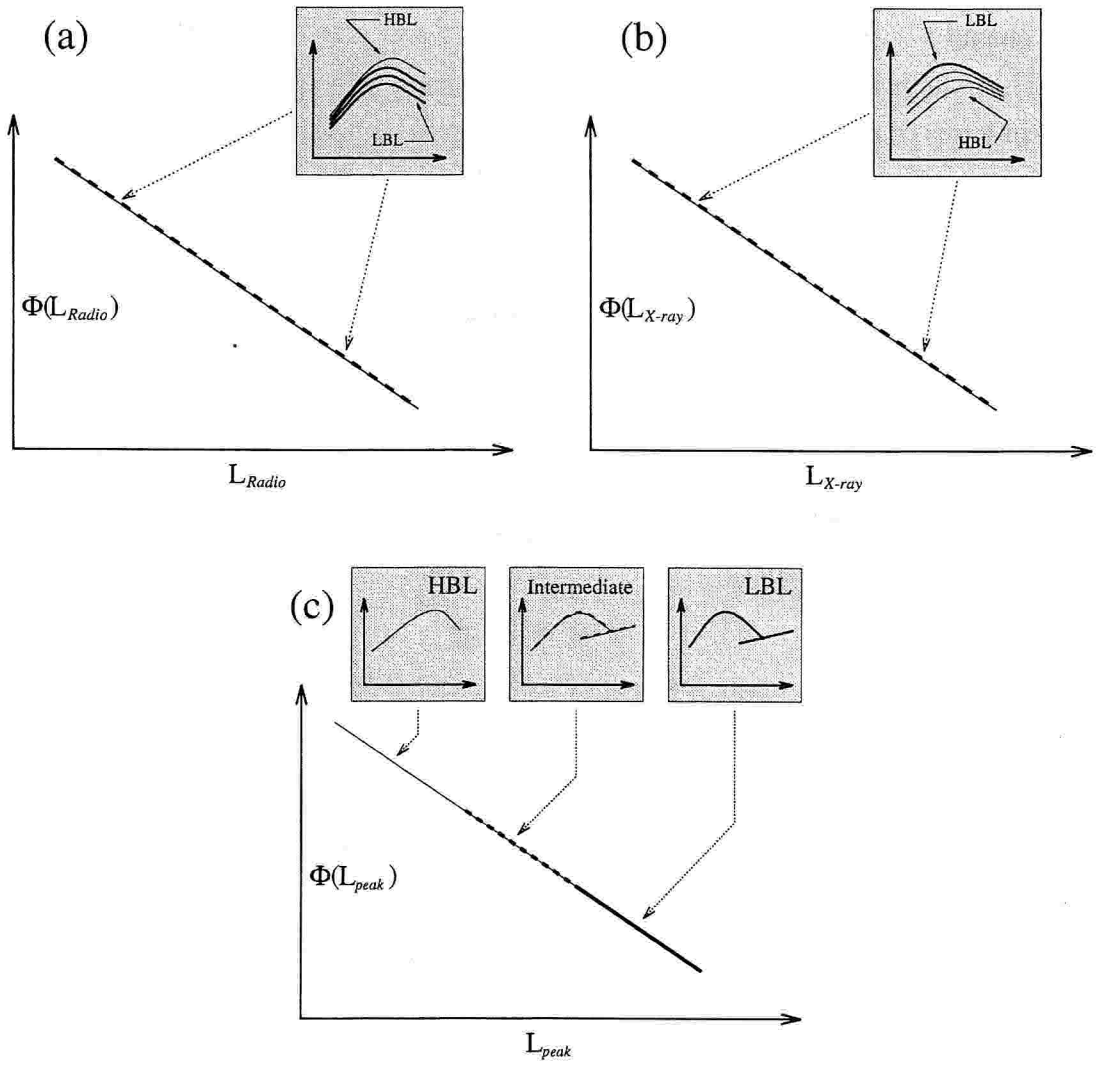

Figure 1.5: Cartoons resuming the basic features and differences between (a) the radio leading, (b) the X–ray leading and (c) the unified bolometric scenario. The plane defined by the two axis shows the leading luminosity function. As shown in the panels in the first two schemes the SED distributions and populations ratios are independent from luminosity, while the bolometric approach links the type of source (i.e. the SED) with the luminosity. The schematic SED represented with thick and thin lines always refer to LBL and HBL, respectively, and the number of SEDs in each panel is suggestive of the relative number density of sources.

1.3 BL Lacs and FSRQ

After this introduction to set the renewed framework in which the study of BL Lacs properties is now being discussed, we would like to summarize the current ideas about the relationship between BL Lacs and quasar-like blazars. There are several ways in which these *different* types of objects might be related. For example they could be:

① *identical*, except that their emission is *anisotropic* and we view them from different angles;

② *identical*, except that they (individual objects) have either stochastic or regular variations in their behavior, which change their observed properties into those of another class;

③ *evolutionary stages* of the same physical objects;

④ *based on the same physical process*, but differing in some critical parameter, such as the central massive object, or the accretion rate;

⑤ *definitely different*.

anisotropy

About ①, we already discussed the arguments against it in relation to BL Lac objects. It would remain the possibility of interpreting the differences between FSRQ and BL Lacs, as effect of different orientation, and in turn different amount of beaming. BL Lacs would be featureless because of the greater beamed jet emission washing out emission lines. They would represent the most extreme version of FSRQs, i.e. those with the most highly boosted continuum. Actually this picture is ruled out both on the beaming and the emission lines sides, because not only BL Lac are less beamed than FSRQs, but also they have *intrinsically* weaker emission lines.

evolution

Points ② and ③ are somewhat difficult to address, and it can even be true that there is an evolution of individual sources from FSRQ to BL Lac properties, or viceversa. There have been several proposals of unification schemes based on the cosmological evolution of some fundamental property, triggering different phenomenologies at different epochs. Vagnetti and collaborators (Vagnetti et al. 1991; Vagnetti and Spera 1994) proposed that the average bulk Lorentz factor of the jet increases with cosmic time, and thus the ratio between beamed and not-beamed emission components is changing with redshift, with BL Lacs objects preferentially found nearby, and FSRQ dominating at earlier epochs. On one hand, this picture has to overcome the same problems of point ①, concerning emission lines and beaming, and on the other hand available data do not show any continuity in redshift between FSRQ and BL Lacs.

They are both present at low z, always occupying different but adjacent regions of "parameter spaces". .

Other possibly important physical parameters are the environment and the characteristics of host galaxies (e.g. gas content). They are plausibly changing with cosmic time, and they could certainly play an important role in determining the accretion rate on the central black hole, its angular momentum, and the conditions of propagation of jets.

same phenomenon

We would like to put more emphasis on the hypothesis ④. We have already mentioned (in § 1.1.3) the observational situation with respect to emission lines properties. The main points is that although the division in emission line luminosities separating BL Lacs and FSRQ is not sharp, a systematic difference between the two classes does clearly exist.

Moreover, the fact that some other phenomenological properties (see e.g. § 1.1.3) are systematically different for BL Lacs and FSRQs corroborate the idea that the optical observational distinction between these sources is not arbitrary, but rather has some physical basis.

However, it is worth stressing that the phenomenology of BL Lacs and FSRQs is strictly "contiguous", and in some sense complementary, basically in any observed property. For instance the inclusion of FSRQ in $L_{1keV} - L_{5GHz}$ and colour–colour distributions shows an interesting continuity of their properties with those of BL Lacs (see Fig. 1.3, and Figs. 1.4a,b and more examples in the following Chapters), and in those cases where there is a trend/correlation between two quantities, this is always strengthened considering together BL Lacs and FSRQs (see Fossati et al. 1997; Fossati et al. 1998; Ghisellini et al. 1998).

The morphology of the extended radio emission of some LBL (see Kollgaard et al. 1992; Perlman and Stocke 1993), and the radio luminosity functions of RBLs and FSRQ also show continuity (Maraschi and Rovetti 1994).
On these basis we exclude that BL Lacs and FSRQ are *definitely different* (⑤).

* * * * *

All these pieces of evidence lead to the suggestion that there is actually a remarkable progression in properties. We propose that blazars can be unified in terms of a *luminosity sequence* HBL–LBL–FSRQ, which is also a sequence of increasing importance of emission lines. It is very unlikely that the pieces of evidence illustrated here, and those that we will discuss hereinafter, result from chance coincidence or from yet another cosmic conspiracy. They rather point to an underlying physical mechanism operating in both classes of objects: they would simply be different *"flavours"* of a single

family, where the physical processes are essentially similar allowing for some scaling factor(s). The identification of these scaling factors would represent a substantial progress in the understanding of the blazar phenomenon.

CHAPTER 2

MODELS

2.1 Overview

The blazars broad band spectra consist of two broad components: one at low energy, peaking (in νF_ν) between the infrared and soft X–ray band, the other at high energy, peaking in γ–rays. The overall energetics is often dominated by the latter, by as much as two–three orders of magnitude over the former. Both components show rapid large-amplitude variability, which indicates a very compact emission region.

Most current models for the structure of blazars, to avoid the problems with excessive opacity of γ–rays to pair production, invoke beaming of the emission from the radiating plasma moving in a jet pointed close to the line of sight towards the observer, in an analogy to the jet-like structure inferred from other observations.

2.1.1 Radiative processes

synchrotron

The non-thermal shape of the spectrum of the low-energy component as well as its polarization suggest synchrotron emission.

On the other hand several models, still in competition, have been proposed to explain the γ–ray emission and the overall SED of blazars.

inverse Compton

A flat *inverse Compton* component due to upscattering of the low energy photons is expected to emerge at high energies as originally discussed in Jones et al. (1974a)

and Jones et al. (1974b). The latter process is therefore a plausible candidate to explain the γ–ray emission. Specific models differ in the adopted geometry (one–zone homogeneous models or inhomogeneous jet models), and in the nature of the target photons which are upscattered in energy by the inverse Compton process.

SSC

Production of high energy radiation was predicted many years ago by synchrotron-self-Compton (SSC) models (Königl 1981; Marscher and Gear 1985). In this process, the same electrons that produce synchrotron radiation also upscatter some of synchrotron photons to γ–ray energies. However, as was recently recognized, the SSC process is not necessarily the one which produces most of the γ–rays. The competing process, at least in quasars, may be the Comptonization of external radiation. Models based on this process are called ERC (External Radiation Compton) and their original variants have been investigated by Dermer et al. (1992), Sikora et al. (1994), Blandford and Levinson (1995), Ghisellini and Madau (1996).

ERC

The target photons for ERC process could be produced in the accretion disk (Dermer et al. 1992; Dermer and Schlickeiser 1993), or in the Broad Line Region (BLR). The BLR itself can be either illuminated by the disk (Blandford 1993; Sikora et al. 1994; Blandford and Levinson 1995), or self–illuminated by the jet (*Mirror Model* by Ghisellini and Madau 1996; Bednarek 1998). Finally, target photons could be produced by a dusty torus surrounding the blazar nucleus (Wagner et al. 1995; Sikora et al. 1997). All these different scenarios have been tested on specific sources, but often more than one model can reproduce the same data with similar accuracy (see Von Montigny et al. 1997 for 3C 273; Ghisellini et al. 1996 for 3C 279; Comastri et al. 1997 for 0836+710).

Comparison of the energy densities of the external radiation fields with the energy density of the synchrotron radiation field (both as measured in the jet comoving frame) suggests that while the SSC model may be adequate to explain the γ–ray emission for BL Lac objects, the ERC models are probably more applicable for flat spectrum radioquasars (FSRQ) (see e.g.. § 2.5.2).

Proton blazar

Production of γ–rays is also predicted by so-called hadronic models, where ultrarelativistic electrons are injected by relativistic protons (Mannheim and Biermann 1992; Mannheim 1993; Bednarek 1993; Dar and Laor 1997). Mannheim (1993) proposed that shock–accelerated electrons and protons give origin to two different populations of particles (electrons and electron–positron pairs), responsible of the entire SED through synchrotron emission.

2.1.2 Inhomogeneous *vs.* homogeneous

The fact that the synchrotron components extend up to UV, and even X–ray bands indicates that jets contain highly relativistic electrons, with Lorentz factors up to $\gamma \simeq 10^4 - 10^6$ (see § 2.3).
Energy losses of such electrons are so rapid that they must be (re-)accelerated/injected *in situ*, i.e. at the locations where they radiate. These locations should be sites of the energy dissipation, which propagate along the jet at moderate ($\Gamma \sim 10$) relativistic speeds.

shock-in-jet

The best developed detailed model of blazar spectra is then based on a shock front moving down a jet (Marscher and Gear 1985).

Part of the available energy is converted to relativistic electrons and protons. The dissipation/shock can result from interaction of the jet with external "obstacles", and/or collisions of inhomogeneities in a jet (Blandford and Konigl 1979).

inhomogeneous

Both the magnetic field and the particle distribution could vary with position, and the observed radiation is a superposition of emission from different parts along the jet (e.g. Ghisellini et al. 1985; Maraschi et al. 1992; Marscher and Travis 1996; Levinson and Blandford 1995). These models are generally called *inhomogeneous*.

However, recent results concerning the rapid variability of blazar sources at all frequencies (see recent reviews by Wagner and Witzel 1995 and Ulrich et al. 1997) and the detection of their emission at energies of up to at least 10 TeV (Aharonian et al. 1997; Protheroe et al. 1997; Catanese et al. 1998) have provided new restrictions on the possible acceleration mechanisms. Especially the observed simultaneous variations in X–rays and TeV gamma-rays (Takahashi et al. 1996; Fossati et al. 1998) indicate that a single population of particles in a relatively localized region is responsible for the emission. Consequently, *homogeneous* models have been widely discussed and there is rough agreement on the parameters of the emission region (Dermer and Schlickeiser 1993; Macomb et al. 1995; Macomb et al. 1996; Bloom and Marscher 1996; Ghisellini et al. 1996; Inoue and Takahara 1996; Comastri et al. 1997; Mastichiadis and Kirk 1997; Stecker et al. 1996).

homogeneous

Proton blazar

PIC

In contrast to these models, the proton-initiated cascade (PIC) model (Mannheim and Biermann 1989; Mannheim and Biermann 1992) predicts that the high-energy emission comes from knots in jets as a consequence of diffusive shock acceleration of *protons* to energies so high that the threshold of secondary particle production is ex-

ceeded.

Actually, in all particle acceleration processes, the injection of relativistic electrons is accompanied by injection of relativistic protons, whose energy can be converted to high energy radiation via processes as direct synchrotron radiation of protons, γ-p pair production, and photomeson production which is the dominant process giving rise to the PIC, in typical blazar condition, the critical parameter being the ambient photon field.

The weakness of the "proton blazar" model is that it requires fine tuning in order to explain the striking regularities in the shape of broad band spectral energy distributions (see Chapters 4, 5, 6), because in principle it is very difficult to "stabilize" the energy of the second synchrotron peak (that due to electrons emerging from the PIC). This is in fact strongly dependent on the initial maximum proton energy, which in turn does not have a firm relationship with that of the directly shock-accelerated electrons.

variability and PIC

A further problem is to avoid excessive X–ray production from $\gamma\gamma$ pair production, that would require an *ad hoc* solution. Finally, simultaneous variability of emission at widely differing wavelengths is more easily interpreted in terms of directly accelerated electrons rather than in the hadronic models, in which only the optical–UV photons arise from directly accelerated electrons.

* * * * *

In the remainder of the Chapter we will first present the basic formulae of relativistic beaming (§ 2.2) and synchrotron and inverse Compton emission processes (§ 2.3), and we then illustrate some examples of constraints and estimates on models that can be derived from the very basic SED properties. We will refer to the emission from where most of the emission comes as *blob*, meaning a region throughout which physical conditions are homogeneous (see also 2.3). This can be more realistically identified with a shocked region, moving along the jet.

Unless otherwise noted we use *primed* variables for quantities measured in the *blob* comoving frame, specifically frequencies, luminosities, energy densities. The electron Lorentz factor γ, the magnetic field B, instead will not be primed, as always referring to the comoving frame. Moreover we drop all the cosmological *redshift* terms, assuming that the observed quantities are already shifted back to their rest frame value, e.g. $\nu_{\rm em} = \nu_{\rm obs}(1+z)$.

2.2 Effects of relativistic beaming

Superluminal motion

Consider a relativistic jet characterized by a velocity βc, corresponding to a bulk Lorentz factor Γ ($\equiv \sqrt{1-\beta^2}$), and an observer looking at it with an angle θ with respect to the jet axis. The observer will measure an apparent transverse speed $\beta_{\rm app}\, c$ of the discrete components moving along the jet equal to:

$$\beta_{\rm app} = \frac{\beta \sin\theta}{1-\beta\cos\theta} \tag{2.1}$$

For a moderately relativistic jet this can easily exceed 1 (e.g. $\beta = 0.9$, $\theta = 45°$ $\rightarrow \beta_{\rm app} \simeq 1.7$), yielding an apparent motion faster than the speed of light, from which the well known phenomenon of the *superluminal motion*. The effect is maximized for $\cos\theta = \beta$, with $\beta_{\rm app} = \gamma\beta$.

Doppler boosting

The characteristics of the emission from the moving material as seen by the observer at rest are altered with respect to those measured in the blob comoving frame. Hereinafter primed quantities will refer to the blob rest frame.

Due to relativistic aberration effects, the radiation emitted isotropically in the blob is *beamed* in a narrow cone in the direction of motion[1]. Photons emitted in the blob frame at an angle $\theta' = \pi/2$ with the direction of the jet, are seen in the observer frame at an angle $\theta = 1/\Gamma$. As a consequence of this the intensity of the emission is increased for an observer looking close to the jet (approaching) direction, while it is decreased for mis–aligned observers. *beaming effects*

The fundamental parameter is the relativistic Doppler factor:

$$\delta = \frac{1}{\Gamma\,(1-\beta\,\cos\theta)} \tag{2.2}$$

which rules the conversion between the blob and observer reference frames. The Doppler factor reaches its maximum value for $\theta = 0°$, namely $\delta \simeq 2\Gamma$,

It is worth noting, and convenient to remind, that at the angle $\theta = 1/\Gamma$, for $\Gamma \gg 1$, such that $\sin\theta \simeq \theta$, happens that $\theta = 1/\Gamma$

$$\delta \simeq \Gamma \simeq \beta_{\rm app}$$

[1] angles are transformed as $\cos\theta = (\beta + \cos\theta')/(1+\beta\cos\theta')$.

The basic relationships for frequency, time, specific intensity, and volume emissivity are the following, where primed quantities refer to the blob frame:

$$\begin{aligned} \nu &= \delta\,\nu' \\ t &= \delta^{-1}\,t' \\ I_\nu(\nu) &= \delta^3\,I'_{\nu'}(\nu') \\ j_\nu(\nu) &= \delta^2\,j'_{\nu'}(\nu') \end{aligned} \tag{2.3}$$

For isotropic emission $I'_{\nu'}$ does not depend on the angle and then the flux density $F'_{\nu'}$ obey the same transformation. For a power law spectrum $F'_{\nu'}(\nu') \propto \nu'^{-\alpha}$, and a moving *isotropic spherical* source, we have

$$F_\nu(\nu) = \delta^{3+\alpha}\,F'_{\nu'}(\nu) \tag{2.4}$$

The additional factor δ^α results from the fact that we are comparing now the emission in the blob frame at the same frequency at which we are observing, and not at $\nu' = \nu/\delta$. For the case of a continuous jet the exponent of the Doppler beaming factor is $p = 2 + \alpha$, because one power is missed in the integration over the emitting volume (Lind and Blandford 1985; Ghisellini et al. 1993). For the luminosity:

$$L_\nu = \delta^p\,L'_\nu \tag{2.5}$$

where again $p = 2 + \alpha$ or $p = 3 + \alpha$ for a continuous jet or a spherical source.
If flux, luminosity and energy density, are integrated over a frequency band:

$$F = \delta^q\,F' \tag{2.6}$$

$$L = \delta^q\,L' \tag{2.7}$$

$$U = \delta^{q-1}\,U' \tag{2.8}$$

where $q = 3$ or $q = 4$ for a continuous jet or a spherical isotropic source, and the integration limits are suitably transformed from on frame to the other ($\nu = \delta\,\nu'$). It is important to remind that this is approximately the case also for νF_ν fluxes and νL_ν luminosities, for which we will then use 2.6 and 2.7.

ERC exceptions

equilibrium Lorentz factor

However in the case of the ERC, Compton scattered radiation, as measured in the blob comoving frame, have quasi-isotropic distribution only for $\Gamma \simeq \Gamma_{\rm eq}$, where $\Gamma_{\rm eq}$ is the Lorentz factor at which the drag force of the external radiation field on the blob is zero (Sikora et al. 1996), which for typical blazar parameters is $\Gamma_{\rm eq} \simeq 2 - 4$, lower

than observed Γ. For $\Gamma > \Gamma_{\rm eq}$ the external radiation is seen by the emitting cloud of plasma moving as coming from the front, and the Compton scattered radiation is produced with a highly anisotropic distribution. As measured in the observer frame, ERC radiation is beamed more strongly than the synchrotron and SSC radiation and the exponent changes to $p = 4 + 2\alpha$ (Dermer 1995).

However, for a given total emitted luminosity, the respective observed luminosities for SSC or ERC are also comparable, if averaged over a cone of semi-aperture $1/\Gamma$, corresponding to the "relevant" part of the emission pattern.

$U'_{\rm ext}$ *vs.* $U_{\rm ext}$

A further important relationship that changes in the ERC case with respect to the general one, is that for the transformation of the energy density of the external radiation, which does not obey eq. 2.8, but has weaker dependence:

$$U'_{\rm ext} \simeq \Gamma^2 U_{\rm ext} \simeq \delta^2 U_{\rm ext} \tag{2.9}$$

This is valid under the assumption that the emitting blob is moving inside a volume filled with photons, which are then approximately surrounding and approaching it isotropically (Sikora et al. 1994). In the blob comoving frame about half of the external photons are thus seen beamed within the $\theta' \lesssim 1/\Gamma$ cone, and blue-shifted. On the other hand, the average frequency of the ambient photons entering the blob from all directions is $\nu'_{\rm ext} \simeq \Gamma \nu_{\rm ext}$, if they are narrowly distributed around $\nu_{\rm ext}$. The factor Γ results from the averaging of the blueshift of the frequency of the external radiation when entering the blob, weighted on the aberrated energies and solid angles.

$\nu'_{\rm ext}$ *vs.* $\nu_{\rm ext}$

2.3 Synchrotron and inverse Compton (SSC & ERC)

As discussed the SED of blazars is explained in terms of synchrotron and inverse Compton emission, by possibly a unique electron population. In this section we review the basic equations which are necessary to investigate the physics of the emitting blob starting from the study of the spectral properties. The most important features of the SED are the frequencies and the luminosities of the synchrotron and inverse Compton peaks, and we will focus on the relationships among them.

the picture

We restrict to the *homogeneous* case, assuming that the radiation is emitted by a single blob emitting isotropically in its rest frame, with a tangled magnetic field B, and size R. The blob moves through an external (isotropic) radiation field of energy density $U_{\rm ext}$, resulting from a fraction ξ of the observed $\rm L_{ext}$ (disk emission, broad line region emission, etc...) which is reprocessed/scattered and "available" to the blob, within a "reprocessing/scattering volume" of radius $R_{\rm ext}$. This external radiation field is assumed to have a peaked ($\nu \rm L_\nu$) spectrum, with a characteristic frequency $\nu_{\rm ext}$, which

will be blueshifted in the blob reference frame at $\nu'_{\rm ext} = \Gamma\,\nu_{\rm ext}$. As mentioned before, dealing νL_ν spectral distribution then the appropriate factor for the transformation of luminosities is $q = 4$.

In equations we will express the quantities in the more compact and convenient form $X_n \equiv X/10^n$.

Frequencies and powers

For isotropic magnetic field and electron momentum distribution, the emitted synchrotron and inverse Compton photon frequencies for electron having Lorentz factor γ are:

$$\nu_{\rm sync} = \frac{4}{3}\,\gamma^2\,\nu_L \tag{2.10}$$

(where $\nu_L = eB/(2\pi m_{\rm e}c) \simeq 2.8 \times 10^6\,B$ Hz is the Larmor frequency)

$$\begin{aligned} \nu_{\rm sync} &\simeq 3.7\cdot 10^6\,\gamma^2\,B \quad {\rm Hz} \\ \nu^{\rm out}_{\rm comp} &\simeq \frac{4}{3}\,\gamma^2\,\nu^{\rm in} \end{aligned} \tag{2.11}$$

that can be considered monochromatic, since the emitted powers are peaked at these values. It is worth reminding that Compton scattering becomes less efficient at high energies, in the so called *Klein-Nishina regime*, resulting in a strong reduction of the scattering cross section. The reduction has a threshold depending on the energies of both electrons and photons, namely $\gamma\,h\nu/m_{\rm e}c^2 \gtrsim 1$. For instance for an electron with Lorentz factor $\gamma = 10^4$, the scattering is less efficient for photons having $h\nu \gtrsim 50$ eV.

Klein-Nishina

The corresponding emitted powers, i.e. electron cooling rates, for synchrotron, SSC and ERC (e.g. Rybicki and Lightman 1979, and Sikora et al. 1996 for ERC) are:

$$\dot\epsilon_{\rm sync} = \dot\gamma_{\rm sync}\,m_{\rm e}c^2 = \frac{4}{3}\,\sigma_{\rm T}c\,\gamma^2\,U'_{\rm B} \tag{2.12}$$

$$\dot\epsilon_{\rm SSC} = \dot\gamma_{\rm SSC}\,m_{\rm e}c^2 = \frac{4}{3}\,\sigma_{\rm T}c\,\gamma^2\,U'_{\rm sync} \tag{2.13}$$

$$\dot\epsilon_{\rm ERC} = \dot\gamma_{\rm ERC}\,m_{\rm e}c^2 \simeq \frac{16}{9}\,\sigma_{\rm T}c\,\gamma^2\,U'_{\rm ext} \tag{2.14}$$

where $\sigma_{\rm T}$ is the Thomson scattering cross section. Emitted luminosities will result integrating these over the electron energy distribution, and will be proportional to the

involved energy densities which are, respectively:

$$U'_{\rm B} = \frac{B^2}{8\pi} \tag{2.15}$$

$$U'_{\rm sync} = \frac{{\rm L}'_{\rm S}}{4\pi\, R^2\, c} = \frac{1}{\delta^4}\,\frac{{\rm L}_{\rm S}}{4\pi\, R^2\, c} \tag{2.16}$$

$$U'_{\rm ext} \simeq \Gamma^2\, U_{\rm ext} = \Gamma^2\,\frac{\xi {\rm L}_{\rm ext}}{4\pi\, R^2_{\rm ext}\, c} \tag{2.17}$$

From the cooling rate it is immediate to define the cooling timescale $\tau \equiv \epsilon/\dot{\epsilon} = \gamma/\dot{\gamma}$, a very useful quantity when comparing different processes at work in the emitting blob. It is immediate to see that in all cases $\tau \propto \gamma^{-2}$, i.e. more energetic particles will suffer more severe cooling.

Peak frequencies $\nu_{\rm S}$ & $\nu_{\rm C}$

In this framework, of a unique electron population, the synchrotron and Compton peak energies are strictly related, being produced by the same electrons, having a Lorentz factor that we will call $\gamma_{\rm peak}$. The equations for the peak frequencies, are then:

$$\nu'_{\rm S} \simeq 3.7\cdot 10^6\, \gamma^2_{\rm peak}\, B \qquad \nu_{\rm S} \simeq 3.7\cdot 10^6\, \gamma^2_{\rm peak}\, \delta\, B \tag{2.18}$$

$$\nu'^{\,\rm SSC}_{\rm C} \simeq \frac{4}{3}\,\gamma^2_{\rm peak}\nu'_{\rm S} \qquad \nu^{\rm SSC}_{\rm C} \simeq \frac{4}{3}\,\gamma^2_{\rm peak}\,\nu_{\rm S} \tag{2.19}$$

$$\nu'^{\,\rm ERC}_{\rm C} \simeq \frac{4}{3}\,\gamma^2_{\rm peak}\nu'_{\rm ext} \qquad \nu^{\rm ERC}_{\rm C} \simeq \frac{4}{3}\,\gamma^2_{\rm peak}\,\delta\,\Gamma\,\nu_{\rm ext} \tag{2.20}$$

left column for blob rest frame, right column for the observed ones.
The ratio between (observed) Compton and synchrotron peaks frequencies is then:

$$\left(\frac{\nu_{\rm C}}{\nu_{\rm S}}\right)_{\rm SSC} \simeq \frac{4}{3}\,\gamma^2_{\rm peak} \tag{2.21}$$

$$\left(\frac{\nu_{\rm C}}{\nu_{\rm S}}\right)_{\rm ERC} \simeq \frac{\Gamma\,\nu_{\rm ext}}{B} \tag{2.22}$$

Peak luminosities: $\rm L_S$ & $\rm L_C$

Another important property is the ratio of the two peak luminosities, $\rm L_C/L_S$, which is usually referred to as *Compton dominance*, that traces the ratio between the radiation

and magnetic energy densities.

$$\left(\frac{\mathrm{L'_C}}{\mathrm{L'_S}}\right)_{\mathrm{SSC}} = \frac{\dot{\gamma}_{\mathrm{peak,SSC}}}{\dot{\gamma}_{\mathrm{peak,sync}}} = \frac{U'_{\mathrm{sync}}}{U'_{\mathrm{B}}} = \frac{1}{\delta^4}\,\frac{2\,\mathrm{L_S}}{B^2\,R^2\,c} \tag{2.23}$$

$$\left(\frac{\mathrm{L'_C}}{\mathrm{L'_S}}\right)_{\mathrm{ERC}} = \frac{\dot{\gamma}_{\mathrm{peak,ERC}}}{\dot{\gamma}_{\mathrm{peak,sync}}} \simeq \frac{U'_{\mathrm{ext}}}{U'_{\mathrm{B}}} = \Gamma^2\,\frac{2\,\xi \mathrm{L_{ext}}}{B^2\,R^2_{\mathrm{ext}}\,c} \tag{2.24}$$

and it can also be interesting to consider the ratio between SSC and ERC luminosities

$$\frac{\mathrm{L'_{ERC}}}{\mathrm{L'_{SSC}}} = \frac{\dot{\gamma}_{\mathrm{peak,ERC}}}{\dot{\gamma}_{\mathrm{peak,SSC}}} \simeq \frac{U'_{\mathrm{ext}}}{U'_{\mathrm{sync}}} \simeq \delta^4\,\Gamma^2\,\frac{\xi \mathrm{L_{ext}}}{\mathrm{L_S}}\,\frac{R^2}{R^2_{\mathrm{ext}}} \tag{2.25}$$

The above formula hold also for the ratio of the *observed* synchrotron, SSC and ERC luminosities, provided that the angular distributions of radiation fields are the same (e.g. isotropic in the blob rest frame). For isotropic magnetic field, the synchrotron and SSC radiation in the source frame are isotropic, and transforms with δ^4. As pointed out in Section 2.2, this is not the case for the ERC process ($\propto \delta^6$), but provided that we are looking at the source within the aperture angle of the beaming pattern $\theta = 1/\Gamma$ we can hold the approximate equality and assume that

$$\frac{\mathrm{L_{ERC}}}{\mathrm{L_{SSC}}} \simeq \frac{\mathrm{L'_{ERC}}}{\mathrm{L'_{SSC}}} \qquad\qquad \frac{\mathrm{L_{ERC}}}{\mathrm{L_{sync}}} \simeq \frac{\mathrm{L'_{ERC}}}{\mathrm{L'_{sync}}}$$

while it is already correct that:

$$\frac{\mathrm{L_{SSC}}}{\mathrm{L_{sync}}} = \frac{\mathrm{L'_{SSC}}}{\mathrm{L'_{sync}}} \tag{2.26}$$

2.4 Characteristic electron energies

In general the observed SEDs require curved electron spectra steepening at higher frequencies, for both the synchrotron and inverse Compton components. There are at least three characteristic energies at which the electron spectrum can change its slope significantly. They are plausibly related to:

① minimum injected electron energy, γ_{min}

② maximum injected electron energy, γ_{max}

③ "cooling" break energy, γ_{break}

These "break γ's" leave their signature in the radiation spectra at energies $\nu \propto \gamma^2_{\mathrm{break}}$.

synchrotron self-absorption

Moreover in the case of synchrotron radiation, there is a cut-off due to synchrotron self-

absorption, which is not usually observed because it occurs at frequencies were the radiation from the homogeneous blob falls below that coming from outer in-homogeneous region of the jet, responsible for the bulk of the radio emission.

Spectra can also show a high energy cut-off due to γ–ray absorption in the pair production process. The ambient radiation field has to be transparent even for most energetic γ–rays to reach us, nevertheless TeV photons could interact with the diffuse infrared background photons and be absorbed. Actually upper limits and detections on TeV radiation from TeV-emission candidates (typically extreme HBLs, with synchrotron peak in the X-ray band) can be used to estimate the energy density of this diffuse component (e.g. De Jager et al. 1994; Stecker and De Jager 1998). *γ-γ absorption*

cooling break energy A very informative spectral feature is the one related to the electron energy, $\gamma_{\rm break}$, below which radiative cooling of electrons is inefficient. This results from the equality of the cooling timescale $\tau_{\rm cool} \equiv \gamma/\dot{\gamma}$, with the escape timescale. For this latter we assumed that $\tau_{\rm esc} \equiv R/v_{\rm esc} \simeq R/c$. This energy is (from eq. 2.12–2.14):

$$\gamma_{\rm break} = \frac{3\, m_{\rm e} c^2}{4\,(U'_{\rm B} + U'_{\rm rad})\,\sigma_{\rm T}\, R} \tag{2.27}$$

where $U'_{\rm rad}$ is the total energy density in target photons, on which electrons cool via inverse Compton scattering.

maximum injected energy The energy of the injected electrons should have a limit reflecting the balance between the efficiency of the acceleration and of the cooling. Its value then reflects the properties of the acceleration mechanism, and it is worth investigating. The most promising scenario for particle acceleration in blazars relativistic jets, is *shock acceleration*, according to which particles gain energy by being scattered by magnetic "disturbances", repeatedly crossing the shock front (e.g. Kirk 1997). In some scenario, shock acceleration can give rise to a maximum acceleration rate on the order of the gyro-frequency of the accelerated particle (e.g. Inoue and Takahara 1996; Kirk 1997).

For electrons this yields a maximum Lorentz factor:

$$\gamma_{\rm max} \simeq \left[\frac{9\, eB}{80\,(U'_{\rm B} + U'_{\rm rad})\,\sigma_{\rm T}\,\eta}\right]^{1/2} \tag{2.28}$$

where η is electron mean free path in units of the Larmor radius ($r_{\rm L} = \gamma\, m_{\rm e} c^2/eB$), which enters in the definition of the acceleration timescale, which in this case we assumed to be $\tau_{\rm acc} \sim \eta\, r_{\rm L}$ (Inoue and Takahara 1996). The value of η is actually

a big unknown and under some assumptions it can be related to the ratio between the non-turbulent and turbulent components of the magnetic field in the acceleration region. Inoue and Takahara (1996) comparing their model with the SED of 3C 279 and Mkn 421 found values ranging from 10^5 to 10^7.

For a reasonable choice of parameters we find that the maximum electron energy is not likely to exceed a few TeV or so in the powerful sources (see § 2.5.4). Higher energies may be attainable in faint BL Lac objects provided that the magnetic field is sufficiently weak. The fact that Mkn 421 and Mkn 501 have been detected at TeV energies implies that at least in these sources electron injection must be very effective. It is not known whether the high energy spectrum of FSRQ extends into the TeV regime.

minimum injected energy The role of $\gamma_{\rm min}$ and its nature are in some sense less "natural" to see than it is for $\gamma_{\rm break}$ and $\gamma_{\rm max}$. There are some –independent– motivations to require the presence of a low energy cut-off in the electron distribution, with $\gamma_{\rm min}$ even up to 100. One of the most important motivations is the need of sort of pre-injection in the shock region: in order to be efficient current scenarios of shock-wave acceleration require that electrons are already mildly relativistic. Other directly phenomenological evidences are for instance related with the problem of *bulk Compton scattering* (i.e. optical depth), Faraday depolarization, or kinetic energy budget (e.g. Sikora et al. 1997; Celotti 1997). Just to detail more one of the argument we can mention the "Sikora bump": cold electrons co-moving with the blob with Γ, up-scatter UV external photons to $\nu \simeq 1\ \Gamma_1^2\ \nu_{\rm ext,15}$ keV, producing a bump whose intensity depends on the scattering optical depth of these cold electrons. We can then set a limit on their density, since we the "Sikora bump" has never been detected.

The point is that we don not want to have much more electrons in the jet than those necessary to account for the emission we detect, on the other hand we are not able to constrain their lowest energy from direct spectral observations. In fact, a spectral break related to $\gamma_{\rm min} < 100$ could not be detected in the synchrotron component, because it would occur below the frequency at which synchrotron-self-absorption becomes important. Neither is the break expected to be imprinted in the SSC component. For ERC, in the case of UV target photons, such a break should be imprinted on the Compton spectrum in the range $\simeq$ 1 keV – 10 MeV, while for IR targets, up to at most a few tens of keVs. In principle the presence of a $\gamma_{\rm min}$ (or equivalently of a significant break in the electron spectrum with a

flattening below some energy) can give rise to a very hard X–ray spectrum, and there are a few sources with very hard medium X–ray spectra (e.g. 0202+149 and other sources in § 4), but it is difficult to firmly claim that this is due to the presence of a minimum electron energy.

To avoid the presence of cold electrons one should require that they are re-accelerated, or that they escape from the emitting volume, but in both cases in seems to be necessary to have a mechanisms able to produce a "truncated" electron injection.

At least a couple of ideas have been proposed, although both are pure speculations: the "hot electron" picture by Sikora et al. (1997), and the "pre-shock" acceleration. To explain the properties of the so called *MeV blazars* (Blom et al. 1995), Sikora et al. (1997) hypothesized that a significant fraction ($\simeq$ half) of the energy available, rather than going into the shock-acceleration producing the power law, is used to pre-heat all electrons which will be afterward accelerated. The pre-heating electron "equilibrium temperature" could be of the order of 100 MeV (i.e. $\gamma_{\rm min} \simeq 2 \cdot 10^3$), and from a simple estimate of the energy balance it seems possible that this happens at a distance r along the jet compatible with other independent requirements, e.g. $r \gtrsim 10^{17} M_8$ cm (for $M_8 = M/10^8 M_\odot$) (Sikora et al. 1997). The second picture is very similar to this one, in envisaging a mechanism to "pre–heat" electrons at a typical energy before experiencing the shock-acceleration itself. It relies on the possibility that in a pre-shock phase there can be a transfer of energy for instance from cold protons, having an energy content $\simeq \Gamma m_{\rm p} c^2$, to electrons to a typical energy $\gamma_{\rm e} \sim \Gamma(m_{\rm p}/m_{\rm e}) \lesssim 10^4$, depending on the power in baryons which is dissipated.

The relative importance of $\gamma_{\rm min}$, $\gamma_{\rm max}$ and $\gamma_{\rm break}$, and their role in the determination of the SED shape, mainly which one is going to correspond to the observed $\nu_{\rm peak}$, i.e. $\gamma_{\rm peak}$, depends also on the slope of the injected electron spectrum, assumed to be a power law $N(\gamma) \propto \gamma^{-s}$, extending from $\gamma_{\rm min}$ to $\gamma_{\rm max}$. Since for thin synchrotron emission the spectral index is related to that of the emitting electron as $\alpha = (s-1)/2$, then it is immediate to see that the peak in the $\nu {\rm F}_\nu$ spectrum occurs where $s = 3$.

In a stationary case, there are a few basic "rules" telling how the electron energy distribution is, and there are only a few possible combinations (Ghisellini 1989). First of all, it is worth reminding that in the range of energies where cooling is dominant the electron spectrum steepens to $s_{\rm inj} + 1$, due to radiative losses, while where escape is dominant the spectrum keeps its injection slope, and finally below $\gamma_{\rm min}$ it is $s = 2$. We

can discuss a few cases (see also 6.2.2). If there actually is escape, then there are the following possibilities.

$3 < s_{\rm inj}$: $\gamma_{\rm peak}$ corresponds to $\gamma_{\rm min}$

$2 < s_{\rm inj} < 3$: $\gamma_{\rm peak}$ corresponds to $\gamma_{\rm break}$

$1 < s_{\rm inj} < 2$: since even above $\gamma_{\rm break}$ the slope $s < 3$, then $\gamma_{\rm peak}$ will fall between $\gamma_{\rm break}$ and $\gamma_{\rm max}$.

$s_{\rm inj} < 1$: again $\gamma_{\rm break} < \gamma_{\rm peak} < \gamma_{\rm max}$.

If there is not significant escape, in any case for $s_{\rm inj} > 2$ the peak will occur at the energies corresponding to $\gamma_{\rm min}$.

2.5 Diagnostics from SED peaks

By comparing ERC/SSC spectra with the synchrotron spectra, we can attempt to derive physical parameters of radiating blob, namely magnetic field, characteristic (maximum/minimum/break) electron energies, in and in turn electron injection function (e.g. Sikora et al. 1994; Ghisellini et al. 1996; Takahashi et al. 1996; Sikora et al. 1997; Mastichiadis and Kirk 1997).

In Chapter 6 we will present the results of an extensive study of the SEDs of γ–ray detected sources, which have been fitted with a detailed jet model.

Here, starting from the basic equations we want to see what can be investigated by simply taking advantage of the study of the basic properties of spectral energy distributions. The main quantities that can be observationally derived from the SEDs are the energies of the synchrotron and Compton peaks, $\nu_{\rm S}$ and $\nu_{\rm C}$, their luminosities, $\rm L_S$ and $\rm L_C$, or *Compton dominance*, and in some cases their relative variations estimated comparing different "snapshots" of the same source.

Adding to these data estimates of other relevant quantities, such as the Doppler factor δ, or Lorentz factor Γ, the size of the blob, the nature of the external radiation field, we can work out interesting results on the physics of the emitting blob, e.g. magnetic field, electron energies.

blob size

Doppler factor

The size of the emitting region, R, can be constrained by measurements of variability timescales imposing the usual causality condition, i.e. $R \lesssim \delta\, c\, t_{\rm var}/(1+z)$, and for $t_{\rm var} = 1$ day and $z \ll 1$ this gives $R \simeq 3 \cdot 10^{16}$ cm. About δ (Γ), there is increasing evidence, from independent methods, that blazars jets are characterized by Lorentz factor of the order of 10, with only a little spread (e.g. Ghisellini et al. 1993, Vermeulen and Cohen 1994).

Since we are looking at peaks of the SED, such analyses are not affected by the fact that the observed spectra, especially their lower energy parts (in both the synchrotron and the Compton components) may well result from the superposition of two or more components (see discussion in § 2.6).

In the following sections we first discuss the constraints on SSC and ERC models (§ 2.5.1), we compare SSC and ERC models to investigate their applicability to different SEDs (§ 2.5.2), in § 2.5.3 we derive estimates of the blob magnetic field for SSC and ERC, and of the "typical" electron energies (§ 2.5.4), and finally in § 2.6 we present the relevant variability features expected in different scenarios.
Hereinafter we will assume that always $\theta \simeq 1/\Gamma \simeq 1/\delta$.

2.5.1 Estimates of $\gamma_{\rm peak}$, B, δ

First of all let us consider the SSC scenario. The important source parameters involved are basically 4, i.e. R, $\gamma_{\rm peak}$, B and δ. As already said, the blob size can be estimated independently, from variability, and then we can write: *SSC*

$$\begin{aligned} \gamma_{\rm peak} &= \left(\frac{3\,\nu_{\rm C}}{4\,\nu_{\rm S}}\right)^{1/2} \\ B\delta &= \frac{\nu_{\rm S}^2}{\nu_{\rm C}\,(e/2\pi m_{\rm e}c)} \\ B^2\delta^6 &= \frac{2\,{\rm L}_{\rm S}^2}{c^3\,t_{\rm var}^2\,{\rm L}_{\rm C}}\,(1+z)^2 \end{aligned} \tag{2.29}$$

We see that since the SSC model is strongly constrained, we are then able to derive $\gamma_{\rm peak}$, B and δ, fixing univocally the SSC parameters using only the main features of the SED, if obtained from simultaneous data.

For ERC the situation is somewhat worse. The model parameters are (R, $\gamma_{\rm peak}$, B, δ), but there are also $R_{\rm ext}$, ${\rm L}_{\rm ext}$, and $\nu_{\rm ext}$, which in turn depends on the nature of the external photon field. It is true that we can reliably estimate them, nevertheless the ERC model is only weakly constrained. For $\nu_{\rm ext}$ it is very likely that for most sources of external radiation it will be around optical-UV energies, $\nu_{\rm ext} \simeq 10^{15}$ Hz. We can work out estimates for ${\rm L}_{\rm ext}$ for FSRQ, thanks to the fact that they show quasar-like emission line spectra, or even UV-excesses, while it is more difficult for BL Lacs, for which we can at most extrapolate or impose upper limits. The worst point is that about $R_{\rm ext}$, for which we can extrapolate results for radio-quiet AGNs for which there are ongoing extensive observational program for the monitoring of broad emission lines variability in order to map the properties of the BLR (e.g. Collier et al. 1998 and references therein). *ERC*

Equations for $\gamma_{\rm peak}$, magnetic field and Doppler factor, for ERC, (for $\theta = 1/\Gamma$, to have $\delta = \Gamma$), are:

$$\gamma_{\rm peak}\,\delta = \left(\frac{3\,\nu_{\rm C}}{4\,\nu_{\rm ext}}\right)^{1/2}$$
$$\frac{B}{\delta} = \frac{\nu_{\rm S}\,\nu_{\rm ext}}{\nu_{\rm C}\,(e/2\pi m_{\rm e}c)} \qquad (2.30)$$

and it is not possible to separate B and δ, increasing even more the "degeneracy" of the ERC case. In fact both the ratio between Compton and synchrotron peak frequencies (eqs. 2.18 and 2.20) and that between their respective luminosities (eq. 2.24) yield the quantity B/δ. We can then write the following relations for the ratio of peak frequencies as a function of the parameters of the external radiation and of the Compton dominance:

$$\frac{\nu_{\rm C}}{\nu_{\rm S}} \simeq 1.4\cdot 10^{9}\,\nu_{\rm ext,15}\,R_{\rm ext,18}\,(\xi {\rm L}_{\rm ext})_{45}^{-1/2}\left(\frac{{\rm L}_{\rm S}}{{\rm L}_{\rm C}}\right)^{1/2} \qquad (2.31)$$

2.5.2 ERC *vs.* SSC, FSRQ *vs.* BL Lacs ?

The comparison of the ERC efficiency with the SSC efficiency for *typical* quasar radiation fields seems to imply that the production of γ–rays in FSRQ should be strongly dominated by Comptonization of external radiation. In fact Equation 2.25 can be re-

FSRQ

written substituting typical values for the involved quantities. We plug-in $\Gamma \simeq \delta \simeq 10$, $\xi {\rm L}_{\rm ext} \simeq 10^{45}$ (e.g. Falcke et al. 1995, Celotti et al. 1997) and ${\rm L}_{\rm S} \simeq 10^{46}$ erg s^{-1}, which are appropriate in the case of FSRQs, and we set the dimensions to $R_{\rm ext} \simeq 10^{18}$ cm, and $R \simeq 10^{17}$ cm.

$$\frac{U'_{\rm ext}}{U'_{\rm sync}} = 10^{3}\,\delta_1^{6}\,\frac{(\xi {\rm L}_{\rm ext})_{45}}{{\rm L}_{\rm S,46}}\,\frac{R_{17}^2}{R_{\rm ext,18}^2} \qquad (2.32)$$

The above formula seems to prove strong domination of the ERC process over the SSC process for quasar-like blazars, for the production of the high energy peak. However, SSC can still contribute visibly to the X–ray band (Kubo 1997; Ghisellini et al. 1998)(see also § 2.6).

BL Lacs

The situation is less clear in BL Lac objects, where the radiative environment in the central region is not very well known. The lack of strong emission lines and of UV excesses (even during lowest states) suggest that in these objects $\xi {\rm L}_{\rm ext}$ can be very low. Noting also that in BL Lac objects Γ factors are typically smaller than in quasars (Padovani and Urry 1992; Maraschi and Rovetti 1994; Vermeulen and Cohen 1994), domination of SSC over ERC in these objects is very likely.

It is also worth reminding that for BL Lac objects whose high energy spectra can extend up to TeV energies the formula 2.25 (and 2.32) could not apply directly. This is because the reduction of the scattering cross section in the Klein-Nishina regime strongly reduces the efficiency of the Compton process.

Compton dominance

The ERC mechanism is then likely to dominate in the powerful γ–ray quasars. Moreover, SSC models have difficulties explaining the high ratio of luminosities of the high and low energy spectral components often seen in the powerful blazars, with the γ–ray component dominating the synchrotron one as much as by 3 orders of magnitude (e.g. see Chapter 4, 5, and 6). On the other hand low power BL Lacs, even, if not especially, those emitting in the TeV range show an approximate equality of the power emitted by synchrotron and inverse Compton. We can for instance compare equations 2.23 and 2.24:

$$\left(\frac{\mathrm{L_C}}{\mathrm{L_S}}\right)_{\mathrm{SSC}} \simeq 0.7 \quad \delta_1^{-4}\, B_{-1}^{-2}\, R_{17}^{-2}\, \mathrm{L_{S,46}} \tag{2.33}$$

$$\left(\frac{\mathrm{L_C}}{\mathrm{L_S}}\right)_{\mathrm{ERC}} \simeq 7 \cdot 10^2\, \delta_1^2\, B_{-1}^{-2}\, R_{\mathrm{ext},18}^{-2}\, (\xi \mathrm{L_{ext}})_{45} \tag{2.34}$$

Therefore, this is a further hint that the SSC mechanism is more likely to be important in the weak BL Lac objects.

2.5.3 ERC, SSC and magnetic field

If both high energy and low energy spectral components are produced by the same population of relativistic electrons, and the production of high energy radiation is dominated by the SSC process, then

$$\frac{\mathrm{L_C}}{\mathrm{L_S}} = \frac{\mathrm{L'_{SSC}}}{\mathrm{L'_S}} = \frac{U'_{\mathrm{sync}}}{U'_{\mathrm{B}}} \tag{2.35}$$

Equations 2.16 and 2.35 give:

$$U'_{\mathrm{B}} \simeq \frac{1}{\delta^4}\, \frac{1}{4\pi R^2\, c}\, \frac{\mathrm{L_S^2}}{\mathrm{L_C}} \tag{2.36}$$

For the case of ERC dominating the equation for the magnetic energy density is instead, from 2.26 and 2.17:

$$U'_{\mathrm{B}} \simeq \delta^2\, \frac{\xi \mathrm{L_{ext}}}{4\pi R_{\mathrm{ext}}^2\, c}\, \frac{\mathrm{L_S}}{\mathrm{L_C}} \tag{2.37}$$

From 2.36 and 2.37 we can derive estimates of the magnetic field based on observed quantities. They are:

$$B_{\rm SSC} \simeq 0.1\, \delta_1^{-2}\, R_{17}^{-1}\, {\rm L}_{\rm S,46}^{1/2} \left(\frac{\rm L_C}{\rm L_S}\right)^{-1/2} \ {\rm Gauss} \tag{2.38}$$

$$B_{\rm ERC} \simeq 3\, \delta_1\, R_{\rm ext,18}^{-1}\, (\xi {\rm L_{ext}})_{45}^{1/2} \left(\frac{\rm L_C}{\rm L_S}\right)^{-1/2} \ {\rm Gauss} \tag{2.39}$$

Thus, the observed high γ–ray luminosities and Compton dominances can be explained in terms of the SSC models only if one assumes that jets are very weakly magnetized.

2.5.4 ERC, SSC and characteristic electron energies

We finally report a numerical estimate of the characteristic electron energies, discussed in § 2.4, expected to arise from the balance between acceleration, cooling and escape of emitting particles. In particular we give expressions for $\gamma_{\rm break}$ (*cooling = escape*) and $\gamma_{\rm max}$ (*cooling = acceleration*), equations 2.27 and 2.28. They can be re-written in terms of the measured or estimated parameters, both for the SSC and for the ERC case, with their different estimates/constraints for the magnetic field:

$$\gamma_{\rm break}^{\rm SSC} \simeq 3.5 \cdot 10^4\, \delta_1^4\, R_{17}\, {\rm L}_{\rm S,46}^{-1} \left(\frac{\rm L_C}{\rm L_S}\right) \left(1+\frac{\rm L_C}{\rm L_S}\right)^{-1} \tag{2.40}$$

$$\gamma_{\rm break}^{\rm ERC} \simeq 35\, \delta_1^{-2}\, R_{17}^{-1}\, R_{\rm ext,18}^{2}\, (\xi {\rm L_{ext}})_{45}^{-1} \left(\frac{\rm L_C}{\rm L_S}\right) \left(1+\frac{\rm L_C}{\rm L_S}\right)^{-1} \tag{2.41}$$

$$\gamma_{\rm max}^{\rm SSC} \simeq 1.5 \cdot 10^5\, \eta_6^{-1/2}\, \delta_1\, R_{17}^{1/2}\, {\rm L}_{\rm S,46}^{-1/4} \left(\frac{\rm L_C}{\rm L_S}\right)^{1/4} \left(1+\frac{\rm L_C}{\rm L_S}\right)^{-1/2} \tag{2.42}$$

$$\gamma_{\rm max}^{\rm ERC} \simeq 2.6 \cdot 10^4\, \eta_6^{-1/2}\, \delta_1^{-1/2}\, R_{\rm ext,18}^{1/2}\, (\xi {\rm L_{ext}})_{45}^{-1/4} \left(\frac{\rm L_C}{\rm L_S}\right)^{1/4} \left(1+\frac{\rm L_C}{\rm L_S}\right)^{-1/2} \tag{2.43}$$

Here for the parameter η entering in the definition of the acceleration timescale, we used the fiducial value $\eta \simeq 10^6$ laying in between the values obtained by Takahashi et al. (1996) for the broad band fits to 3C 279 and Mkn 421.

2.6 Variability and relative luminosities

The limited data that we have on most of blazars prevent us from being able to distinguish between the different theoretical models on the basis of the spectra alone. For example, both the SSC and ERC models have been able to reproduce the SED of 3C 279 rather well (e.g. Maraschi et al. 1992; Hartman et al. 1996). Similarly the SSC model fits well the data of the March 1993 flare of PKS 0528+134 (Mukherjee et al. 1996), while its low state (August 1994) were fitted well with the ERC model by Sambruna et al. (1997). The SSC, ERC, and PIC models give good results when compared with the SED of 3C 273 (Von Montigny et al. 1997).

It could then be important to consider the opportunity offered by the comparison of different "snapshots" of the same source at different levels of activity and brightness. Correlations between the fluxes at different energies over a broad energy range may actually be anticipated, even though naively, from the basic properties of the different scenarios. Presumably, different mechanisms would give rise to different characteristics of the time dependent emission in blazars, For example, changes in either of the following quantities might lead to variations for the SED properties:

- particle injection rate,
- magnetic field,
- the bulk speed,
- intensity of ambient radiation in ERC models.

According to the various models, variations in the above quantities can affect the synchrotron and Compton components in different way. On the basis of equations 2.12 – 2.17 we can work out the expressions giving the dependencies of the luminosities of the various emission components on the magnetic field B, electron density N_e, jet bulk Lorentz factor Γ, and external photon field energy density $U_{\rm ext}$. Under the assumption that $\theta = 1/\Gamma$ we have:

$$\mathrm{L_S} \propto \Gamma^4 \, N_e \, B^2 \tag{2.44}$$

$$\mathrm{L_{SSC}} \propto \Gamma^4 \, N_e^2 \, B^2 \tag{2.45}$$

$$\mathrm{L_{ERC}} \propto \Gamma^6 \, N_e \, U_{\rm ext} \tag{2.46}$$

$$\mathrm{L_{MC}} \propto \Gamma^8 \, N_e^2 \, B^2 \tag{2.47}$$

We added here the further case (2.47), not discussed before, of the *mirror Compton model* (Ghisellini and Madau 1996), that show the strongest dependence on the jet bulk Lorentz factor .

2.6.1 Examples, comments and complications

Since both the ERC luminosity and the synchrotron luminosity scale linearly with the injection rate of electrons, the ratio L_{ERC}/L_S is predicted to be constant during a flare.

3C 279

Contrary to this prediction, the observations of the best studied blazar, 3C 279, show much higher amplitudes of variability in the γ–ray band than in the optical/UV band (e.g. Wehrle et al. 1998). Such variability patterns are predicted by the SSC model, where $L_{SSC,high}/L_{SSC,low} = (L_{S,high}/L_{S,low})^2$. However, the amplitude ratio observed in the January 1996 flare of 3C 279 was even larger than that predicted by the SSC model (Wehrle et al. 1998). This behaviour instead can be reconciled with the one-zone ERC model (either *pure* or in its *mirror* varieties) only if the increased injection rate of relativistic electrons is accompanied by an increase of the bulk Lorentz factor, upon which synchrotron and Compton components have a different dependence (for an application of the *mirror* model to this case see Bednarek 1998).

complications

Things are complicated by the fact that comparable contributions to the emission in a band can come from different components, that have different variability properties or even be not variable.

For instance the synchrotron emission from the jet can be diluted by a thermal component from the accretion disk in the optical/UV, or from emission from dust (e.g. from a nuclear torus) in the infrared band, or even, for low power sources, can be diluted by the emission of the host galaxy.

Last but not least, there is even the possibility that the jet itself has a steady emission, over which highly variable flaring components are superposed.

ERC+SSC mixing

A further point to stress is that not only the variability of the low energy component can be diluted by the presence of non-variable contributions, but, because of the different energy distributions of the target radiation fields, the corresponding Compton components do not overlap entirely, giving rise to a complex phenomenology at high energies.

X-rays

For instance, in X–ray band, beside the mixing of the high energy tail of the synchrotron component with the onset of the inverse Compton one, which however we can reasonably believe to be able to recognize because of the marked difference in spectral shape, there could also be the case of a mixture of ERC and SSC radiation, which is more subtle to distinguish.

As a result, a less luminous SSC component produced by up-scattering far infrared radiation can still be visible in soft/mid X–rays, while ERC scattering on the external UV radiation, blueshifted of a factor $\Gamma\delta$, can produce a separate peak at higher energy.

In the worst case, envisaged by Sikora et al. (1997), there could be a further ERC component coming from the Comptonization of external near-IR radiation, originated by the hypothesized dusty torus.

An interesting example of this mixing of Compton components is possibly provided by the FSRQ PKS 0528+134. Ghisellini et al. (1998) explain the peculiar relationship between brightness and hardness shown by this source in X–rays, as due to the mixing of two different components. In the 0.1 – 10 keV band flux this source is apparently *softer when brighter*, at odds with what was so far believed to be the "normal" behaviour, i.e. *harder when brighter*. This can be due to the an extra contribution from SSC occurring exactly in the medium X–ray band.

0528+134

2.7 SSC *vs.* ERC beaming patterns and source statistics

Another interesting aspect of comparing ERC and SSC radiation components with the synchrotron component is the angular distribution of these radiation fields. As was shown by Dermer (1995) and discussed in § 2.2, ERC radiation is much more strongly collimated than the synchrotron and SSC radiation. Since SSC and synchrotron radiation fields have the same angular distribution (they both are produced isotropically in the source comoving frame), the predicted high-energy to low-energy luminosity ratio does not depend on $\theta_{\rm obs}$. In contrast, the ERC model predicts this ratio to drop very rapidly with viewing angle outside the $1/\Gamma$–cone. Dermer proposed that this can explain why a significant fraction of FSRQ do not show γ–ray activity, even though they are otherwise recognized as typical blazars on the basis of the low energy component properties.

CHAPTER 3

SIMULATIONS OF BL LAC SAMPLES

3.1 Introduction

Given the general "panorama" that we summarized in section 1.2 and because of the implications for physical models of relativistic jets and the understanding of the physical conditions within the emission region, we decided to explore more thoroughly the fundamental *hypothesis that BL Lacs are a single class*, whose SEDs are characterized by different physical parameters, and to test any prediction against the available observations.

Our aim here was to perform a further step with respect to the work done by Giommi and Padovani (Giommi and Padovani 1994; Padovani and Giommi 1995) who proposed the radio leading scenario (§ 1.2.4). We then started by considering BL Lac objects, and we introduced the X–ray leading and bolometric models (see § 1.2.5 and § 1.2.6).

The predictions of these models, derived by a Montecarlo technique, are compared in detail with observations, in particular considering with care the redshift distributions.

We test the three pictures against the best (whole) body of data now available: the

radio and X–ray fluxes (uniformly measured by *ROSAT*, Urry et al. 1996) of the 1 Jy BL Lac sample (Stickel et al. 1991) and the radio and X–ray fluxes of the BL Lac sample derived from the *Einstein* Slew survey sample (Elvis et al. 1992; Perlman et al. 1996), which we are going to consider quasi-complete.

Specifically, we compute the distributions of radio and X–ray luminosities and redshift, predicted for the sub-samples of HBLs and LBLs. The observational quantities to match are therefore 16, 2 luminosities plus the redshift distribution plus the number of detections, for two "classes" of objects for two surveys.

3.2 The reference samples

3.2.1 The 1 Jy survey sample

The complete 1 Jy BL Lac sample was derived from the catalog of radio selected extragalactic sources with $F_{5GHz} \geq 1$ Jy (Kühr et al. 1981) with additional requirements on radio flatness ($\alpha_R \leq 0.5$, with $F_\nu \propto \nu^{-\alpha}$), optical brightness ($m_V \leq 20$) and the absence of optical emission lines ($EW_\lambda \leq 5$ Å, evaluated in the source rest frame) (Stickel et al. 1991). This yielded 34 sources matching the criteria, 26 with a redshift determination and 4 with a lower limit on it (Stickel et al. 1994). It is the largest complete radio sample of BL Lacs compiled so far.

We computed the luminosities using the monochromatic 1 keV fluxes measured by *ROSAT* (Urry et al. 1996, where the listed values are those from fits with Galactic absorption) and the 5 GHz values from the Kühr et al. catalogue. We considered only the subsamples of sources with at least a lower limit on the redshift. The fluxes were K–corrected using a radio spectral index $\alpha_R = -0.27$ and the average X-ray spectral index measured in the *ROSAT* band, $\alpha_X = 1.16$.

3.2.2 The Slew survey sample

The *Einstein* Slew survey (Elvis et al. 1992) was derived from data taken with the IPC in between pointed observations. A catalog of 809 objects has been assembled with a detection threshold fixed at 5 photons. It does not reach high sensitivity, having a flux limit of $\simeq 5 \times 10^{-12}$ erg/cm^2/sec in the IPC band ($0.3 - 3.5$ keV), but it covers a large fraction of the sky (~ 36600 deg^2). Based on radio imaging and spectroscopy Perlman et al. (1996) selected from this sample a set of 62 BL Lac objects (33 previously known and 29 new candidates) and, in a restricted region of the sky, a quasi–complete sample of 48 BL Lacs. The sources are almost completely identified, and therefore constitute a

quasi–complete sample of 48 BL Lacs. The redshift is known for 41 out of 48 objects. Based on the data and the discussion by Perlman et al. we treat the Slew survey sample available to date as a tentative, but quasi–complete one. This is the largest available X–ray selected sample of BL Lacs (Perlman et al. 1996), with more than twice the number of sources contained in the fairly rich X–ray selected sample derived from the *Einstein* Medium Sensitivity Survey (EMSS, Morris et al. 1991; Wolter et al. 1994; Perlman et al. 1996), extended to 23 objects by Wolter et al. (1994).

K–corrections of the radio and X–ray monochromatic fluxes were computed using spectral indices $\alpha_{\rm R} = 0.0$ and $\alpha_{\rm X} = 1.5$, respectively.
The values $H_0 = 50$ km/sec/Mpc and $q_0 = 0.0$ have been adopted.

3.3 The *"different energy cut–off"* framework

The framework which we decided to investigate lies on the idea that BL Lacs are a single population of objects whose SED can be characterized phenomenologically by the distribution of the values of the frequency at which the peak in the energy emitted per logarithmic bandwidth occurs (i.e. the peak in the νF_ν representation of the broad band energy distribution) for the putative synchrotron component.

A good quantitative indicator of the overall broad band shape of SEDs is the ratio between X–ray and radio fluxes, conventionally taken at 1 keV and 5 GHz, equivalent to a characterization in terms of $\alpha_{\rm RX}$ and/or $\alpha_{\rm RO}$. SEDs peaking at lower frequencies correspond to higher ratios (see § 5; for a representation of the relation between SED shape and for instance $\alpha_{\rm RO}$ see Fig. 1.2). The X–ray to radio flux ratio is typically two orders of magnitude larger in BL Lac objects derived from X–ray surveys than in objects derived from radio surveys.

flux ratio

It is clearly more convenient to work with flux ratios since they are easier to determine then the peak frequency of a broad band energy distribution. One can even observationally derive a distribution for the X–ray/radio luminosity ratio as if this is the relevant intrinsic quantity which characterizes the SED distribution. This is what we consider hereafter, following the approach by Giommi and Padovani.

Starting from these hypothesis, one can derive the statistical properties of BL Lacs simply by assuming a *primary* luminosity $\mathcal{L}$ (radio, X–ray or "bolometric"), and relative luminosity function $\Phi(\mathcal{L})$, and a probability distribution, $\mathcal{P}(\mathrm{L_X/L_R};\ \mathcal{L})(\equiv \mathcal{P}_{\rm X/R})$, of the X–ray to radio luminosity ratio. In the following sections we present the assumptions on these two quantities, according to different models.

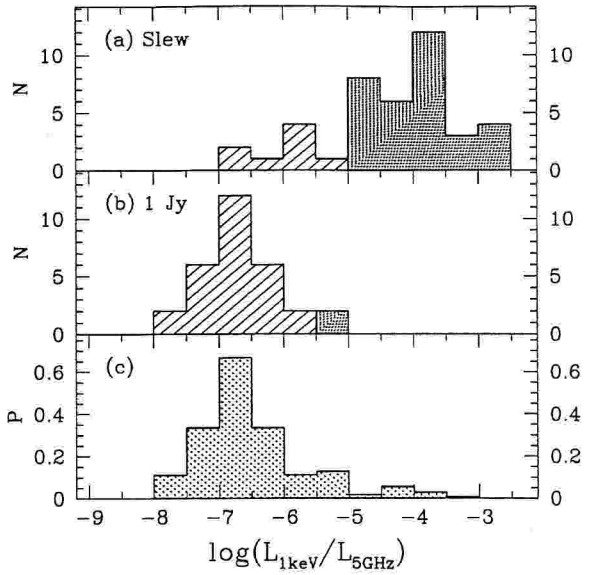

Figure 3.1: (a,b) Distribution of the observed ratio L_{1keV} /L_{5GHz} for the two surveys. Dashed areas represent LBL, while dotted areas indicate HBL sources. The distribution $\mathcal{P}_{X/R}$ used in the computations of the radio leading scenario is shown in (c). It is obtained summing up that observed for the LBLs in the 1Jy sample and that of the EMSS sample, weighted by a factor 1/10.

3.3.1 Radio leading scenario

Since a radio selected sample would be unbiased with respect to the X–ray to radio luminosity ratio, we considered the 1 Jy sample of BL Lacs (Stickel et al. 1991) and built the probability distribution $\mathcal{P}_{X/R}$. To improve the statistics for the HBL objects part of $\mathcal{P}_{X/R}$, we considered, following Padovani and Giommi (1995), the distribution deduced from the EMSS sample, weighted by a factor 1/10 (see Fig. 3.1). In fact the ratio of HBL to LBL objects derived from various radio selected samples (1 Jy, Stickel et al. 1991; S4, Stickel and Kühr 1994; S5, Stickel and Kühr 1996) covers the range $N_{HBL}/N_{LBL} = 1/16 - 1/6$. Therefore, with the given hypothesis, this factor 1/10 represents the intrinsic ratio of HBL to LBL populations in the whole BL Lac class: in the radio leading scenario only a minority of sources would intrinsically have the SED peaking in the UV range, while most of the energy distributions would peak in the $\sim$ IR range.

As "primary" (i.e. radio) luminosity function we used that calculated by Giommi and Padovani in the luminosity range $10^{28} - 10^{36}$ [erg/sec/Hz], extrapolating the observed one to lower luminosities. The extrapolation is based on the beaming model scheme (see Urry and Shafer 1984; Urry et al. 1991; Urry and Padovani 1991), applied to the luminosity function derived from the 1 Jy sample data (covering the range $10^{32} - 10^{35}$ erg/sec/Hz, Stickel et al. 1991), in the non evolutionary case. We note that

the predictions of the model are indeed strongly dependent on the number density of the low luminosity sources.

We used a third degree polynomial fit[1] to the luminosity function published in Fig. 1 of Padovani and Giommi (1995).

warning on L_{min}

Clearly, the assumption of a minimum radio luminosity $L_{5GHz,min}$ introduces a limiting luminosity in the X–ray band, $L_{1keV,min}$. However, it is worth noting that, because of the different spectral shape of HBL and LBL objects, their corresponding minimum luminosities will be different, with $L_{1keV,min}|_{LBL} < L_{1keV,min}|_{HBL}$.

Giommi and Padovani found a good agreement between the predicted X–ray counts and those derived from all the main X–ray surveys (EMSS, EXOSAT High Galactic Latitude Survey, HEAO-1 surveys; see Fig. 3 of Padovani and Giommi 1995) and with the EMSS luminosity function.

3.3.2 X–ray leading scenario

Again, the starting points are the primary (X–ray) luminosity function and a probability distribution of luminosity ratios, but in this case this should be observationally derived from an X–ray survey, that by construction is now supposed to be the objective one.

evolution

An important assumption, which we had necessarily to take into account in the X–ray case, concerns the cosmological evolution of BL Lacs. Recently Wolter et al. (1994) and Perlman et al. (1996) confirmed the strong negative evolution in the X–ray band: X–ray bright objects are much less luminous or common at high redshifts. In analogy with the radio case, we first evaluated the predictions of the X–ray leading model assuming no evolution. The results have been presented in Fossati et al. (1996) where we showed that they are not compatible with the 1 Jy survey sample properties, predicting a number of LBL objects in large excess with respect to the observed one ($\sim$ 140 instead of 32 observed).

Then, in order to be able to reproduce the observational results and in particular the redshift distributions (see below), here we assumed a negative luminosity evolution in the X–ray band.

We derived the distribution $\mathcal{P}_{X/R}$ from the Slew survey X–ray selected sample, but using only objects with redshift lower than 0.25, in order to better approximate a distribution appropriate for a sample of sources at the same redshift, Fig. 3.1.

luminosity function

Unfortunately, the X–ray luminosity function for this sample is not (yet) avail-

[1]The polynomial fit is expressed as $\log\Phi = a + b\log L_{5GHz,28} + c(\log L_{5GHz,28})^2 + d(\log L_{5GHz,28})^3$ Gpc^{-3} L^{-1}, where $L_{5GHz,28} = L_{5GHz}/10^{28}$ erg/s/Hz, and the values of the coefficients are $a = -25.204616$, $b = -2.1376271$, $c = -0.0455836$ and $d = -0.0059641$.

able. For this reason we considered the EMSS and its well studied X–ray luminosity function (Morris et al. 1991; Wolter et al. 1994). We tentatively adopted an X–ray luminosity function matching that derived by Wolter et al. (1994), represented as a single power law $\Phi(L) \propto L^{-\alpha_\Phi}$, with slope $\alpha_\phi = -1.62$. Since the normalization of the luminosity function would substantially affect only the total number of sources, but neither their relative number nor the average luminosities, in order to recover the correct absolute number of objects we fixed the normalization (for the case with best results reported in Table 3.1) at the value $\log \Phi_0(L_{1keV}) = -36.3$. This value is within the confidence range given by Wolter et al. (1994), for the L_{1keV} corresponding to $L_{0.3-3.5keV} = 10^{40}$ erg/sec.

The luminosity evolution parameter is $\tau = 0.142$, according to the definition $L(z) = L(0) \exp(-t_{LB}/\tau)$, where t_{LB} is the look–back time in units of t_0 (for $q_0 = 0.0$, $t_0 = 1/H_0$). The luminosity range is $10^{24} - 10^{30}$ [erg/sec/Hz]. Also in this case we stress that LBLs and HBL reach different values of the minimum radio luminosity (see § 3.3.1).

3.3.3 Unified bolometric scenario

We parameterize the shape of the SED in terms of its synchrotron peak frequency, and *assume a power law relation between peak frequency and bolometric luminosity*. Adopting an estimate of the bolometric luminosity function we can derive all the observable properties and again compare them with observations.

The relation between the bolometric luminosity and the SED has been based on observed trends. More luminous objects seem to have LBL spectral properties, with the peak of the energy distribution in the IR–optical range and Compton dominated soft X–ray spectra.

The less luminous sources tend to display HBL SEDs, steep soft X–ray spectra and a synchrotron component peaking in the UV–soft X–ray band (e.g. Fig. 1.4b). The distribution between this two extremes seems to be continuous and we propose that it is governed by the now leading parameter $L_{bol,sync}$. Therefore, if we characterize the SED with the frequency at which the (synchrotron) energy distribution has a maximum, a fundamental (inverse) relation must exist between the bolometric luminosity and this frequency. The inverse dependence is qualitatively based on the trend found by Fossati et al. (1998), which will be discussed in Chapter 5.

SEDs parameterization

In order to reproduce the basic features of the observed SEDs we considered a simple geometric two component model. The synchrotron radio to soft X–ray component is

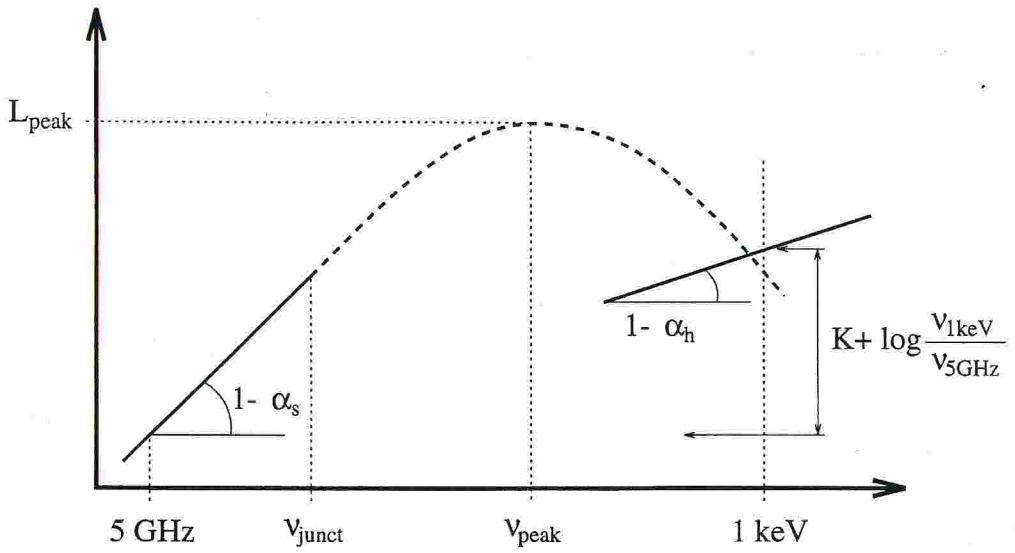

Figure 3.2: Schematic representation of the parameterization of the SEDs, according to the "unified bolometric" model. All the basic parameters are shown. Note that the difference between radio and X–ray luminosities in the νL_ν representation differs from the relative normalization of the two component, defined as K, by the term $\log(\nu_{1keV}/\nu_{5GHz})$.

represented with a power law in the radio domain, with spectral index α_s, smoothly connecting, at ν_{junct}, with a parabolic branch ranging up to ν_{peak}. Beyond ν_{peak} the synchrotron component steepens parabolically.

The hard X–ray Compton component is simply represented with a single power law with spectral index α_h. The normalization at 1 keV of this hard component ($L_{1keV,Comp}$) is kept fixed relative to the synchrotron one at 5 GHz (L_{5GHz}). This immediately implies a correlation between the radio and X–ray luminosity in sources where the emission at 1 keV is dominated by the Compton emission.

The parameters describing this representation of the SED are then five: α_s, α_h, the hard (Compton) X–ray normalization K= $\log(L_{1keV,Comp}/L_{5GHz})$, ν_{junct} and either the width of the parabolic branch σ or ν_{peak}. This is because we require that the parabolic branch matches the flat radio component at ν_{junct} also in its first derivative, and therefore we cannot fix independently both its width and peak frequency. A schematic representation of this parameterization is shown in Fig. 3.2, while its analytical expression is given in Appendix 3.6.

For simplicity, we use the luminosity at the peak of the synchrotron component, $L_{bol,sync}$ instead of the bolometric luminosity. In fact, for various complete samples of BL Lacs, Sambruna et al. (1996) find that the ratio between $L_{bol,sync}$ and ν_{peak} $L_{peak,sync}$ is consistent with being constant, $\simeq 8$.

We then specify the relation between ν_{peak} (the frequency at which the first peak in the νL_ν representation occurs) and the value of the corresponding luminosity $\nu L_\nu|_{\nu_{peak}}$. We note that for simplicity hereafter L_{peak} indicates the equivalent of a bolomet- ν_{peak} & L_{peak}

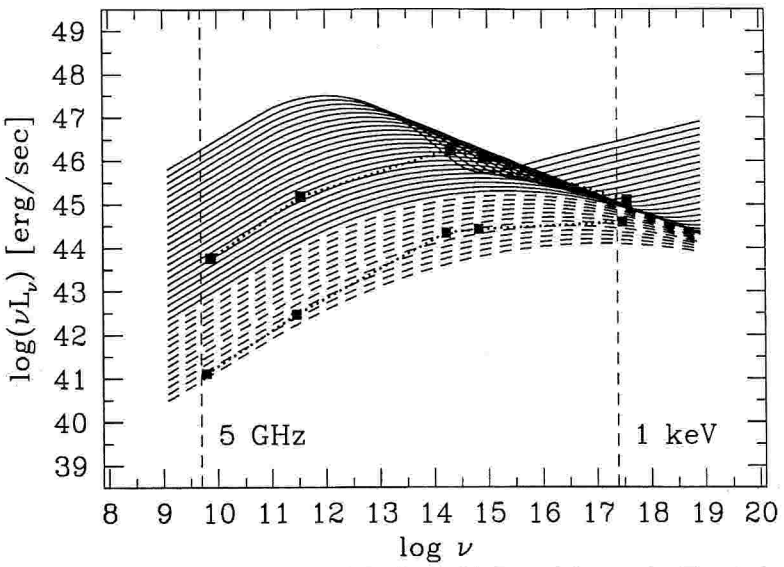

Figure 3.3: Set of SEDs used in the simulations of the "unified bolometric" scenario. The dashed SEDs are those with $\log(L_{1keV}/L_{5GHz}) > -5.5$, corresponding to HBL objects. The solid SEDs, on the contrary, correspond to LBL objects. Note that this subdivision is not strictly equivalent to the classification defined in terms of the flux ratio, that differs by a term $[(\alpha_R - \alpha_X)\log(1+z)] \simeq -0.3$. The squares indicate the average observed SEDs of HBL and LBL, as reported by Sambruna et al. (1996).

ric luminosity, i.e. νL_ν evaluated at ν_{peak}. This is the *key* physical relation of the proposed model. For simplicity we here consider a simple power law dependence $\nu_{peak} = \nu_{peak,0}(L_{peak}/L_{peak,0})^{-\eta}$ ($\eta > 0$). We then have three more parameters: η, $L_{peak,0}$ and $\nu_{peak,0}$.

In Fig. 3.3 a set of SEDs following the adopted parameterization is shown. The dashed lines represent those with $\log(L_{1keV}/L_{5GHz}) > -5.5$, roughly corresponding to HBL objects, while the opposite is true for the solid ones, LBL objects. Remember that the distinction is actually defined in terms of the flux ratio, and that $\log(F_{1keV}/F_{5GHz}) = \log(L_{1keV}/L_{5GHz}) + (\alpha_R - \alpha_X)\log(1+z)$.

To summarize: the adopted parameterization requires 8 inputs, 5 describing the shape of the SED (α_s, α_h, K, ν_{junct}, ν_{peak}) and three its relation with the luminosity ($\nu_{peak,0}$, $L_{peak,0}$, η). However, the family of SEDs is completely determined by a set of 7 parameters: α_s, α_h, K, ν_{junct}, $\nu_{peak}(\nu_{peak,0}, L_{peak,0}, \eta)$. In addition we must specify the normalization Φ_0 and the slope α_Φ of the adopted luminosity function.

luminosity function

We adopted a luminosity function for L_{peak} based on that calculated by Urry and Padovani (1995) (see their Fig. 13) for the 1 Jy and EMSS BL Lacs. Their (bivariate) luminosity function is obviously affected by selection effects both in the X–ray and radio bands, but constitutes the available distribution closest to a truly 'bolometric' one. The normalization has been chosen in the range $\log\Phi(L_{peak} = 45.0) = -44.8$ to -44.5 and the index $\alpha_\Phi = -1.90$ to -2.3. Finally, we stress that for simplicity no

evolution has been assumed in the bolometric scenario.

SEDs: parameterization *vs.* observations

We *formally* have 9 free parameters, but there is only a limited freedom in the choice of their values, which are constrained by observations.

α_s : it only takes values in a narrow range around 0, and we perform our simulations with the fiducial values 0.0, 0.1, 0.2.

α_h : its value is constrained by the assumption that, in the case of extremely hard X–ray spectra, we are only looking at the Compton component. We then considered a single value of $\alpha_h = 0.7$ equal to the average slope of the flatter X–ray spectra of LBLs (Lamer et al. 1996; Urry et al. 1996), for which we can think that we are measuring only their Compton emission.

K : on the same basis, the relative normalization between the radio and the X–ray components can be constrained by the value of $\log(L_{1keV}/L_{5GHz})$ of extreme LBL type objects, i.e. in the range $[-8 ; -7]$. We adopted the values K$= -7.0$ and K$= -7.5$.

η: can be limited by the ranges of observed L_{peak} and ν_{peak}, which imply values of η between ~ 1 and 2.

ν_{junct}: it is the parameter less determined by observations, being difficult to identify a spectral break even in the case of the best sampled and simultaneous SED. We considered values between 10^{10} and 10^{12} Hz. In the context of this parameterization the actual importance of ν_{junct} is indirect: its position affects the width of the parabolic branch extending up to the X–ray band. For a fixed value of ν_{peak} the higher is ν_{junct}, the narrower will be the parabola (i.e. the steeper the cut–off).

There is a limited freedom also on the luminosity function parameters. Note that the normalization is not actually an interesting parameter and, as already mentioned in § 3.3.2, varying Φ_0 only affects the absolute number of sources, neither the relative number of the two kinds nor the average luminosities.

Let us consider now some observed properties of complete BL Lac samples, which allow us to check the goodness of our parametric representation. *more checks*

In Fig. 3.4 the α_{OX} *vs.* α_{RO} plane for BL Lacs is shown, with points representative of the 1 Jy, Slew and EMSS samples. The line crossing the diagram is the locus of points derived from our "best fit" SEDs. It basically reproduces the observed pattern

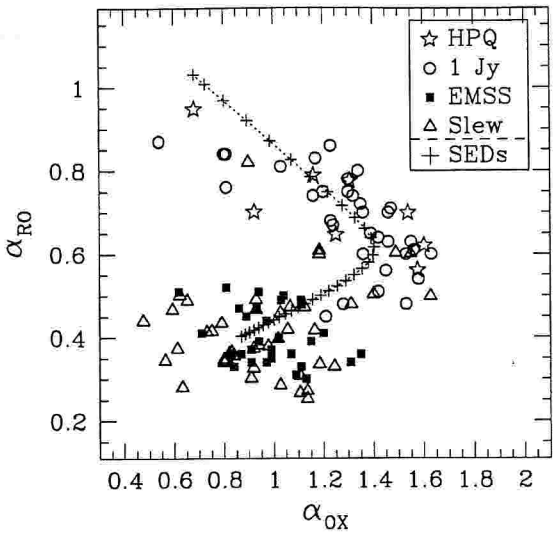

Figure 3.4: Distribution of sources in the α_{OX} *vs.* α_{RO} diagram (taken from Fossati et al. 1997). Different complete-samples are considered: EMSS, Slew and 1 Jy BL Lacs, and FSRQ (here referred to as HPQ) from the Brunner et al. (1994) sample. Symbols are defined in the inlet. The crosses connected by a dotted line show the spectral indices predicted by the adopted "best fit" parameterization of the SEDs.

of two different branches, where LBLs and HBLs are concentrated, apparently with no overlap. The fact that the "synthetic path" does not extend beyond $\alpha_{OX} \simeq 0.8$ is related with the narrow range of parameters (and tight relation among them) adopted in the samples simulation, namely to the minimum allowed bolometric luminosity.

It is also possible to compare the SEDs with the observed average spectral energy distributions of LBLs and HBLs, taken from Sambruna et al. (1996). Their data points, given in flux units and converted in luminosities (considering a typical redshift of 0.5 for the RBLs and 0.2 for XBLs), are plotted in Fig. 3.3 together with our SED family. Also in this case the agreement is satisfactory.

We can say that our schematic representation of the SEDs well reproduces the basic properties of the observed BL Lacs broad band spectra.

3.4 The simulations

Given these assumptions, we computed the predictions of the models. We used a Montecarlo technique to simulate the distribution of sources in space and luminosity. This method is very convenient because it allows us to store "single source" attributes and not only to compute sample integrated average properties. In other words, we can actually simulate a catalogue and from it compute the desired average quantities. In all cases simulations have been performed within the redshift range $0 - 2$.

In Fig. 3.1a,b the observed L_{1keV}/L_{5GHz} distributions are shown, taking into ac-

count only objects with redshift estimate. The dashed histograms represent LBL objects, the dotted ones HBLs. Note that there is a superposition of the two classes due the fact that the actual distinction between LBL and HBL is based on the flux ratio (while here luminosities are considered). In Fig. 3.1c the distribution $\mathcal{P}_{\mathrm{X/R}}$, used in the calculations for the radio leading scenario, is shown. The actual computation can be summarized in five steps:

① "draw" a redshift and a luminosity from the luminosity function assumed as primary (radio for the radio leading, X–ray for the X–ray leading scenarios);

$$\begin{aligned} \mathcal{P}(z,\mathcal{L})\,dz\,d\mathcal{L} &\equiv \frac{n(z,\mathcal{L})\,dz\,d\mathcal{L}}{N_{\mathrm{tot}}} \\ &= \frac{1}{N_{\mathrm{tot}}}\,\Phi(\mathcal{L};z)\,\frac{dV}{dz}(z;q_0,H_0)\,d\mathcal{L}\,dz \end{aligned} \tag{3.1}$$

where N_{tot} is the whole number of sources integrated both in z and L, up to the maximum considered redshift. Since we are considering pure luminosity evolution, i.e. the *number* of sources for unit of comoving volume is constant at any epoch, the term giving the distribution in luminosity can be separated from that of the distribution in space, and the two probabilities for z and $\mathcal{L}$ can be considered separately, yielding a great simplification of the computation.
The distribution in "space" is then only depending on the the comoving volume element

$$\frac{dV}{dz}(z;q_0,H_0) = \frac{c}{H_0}\,\frac{4\pi d_{\mathrm{L}}^2(z;q_0,H_0)}{(1+z)^3\sqrt{1+2q_0z}} \tag{3.2}$$

which for our choice of $q_0 = 0$ yields:

$$\frac{dV}{dz}(z;H_0) = \left(\frac{c}{H_0}\right)^3 \frac{z^2\,(1+z/2)^2}{(1+z)^3} \tag{3.3}$$

Due to the properties of pure luminosity evolution the probability for the primary luminosity at any z is simply related to the "local" one:

$$\begin{aligned} \mathcal{P}(\mathcal{L};z)\,d\mathcal{L} &= \mathcal{P}(\mathcal{L}_0 = \mathcal{L}\,e^{t_{\mathrm{BL}}/\tau};z=0)\,d\mathcal{L}_0 \\ &\equiv \Phi(\mathcal{L}_0,0)\,d\mathcal{L}_0 \Big/ \int_{\mathcal{L}_{0,\min}}^{\mathcal{L}_{0,\max}} \Phi(\mathcal{L}_0,0)\,d\mathcal{L}_0 \end{aligned} \tag{3.4}$$

② the "secondary" luminosity (i.e. in the other spectral band) is deduced by choosing a luminosity ratio by means of its probability distribution $\mathcal{P}(\mathrm{L_{1keV}/L_{5GHz}};\,\mathcal{L})$. For the radio leading and X-ray leading models this probability is not actually

depending on the value of $\mathcal{L}$, begin fixed a priori by the observational data, i.e. $\mathcal{P}(L_{1keV}/L_{5GHz})$. On the contrary for the bolometric picture there is a unique value of L_{1keV} /L_{5GHz} for any given $\mathcal{L}$, and so this second step is not actually being performed.

③ radio and X–ray fluxes are computed for the simulated source taking into account the "inverse" K–correction

$$F = \frac{L}{4\pi\, d_L^2(z; q_0, h_0)}\,(1+z)^{1-\alpha} \tag{3.5}$$

where α is the spectral index in the observed band. The "inverse" refers to the fact that usually the K–correction is meant to convert observer–frame to source–frame quantities, while here we are using it in the other direction.

④ check if the simulated source would be detected in a survey with a given flux limit and, if so, store its set of parameters.

The detectability criteria take into account the sky coverage $\Delta\Omega$ that in the radio case is a step function of the monochromatic 5 GHz flux, while in the X–ray survey it is an increasing function of the flux integrated over the whole IPC band ($0.3 - 3.5$ keV). In the X–ray case we then simulated N surveys (typically $15 - 20$) each with a different flux limit F_i and a corresponding $\Delta\Omega_i$. The results of the N surveys are then summed up to construct the full X–ray survey result.

Slew sky coverage

The flux dependent sky coverage for the Slew survey has been derived from the "exposure time" *vs.* "percentage of sky" diagram published in Elvis et al. (1992). A limiting flux corresponding to a given exposure time is deduced considering a detection limit of 5 IPC counts, and a conversion factor from IPC counts to flux of 3.26×10^{-11} erg/cm^2/sec (Elvis et al. 1992), valid for values of $\alpha_X = 1.2$ and $N_H = 3 \times 10^{20}$ cm^{-2}. In fact, in order to convert to monochromatic flux we adopted an X–ray spectral index $\alpha_X = 1.2$, a fiducial average value for the class of sources that we are considering. This gives the conversion relation: log F_{1keV} = log $F_{[0.3-3.5keV]} - 17.776$. This conversion factor varies only of a few tenth for changes of the spectral index in the range 0.7–1.5, and of the N_H from 1 to 3×10^{20} cm^{-2}, intervals including most of the observed values of blazars.

It is important to stress here that we use an approximated sky coverage by using the information currently available. An exact correction cannot be computed, but plausibly this would mostly affect the *normalization* of the assumed luminosity functions.

⑤ finally, a detected source is classified as HBL or LBL according to its F_{1keV}/F_{5GHz} ratio, as already defined.

TABLE 3.1: SUMMARY OF RESULTS OF SAMPLES SIMULATIONS[a]

				LBL		HBL	
	N_{TOT}	N_{LBL}	N_{HBL}	L_{5GHz}	L_{1keV}	L_{5GHz}	L_{1keV}
(1)	(2)	(3)	(4)	(5)	(6)	(7)	(8)
1Jy Survey							
Observed	34.0	32.0	2.0	34.05	27.30	32.10	26.84
				(0.76)	(0.30)	(0.30)	(0.23)
Radio leading	29.1	26.7	2.4	33.73	26.83	33.54	28.93
				(0.97)	(1.24)	(0.86)	(1.05)
				[···]	[94.50 %]	[···]	[···]
X–ray leading	33.7	29.0	4.7	34.13	27.51	33.34	28.50
				(0.80)	(0.83)	(0.78)	(0.78)
				[···]	[···]	[···]	[91.00 %]
Bolometric[b]	35.1	33.3	1.8	34.87	27.83	32.43	27.31
				(0.78)	(0.33)	(0.46)	(0.21)
				[99.93 %]	[98.58 %]	[···]	[···]
Slew Survey							
Observed	48.0	8.0	40.0	33.74	27.56	31.60	27.53
				(0.88)	(0.96)	(0.49)	(0.64)
Radio leading	50.7	7.1	43.6	33.10	27.31	32.43	28.20
				(0.99)	(1.06)	(0.98)	(1.01)
				[···]	[···]	[99.99 %]	[99.83 %]
X–ray leading	49.4	6.7	42.7	34.10	27.74	32.07	27.72
				(1.03)	(0.90)	(1.10)	(0.96)
				[···]	[···]	[97.74 %]	[···]
Bolometric[b]	47.2	8.2	39.0	33.57	27.64	31.85	27.28
				(0.76)	(0.21)	(0.49)	(0.35)
				[···]	[···]	[···]	[···]

Notes to Table 3.1

(a) A Poisson error should be considered on the source numbers. The variances on the average luminosities and the significance of rejection of the "null" hypothesis as evaluated with the Student's t–test are reported in "( )" and "[ ]", respectively. Dots are reported when the significance is lower than 90 %.

3.5 Results and comparison of the models

The comparison of the three models with the 1 Jy and Slew survey samples are presented in Figs. 3.5a, 3.5b respectively. The average observed and predicted radio and X-ray luminosities are reported in Table 3.1, together with the numbers of objects.

The consistency of the predicted and observed distributions has been quantitatively

TABLE 3.2: SURVIVAL ANALYSIS RESULTS[a]

	Radio leading	X–ray leading	Bolometric
1 Jy Survey[b]			
z	95.80	93.45	92.70
L_{5GHz}	...	...	99.85
L_{1keV}	94.00	...	94.80
Slew Survey[c]			
z	99.96	...	...
L_{5GHz}	99.96	95.60	...
L_{1keV}	97.20	...	...

Notes to Table 3.2

(a) A variety of statistical test has been applied: Gehan Generalized with both permutation and hypergeometric variance, Peto & Peto and Peto & Prentice, all of them as implemented in the ASURV package (Rev. 1.1, Lavalley et al. 1992). The reported values are the simple averages of the results of these four tests, expressed in percentual probability. Dots are reported when the significance is lower than 90 %.

(b) In the "1 Jy survey" case the tests have been performed only on the LBLs subsample.

(c) In the "Slew survey" case the tests have been performed only on the HBLs subsample.

statistical tests

estimated through the use of the Student's t–test for comparison of the means, and also of the more sophisticated survival analysis non-parametric and univariate methods (Feigelson and Nelson 1985) allowing to take into account lower limits, and sensitive to the shape of the distributions. Student's t–test has been performed on all average luminosities, while the survival analysis has been applied only to the cases with a significant number of objects, namely for the LBLs subsample in the "1 Jy" and HBLs in the Slew survey. The results of the statistical tests are reported as an entry in Table 3.1 for Student's t–test, and separately in Table 3.2 for the survival analysis.

3.5.1 Radio and X-ray leading

We first discuss the results of the radio and X–ray leading scenarios

Radio survey: let us consider first the comparison of the models with the 1 Jy sample (Fig. 3.5a). Both models predict luminosities for the HBL in both bands more than one order of magnitude larger than observed. However the extreme paucity of objects does not allow these discrepancies to be significant from a statistical point of view. The Student's t–test indicates that the radio leading scenario predicts the X–ray luminosity of the LBLs in disagreement, at the > 94.0 per cent level, with the observed one, while the X–ray leading one has difficulties

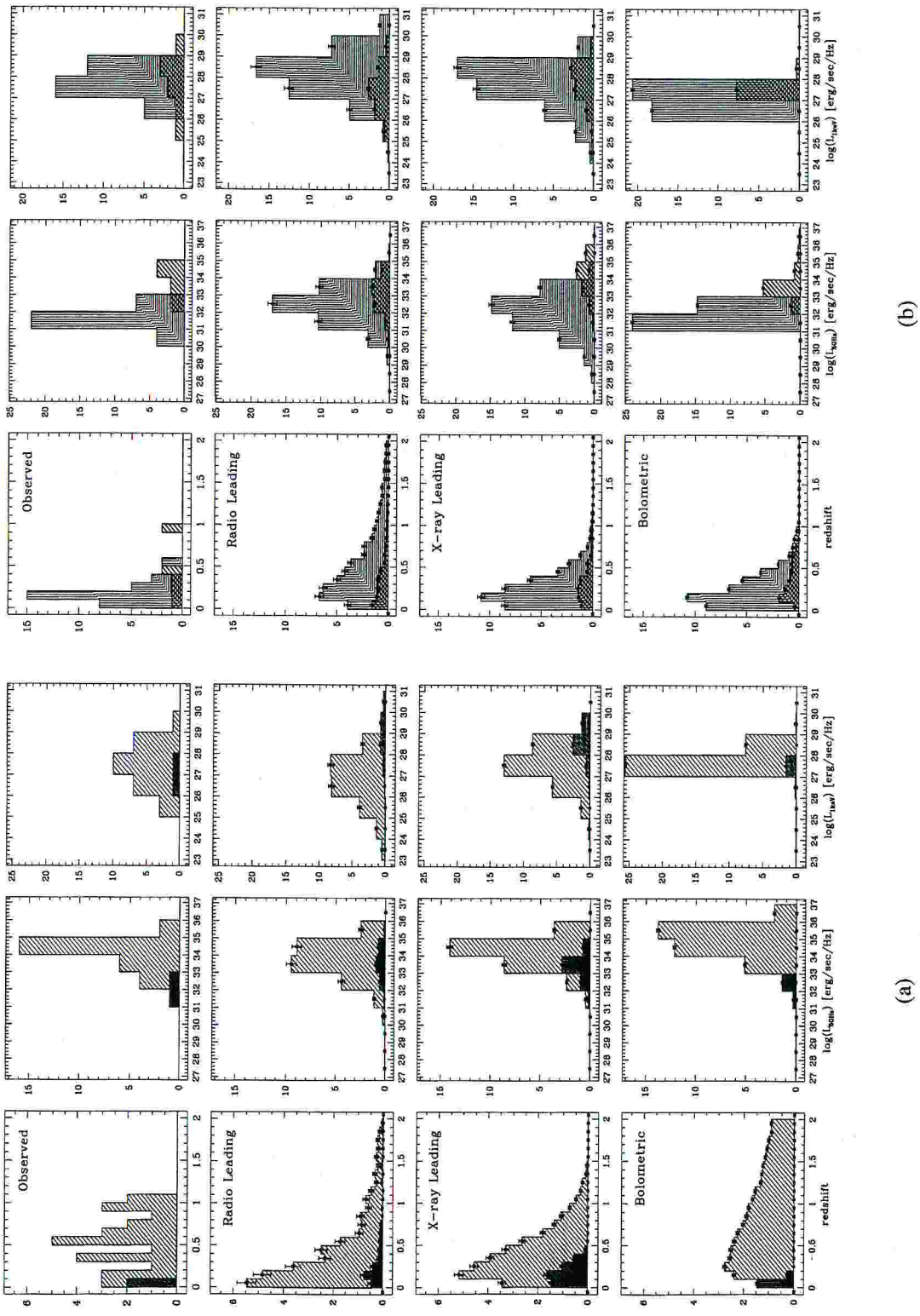

Figure 3.5: Results of the simulations of the 1 Jy survey compared with observations. From top to bottom: observations, radio leading, X–ray leading and bolometric models, respectively. From left to right: histograms of the redshift distributions, radio and X–ray luminosities for the two classes. Again dashed and dotted areas represent LBL and HBL, respectively. The error bars are derived from the simulations.

at reproducing the average luminosity of the HBL at the 91 per cent confidence level.

The relative number of objects detected in both scenarios is in reasonably good agreement with the observed one (5/29 and 3/27 instead of 2/32).

X–ray survey: the predictions of the two models concerning the Slew survey objects are instead quite different (Fig. 3.5b).

The radio leading scheme leads to incorrect X–ray and radio luminosities of HBL: from survival analysis 97.2 and 99.96 per cent confidence (Table 3.2), respectively, and even worse according to the Student's t–test (Table 3.1).

The average radio luminosity of HBL is also overestimated within the X–ray leading scenario (> 95.6 per cent level). Again, nothing can be said from these tests on the distributions of the less numerous source population.

The predicted numbers of HBLs and LBLs in the Slew survey (43/7 and 43/7) are in good agreement with the observed one (i.e. 40/8).

Summarizing, in terms of source numbers and average luminosities the X–ray leading model is better than the radio leading one, sharing with it the problem of HBL luminosities in radio surveys. Nevertheless, it should be noted that HBL objects in the 1 Jy survey are only 2 and so their measured properties could mis–represent the true ones. Moreover, in the radio leading scenario the average radio luminosities of the LBL and HBL subsamples tends unavoidably to be the same: as immediate consequence of the radio leading hypothesis, all BL Lac objects should share the same range of radio luminosity, in contrast with observations of complete samples (see also Fig. 1.4b). In the X–ray leading case the included negative luminosity evolution remove this "structural" problematic feature.

Redshift distribution: finally, there is a significant disagreement on the redshift distributions (see the panels of the first columns in Figs. 3.5a,b): both models predict a sharp peak of simulated LBL sources at low redshift, in contrast with the observed flat distributions.

This is a *built–in* feature of this kind of approach in which we take the relative number of the the two types of sources fixed for any value of the leading luminosity.

evolution

We should however note that the inconsistency between the distribution predicted by the radio leading scenario and the one observed in the 1 Jy sample is in agreement with the assumption of no evolution adopted here. If we had introduced the slight positive evolution apparent from 1 Jy data we would have (probably) obtained a redshift distribution completely consistent with the ob-

served one.

As expected, the inclusion of the negative evolution in the X–ray leading model tends to improve the agreement with observations. Indeed the redshift distributions obtained in the X–ray leading non evolving case were qualitatively similar to the ones of the radio leading scenario (see Fossati et al. 1996). In fact in the 1 Jy survey HBLs are sharply concentrated at lower redshifts, while LBLs show a "flatter" distribution. These trends are closer to the observed ones than those derived in the radio leading scenario (Fig. 3.5a). The same is true for the Slew survey (Fig. 3.5b).

survival analysis

The use of the survival analysis allowed us to perform a quantitative analysis. The comparison of only the LBLs in the 1 Jy survey indicates that the predicted distributions are not compatible with the observed one at the 95.80 and 93.45 per cent level for the radio and X–ray leading scenarios, respectively. A much more significant disagreement is found in the Slew survey (considering only HBLs), which is inconsistent with the predictions of the radio leading scenario at the 99.96 per cent level.

Comment on Evolution

This last point on the redshift distribution is particularly important. In fact it indicates that evolutionary effects should be taken into account. However it is possible that it is the distribution $\mathcal{P}_{X/R}$ which changes with redshift, rather than the luminosity in one of the two bands: clearly one can re–express the different evolution in the two bands by saying that $\mathcal{P}_{X/R}$ evolves.

From an observational point of view, if one considers different intervals in redshifts in the Slew survey sample there are 5 LBL and 7 HBL objects at high redshifts, while these numbers become 3 and 26 at low redshifts (taking a dividing value at $z = 0.25$). The only two HBL sources with known redshift present in the 1 Jy sample are both at $z < 0.1$.

We then considered an evolving probability distribution $\mathcal{P}_{X/R}$, i.e. we introduced a redshift dependence on the relative ratio of the two populations of BL Lac objects. Basically $\mathcal{P}_{X/R}$ has a bimodal shape, described with two gaussians centered at $\log(L_{1keV}/L_{5GHz}) = -6.5$ and -3.5 for LBLs and HBLs, respectively. The relative normalization of these gaussians evolves as $N_{HBL}/N_{LBL} \propto (1+z)^{-\gamma}$ (with $\gamma \geq 0$), in such a way that the RBL part of the distribution becomes more and more dominant at higher redshifts. With this evolution of $\mathcal{P}_{X/R}$ we can induce the observed difference in the redshift distribution of HBLs and LBLs.

In this case the luminosity function is not self–consistently derived. Instead, we have to deal with a *tentative* luminosity function, in the sense that it is by no means consistent with the evolution that we are introducing. It would therefore be necessary to derive "backwards" how the evolution of $\mathcal{P}_{\rm X/R}$ translates in terms of luminosity function evolution.

We considered only a limited region of the parameter space of $N_{\rm HBL}/N_{\rm LBL}|_{(z=0)}$ and γ, without finding a solution which improves the results already obtained. Actually, in the case of the radio leading scenario, there is a hint that better solutions are obtained by changing the parameters progressively towards the *no evolution* case, as in the "original" model.

While we cannot exclude that a suitable solution could be found following these assumptions, we did not yet go further with this investigation.

3.5.2 Bolometric

Even a simple "first attempt" set of the 9 input parameters gives a surprisingly good output. In Table 3.1 the best results, found after a systematic check for a grid of parameter values within the allowed ranges, are reported. The corresponding input parameters are:

$$\begin{array}{lll} \alpha_{\rm s} = 0.2, & \log \nu_{\rm peak,0} = 16.5, & \nu_{\rm junct} = 5 \times 10^{10}\,{\rm Hz} \\ \alpha_{\rm h} = 0.7, & \log {\rm L}_{\rm peak,0} = 44.5, & \Phi_0 = -44.76 \\ {\rm K} = -7.5, & \eta = 1.5, & \alpha_\Phi = -2.25 \end{array}$$

Radio survey: the Student's t–test implies that the model predicts too high luminosities for the LBL both in the radio and X–ray band (at the 99.9 and 98.6 per cent level, respectively, see Table 3.1) when compared with the observed 1 Jy Survey distributions. The result is confirmed by the survival analysis (see Table 3.2). It should be noted that probably the discrepancy is strengthened by the fact that the scheme in the used implementation is very rigid, and this for instance leads to the very narrow histograms in Fig. 3.5.

X–ray survey: for the Slew survey instead no significant disagreement has been found.

Redshift distribution: a very positive consequence of this scenario is that it implies a qualitatively 'better' redshift distribution, as can be seen in Figs. 3.5a and 3.5b, with respect to the previous schemes. In particular we stress that the bolometric scenario is the only one which predicts, as direct result of the SED dependence on the bolometric luminosity, that the redshift distributions of the two populations can be such that LBL would tend to dominate at high redshifts, while the

opposite would be true at low z (see Fig. 3.5b). This behaviour could be seen as equivalent to either a redshift dependence of the X–ray-to-radio–flux ratio distribution $\mathcal{P}(L_{1keV}/L_{5GHz})$ or a negative X–ray luminosity evolution.
In fact, note that the different redshift distributions of the two kinds of BL Lacs is a natural outcome of this scenario. HBLs objects come from the lower (and richer) part of the luminosity function and so they dominate at low redshift, but they disappear at large distances despite the increase of the available volume. On the contrary, LBLs, even though coming from the poorer part of the luminosity function, become predominant at higher redshifts, being still detectable.

There is still a problem with LBLs in the radio survey. Even though the shape of the z distribution is correctly flat (and this is the major difficulty of the two other models), it extends well beyond $z = 1$, which leads to a disagreement significant at the 92.7 per cent level (survival analysis, see Table 3.2). We believe this fact is directly connected with the excessive average radio luminosities predicted by the model.
In order to explore the consistency of the *shape* of the predicted and observed redshift distributions, we applied the survival analysis test only up to $z = 1$, and did not find inconsistency between the two. with the observed one. Clearly, this result only indicates that the shape of the predicted distribution can resemble the real one over the considered redshift interval.

Comment on "Bolometric" model results and problems

The main characteristic of the bolometric model is the link between the bolometric luminosity with the energy of the synchrotron cut–off. We stress that while it is true that the bolometric scenario contains a significant number of (quite constrained) parameters with respect to the two other models, it also predicts the statistical and cosmological properties of the two 'types' of sources directly from a unified description of their spectral distribution. Despite the rigid formulation of the one–to–one correspondence between the SED properties and the luminosity, in this scenario the main observational data can be reproduced at least with the same "accuracy" as the other two models. Particularly interesting is the prediction of the different HBL and LBL redshift distributions, which tend to favour the detection of objects of the first class at low redshifts and of LBL at higher z.

The predictions of the bolometric model of luminosities of sources detected in radio surveys higher than observed is plausibly related to the problem with their redshift

distribution.

problems

We suggest that the excess of objects predicted at higher redshift (and/or their overestimated radio power) could be understood in the broader unifying picture, where BL Lacs objects are the less powerful member of a sequence including also Flat Spectrum Radio Quasars. If a fraction of the sources with the highest bolometric luminosities could be indeed "classified" as FSRQ rather than LBL (in a way analogous to the transition from HBLs to LBLs), this fact could plausibly explain the discrepancies in the high luminosities and redshift distributions predicted by the model.

In Chapter 5 and 6 we will illustrate and discuss some pieces of evidence which are supporting this view, leading us to the definitive inclusion of BL Lacs and FSRQ in a unique sequence.

3.6 Perspectives

We have considered three different scenarios, which assume that BL Lac objects constitute a single population of sources, with different spectral energy distributions (mainly different peak frequencies of the synchrotron component), which was considered as an indication of the existence of two classes of BL Lacs. The discussed scenarios can correctly predict a significant number of quantities in agreement with current observations. However they (and in particular the radio leading one) fail to reproduce some of the distributions of observed quantities.

Predictions

To conclude, we consider here the predictions of the three models on the results of deeper surveys. In particular we compute the expected ratio of objects of the two "flavours" in more sensitive radio and X–ray surveys, as a function of their flux limits. The results are reported in Table 3.3 as the relative ratio N_{LBL}/N_{HBL} normalized to the value predicted for the 1 Jy and Slew surveys.

From Table 3.3, one can clearly see the opposite trends expected from the radio and X–ray leading scenarios in radio surveys. Distinct features of the bolometric scenario are a rapid decline in the fraction of LBL in radio surveys and a weak decrease in X–ray surveys. This behaviour follows from the one–way relation between LBL and HBL SED properties with luminosity.

It should be stressed that predictions are a delicate matter to deal with, because the change of numbers is not only responding to the detail of the specific model, but it is very sensitive to a variety of other effects, basically selection effects induced by

TABLE 3.3: MODEL PREDICTIONS[a]

Radio Survey				X–ray Survey			
Flux limit[b] (F_{5GHz})	Radio leading	X–ray leading	Bolometric	Flux limit[c]	Radio leading	X–ray leading	Bolometric
1.00	1.0	1.0	1.0	1/1	1.0	1.0	1.0
0.10	1.3	0.89	0.29	1/10	1.63	1.13	0.95
0.01	1.5	0.62	0.09	1/100	2.43	1.26	0.88

Notes to Table 3.3

(a) The numbers represent the predicted N_{LBL}/N_{HBL} ratio normalized to the value predicted for the 1 Jy or Slew survey

(b) Radio fluxes are expressed in Janskys

(c) The flux limit is expressed relative to the Slew survey one. The sky coverage used is simply that of the Slew survey shifted, in logarithm, by the appropriate factor

observational limitations, sometimes not immediately recognizable. We would like to mention here at least three of these sources of bias.

Browne-Marchã effect

Browne and Marchã (1993) pointed out the possible effect of mis-identification of faint BL Lacs caused by the lack of contrast of the active nucleus with the host galaxy. It should be noted here that, while we were able to ignore the Browne and Marchã selection effect for the results of the Slew survey, this would be progressively relevant in surveys with decreasing flux limit, as the ones we are simulating here.

K–correction

We noted in § 1.2.2 that the HBL/LBL ratio is a function of the flux limit even in the radio survey for the radio leading scenario (and X–ray survey for the X–ray leading one), despite the "construction" assumption that the *intrinsic* ratio is constant at any epoch. This is due to the different dominant range of redshifts at different flux limits, which causes objects at the border of the definition of HBL/LBL to "move" into the LBL class, because of the term $(\alpha_R - \alpha_X)\log(1+z)$ (always negative) in the relation between flux and luminosity ratios.

minimum luminosity

Another factor to take into account in the interpretation of these predictions is the role of the existence of the minimum luminosities. As mentioned in Section 3.3.1, a minimum luminosity in the "leading" band leads to different minimum luminosities for LBL and HBL in the "secondary" band, due to their intrinsically different SEDs. Therefore, at flux limits which allow the detection of the faintest sources, only objects with SEDs which favour very low fluxes in that band will be detected. This effect is observable mainly in radio surveys in the X–ray leading scenario and in X–ray surveys in the radio leading one.

In Fig. 3.6 we show another set of predictions for the radio leading, X–ray leading and bolometric scenarios. In the diagram we reported the predicted fraction (in

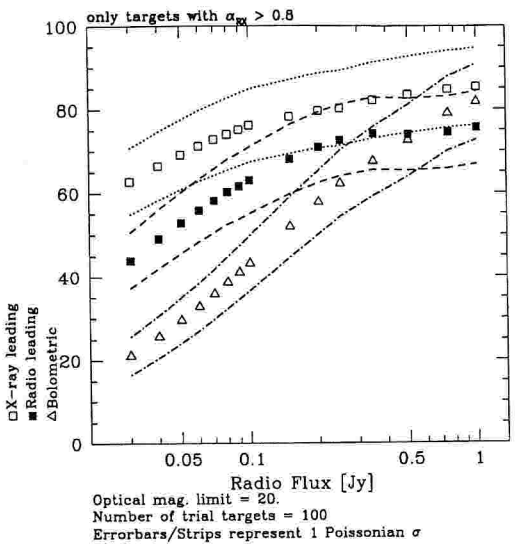

Figure 3.6: Fraction of objects having $\alpha_{RX} > 0.8$, i.e. *extreme* LBLS, in deeper radio selected samples, with an additional optical flux limit $m_V \lesssim 20$.

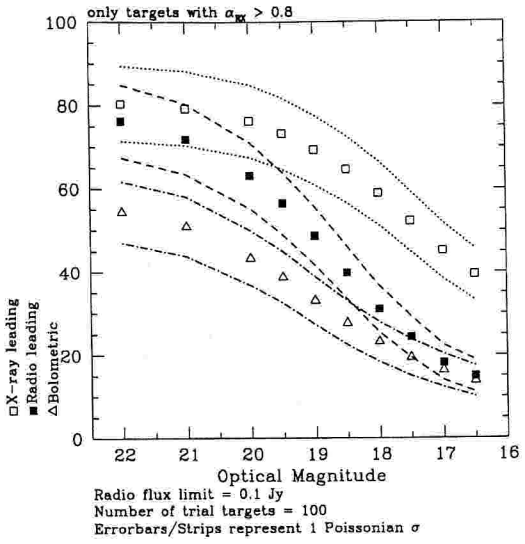

Figure 3.7: Fraction of objects having $\alpha_{RX} > 0.8$, i.e. *extreme* LBLS, in a deeper radio selected sample having a flux limit $F_{5GHz} = 0.1$ Jy, plotted as a function of the *secondary* optical magnitude limit.

percentage) of objects having $\alpha_{RX} > 0.8$, i.e. kind of "extreme" LBLs. We focused on $\alpha_{RX} > 0.8$, in order to have a "cleaner" estimate, getting rid of the problem of the drift of HBLs towards the LBLs due to the K–correction effect, which could hamper the power of discrimination of the different scenarios.

We are here considering deeper radio surveys, with flux limits in the range 30 mJy to 1 Jy at 5 GHz, with a secondary selection in the band optical at a limiting magnitude of $m_V \lesssim 20$. The addiction of the optical cut has been introduced to be make these results more realistic. In fact the need of optical identification, in particular for BL Lac objects, imposes a quite strong constraint on the observational properties of the recognizable sources, that can not be ignored when going deeper in the "primary" selection band. To be more quantitative, a survey with a flux limit of $F_{5GHz} = 0.1$ Jy, and $m_V \lesssim 20$, is complete in spectral shape only up to $\alpha_{RO} = 0.68$. Above this value the radio–optical index is too steep to have an optical flux above the detection/identification threshold. Just to give a couple more of numbers, to be complete down to $\alpha_{RO} = 0.95$, the maximum know value reached by LBLs, i.e. to include all LBLs, require a limiting magnitude $m_V \simeq 23.3$ for $F_{5GHz} = 0.1$ Jy, and $m_V \simeq 24.6$ for $F_{5GHz} = 0.05$ Jy.

To better illustrate this bias we plot in Fig. 3.7 the predictions (again fraction of objects with $\alpha_{RX} > 0.8$) for a radio survey with $F_{5GHz} \gtrsim 0.1$ Jy for several values of the optical magnitude limit. The effect of the presence/change of the optical limit, i.e.

the bias against LBLs for low radio flux limits, is clearly noticeable, as it is in Fig. 3.6, where the fraction of LBLs decreases as the radio limits decreases.

The width of the strips marked by the dashed lines represents the poissonian error computed for the case of a sample of 100 objects, and it should be taken with care. Actually the real number of sources belonging to such samples is well above 100 for $F_{5GHz} \lesssim 0.25$ Jy, whilst it is smaller for higher flux limits, and therefore the 1 sigma confidence width for these cases should be broader.

From the results presented in Fig. 3.6 we can say that it seems to be possible to discriminate the three current unified pictures for BL Lac objects already with moderately deep radio(–optically) selected samples ($F_{5GHz} \gtrsim 0.1 - 0.2$ Jy, $m_V \lesssim 20$). Such kind of samples are going to be available soon.

Finally it is important to remind that these examples do not take into account other observational quantities, e.g. absolute number of HBLs and LBLs, redshift distribution, average luminosities, that can be even more discriminant than it is the study of the fraction of LBLs.

Appendix:SED analytical expression

The analytical expression of the parameterized SEDs in the "bolometric" model is given by:

$$\begin{aligned}
\psi_{\rm S,1}(x) &= \log(\nu F_\nu)_{s,1} = \beta(x - 9.698) + \psi_{\rm S}(5{\rm GHz}) \\
\psi_{\rm S,2}(x) &= \log(\nu F_\nu)_{s,2} = -\left[(x - x_{\rm peak})/\sigma\right]^2 + 0.25\,\sigma^2\beta^2 + \psi_{\rm S,1}(x) \\
\psi_{\rm C}(x) &= \log(\nu F_\nu)_h = (1 - \alpha_h)(x - 17.383) + \psi_{\rm C}(1{\rm keV}) = \\
&= (1 - \alpha_h)(x - 17.383) + \psi_{\rm S}(5{\rm GHz}) + K + 7.685
\end{aligned}$$

where $x \equiv \log\nu$, and $\beta = (1 - \alpha_s)$, and $\sigma = \left[2\,(x_{\rm peak} - x_{\rm junct})/\beta\right]^{1/2}$.
$\psi_{\rm S,1}(x)$ and $\psi_{\rm S,2}(x)$ are defined on the frequency ranges $x < x_{\rm junct}$ and $x > x_{\rm junct}$, respectively.
The SED expression can be re-scaled as a function of the value of $L_{\rm peak} = 10^{\psi(x_{\rm peak})}$, and in particular the luminosities at 5 GHz and 1 keV can then be written as:

$$\begin{aligned}
\psi_{\rm S}(5{\rm GHz}) &= (1 + 0.5\,\eta\beta)\psi_{\rm peak} = \\
&= -0.5\,\beta(x_{\rm peak,0} + \eta\psi_{\rm peak,0} - x_{\rm junct}) - \beta(x_{\rm junct} - 9.698) \\
\psi_{\rm S}(1{\rm keV}) &= \psi(x_{\rm peak}) - \left[(17.383 - x_{\rm peak})/\sigma\right]^2 \\
\psi_{\rm C}(1{\rm keV}) &= \psi_{\rm S}(5{\rm GHz}) + K + 7.685 \\
\psi_{\rm tot}(1{\rm keV}) &= \log(10^{\psi_{\rm S}} + 10^{\psi_{\rm C}})
\end{aligned}$$

CHAPTER 4

HIGH ENERGY EMISSION: X– AND GAMMA–RAY BANDS

We have discussed the viability of unification scenarios for BL Lac objects, introducing the new "bolometric luminosity" model and envisaging the possibility to include also FSRQ in the picture. In view of the work specifically focused on SEDs and the extension of the unifying scheme from BL Lacs to FSRQs, which is matter of Chapters 5 and 6, we consider here the spectral properties of the high energy emission, in particular putting emphasis on the γ–ray band. As mentioned in Chapter 1 these data are crucial in many senses for the understanding of the physics of blazars. The main purpose of the work presented in this Chapter is therefore to study, for a sizeable sample of bright γ–ray sources, the role of the X–ray emission with respect to the SED, with particular emphasis on the relation between the X– and γ–rays.

4.1 The sample

A list of γ–ray blazars has been compiled collecting all the data available in the literature up to September 1996 and contains about 60 sources. The γ–ray bright source list has been cross–correlated with the *ROSAT* PSPC pointed observations public archive. About half (27) of the sources were either the target of pointed observations or in the

field of view (within about 40 arcmin) of a different target. For 19 of the sources, which were not observed in pointing mode, *ROSAT* All Sky Survey (RASS) data were available in the literature (Brinkmann et al. 1994; Brinkmann et al. 1995). Finally we have included 7 more sources with X–ray fluxes retrieved from missions other than *ROSAT*.

This selection yielded 53 bright γ–ray blazars which are listed in Table 4.1. A concern regards the selection of the γ–ray data, given the large amount of available observations and analyses of the same data by different authors. For most of the objects there exist several EGRET observations and/or for some of these more than one analysis is available. In these cases we have chosen the γ–ray flux and spectral slope according to the following criteria:

① spectral index and flux referring to the same observation,

② data corresponding to a single observing period,

③ when the same data are analyzed by different authors, the results of the most recent analysis are preferred.

Even though not complete, this sample includes about 80 % of all known γ–ray blazars and therefore we feel justified in considering it representative of the entire population.

4.2 *ROSAT* Observations and data analysis

4.2.1 Data reduction

The data reported here are from observations carried out with the *ROSAT* X–ray telescope (Trümper 1982) with the PSPC in the focal plane (Pfeffermann and Briel 1986; Pfeffermann et al. 1987). The PSPC provides a bandpass in the range $\sim$ 0.1–2.4 keV over a $\sim 2^\circ$ diameter field of view, with a moderate spectral resolution. Most of the observations have been performed in the "wobble" mode. In this mode the detector is moved from the pointing direction with a period of $\sim$ 400 s and an amplitude of $\sim$ 3 arcmin. In this way the effect of shadowing of the X–ray sources by the detector window structures like struts and wire mesh is minimized.

The spatial profiles of the images for all the observations in the $\simeq$ 0.1–2.4 keV range are consistent with those of point sources convolved with the PSPC point spread function (PSF) according to the source spectral properties and keeping into account the background level. Source spectra were extracted from circular regions with radii large enough (from 2 to 4 arcmin) to ensure that all the soft counts be included, given the electronic ghost imaging which widens the PSF below $\sim$ 0.2–0.3 keV (Hasinger et al.

TABLE 4.1: X/γ SELECTED SAMPLE[a]

IAU Name (1)	Other Name (2)	class (3)	z (4)	σ_γ^b (5)	VP[c] (6)	Ref. (7)	X-ray class (8)	Ref. (9)
0202+149	4C 15.05	FSRQ	1.202	5.3	21.0	1st/Lin96	pointed	tw
0208−512	PKS	FSRQ	1.003	21.5	10.0	Ber93/ Lin96	pointed	tw
0219+428	3C 66A	BL Lac	0.444	6.3	I+II	Din96	pointed	tw
0234+285	CTD 20	FSRQ	1.213	6.0	I+II	Din96	RASS	Br95
0235+164	AO	BL Lac	0.940	13.0	21.0	Lin96	pointed	tw
0336−019	CTA 26	FSRQ	0.852	>4	...	6161	RASS	Br94
0420−014	PKS	FSRQ	0.915	6.7	21.0	Lin96	RASS	Br94
0454−234	PKS	FSRQ	1.009	>4	29.0	Tho93	—	Wi94
0454−463	PKS	FSRQ	0.858	>5	6.0	vMon95	RASS	Br94
0458−020	4C −2.19	FSRQ	2.286	4.4	29.0	2nd	—	Wi94
0506−612	PKS	FSRQ	1.093	>4	I+II	vMon95	RASS	Br94
0521−365	PKS	FSRQ	0.055	>4	29.0	Lin95	pointed	tw
0528+134	OG 147	FSRQ	2.07	13.0	1.0	2nd	pointed	tw
0537−441	PKS	BL Lac	0.894	5.3	6.0	Lin96	pointed	tw
0716+714	S5	BL Lac	≥ 0.3	5.9	18.0	Lin95	pointed	tw
0735+178	PKS	BL Lac	≥ 0.424	4	I+II	2nd	pointed	tw
0804+499	OJ 508	FSRQ	1.433	6.0	I+II	Nol96	pointed	tw
0827+243	OJ 248	FSRQ	0.939	5.2	I+II	Nol96	RASS	Br95
0829+046	OJ 049	BL Lac	0.18	4.1	I	2nd	—	WW90
0836+710	4C 71.07	FSRQ	2.172	6.0	18.0+22.0	Tho93	pointed	tw
0851+202	OJ 287	BL Lac	0.306	4.0	...	Shr96	pointed	tw
0906+430	3C 216	FSRQ	0.670	>4	4.0	Tho93	pointed	tw
0917+449	S4	FSRQ	2.18	6.5	I+II	Sre96/ 2nd	pointed	tw
0954+556	4C 55.17	FSRQ	0.901	4.2	I+II	Sre96	pointed	tw
0954+658	S4	BL Lac	0.368	5.7	227.0+228.0	Muk95	pointed	tw
1101+384	Mkn 421	BL Lac	0.031	8.5	I+II	Sre96/2nd	pointed	tw
1127−145	PKS	FSRQ	1.187	6.0	206.0	Sre96/ 2nd	RASS	Br94
1156+295	4C 29.45	FSRQ	0.729	6.8	206.0	Sre96	RASS	Br95
1219+285	ON 231	BL Lac	0.102	5.0	I+II	Sre96	pointed	tw
1222+216	4C 21.35	FSRQ	0.435	>4	3.0+4.0	Sre96	RASS	Br95
1226+023	3C 273	FSRQ	0.158	4.1	3.0	2nd	pointed	tw
1229−021	PKS	FSRQ	1.045	4.8	I+II	Sre96/ 2nd	—	Wi94
1253−055	3C 279	FSRQ	0.538	44.6	3.0	Sre96/2nd	pointed	tw
1317+520	4C 52.27	FSRQ	1.060	4.0	I+II	2nd	RASS	Br95
1510−089	PKS	FSRQ	0.361	4.7	I+II	Sre96/ 2nd	pointed	tw
1604+159	4C 15.54	BL Lac	0.357	4.9	25.0	Sre96	—	Gi94
1606+106	4C 10.45	FSRQ	1.227	7.8	I	2nd	RASS	Br95
1611+343	DA 406	FSRQ	1.404	7.9	II	2nd	pointed	tw
1622−297	PKS	FSRQ	0.815	>25	421.0–423.5	Mat96	RASS	Mat97

continued on next page

TABLE 4.1: CONTINUED

IAU Name	Other Name	class	z	σ_γ^b	VP[c]	Ref.	X–ray class	Ref.
(1)	(2)	(3)	(4)	(5)	(6)	(7)	(8)	(9)
1633+382	4C 38.41	FSRQ	1.814	17.3	9.2	Sre96/2nd	pointed	tw
1652+398	Mkn 501	BL Lac	0.055	8.4	···	Q96[d]	pointed	tw
1730−130	NRAO 530	FSRQ	0.902	5.7	I+II	Nol96	RASS	Br94
1739+522	4C 51.37	FSRQ	1.375	7.2	I+II	Nol96	RASS	Br95
1741−038	OT 68	FSRQ	1.054	>5	I+II	vMon95	RASS	Br94
1933−400	PKS	FSRQ	0.966	6.6	I+II	Din96	RASS	Br94
2005−489	PKS	BL Lac	0.071	3.7	I	Lin96	pointed	tw
2032+107	PKS	BL Lac	0.610	6.2	I+II	Din96	—	Gi94
2052−474	PKS	FSRQ	1.489	4.2	I	2nd	RASS	Br94
2155−304	PKS	BL Lac	0.117	∼4	404.0	Ves95	pointed	tw
2230+114	CTA 102	FSRQ	1.037	7.0	19.0	2nd	RASS	Br94
2251+158	3C 454.3	FSRQ	0.859	13.4	19.0	Har93/Lin96	pointed	tw
2344+514	PKS	BLLac	0.044	∼5	···	Feg96[d]	—	Per96
2356+196	PKS	FSRQ	1.066	4.6	42.0	Lin96	RASS	Br95

Notes to Table 4.1

(a) Meaning of columns: (1) IAU name and (2) other names; (3) classification; (4) redshift; (5) significance of the EGRET detection of the (6) chosen viewing period; (7) the reference for the γ–ray data; (8) the type of the X–ray observation and (9) its reference.

(b) Significance of the γ–ray detection. For EGRET data this corresponds to the standard estimator $\sqrt{TS}$.

(c) Viewing period number, or if "I", "II", "I+II", data averaged over the whole phase one, phase two or phase one plus two respectively.

(d) This source has been detected only by Whipple Observatory above 300 GeV.

References for Table 4.1:

(tw) = this work, see Table 4.2, and 4.3; (1st) = Fichtel et al. 1994 (First EGRET sources catalog); (2nd) = Thompson et al. 1995; Thompson et al. 1996 (Second EGRET sources catalog, and Supplement); (6161) = Mattox et al. 1995; (Ber93) = Bertsch et al. 1993; (Br94) = Brinkmann et al. 1994; (Br95) = Brinkmann et al. 1995; (Din96) = Dingus et al. 1996; (Feg96) = Fegan private communication; (Gi94) = Giommi et al. 1995; (Har93) = Hartman et al. 1993; (Lin95) = Lin et al. 1995; (Lin96) = Lin et al. 1996; (Mat97) = Mattox et al. 1997; (Muk95) = Mukherjee et al. 1995; (Nol96) = Nolan et al. 1996; (Per96) = Perlman et al. 1996; (Q96) = Quinn et al. 1996; (Shr96) = Shrader et al. 1996; (Sre96) = Sreekumar et al. 1996; (Tho93) = Thompson et al. 1993; (Ves95) = Vestrand et al. 1995; (vMon95) = Von Montigny et al. 1995; (Wi94) = Wilkes et al. 1994; (WW90) = Worrall and Wilkes 1990

TABLE 4.2: *ROSAT* PSPC OBSERVATIONS OF EGRET SOURCES[a]

Name[b]	ROR[c]	Start Time	Off–axis (arcmin)	exposure (seconds)	count rate (cts/s)
(1)	(2)	(3)	(4)	(5)	(6)
0202+149	300003p	30/07/91	29.8	25174	0.019 ± 0.002
0208−512[1]	701161p	30/05/93	0.2	1811	0.268 ± 0.013
0208−512[2]	701164p	01/06/93	0.2	1780	0.254 ± 0.012
0208−512[3]	701156p	09/06/93	0.2	2160	0.270 ± 0.012
0208−512[4]	701158p	07/06/93	0.2	2149	0.277 ± 0.012
0208−512[5]	701157p	08/06/93	0.2	2220	0.267 ± 0.012
0208−512[6]	701168p	06/06/93	0.2	2534	0.275 ± 0.011
0208−512[7]	701159p	28/05/93	0.2	2698	0.241 ± 0.010
0208−512[8]	701167p	05/06/93	0.2	2701	0.265 ± 0.010
0208−512[9]	701163p	01/06/93	0.2	2735	0.254 ± 0.010
0208−512[10]	701160p	29/05/93	0.2	4026	0.262 ± 0.009
0208−512[11]	701162p	31/05/93	0.2	1472	0.252 ± 0.014
0208−512[12]	701166p	04/06/93	0.2	1154	0.243 ± 0.015
0219+428[1]	500266p	05/08/93	41.1	31528	0.316 ± 0.005
0235+164[d,1]	701379p	21/07/93	0.2	2083	
	701380p	24/07/93	0.2	1903	
	701381p	26/07/93	0.2	1508	0.293 ± 0.007
0235+164[d,2]	701384p	04/08/93	0.2	2023	
	701385p	06/08/93	0.2	4099	
	701387p	12/08/93	0.2	1664	
	701388p	15/08/93	0.2	1708	0.108 ± 0.003
0521−365	701179p	29/08/92	0.1	4845	0.780 ± 0.013
0528+134[1]	700059p	15/03/91	0.5	3791	0.069 ± 0.005
0528+134[2]	900340p	21/09/92	0.5	4514	0.091 ± 0.005
0537−441	700199p	10/04/91	3.6	2598	0.355 ± 0.013
0716+714	700210p	08/03/91	0.2	21043	0.802 ± 0.006
0735+178	700829p	27/10/02	0.3	6684	0.089 ± 0.004
0804+499	700846p	26/10/92	0.3	2999	0.053 ± 0.005
0836+710[1]	700493p	23/03/92	0.3	6993	0.742 ± 0.011
0836+710[2]	701061p	02/11/92	0.3	5026	0.378 ± 0.010
0851+202[1]	700219p	16/04/91	0.2	3622	0.273 ± 0.009
0851+202[2]	700426p	09/11/91	0.2	6785	0.606 ± 0.010
0851+202[3]	701391p	17/10/93	0.2	3285	0.641 ± 0.015
0906+430	700329p	13/11/91	0.2	23561	0.050 ± 0.002
0917+449	701398p	25/11/93	0.5	3367	0.201 ± 0.008
0954+556	701401p	07/11/93	0.2	4472	0.089 ± 0.005
0954+658	700042p	16/04/91	0.3	6772	0.052 ± 0.003
1101+384[1]	700129p	04/05/93	0.2	4304	30.650 ± 0.084

continued on next page

TABLE 4.2: CONTINUED

Name[b]	ROR[c]	Start Time	Off–axis (arcmin)	exposure (seconds)	count rate (cts/s)
(1)	(2)	(3)	(4)	(5)	(6)
1101+384[2]	700925p	04/06/93	0.2	9531	30.570 ± 0.058
1219+285	700223p	14/06/91	0.2	15223	0.224 ± 0.005
1226+023	700191p	14/12/91	0.2	6243	6.410 ± 0.033
1253−055	700305p	02/01/92	0.2	8513	0.578 ± 0.090
1510−089	700854p	16/08/92	0.0	5153	0.191 ± 0.007
1611+343	700842p	30/08/92	0.2	6804	0.122 ± 0.046
1633+382	700841p	28/08/92	0.3	5781	0.214 ± 0.007
1652+398	700130p	24/02/91	0.2	7649	6.950 ± 0.031
2005−489[1]	700488p	27/04/92	0.2	11487	2.780 ± 0.016
2005−489[2]	701057p	28/10/92	0.2	11462	1.704 ± 0.013
2155−304	700924p	16/11/92	0.4	1537	36.390 ± 0.158
2251+158[1]	700076p	26/11/91	0.1	6413	0.269 ± 0.007
2251+158[2]	700759p	26/05/92	0.1	8154	0.441 ± 0.008
2251+158[3]	900339p	15/12/92	0.1	22156	0.358 ± 0.004

Notes to Table 4.2

(a) compiled collecting all the data available in literature for γ–rays, and *ROSAT* public archive for X–rays up to September 1996.

(b) The source numbering is for reference to Table 4.3 reporting the spectral analysis results.

(c) *ROSAT* observation number (ROR).

(d) for AO 0235+164 eight RORs are available, covering the period 21/07/1993–15/08/1993. The inspection of the light curve revealed a significant variability in terms of source count rate, so that we have NOT merged the full data set. Instead we have merged only the RORs having a source count rate at the same level, without including the two RORs: 701382p and 710383p. The detailed analysis of the full data set is reported in Madejski et al. (1996).

1992). Background spectra were taken either from annulii centered on the sources or from circular regions uncontaminated by nearby sources with extraction radii as large as 10 arcmin. The large extraction cells ensure a good statistics for the modeling of the background spectrum and allow to average the background small scale spatial fluctuations. Different background regions for each source have been extracted and compared. In all the cases the background was stable without any appreciable variability within the statistical errors. Corrections were included for vignetting, especially important for the off–axis sources, and PSPC dead time. The *ROSAT* observation log is shown in Table 4.2. The reported count rates are in pulse invariant (PI) channels and are background subtracted. The lowest channel used was 11, as the detector response matrix is not calibrated below this channel, the highest channel depends on the source spectrum and the signal–to–noise ratio of the observation, ranging from channel 200 to 240.

response matrix

A major concern in the analysis of X–ray spectra is the uncertainty in the PSPC response matrix calibration. Actually two matrices have been officially released in order to take into account the $\sim$ 60 Volts gain change applied on October 14, 1991. The first matrix (MPE No. 06) has been adopted for the observations carried out before this date (PV and AO1 targets), while the latest release (MPE No. 36) has been used for all the other observations. The photon event files were analysed using the `EXSAS/MIDAS` software (version 94NOV, Zimmermann et al. 1993) and the extracted spectra were analysed using version 9.0 of `XSPEC` (Shafer et al. 1991).

For some of the sources in our sample X–ray data have been previously published by different authors. In order to ensure a uniform procedure for all the sample we have re–analysed all of them obtaining consistent results. For two of the sources in our sample (1226+023≡3C 273 and 1253–055≡3C 279) several tens of pointed observations are available in the public archive as they were the subject of simultaneous multiwavelength campaigns. In this case we have chosen only one (the longest) pointing in order to derive the spectral parameters.

4.2.2 Spectral analysis

All the 27 sources have been clearly detected with enough counts to allow spectral analysis. The source spectra were rebinned in order to obtain a significant S/N (> 5) for each bin and fitted with a single power–law model plus absorption arising from cold material with solar abundances (Morrison and McCammon 1983). The derived spectral parameters are given in Table 4.3, where the reported errors are at 90 per cent confidence level (Lampton et al. 1976). All the spectra were fitted with i) the column density fixed at the Galactic value, ii) and free to vary. Accurate values for the Galactic

column densities towards most of the objects in our sample have been retrieved from 21 cm radio surveys (Elvis et al. 1989; Lockman and Savage 1995; Murphy et al. 1996). The typical error in such measurements is estimated to be of the order of $\simeq 1 - 3 \times 10^{19}$ cm^{-2}. For the remaining objects the Galactic column density values are from Dickey and Lockman (1990). The errors in this case are of the order of $\simeq 1 \times 10^{20}$ cm^{-2}.

molecular absorption

It should be noted that radio observations only detect interstellar atomic hydrogen and not molecular gas (i.e. H_2, CO, etc.). Therefore the total effective absorbing column density could be underestimated by 21 cm measurements. Given this possibility we checked for Galactic CO emission in the direction of all the blazars in our sample. Carbon monoxide emission has been detected in the direction of two of the objects in our sample namely: 0528+134 and 2251+158 (Liszt 1994; Liszt and Wilson 1993). Accurate measurements of the CO profile intensity have been recently obtained by Liszt (1996; private communication) as 2.15 K km/s for 0528+134 and 0.77 K km/s for 2251+158.

0528+134

The molecular hydrogen column density depends on the assumed CO–to–H_2 conversion factor. For 0528+134 a rather conservative assumption of 3×10^{20} molecules cm^{-2} K^{-1} km^{-1} s (Strong et al. 1988) yields an equivalent molecular hydrogen column density $N(H_2) \simeq 1.3 \times 10^{21}$ cm^{-2}, which combined with the atomic value of 2.8×10^{21} cm^{-2} (Dickey and Lockman 1990) gives a total absorbing column of $\sim 4.1 \times 10^{21}$ cm^{-2}.

2251+158

Given the relatively high Galactic latitude of 2251+158 ($b^{II} \lesssim -40°$) a much lower conversion factor of 0.5×10^{20} molecules cm^{-2} K^{-1} km^{-1} s has been assumed (see De Vries et al. 1987). The molecular hydrogen column density of $\simeq 0.77 \times 10^{20}$ cm^{-2}, combined with the atomic value of 7.06×10^{20} cm^{-2} (Murphy et al. 1996) gives a total absorbing column of 7.83×10^{20} cm^{-2}.

In most cases a single power law spectrum with the absorption fixed at the Galactic value provides an excellent description of the data, while for some of the objects either the fits are statistically unacceptable and/or the column density inferred from the fit is not consistent with the Galactic value, even considering the errors on the Galactic N_H (see column 6 in Table 4.3), thus requiring a more complex description of the spectral shape.

A double–power–law model has been fitted to all these objects and the results are reported in Table 4.4. We point out that for all of the objects the improvement with respect to the single power law fit with $N_H \equiv N_H^{Gal}$ is statistically significant, as indicated by the F–test, at $> 99.9\%$ level.

TABLE 4.3: SINGLE POWER LAW SPECTRAL FITS

Name	$N_H^{gal.}$ [a]	α [b]	F_{1keV} [c]	$\chi^2/d.o.f.$ [d]	Free N_H [e]	α [b]	$\chi^2/d.o.f.$ [d]	Ref.
(1)	(2)	(3)	(4)	(5)	(6)	(7)	(8)	(9)
0202+149	5.89	$-0.32^{+0.54}_{-0.56}$	0.06	5.94/5	...	...	...	...
0208−512[1]	2.91	$1.08^{+0.14}_{-0.13}$	0.61	19.3/15	2.02 (1.02 − 3.27)	$0.79^{+0.43}_{-0.39}$	16.8/14	...
0208−512[2]	2.91	$1.11^{+0.12}_{-0.13}$	0.58	6.68/10	2.38 (1.13 − 3.90)	$0.93^{+0.54}_{-0.47}$	6.03/9	...
0208−512[3]	2.91	$1.10^{+0.12}_{-0.12}$	0.60	24.1/16	1.75 (0.72 − 3.06)	$0.75^{+0.42}_{-0.39}$	20.4/15	...
0208−512[4]	2.91	$0.88^{+0.12}_{-0.12}$	0.71	13.4/18	1.94 (0.77 − 3.38)	$0.58^{+0.47}_{-0.44}$	11.2/17	...
0208−512[5]	2.91	$0.98^{+0.11}_{-0.13}$	0.66	15.2/18	1.97 (0.87 − 3.35)	$0.67^{+0.47}_{-0.43}$	13.0/17	...
0208−512[6]	2.91	$0.95^{+0.11}_{-0.12}$	0.67	25.9/21	1.76 (0.91 − 2.77)	$0.57^{+0.36}_{-0.34}$	20.1/10	...
0208−512[7]	2.91	$1.08^{+0.12}_{-0.13}$	0.55	26.1/19	0.85 (0.58 − 1.95)	$0.36^{+0.43}_{-0.37}$	12.6/18	...
0208−512[8]	2.91	$1.01^{+0.10}_{-0.12}$	0.63	34.5/22	1.88 (0.93 − 3.05)	$0.66^{+0.41}_{-0.39}$	30.8/21	...
0208−512[9]	2.91	$1.20^{+0.10}_{-0.11}$	0.56	20.1/21	2.46 (1.43 − 3.68)	$1.05^{+0.42}_{-0.39}$	19.4/21	...
0208−512[10]	2.91	$1.04^{+0.09}_{-0.09}$	0.62	42.7/23	1.80 (0.98 − 2.77)	$0.68^{+0.34}_{-0.31}$	36.8/22	...
0208−512[11]	2.91	$0.99^{+0.15}_{-0.16}$	0.60	13.9/11	1.75 (0.50 − 3.41)	$0.60^{+0.58}_{-0.53}$	11.5/10	...
0208−512[12]	2.91	$0.98^{+0.16}_{-0.18}$	0.60	8.8/8	2.27 (0.76 − 4.29)	$0.78^{+0.62}_{-0.56}$	8.2/7	...
0219+428[1]	9.15	$1.49^{+0.04}_{-0.04}$	1.25	8.9/19	10.1 (8.9 − 11.5)	$1.60^{+0.17}_{-0.17}$	6.19/18	...
0235+164[1]	7.60	$0.51^{+0.13}_{-0.13}$	1.15	25.56/16	24.6 (12.4 − 41.3)	$1.59^{+0.97}_{-0.76}$	13.32/15	M96
0235+164[2]	7.60	$0.41^{+0.17}_{-0.18}$	0.41	17.58/12	26.12 (10.3 − 48.9)	$1.54^{+0.88}_{-0.97}$	10.01/11	M96
0521−365	3.37	$0.89^{+0.04}_{-0.05}$	2.12	14.76/22	3.83 (3.45 − 4.23)	$1.04^{+0.11}_{-0.11}$	10.02/21	P96
0528+134[1]	41.0	$0.75^{+0.51}_{-0.53}$	0.59	4.7/8	...	...	...	Z94
0528+134[2]	41.0	$0.45^{+0.35}_{-0.36}$	0.70	8.9/9	...	...	...	Z94
0537−441	2.91	$1.16^{+0.08}_{-0.09}$	0.81	21.1/14	2.94 (1.97 − 4.04)	$1.16^{+0.36}_{-0.33}$	21.1/13	T93,C95
0716+714	3.05	$1.76^{+0.02}_{-0.02}$	1.28	78.2/69	2.91 (2.69 − 3.14)	$1.71^{+0.09}_{-0.08}$	76.5/68	C94
0735+178	4.35	$1.25^{+0.16}_{-0.17}$	0.24	8.72/8	3.04 (1.64 − 4.28)	$0.89^{+0.50}_{-0.47}$	5.74/7	C95
0804+499	4.61	$0.56^{+0.33}_{-0.39}$	0.17	2.8/4	...	...	...	...
0836+710[1]	2.83	$0.42^{+0.05}_{-0.04}$	2.20	15.6/18	3.23 (2.74 − 3.75)	$0.52^{+0.14}_{-0.11}$	12.5/17	B94
0836+710[2]	2.83	$0.44^{+0.08}_{-0.08}$	1.11	27.8/18	3.60 (2.72 − 4.61)	$0.63^{+0.24}_{-0.24}$	24.3/17	B94
0851+202[1]	2.75	$1.14^{+0.09}_{-0.08}$	0.62	8.25/11	3.06 (2.11 − 4.14)	$1.25^{+0.37}_{-0.35}$	7.8/10	C95
0851+202[2]	2.75	$1.60^{+0.04}_{-0.04}$	1.00	24.0/29	2.29 (1.89 − 2.71)	$1.43^{+0.17}_{-0.16}$	18.6/28	...
0851+202[3]	2.75	$1.29^{+0.06}_{-0.05}$	1.30	16.0/20	2.68 (2.11 − 3.31)	$1.27^{+0.22}_{-0.21}$	15.9/19	...
0906+430	1.40	$0.57^{+0.10}_{-0.11}$	0.11	23.9/13	< 0.58	$0.01^{+0.28}_{-0.11}$	6.1/12	...
0917+449	1.50	$0.39^{+0.10}_{-0.09}$	0.47	20.3/14	2.82 (1.70 − 4.12)	$0.80^{+0.38}_{-0.36}$	13.7/13	...
0954+556	0.88	$1.17^{+0.14}_{-0.13}$	0.10	13.0/10	0.79 (0.09 − 1.89)	$1.13^{+0.52}_{-0.42}$	13.0/9	...
0954+658	3.71	$0.23^{+0.24}_{-0.26}$	0.17	5.53/7	7.19 (2.42 − 32.22)	$0.67^{+1.55}_{-0.74}$	3.6/6	C95
1101+384[1,f]	1.61	$1.95^{+0.03}_{-0.03}$	31.5	56.2/25	5.06 (3.57 − 6.95)	$2.23^{+0.15}_{-0.12}$	18.5/24	...
1101+384[2,f]	1.61	$1.82^{+0.02}_{-0.02}$	36.1	125.5/55	5.33 (4.23 − 6.57)	$2.10^{+0.09}_{-0.08}$	43.5/54	...
1219+285	1.95	$1.19^{+0.05}_{-0.05}$	0.41	22.86/19	2.25 (1.76 − 2.70)	$1.30^{+0.21}_{-0.20}$	21.22/18	...
1226+023	1.69	$0.95^{+0.01}_{-0.01}$	12.3	88.6/47	1.53 (1.42 − 1.64)	$0.89^{+0.05}_{-0.05}$	79.4/46	...
1253−055	2.22	$0.83^{+0.04}_{-0.03}$	1.34	27.8/36	2.40 (1.99 − 2.82)	$0.89^{+0.14}_{-0.14}$	27.0/35	...
1510−089	7.88	$0.90^{+0.16}_{-0.17}$	0.74	13.6/15	8.17 (5.82 − 12.76)	$0.93^{+0.42}_{-0.36}$	13.6/14	...
1611+343	1.44	$0.76^{+0.06}_{-0.05}$	0.24	15.4/12	0.87 (0.28 − 1.62)	$0.53^{+0.32}_{-0.30}$	12.6/11	...
1633+382	1.02	$0.53^{+0.08}_{-0.07}$	0.42	27.7/16	1.68 (0.91 − 2.58)	$0.78^{+0.32}_{-0.41}$	24.4/15	...

continued on next page

TABLE 4.3: CONTINUED

Name	$N_H^{gal.}$ [a]	α [b]	F_{1keV} [c]	$\chi^2/d.o.f.$ [d]	Free N_H [e]	α [b]	$\chi^2/d.o.f.$ [d]	Ref.
(1)	(2)	(3)	(4)	(5)	(6)	(7)	(8)	(9)
1652+398	1.73	$1.35^{+0.02}_{-0.02}$	10.1	299.0/110	2.37 (2.26 – 2.49)	$1.60^{+0.05}_{-0.04}$	117.1/109	C95
2005–489[1]	4.96	$2.21^{+0.02}_{-0.02}$	5.30	227.2/94	3.97 (3.79 – 4.15)	$1.89^{+0.07}_{-0.07}$	99.8/93	C95,S95
2005–489[2]	4.96	$2.39^{+0.02}_{-0.02}$	2.79	245.0/94	3.51 (3.29 – 3.73)	$1.89^{+0.08}_{-0.08}$	77.5/93	S95
2155–304	1.36	$1.38^{+0.01}_{-0.01}$	43.90	146.1/93	1.27 (1.19 – 1.36)	$1.34^{+0.04}_{-0.03}$	141.4/92	...
2251+158[1]	7.83	$0.46^{+0.13}_{-0.13}$	1.04	14.7/16	10.01 (6.78 – 16.98)	$0.65^{+0.45}_{-0.34}$	13.1/15	...
2251+158[2]	7.83	$0.50^{+0.08}_{-0.09}$	1.70	28.3/29	8.61 (7.06 – 10.96)	$0.57^{+0.21}_{-0.19}$	27.3/28	...
2251+158[3]	7.83	$0.72^{+0.06}_{-0.06}$	1.38	35.0/28	7.07 (6.28 – 8.02)	$0.65^{+0.12}_{-0.12}$	31.9/27	...

Notes to Table 4.3

(a) Galactic column density (units of 10^{20} cm^{-2}). For 0235+164, 0521–365, 0735+178, 0851+202, 1611+343, 1641+399, 1652+398, 2251+158 the Galactic column densities are from Elvis et al. (1989). For 0537-441, 0716+714, 0836+710, 0906+430, 0954+556, 1633+382 from Murphy et al. (1996). For 0851+202, 1101+384, 1226+023, 1510–089, 2155–304, 2251+158 from Lockman and Savage (1995). For the other objects the values are from (Dickey and Lockman 1990).
(b) Energy spectral index. (c) mathrmFlux at 1 keV (in μJy). (d) Total χ^2 and degrees of freedom.
(e) Column density obtained from the X–ray spectral fits (units of 10^{20} cm^{-2}). For the weak sources only spectral fits with N_H fixed at the Galactic value are reported. Errors are quoted at 90% confidence intervals for one interesting parameter ($\chi^2_{min}+2.71$, column 3), and for two parameters ($\chi^2_{min}+4.61$, columns 6 and 7).
(f) Due to problems related with a gain shift the data were fitted only in the interval $0.5-2.2$ keV.

References for Table 4.3:
(B94) Brunner et al. 1994; (C94) Cappi et al. (1994); (C95) Comastri et al. (1995); (M96) Madejski et al. (1996); (P96) Pian et al. (1996); (S95) Sambruna et al. (1995); (T93) Treves et al. (1993); (Z94) Zhang et al. (1994)

TABLE 4.4: DOUBLE POWER–LAW SPECTRAL FITS

Name	$N_H^{gal.}$ [a]	α_1 [b]	E_{break} [c]	F_{1keV} [d]	α_2 [e]	F_{1keV} [f]	$\chi^2/d.o.f.$ [g]
(1)	(2)	(3)	(4)	(5)	(6)	(7)	(8)
0235+164[1]	7.60	< 0.21	0.86	...	$0.99^{+0.57}_{-0.31}$	1.29	12.8/13
0235+164[2]	7.60	< -0.1	0.68	...	$0.77^{+0.33}_{-0.28}$	0.44	8.2/9
0906+430[h]	1.40	$6.57^{+0.11}_{-0.14}$	...	$6.2\cdot10^{-6}$	0.10	0.10	5.8/12
1101+384[1]	1.61	$1.69^{+0.16}_{-0.45}$	0.85	...	$2.15^{+0.29}_{-0.11}$	32.5	17.2/23
1101+384[2]	1.61	$1.44^{+0.20}_{-0.78}$	0.75	...	$1.95^{+0.08}_{-0.05}$	36.7	49.4/53
1226+023[i]	1.69	$1.37^{+0.16}_{-0.14}$	...	4.50	0.54	7.66	61.3/46
1652+398	1.73	$0.43^{+0.31}_{-0.31}$	0.31	...	$1.57^{+0.05}_{-0.05}$	9.85	122.1/108
2005–489[1]	4.96	$4.69^{+1.46}_{-1.02}$	...	0.066	$1.88^{+0.06}_{-0.12}$	5.32	97.8/92
2005–489[2]	4.96	$4.85^{+1.32}_{-1.11}$	...	0.049	$1.86^{+0.10}_{-0.21}$	2.84	72.1/93

Notes to Table 4.4

(a) Galactic column density (units of 10^{20} cm^{-2}). (b) Energy spectral index of the soft component. (c) Break energy in keV for the sources fitted with a broken power law model. (d) Flux at 1 keV (in μJy) of the soft component, for the sources fitted with a double power law model. (e) Energy spectral index of the hard component. (f) Flux at 1 keV (in μJy) of the hard component. (g) Total χ^2 and degrees of freedom.
(h) The adopted value for the hard X–ray spectral index has been fixed at the best fit value found in the fit. Due to the poor statistical quality of the PSPC spectrum the errors on the soft component have been computed freezing all the other fit parameters.
(i) The hard slope has been fixed at the best fitting value of Ginga (2–10 keV; Lawson and Turner 1997), which is consistent with our fit.

On the basis of the analysis presented in this subsection it appears that a two component (i.e. a double–power–law) model is required to describe the soft X–ray spectrum for some of the objects, usually the ones with the highest counting statistics in the sample. It is suggested that deeper and/or broader band ($\sim$ 0.1–10 keV) observations will reveal spectral complexity for other objects.

4.3 X–ray spectral properties

The range of measured values of the energy spectral indices is quite large, going from $\simeq$–0.3 to 2.3. We find a significantly different distribution of spectral indices between BL Lacs and FSRQ, as can be clearly seen from the histogram shown in Figure 4.1. The mean spectral properties have been computed assuming the slopes derived with $N_H \equiv N_H^{Gal}$ if the X–ray absorption is consistent with the Galactic value (col. 3 in Table 4.3), while the slopes derived from the fit with N_H free have been adopted in the other cases (col. 7 in Table 4.3). This choice allows a better estimate of the continuum shape for the objects showing either intrinsic absorption or soft excess emission (cfr. Table 4.4). We have also included the FSRQ 1156+295 using the 2–10 keV *Ginga* slope (Lawson and Turner 1997). When more than one observation was available (see Table 4.2) a weighted mean spectral slope for each object has been adopted.

maximum likelihood

A method for estimating the mean and the intrinsic dispersion of the parent population is the maximum–likelihood algorithm (see Maccacaro et al. 1988). The algorithm assumes that the intrinsic distribution of energy indices is Gaussian, and allows the determination of the mean α, the intrinsic dispersion σ, and the respective errors, weighting the individual energy indices according to their measured errors. The results are as follows:

$$\text{BL Lacs}: \quad \langle \alpha_X \rangle = 1.43 \pm 0.21 \qquad \langle \sigma_{\alpha_X} \rangle = 0.43^{+0.22}_{-0.12}$$

$$\text{FSRQ}: \quad \langle \alpha_X \rangle = 0.67 \pm 0.13 \qquad \langle \sigma_{\alpha_X} \rangle = 0.29^{+0.14}_{-0.07}$$

where the confidence intervals are at the 90 per cent confidence level for one interesting parameter.

simple mean

In order to test if the obtained values are dominated by the brightest sources a simple unweighted mean has been computed. The obtained values: $\langle \alpha_X \rangle = 0.63$, σ = 0.23 for the 16 FSRQ, and $\langle \alpha_X \rangle = 1.43$, σ = 0.50 for the 12 BL Lacs objects, where σ is the dispersion on the mean index, are consistent with the maximum likelihood analysis.

The two means are significantly different at $> 99.99\%$ level according to a Student t–test and taking into account the unequal variances of the two populations. A Kolmogorov–Smirnov (K–S) test for the distribution of the observed values gives almost identical results for the significance of the difference between the two populations (> 99.99 %).

The obtained results indicate that the X–ray spectra of BL Lacs objects are steeper than FSRQ as first suggested by Worrall and Wilkes (1990), and that the intrinsic distribution of spectral indices is not consistent with a single value.

Among the BL Lac objects present in our list, 4 are classified as HBL (1101+384, 1652+398, 2005–489 and 2155–304), according to their radio to X–ray flux ratio. The mean X–ray slope for these 4 objects is 1.75 ± 0.33, while for the remaining 8, LBLs, we find $\langle \alpha_X \rangle = 1.26 \pm 0.46$. Despite the low number of HBLs, the two slopes are different at > 96.6 % as indicated by the Student t–test.

4.4 γ–ray spectral properties

maximum likelihood

In Table 4.5 we list the γ–ray fluxes for all the sources in our sample, together with spectral indices if available. With the same maximum–likelihood algorithm applied in Section 4.3 we have computed the mean γ–ray slope for BL Lacs (10 out of 16 objects) and FSRQ (30 out of 37 objects); the results are as follows:

$$\text{BL Lacs}: \quad \langle \alpha_\gamma \rangle = 0.87 \pm 0.13 \qquad \langle \sigma_{\alpha_\gamma} \rangle < 0.26$$

$$\text{FSRQ}: \quad \langle \alpha_\gamma \rangle = 1.25 \pm 0.10 \qquad \langle \sigma_{\alpha_\gamma} \rangle = 0.25^{+0.10}_{-0.07}$$

where the confidence intervals are at 90 per cent level for one interesting parameter. The fact that the intrinsic dispersion of BL Lac spectral indices is consistent with zero is probably due to the small number of objects.

simple mean

A simple unweighted mean returns almost identical values:

$$\text{BL Lacs}: \quad \langle \alpha_\gamma \rangle = 0.87 \qquad \sigma = 0.32$$

$$\text{FSRQ}: \quad \langle \alpha_\gamma \rangle = 1.29 \qquad \sigma = 0.34$$

The two means are significantly different at $> 99.7\%$ level according to a Student t–test. Similar results (> 99.8 %) for the significance of the difference between the two populations are returned from a K–S test on the distribution of the observed values.

α_X and α_γ

The distributions of spectral indices indicate an opposite behaviour at γ–ray ener-

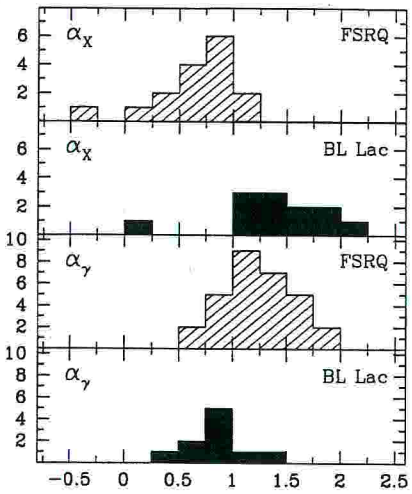

Figure 4.1: Histograms of the X–ray and γ–ray spectral indices for BL Lacs and FSRQ. The adopted values for the X–ray spectral indices are those listed in Table 4.5.

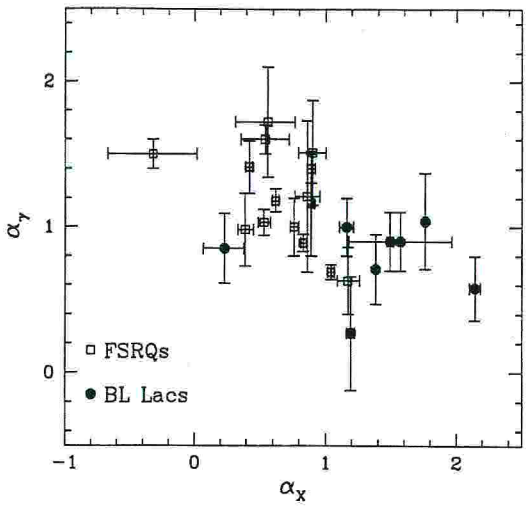

Figure 4.2: γ–ray *vs.* X–ray spectral index for the sources in our sample. The adopted values for the X–ray spectral indices are those listed in Table 4.5. Filled symbols refer to BL Lac objects, empty symbols refer to FSRQ.

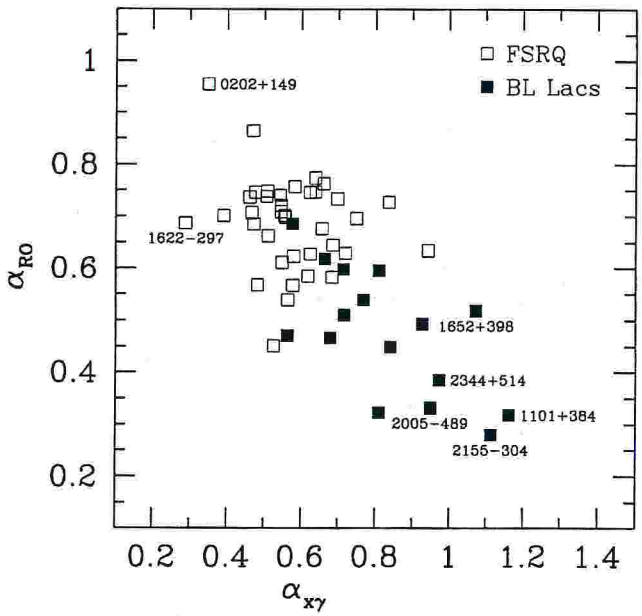

Figure 4.3: Correlation between the broad band spectral indices α_{RO} and $\alpha_{X\gamma}$ for the objects in our sample. Filled symbols refer to BL Lac objects, empty symbols refer to FSRQ. HBL have been highlighted with their name, they cluster in the lower-right part of the diagram. We have also labeled the object with the steepest α_{RO}. For 1652+398 and 2344+514, which have not been detected by EGRET, we have assumed a γ–ray flux of 0.8×10^{-7} photons cm^{-2} s^{-1}, approximately equal to the sensitivity threshold of EGRET.

gies with respect to the X–ray band (Figure 4.1). For the subsample of 23 objects for which both X– and γ–ray spectral slopes are available, a significant, at $> 98.6\%$ level using a non–parametric Spearman rank test, anti–correlation has been found between the two spectral indices (Figure 4.2) when both FSRQ and BL Lacs are considered.

The correlation is however much weaker considering FSRQ only (82 %) and is not present for BL Lacs only (15 %). FSRQ and BL Lacs occupy two different regions in the $\alpha_X - \alpha_\gamma$ plane. A flat X–ray spectrum is thus associated with a steep γ–ray slope for FSRQ while the reverse is true for BL Lacs. A similar correlation was found by Wang et al. (1996) with a smaller sample (10 objects) and inhomogeneous X–ray data.

These findings suggest that either the $\alpha_X - \alpha_\gamma$ correlation is just the result of a fortuitous proximity of the loci occupied by BL Lacs and FSRQ in the $\alpha_X - \alpha_\gamma$ plane, or the correlation *points to an underlying physical mechanism* operating in both classes of objects.

4.5 Spectral energy distributions

Radio and optical data for all the 53 objects in our sample have been collected from the literature in order to characterize the SED (Table 4.5). Since the γ–ray detection is likely to be associated with a high state of the source we have chosen to list the brightest radio and optical fluxes, the latter corrected for reddening.

We have computed the broad band spectral indices α_{12} using the rest–frame luminosities observed at the frequencies ν_1 and ν_2, where ν_R = 5 GHz, ν_{opt} = 5500 Å, ν_x = 1 keV and ν_γ = 100 MeV. The K–correction has been applied using the listed values of α_X and α_γ whenever available and the mean spectral indices for BL Lacs and FSRQ derived in the previous sections (cfr. § 4.3 and 4.4) for sources with unknown spectra. Finally, $\alpha_R = 0$ and $\alpha_{opt} = 1$ have been assumed at radio and optical frequencies.

A highly significant anti–correlation, (at > 99.99 % using a non–parametric Spearman rank test), has been found between α_{RO} and $\alpha_{X\gamma}$ (Figure 4.3), when considering the entire class of blazars. A similar level of significance is present applying a bi–dimensional K–S test (see Press et al. 1992). The correlation persists for each class of objects, although with less significance (99.3% for BL Lacs and 96.9% for FSRQ).

Moreover, BL Lacs and FSRQs occupy different regions of the $\alpha_{RO} - \alpha_{X\gamma}$ plane. A relatively steep radio to optical spectral index implies a flat X–ray to γ–ray flux ratio and is common among FSRQ, while the opposite is true for BL Lac objects. The average values are as follow:

$$\text{BL Lacs}: \quad \langle\alpha_{RO}\rangle = 0.47 \pm 0.12 \qquad \langle\alpha_{X\gamma}\rangle = 0.83 \pm 0.18$$

$$\text{FSRQ}: \quad \langle\alpha_{RO}\rangle = 0.69 \pm 0.10 \qquad \langle\alpha_{X\gamma}\rangle = 0.58 \pm 0.12$$

Even if the broad band indices α_{RO} and $\alpha_{X\gamma}$ are independent quantities, so that the effects of spurious correlations are minimized, the observed correlation could be induced

Table 4.5: MULTIFREQUENCY DATA FOR FSRQ

IAU Name	z	F_{5GHz} (Jy)	Ref.	$F_{5500Å}$ (mJy)	Ref.	F_{1keV} (μJy)	α_X	Ref.	F_γ [a]	α_γ	Ref.
(1)	(2)	(3)	(4)	(5)	(6)	(7)	(8)	(9)	(10)	(11)	(12)
0202+149	1.202	2.40	Pe82	0.017	IT90	0.06	-0.32 ± 0.55	tw	2.6	1.5 ± 0.1	1st
0208−512	1.003	3.26	K81	0.64	IT88	0.61	1.04 ± 0.04	tw	9.1	0.69 ± 0.05	Ber93
0234+285	1.213	2.36	Pe82	0.186	K81	0.09	...	Br95	1.51	1.7 ± 0.3	Din96
0336−019	0.852	2.84	K81	0.45	K81	0.10	...	Br94	~ 10.0	...	6161
0420−014	0.915	3.72	Pe82	0.34	WP85	0.44	...	Br94	4.96	0.9 ± 0.3	Lin96
0454−234	1.009	2.2	Le85	0.91	IT88	0.09	...	Wi94	1.4	...	Tho93
0454−463	0.858	2.97	K81	0.246	K81	0.16	...	Br94	2.9	0.9 ± 0.4	vMon95
0458−020	2.286	2.04	Le85	0.17	K81	0.10	...	Wi94	3.11	...	2nd
0506−612	1.093	2.1	K81	0.68	IT90	0.28	...	Br94	0.6	...	vMon95
0521−365	0.055	9.7	K81	2.38	Pi94	2.12	0.89 ± 0.05	tw	1.8	1.16 ± 0.36	Lin95
0528+134	2.07	4.3	Pe82	0.308	WP85	0.65	0.54 ± 0.29	tw	8.39	1.6 ± 0.1	2nd
0804+499	1.433	2.05	K81	0.39	K81	0.17	0.56 ± 0.36	tw	1.49	1.72 ± 0.38	Nol96
0827+243	0.939	0.67	Be91	0.391	Ma93	0.34	...	Br95	2.46	1.21 ± 0.47	Nol96
0836+710	2.172	2.67	Pe82	0.98	K81	1.60	0.42 ± 0.04	tw	2.1	1.41 ± 0.18	Tho93
0906+430	0.670	1.80	K81	0.383	Ma86	0.11	0.01 ± 0.28	tw	3.2	...	Tho93
0917+449	2.18	1.03	GC91	0.065	K81	0.47	0.39 ± 0.10	tw	1.19	0.98 ± 0.25	Sre96
0954+556	0.901	2.28	K81	0.374	K81	0.10	1.17 ± 0.14	tw	0.61	0.63 ± 0.23	Sre96
1127−145	1.187	7.46	K81	0.652	K81	0.34	...	Br94	9.27	1.15 ± 0.36	Sre96
1156+295	0.729	1.65	Ge94	5.1	Gh86	0.8	0.86 ± 0.15 [b]	Br95	19.22	1.21 ± 0.52	Sre96
1222+216	0.435	0.81	GC91	0.39	HB93	0.41	...	Br95	2.34	1.50 ± 0.21	Sre96
1226+023	0.158	44.6	K81	24.6	K81	12.30	0.89 ± 0.05	tw	2.38	1.4 ± 0.1	2nd
1229−021	1.045	1.1	K81	0.744	K81	0.08	...	Wi94	1.02	1.92 ± 0.44	Sre96
1253−055	0.538	16.6	K81	15.10	Shr94	1.34	0.83 ± 0.04	tw	28.68	0.89 ± 0.06	Sre96

continued on next page

TABLE 4.5 CONTINUED

IAU Name	z	F_{5GHz} (Jy)	Ref.	$F_{5500Å}$ (mJy)	Ref.	F_{1keV} (μJy)	α_X	Ref.	F_γ[a]	α_γ	Ref.
(1)	(2)	(3)	(4)	(5)	(6)	(7)	(8)	(9)	(10)	(11)	(12)
1317+520	1.060	0.66	GC91	0.62	HB93	0.06	···	Br95	0.77	···	2nd
1510−089	0.361	3.35	K81	1.39	WP85	0.74	0.90 ± 0.16	tw	2.30	1.51 ± 0.36	Sre96
1606+106	1.227	1.78	K81	0.155	K81	0.08	···	Br95	3.35	1.2 ± 0.3	2nd
1611+343	1.404	3.08	Ge94	0.39	K81	0.24	0.76 ± 0.06	tw	4.79	1.0 ± 0.2	2nd
1622−297[c]	0.815	1.92	K81	0.367	Mat97	0.08	···	Mat97	27.0[c]	1.2 ± 0.1	Mat97
1633+382	1.814	4.08	WP85	0.246	WP85	0.42	0.53 ± 0.08	tw	10.51	1.03 ± 0.09	Sre96
1730−130	0.902	6.9	Wr94	0.52	RS85	0.63	···	Br94	2.18	1.39 ± 0.27	Nol96
1739+522	1.375	1.98	K81	0.155	K81	0.16	···	Br95	2.38	1.23 ± 0.38	Nol96
1741−038	1.054	3.72	K81	0.486	K81	0.61	···	Br94	3.4	2.0 ± 0.4	vMon95
1933−400	0.966	1.48	K81	0.13	K81	0.30	···	Br94	1.3	1.4 ± 0.2	Din96
2052−474	1.489	2.52	K81	0.296	K81	0.23	···	Br94	2.22	1.4 ± 0.4	2nd
2230+114	1.037	4.1	Pe82	0.47	K81	0.29	···	Br94	2.69	1.6 ± 0.2	2nd
2251+158	0.859	23.3	WP85	1.58	K81	1.37	0.62 ± 0.04	tw	8.0	1.18 ± 0.08	Har93
2356+196	1.066	0.70	Be91	0.246	Pr85	0.28	···	Br95	3.02	···	Lin96

MULTIFREQUENCY DATA FOR BL LACS

0219+428	0.444	1.04	VV93	3.96	VV93	1.25	1.49 ± 0.04	tw	1.63	0.9 ± 0.2	Din96
0235+164	0.940	2.85	St91	6.6	Gh86	0.78	1.57 ± 0.86	tw	8.25	0.90 ± 0.20	Lin96
0537−441	0.894	4.00	St91	2.05	Tr93	0.81	1.16 ± 0.09	tw	3.64	1.0 ± 0.2	Lin96
0716+714	≥ 0.3	1.12	K81	20.5	Bo90	1.28	1.76 ± 0.02	tw	2.0	1.04 ± 0.33	Lin95
0735+178	≥ 0.424	3.65	Ge94	6.9	Gh86	0.24	1.25 ± 0.17	tw	1.29	···	2nd
0829+046	0.18	1.65	Ge94	1.4	Gh86	1.07	···	WW90	1.9	···	2nd
0851+202	0.306	2.7	K81	4.0	Gh86	0.97	1.45 ± 0.18	tw	2.9	···	Shr96

continued on next page

TABLE 4.5 CONTINUED

IAU Name	z	F_{5GHz} (Jy)	Ref.	$F_{5500\AA}$ (mJy)	Ref.	F_{1keV} (μJy)	α_X	Ref.	F_γ[a]	α_γ	Ref.
(1)	(2)	(3)	(4)	(5)	(6)	(7)	(8)	(9)	(10)	(11)	(12)
0954+658	0.368	1.46	K81	0.82	PR88	0.17	0.23 ± 0.25	tw	1.2	0.85 ± 0.24	Muk95
1101+384	0.031	0.73	Ge94	17.8	Gh86	33.8	2.14 ± 0.07	tw	1.43	0.58 ± 0.22	Sre96
1219+285	0.102	0.97	GC91	2.9	Gh86	0.41	1.19 ± 0.05	tw	0.58	0.27 ± 0.39	Sre96
1604+159	0.357	0.50	Le85	0.13	Le85	0.17	...	Gi94	3.98	0.99 ± 0.50	Sre96
1652+398	0.055	1.42	K81	3.3	Gh86	10.1	1.60 ± 0.05	tw	0.81[d]	...	Q96
2005−489	0.071	1.5	Gh86	30.0	Gh86	4.04	1.89 ± 0.05	tw	1.38	...	Lin96
2032+107	0.601	0.77	WB92	2.05	Gi94	0.10	...	Gi94	1.53	1.5 ± 0.3	Din96
2155−304	0.117	0.27	Le85	21.33	VV93	43.90	1.38 ± 0.01	tw	2.73	0.71 ± 0.24	Ves95
2344+514	0.044	0.215	Per96	2.366	Per96	3.22	...	Per96	0.62[d]	...	Feg96

Notes to Table 4.5

[a] γ–ray flux measured by EGRET above 100 MeV, except that for 1652+398 and 2344+514 (see note (d)). Units are 10^{-7} photons/cm^2/sec

[b] The spectral index is by Ginga, 2−10 keV, i Lawson and Turner (1997)

[c] For 1622−297 the adopted γ–ray flux is not the peak value observed during the June–July 1995 flare reported in Mattox et al. (1997), i.e. 170 $\times 10^{-7}$ photons/cm^2/sec. We have chosen the flux value measured shortly before and after the short-lasting flaring value. We think it is more homogeneous with all the other sources fluxes because it is very unlikely to observe such a large flare.

[d] γ–ray flux detected by Whipple above 300 GeV, units are 10^{-11} photons/cm^2/sec

References for Table 4.5:

(tw) = this work, see Table 4.2, and 4.3; (1st) = Fichtel et al. 1994 (First EGRET source catalog); (2nd) = Thompson et al. 1995; Thompson et al. 1996 (Second EGRET sources catalog, and Supplement); (6161) = Mattox et al. 1995; (Ber93) = Bertsch et al. 1993; (Be91) = Becker et al. 1991; (Bo90) = Bozyan et al. 1990; (Br94) = Brinkmann et al. 1994; (Br95) = Brinkmann et al. 1995; (Din96) = Dingus et al. 1996; (Feg96) = Fegan private communication; (GC91) = Gregory and Condon 1991; (Ge94) = Gear et al. 1994; (Gh86) = Ghisellini et al. 1986; (Gi94) = Giommi et al. 1995; (Har93) = Hartman et al. 1993; (HB93) = Hewitt and Burbidge 1993; (IT88) = Impey and Tapia 1988; (IT90) = Impey and Tapia 1990; (K81) = Kühr et al. 1981; (Le85) = Ledden and O'Dell 1985; (Lin95) = Lin et al. 1995; (Lin96) = Lin et al. 1996; (Ma86) = Maraschi et al. 1986; (Ma93) = Maoz et al. 1993; (Mat97) = Mattox et al. 1997; (Muk95) = Mukherjee et al. 1995; (Nol96) = Nolan et al. 1996; (Pe82) = Perley 1982; (Per96) = Perlman et al. 1996; (Pr85) = Preston et al. 1985; (PR88) = Pearson and Readhead 1988; (Pi94) = Pian et al. 1994; (Q96) = Quinn et al. 1996; (RS85) = Rusk and Seaquist 1985; (Shr94) = Shrader et al. 1994; (Shr96) = Shrader et al. 1996; (Sre96) = Sreekumar et al. 1996; (St91) = Stickel et al. 1991; (Tho93) = Thompson et al. 1993; (Tr93) = Treves et al. 1993; (Ves95) = Vestrand et al. 1995; (vMon95) =Von Montigny et al. 1995; (VV93) = Veron-Cetty and Veron 1993; (Wi94) = Wilkes et al. 1994; (WB92) = White and Becker 1992; (WP85) = Wall and Peacock 1985; (Wr94) = Wright et al. 1994; (WW90) = Worrall and Wilkes 1990

by other variables such as redshift and/or luminosity.

Indeed significant correlations (at > 99.9 %) have been found between both $\alpha_{X\gamma}$ and α_{RO} with redshift and γ–ray luminosity. This is not surprising given that BL Lac objects have, on average, lower luminosities and redshifts, compared to FSRQ.

The dependence on redshift and luminosity in the $\alpha_{RO} - \alpha_{X\gamma}$ correlation can be removed applying a partial correlation analysis (Kendall and Stuart 1979).

The results indicate that excluding the effect of z, the $\alpha_{RO} - \alpha_{X\gamma}$ correlation is significant at the 99.1 % level. By the same partial correlation analysis, we have investigated the dependence of the $\alpha_{RO} - \alpha_{X\gamma}$ correlation upon the γ–ray luminosity L_γ. The significance, excluding the effect of L_γ, decreases to the 97.2 % level. Therefore we conclude that the $\alpha_{RO} - \alpha_{X\gamma}$ correlation is not induced by redshift and it is significant even when considering the dependence on L_γ, which however plays a relatively important role.

4.6 Implications for emission models

The findings of § 4.5 coupled with the $\alpha_X - \alpha_\gamma$ relation described in § 4.4 points to an underlying physical mechanism linking the two classes of objects. We briefly discuss here a couple of issues which will be again and thoroughly considered in the next Chapters (§ 5, § 6): the nature of the emitting particles, and of the inverse Compton target photons.

4.6.1 One or two electron population ?

As discussed in the Introduction and in the overview of models (Chapter 2) the overall νF_ν spectrum of blazars shows two peaks: the low energy one at IR/soft X–ray energies, and the high energy one peaking in the MeV/GeV range.

These two peaks can be due to a *single* population of electrons, emitting synchrotron and inverse Compton radiation, or can be the result of the emission of *two* different electron populations, emitting both by the synchrotron process, as in the 'proton blazar' model of Mannheim (1993). In the former case (one population), the two frequencies at which the overall emission peaks are obviously related, being produced by the same electrons. This holds whatever the origin of the seed photons to be upscattered at higher energies. If this is the case, then one expects correlations between fluxes and slopes in different energy bands, of the kind reported here in the previous sections, between the slopes at X–rays and γ–ray energies, and between the broad band spectral indices connecting the radio with the optical, and the X–ray with the γ–rays.

one population

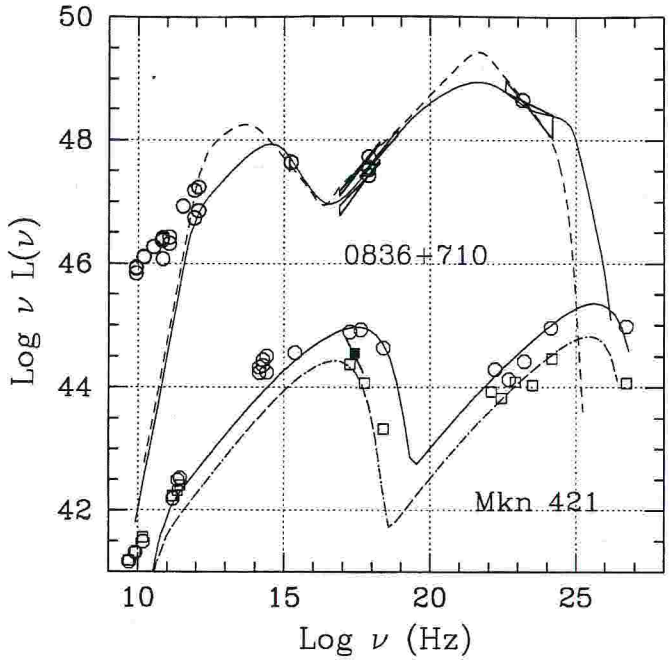

Figure 4.4: Examples of SEDs illustrating the difference among BL Lac objects and FSRQ. The data have been collected from the literature and references are reported in Table 5.1. Model parameters are listed in Table 4.6. The SED of 0836+710 is fitted with the SSC model (solid line) and the ERC (external Compton) model (dashed line), as explained in the text. For Mkn 421, the SEDs refer to the May 1994 flare (circles) and to the preceding quiescent period (squares) (Macomb et al. 1995; Macomb et al. 1996). Both states have been fitted with a pure one–zone homogeneous SSC model.

examples

To illustrate our findings, we plot in Fig. 4.4 the overall spectra of two blazars: the low redshift BL Lac object Mkn 421, and the high redshift low polarized quasar 0836+710. We have chosen these two sources because they are representative of the BL Lac and FSRQ classes and have very different SEDs.

Mkn 421

Note that the X–ray emission of Mkn 421 connects smoothly with the lower energy part of the spectrum, suggesting that in this source the X–rays are due to the synchrotron mechanism. This implies the presence of very energetic electrons, whose inverse Compton emission can then account for the observed emission in the TeV band.

0836+710

Instead, the SED of 0836+710 suggests that the synchrotron peak occurs in the IR part of the spectrum, indicating that the electrons radiating at this peak have smaller energies than in the Mkn 421 case. As can be seen, both peaks are at smaller energies for 0836+710, and in this object the γ–ray luminosity is more dominant. As a result, the high energy peak should move to the MeV range. The extrapolations of the steep γ–ray and the flat X–ray spectra indeed form a peak at a few MeV.

The found anti–correlation between α_X and α_γ can be easily interpreted in the "one electron population" scenario. Steep X–ray spectra smoothly connecting with lower frequencies emission imply synchrotron radiation and therefore a high frequency for

TABLE 4.6: MODEL PARAMETERS FOR THE FITS TO 0836+710 AND MKN 421

Parameter		Mkn 421		0836+710	
		High State[a]	Low State[a]	SSC	ERC
size of blob	R (cm)	$1 \cdot 10^{16}$	$1 \cdot 10^{16}$	$5 \cdot 10^{16}$	$7 \cdot 10^{16}$
Doppler beaming factor	δ	11	11	19	19
magnetic field	B (Gauss)	0.16	0.16	0.36	10.3
BLR compactness[b]	$\ell'_{\rm BLR}$	0	0	0	6
electron injected spectrum					
compactness[b]	$\ell_{\rm inj}$	$6 \cdot 10^{-3}$	$3 \cdot 10^{-3}$	0.3	0.4
slope[c]	s	1.7	1.7	3.7	3.1
minimum energy[d]	$\gamma_{\rm min}$	1	1	$\boxed{4 \cdot 10^3}$ [e]	$\boxed{150}$ [e]
maximum energy[d]	$\gamma_{\rm max}$	$\boxed{8 \cdot 10^5}$ [e]	$\boxed{3.3 \cdot 10^5}$ [e]	$1 \cdot 10^5$	$1 \cdot 10^4$

Notes to Table 4.6

[a] The SEDs for both states have been "fitted" only with SSC model. [b] quantities measured in the blob rest frame. [c] the slope is defined as $N(\gamma) \propto \gamma^{-s}$. [d] electron energy expressed in units of $m_e c^2$. [e] this *boxed* values are those corresponding to the synchrotron and inverse Compton peaks in the SED, $\equiv \gamma_{\rm peak}$.

the Compton peak, possibly beyond the EGRET band is expected. This in turn implies flat γ–ray slopes, signature of the still rising Compton component.

This scenario can also account for the anti–correlation between $\alpha_{\rm RO}$ and $\alpha_{\rm X\gamma}$. As in Mkn 421 a flat $\alpha_{\rm RO}$ occurs when the synchrotron component peaks at frequencies above the optical band. This implies a large X–ray flux, due to synchrotron emission, and a relatively small 100 MeV flux, since the peak of the γ–ray emission is above 100 MeV: as a consequence, flat $\alpha_{\rm RO}$ imply steep $\alpha_{\rm X\gamma}$ indices.

two populations

In the case of *two* electron populations (e.g. *Proton blazar* model) an explanation of all these findings would require a fine tuning between the extension in energies and total energy content of the two distributions.

Moreover it is worth reminding that a strong argument in favour of a *single* electron population is provided by the observed coordinated variability, for instance of the optical and γ–ray flux (Maraschi et al. 1994 and Hartman et al. 1996 for 3C 279; Wagner et al. 1995 for 1406–076), which can be naturally accounted for by a *single* population model, while in the case of *two* electron distribution scenario the correlated variability would require a even tighter tuning (see § 2).

We then conclude that one electron population is a simpler explanation of the SED of γ–ray bright blazar, with respect to the proton blazar scenario. If true, this means that the overall synchrotron behaviour at IR–UV frequencies (peak energy and variability) allows to predict the behaviour at high energies: by monitoring blazars in the

optical UV we therefore monitor the same electrons making the high energy emission.

Note that the α_{RO}–$\alpha_{X\gamma}$ relation suggests that the more γ–ray dominated sources are on average optically faint and are also expected to have a steep spectrum in the infrared–optical range. If this is the case, relatively bright γ–ray sources could then be discovered among red FSRQ. We point out that the source with the steepest α_{RO} (and the flattest α_X) in our sample (i.e. 0202+149) shows an extremely red optical–infrared spectrum without any evidence of reddening (Stickel et al. 1996). A selection based on optical colors may provide a starting sample for future more sensitive γ–ray missions (i.e. GLAST, the *Gamma Ray Large Area Space Telescope*).

4.6.2 Seed photons

A single population of electrons can produce the entire SED of blazars by the synchrotron and the inverse Compton process. However, as mentioned in the introduction, we still do not know the origin of the seed photons for the inverse Compton process.

As it will be discussed in the next Chapters, the γ–ray emission in BL Lac objects is less dominant than in FSRQ, even if it extends to higher energies. Together with the absence of emission lines, this suggests that the main radiation mechanism in BL Lac objects is the SSC process (see also § 2.5.2). The (very approximate) equality of the luminosity of the two components suggests that the magnetic field is close to equipartition with the synchrotron radiation energy density.

To preliminary address the subject here we present the fits with a one–zone homogeneous model to the SED of Mkn 421 and 0836+710. An extensive study of the properties of the SEDs of γ–ray bright blazars, and the resulting physical parameters, will be the subject of Chapter 6.

Mkn 421

For Mkn 421, for which simultaneous data are available both for a "quiescent" state and a flaring state (Macomb et al. 1995; Macomb et al. 1996), we applied a pure SSC model. The results are shown in Fig. 4.4, and the best "fit" parameters are reported in Table 4.6. The synchrotron and self Compton peaks are due to electrons of Lorentz factor $\gamma_{peak} \gtrsim 10^5$. Both states of the source can be reproduced by varying only the injected luminosity (by a factor 2), and γ_{max} (by almost a factor 3).

0836+710

For 0836+710, we have applied both the SSC model and the ERC model. The radiation produced external to the jet is distributed in energy as a diluted blackbody, peaking in the UV band. The input parameters are listed in Table 4.6. The "synchrotron" and "Compton" peaks for the ERC case are due to electrons with Lorentz factors $\gamma_{peak} \simeq 150$.

The main difference between the SSC and the ERC models for 0836+710 concerns

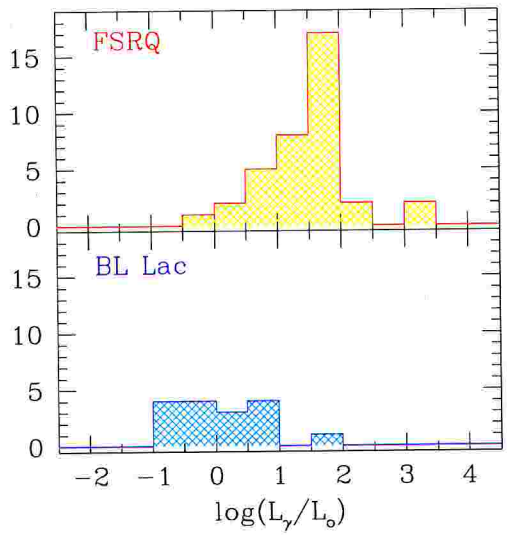

Figure 4.5: Histograms of the ratio between γ–ray and optical luminosity for BL Lacs and FSRQ included in our γ/soft-X-ray selected sample.

the value of the magnetic field, which is close to equipartition with the synchrotron radiation energy density in the ERC case, and much weaker in the SSC case.

Note that both models account for the main characteristics of the overall emission of 0836+710. On the basis of the pure SED, therefore, one *cannot discriminate* among the two models.

Other information, such as the broad line luminosity, and the variability pattern in the IR–UV band with respect to the γ–ray band, is necessary in order to select which are the dominant seed photons for the inverse Compton process (e.g. see § 2 and § 6).

We can nevertheless draw the conclusion that the different SEDs of Mkn 421 and 0836+710 are mainly due to a difference in the value of their typical electron energies $\gamma_{\rm peak}$. A distribution of $\gamma_{\rm peak}$, therefore, could well be responsible for the observed variety of SEDs of blazars.

4.6.3 BL Lacs *vs.* FSRQ

As extensively discussed in the previous sections BL Lacs differ from FSRQ as:

① they tend to have steeper X–ray and flatter γ–ray spectra,

② they separate from FSRQ in the $\alpha_{\rm RO} - \alpha_{\rm X\gamma}$ plane.

A new result, confirming previous findings by Dondi and Ghisellini (1995), is that:

③ the ratio between the γ–ray and optical luminosity $L_\gamma/L_{\rm opt}$, which can be considered as a measure of the γ–ray dominance, is different for BL Lacs and FSRQ.

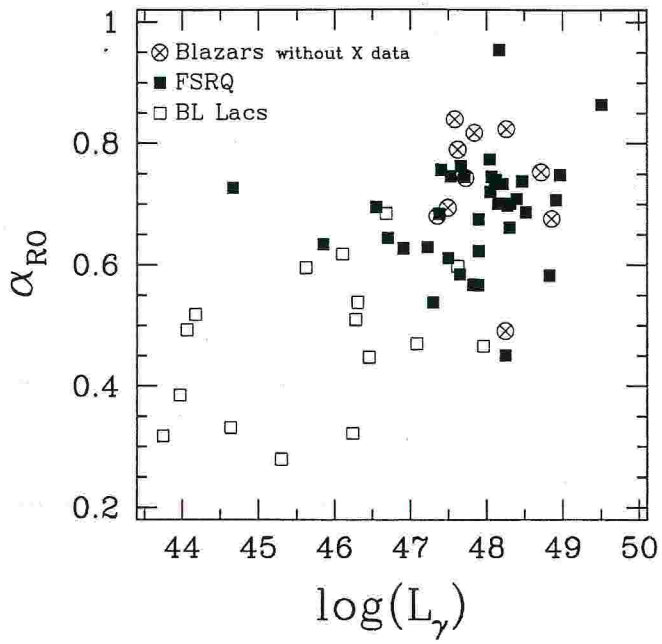

Figure 4.6: α_{RO} *vs.* L_γ for BL Lacs and FSRQ included in our γ/soft-X-ray selected sample, with a few more objects added which have not been included in the studied sample due to the lack of information on their X–ray properties.

In Fig. 4.5 are shown the distributions for "our" 12 BL Lacs and 37 FSRQ, from which it is clear that the "typical" values are:

$$\text{BL Lacs}: \quad \langle L_\gamma/L_{opt}\rangle \simeq 1 \qquad \text{FSRQ}: \quad \langle L_\gamma/L_{opt}\rangle \simeq 30$$

We have already argued that points ① and ② can be explained if the overall spectrum is produced by a single population of electrons whose distribution is characterized by a break energy γ_{peak}, which is, on average, smaller in FSRQ with respect to BL Lacs. Point ③ above suggests that the value of γ_{peak} may be related to the ratio of the Compton to synchrotron luminosity: the smaller γ_{peak}, the larger the Compton dominance. This can also explain the found dependence of the $\alpha_{RO} - \alpha_{X\gamma}$ correlation upon L_γ.

In Fig. 4.6 is shown that there exists a significant relationship between the γ–ray luminosity and α_{RO}, which is a very good tracer of the position of the synchrotron peak (see § 5).

Compton cooling rate

We speculate that this relationship may be related to the electron Compton cooling rate. In less compact sources, with no important emission lines, the electron cooling time is long. Large values of γ_{peak} are then possible as a result of a competition between acceleration and cooling rates, or, alternatively, between cooling and adiabatic expansion (or particle escape) rates.

The fact that BL Lac objects have no or weak emission lines then suggests that one key parameter to explain the SED of all objects is the relative importance of the broad emission lines. If present, they can contribute significantly to the Compton cooling, resulting in small value of $\gamma_{\rm peak}$ and a dominating γ–ray emission. If absent, the γ–ray emission is instead ruled by the synchrotron radiation energy density, with a relatively lower γ–ray dominance and larger $\gamma_{\rm peak}$.

4.7 Summary

We have analysed *ROSAT* PSPC data for 27 bright EGRET and TeV sources, X–ray fluxes for further 26 sources have been retrieved from the *ROSAT* All Sky Survey and from other X–ray missions. The main conclusions can be summarized as follow:

- ✔ The measured X–ray spectra show a very broad distribution with energy indices in the range $\alpha_{\rm X} \simeq -0.3 - 2.3$. In the soft $\sim$ 0.1–2.0 keV X–ray band the mean spectral slope of BL Lac objects is significantly steeper than the mean slope of FSRQ. The reverse is true in the γ–ray band where FSRQ spectra are steeper than BL Lac ones.
- ✔ Significant anti–correlations have been found between $\alpha_{\rm X}$ and α_γ and $\alpha_{\rm RO}$ and $\alpha_{\rm X\gamma}$. The distribution of BL Lacs and FSRQ in these two diagrams (Figures 4.1 and 4.2) suggests that the two classes of objects represent the extremes of a continuous distribution rather than two distinct populations. These correlations can be explained if the same relativistic electrons are responsible for both the radio to optical and the hard X–ray to γ–ray emission, via, respectively, the synchrotron and the inverse Compton processes.
- ✔ The important parameter in describing the observed SEDs is the synchrotron peak energy [in a $\nu {\rm F}_\nu$ plot], greater in BL Lac objects than in FSRQ.
- ✔ We speculate that the proposed distribution in the values of the peak energy of the synchrotron component may be due to the different amount of radiative cooling suffered by the relativistic electrons. More severe radiative cooling would result in a small value of the synchrotron peak energy and a more dominating γ–ray emission.
- ✔ It is predicted that relatively bright γ–ray sources have red optical colors (or viceversa). Future missions in the γ–ray (i.e. GLAST) and near infrared optical spectrophotometry should be able to test this hypothesis.

CHAPTER 5

SPECTRAL ENERGY DISTRIBUTIONS

Following the interesting results of Chapter 4, giving us the picture of a striking coherence in the broad band properties of blazars and a suggestion on the physical mechanism regulating it, here we study the systematics of the SEDs of blazars using data from the radio to the γ–ray band, considering a larger sample of sources comprising both BL Lacs and FSRQs. With respect to previous studies (Maraschi et al. 1995; Sambruna et al. 1996) we improve the analysis by:

① *extending the SED to the γ–ray range*, and improving the frequency coverage;

② using a larger complete sample of FSRQ;

③ using the richer and brighter sample of X–ray selected BL Lacs recently derived from the Slew Survey.

5.1 The data

5.1.1 The samples

We decided to consider the following three samples of blazars, motivated by the need of completeness, sufficient number of objects and observational coverage at other fre-

quencies, as detailed below.

- BL Lacs radio selected: the 1 Jy sample (refer to § 3.2.1),
- BL Lacs X-ray selected: the *Einstein* Slew survey sample (refer to § 3.2.2),
- Flat spectrum quasars: 2 Jy sample drawn by Padovani and Urry (1992) requiring $\alpha_R \leq 0.5$, from the "2 Jy sample" by Wall and Peacock (1985), a complete flux–limited catalogue selected at 2.7 GHz, covering 9.81 sr, and including 233 sources with $F_{2.7GHz} > 2$ Jy. It consists of 50 sources with almost complete polarization data, of which 20 are detected in γ–rays (all with EGRET).

We use the available γ–ray data for each sample but also indirect information derived from the γ–ray detected (not complete) sample discussed in Chapter 4.
Since we find that the continuity hypothesis among blazars holds we also consider a merged "global" sample irrespective of the original classification of the objects. Combining the three samples yields a total of 126 blazars (six of them are present in both the radio and X–ray selected samples of BL Lacs), of which 33 detected in γ–rays. We will refer to them as the *total blazar sample*.

5.1.2 Multi-frequency data

In view of building average SEDs minimizing the bias introduced by incompleteness, we decided to focus on a few well covered frequencies, at which fluxes are available for most objects.

We chose the following seven well sampled frequencies, that are sufficient to give the basic information on the SED shape from the radio to the X–ray band:

$\Longrightarrow$	radio at 5 GHz	$\log \nu \simeq 9.7$
$\Longrightarrow$	millimeter at 230 GHz	$\log \nu \simeq 11.4$
$\Longrightarrow$	far infrared (IRAS data) at $60\mu m$	$\log \nu \simeq 12.7$
$\Longrightarrow$	far infrared (IRAS data) at $25\mu m$	$\log \nu \simeq 13.1$
$\Longrightarrow$	near infrared (K band) at $2.2\mu m$	$\log \nu \simeq 14.1$
$\Longrightarrow$	optical (V band) at 5500 Å	$\log \nu \simeq 14.7$
$\Longrightarrow$	soft X rays at 1 keV	$\log \nu \simeq 17.4$

Moreover we collected X–ray spectral indices (see § 5.1.2) as well as γ–rays fluxes and spectral indices (see § 5.1.2).

Data were assembled from a careful search in the literature and extensive usage of the NASA Extragalactic Database (NED)[1].

de-reddening

The optical magnitudes have been de-reddened using values of A_V derived from the A_B reported in the NED database according to the law $A_V = A_B/1.324$ (Rieke and Lebofsky 1985).

In the radio and optical bands the coverage is complete for all the objects in the three samples, while unfortunately for mm, far and near IR and X–ray fluxes data for some sources are lacking (see Table 5.1). The worse case is the far IR (25 μm) band where only 28/126 objects have measured fluxes.

In Table 5.1 (which is at the end of the Chapter) a summary of the collected broad band data is reported, where as detailed below we report the computed average fluxes for each object.

Average *vs.* maximum fluxes

For each source, at each frequency *from radio to optical* we assigned the average of all the fluxes found in literature. Given the large variability these averages were performed logarithmically (magnitudes).

In principle a suitable alternative to the averaging would be to consider in each band the maximum detected flux (see for instance Dondi and Ghisellini 1995). On the one hand this choice could be particularly meaningful in view of the fact that in the γ–ray band, due to the limited sensitivity of detectors, we are biased towards measuring the brightest states. On the other hand also this option is biased since the value of the maximum flux is strongly dependent on the observational coverage and for most of the objects we only have a few (sometimes a single) observations. Moreover the strength of this bias is "band–dependent" and can thus significantly affect the determination of the broad band spectral shape. As both choices present advantages and disadvantages, and since our goal is a statistical analysis, we consider them equally good. The "averages" option has been preferred because it is likely to be more robust with respect to the definition of radio–optical SED properties.

X–ray data

Given the special relevance of the knowledge of the X–ray properties, and in particular of the fact that the shape of the X–ray spectrum can be fundamental for disentangling the synchrotron and inverse Compton components, and inferring the respective peak

[1]NED, NASA/IPAC Extragalactic Database, is operated by the Jet Propulsion Laboratory, Caltech, under contract with the National Aeronautics and Space Administration.

frequencies, the most suitable choice for X–ray data is the large and homogeneous *ROSAT* data base. .

ROSAT

In fact, a large fraction of the 126 sources (90/126) has been observed with the *ROSAT* PSPC allowing to uniformly derive X–ray fluxes and in many cases, that is for 73 targets of pointed observations, spectral shapes in the 0.1–2.4 keV range (Brunner et al. 1994; Lamer et al. 1996; Perlman et al. 1996; Urry et al. 1996; Comastri et al. 1995; Sambruna 1997; Comastri et al. 1997, see also Chap. 4).

X–ray spectral indices were derived from the same observation and, when available, we adopted the α_X resulting from fits with neutral hydrogen column density N_H allowed to vary. Some of these 90 objects (17) have been only detected in the RASS and fluxes are published by Brinkmann et al. (1994) and Brinkmann et al. (1995). Monochromatic fluxes (at 1 keV) for these sources have been derived from the 0.1 – 2.4 keV integrated flux adopting the average spectral index of the sample to which they belong (see Table 5.3 and 5.5) and the value of the Galactic column in the source direction (Elvis et al. 1989; Dickey and Lockman 1990; Lockman and Savage 1995; Murphy et al. 1996). When more than one observation was available we give the average flux.

other data

Of the remaining 36 sources, 24 belong to the Slew survey sample and for them we used directly the *Einstein* IPC flux from Perlman et al. (1996). The fluxes at 2 keV listed by Perlman et al. (1996) were converted to 1 keV using the average *ROSAT* spectral index of the Slew survey sample ($\langle\alpha_X\rangle$ = 1.40), derived from the 24 sources with a *ROSAT* measured value.

For other 3 sources, without *ROSAT* data, we used an *Einstein* IPC flux, bringing the total number of sources with measured X–ray flux to 117/126.

γ–ray data

Within the three samples only a fraction of blazars were detected in γ–rays, namely 9/34 in the 1 Jy sample, 8/48 in the Slew sample, 20/50 in the FSRQ sample. Four of these sources (0235+164, 0735+178, 0851+202 and 1652+398) are present in both the BL Lac object samples, giving a net number of γ–ray detections of 33 out of 126 blazars. All but one of them have been observed by EGRET in the 30 MeV – 30 GeV band. For 28/32 a γ–ray spectral index has been determined.

One source, 1652+398 (Mkn 501), has only been detected at very high energies, beyond 0.3 TeV by ground based Cherenkov telescopes (Whipple and HEGRA, Punch et al. 1992; Weekes et al. 1996; Krennrich et al. 1997; Bradbury et al. 1997; Aharonian et al. 1997; Samuelson et al. 1998), while EGRET yielded only an upper limit.

γ–detection fraction

It is noteworthy that the detected fraction is significantly different between FSRQs and BL Lacs, being respectively 40 ± 10.6 % and 17.1 ± 5.1 % for XBLs+RBLs. However for RBLs only the fraction detected in γ–rays is 26.5 ± 9.9 %, consistent with that of quasars while XBLs only yield 16.7 ± 6.4 %.

other γ–ray blazars

Many other blazars ($\sim$ 30) have been detected by EGRET, but do not fall in our samples. One can consider the whole group of γ–ray detected objects as a sample in its own right, though not a complete one at present, since a significant fraction of the sky has been surveyed though not uniformly. This larger sample comprises 66 sources (Fichtel et al. 1994; Von Montigny et al. 1995; Thompson et al. 1995; Thompson et al. 1996; Mattox et al. 1997; Kanbach 1996; Mukherjee et al. 1997 and references therein), of which 60 have a measured redshift, and 48 an estimate of the spectral index. To this set we can add Mkn 501 (already included in both our BL Lac samples), and 2344+514 (Catanese et al. 1998), detected only by the Whipple telescope. We will use this additional information to discuss whether the γ–ray properties of our samples can be representative of the whole γ–ray loud population and if so, to increase the statistics (see section 5.4). We therefore collected basic data also on all of the 30 (29 EGRET plus 2344+514) γ–ray detected AGN/blazars not included in the complete samples. They are reported in Table 5.2.

γ–data selection

Given the large amount of observations and analysis of the same data by different authors, for the selection of the flux and spectral index we used the criteria adopted in Chapter 4 (§ 4.1). γ–ray data are usually given in units of photons cm^{-2} s^{-1} above an energy threshold (e.g. for EGRET E $\gtrsim$ 100 MeV). We converted them to monochromatic fluxes at 100 MeV integrating a power law in photons with the measured or assumed (the average) spectral index.

Luminosities and K–correction

All fluxes were K-corrected and luminosities were computed with the following choices:

(a) we considered lower limits on redshift (4 sources) as detections, while we assigned the average redshift of the sample to the few sources without any estimate (4 in the 1 Jy sample, for which $\langle z \rangle = 0.492$, and 6 in the Slew survey sample, $\langle z \rangle = 0.194$);

(b) radio–to–optical fluxes were K–corrected using the average spectral indices derived from the literature (see Table 5.3). For X–ray and γ–ray data we used measured power law spectral indices, when available, or the average index derived for the sources of the same sample (see Tables 5.3, 5.5).

TABLE 5.3: SPECTRAL INDICES USED FOR K–CORRECTION[a]

band	Slew	1 Jy	FSRQ	refs.
(1)	(2)	(3)	(4)	(5)
radio	0.20	−0.27	−0.30	1
mm	0.32	0.32	0.48	2
IRAS	0.60	0.80	1.00	3
IR–opt	0.67	1.21	1.52	4
X–rays	1.40	1.25	0.83	5
γ–rays	0.98	1.26	1.21	5

Notes to Table 5.3

(a) spectral indices used for K–correction of monochromatic fluxes: (1) spectral band; (2) Slew; (3) 1Jy; (4) FSRQ; (5) references.

References for Table 5.3:
(1) Stickel et al. 1994; (2) Gear et al. 1994; (3) derived from IRAS data; (4) Bersanelli et al. 1992; (5) this work, see Table 5.1.

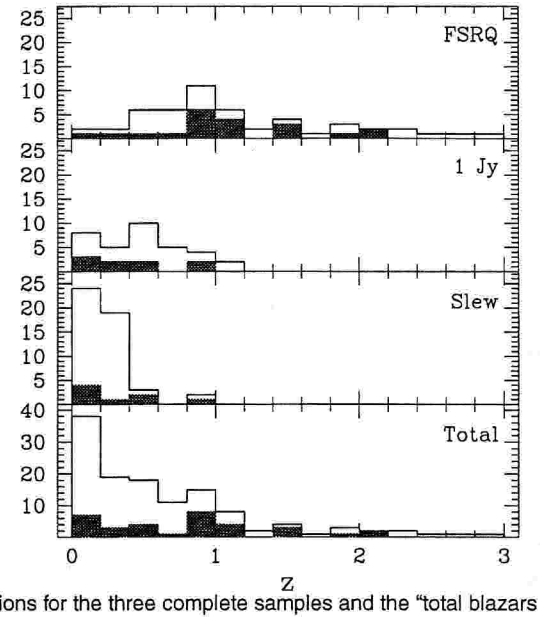

Figure 5.1: Redshift distributions for the three complete samples and the "total blazars sample". Sources detected in the γ–rays are indicated by the grey areas.

5.2 Results A: distributions of properties

5.2.1 Comparison of γ–detected/not–γ–detected sources

Since the fraction of objects detected in γ–rays in the three samples is rather small, it is important to ask whether the detected sources are representative of each sample as a whole or are distinguished in other properties from the rest of the objects in it. Moreover we want to verify whether the γ–ray detected sources in general differ from those belonging to the complete samples.

We therefore computed the distributions of various quantities, i.e. redshift, luminosities and broad band spectral indices, for objects belonging to each sample. These

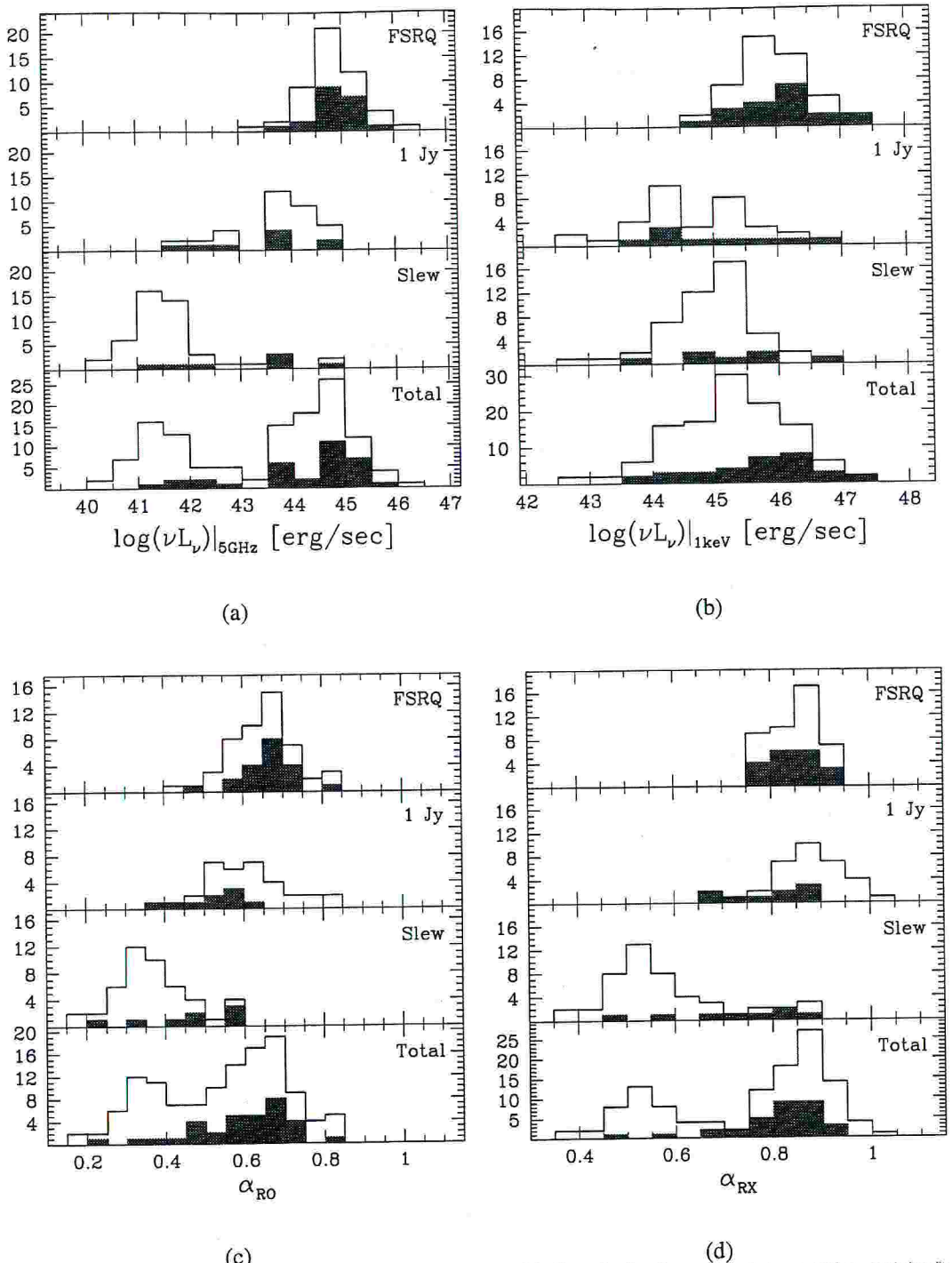

Figure 5.2: Distribution of luminosities and broad band spectral indices for the three complete samples and the "total blazars sample": (a) L_{5GHz} , (b) L_{1keV} , (c) α_{RO} , (d) α_{RX} . Grey areas indicate γ–ray detected objects.

are shown in Figs. 5.1, 5.2a-d for the three samples and the total blazar one, highlighting those sources detected in the γ–ray band as grey shaded areas in the histograms.

The redshift distributions (Fig. 5.1) of the three complete samples show the known tendency towards the detection of FSRQs at higher z, being the latter ones more pow-

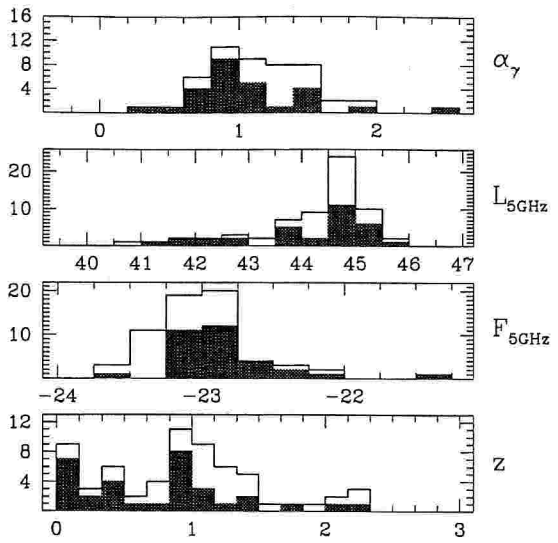

Figure 5.3: Distributions of redshift z, radio luminosity and flux and γ–ray spectral index for the γ–ray loud sources detected by EGRET, where the shaded ones refer only to sources in our three complete blazar samples.

erful radio sources, as shown in Fig. 5.2a.

In the same figure and in Fig. 5.2b, the tendency for XBL to have similar X–ray but lower radio luminosities compared to RBL is also apparent. Correspondingly, it appears from Figs. 5.2c,d that $\alpha_{\rm RO}$ and $\alpha_{\rm RX}$ increase from XBL to RBL while FSRQ have $\alpha_{\rm RO}$ slightly larger and $\alpha_{\rm RX}$ similar to RBLs. Later on (section 5.3.2) we will show that there is a relationship between these spectral indices and the peak frequency of the synchrotron component.

We note that for all of the distributions there is *continuity* in properties not only between the two BL Lac samples, but also between BL Lacs and FSRQs.

It is clear from Figs. 5.1, 5.2a-d that for the RBL and FSRQ samples the γ–ray detected sources do not differ from non–detected ones in any of the considered quantities while for the Slew sample there is a tendency for γ–ray loud sources to have larger L_{5GHz}, $\alpha_{\rm RX}$ and $\alpha_{\rm RO}$. This indicates that either the radio luminosity or radio–loudness are important in determining the γ–ray detection. On the contrary, and in some sense surprisingly, the X–ray luminosity does not seem to play an important role with respect to the γ–ray emission, although the X-ray band is the closest in energy to the γ–rays . We will come back to this issue later on (§ 5.5.1). We checked the possible difference of means and variances of the distributions with the Student's t–test and only for the $\alpha_{\rm RX}$ of the Slew sample the significance is higher than 95 per cent.

Except for the case of the Slew survey, we conclude that the γ–ray detected sources are representative of the samples as a whole, being indistinguishable from the others in terms of radio to X-ray broad band properties and power.

5.2.2 Comparison with the whole γ–ray detected sample

We also checked that the γ–ray detected sources belonging to our samples are homogeneous with respect to all of the γ–ray blazars detected so far. In Fig. 5.3 we compare the redshift distributions, the radio luminosities and fluxes and the γ–ray spectral index. The grey shaded areas represent the γ–ray sources belonging to the complete samples considered here. We conclude that there is no significant difference.

5.2.3 Comment on γ–ray detected/(bright ?) sources

We are aware that the limited sensitivity of the EGRET instrument implies that at a given radio flux, only the γ–ray loudest sources are detected. Therefore the non detected ones are probably on average weaker in γ–rays.

A fraction of $\simeq$ 10% of all blazars have been detected in the EGRET bandpass (Mattox et al. 1997). This *blazar fraction* refers to those flat spectrum radio sources which would have been above the EGRET flux sensitivity if the ratio between their γ–ray and 5 GHz radio fluxes were at least as large as the lowest value for the EGRET detected blazars.

true γ–ray loudness

Impey (1996) quantified this effect by taking into account the correlation between radio and γ–ray luminosities (see also § 5.4.2), and other observables. Assuming a Gaussian distribution of the γ–ray–to–radio flux ratio he estimated the width of the distribution and the "true" ratio referring to the whole population, which could be a factor 10 lower than the observed one.

It is clear that there is a strong empirical relationship between the radio properties (i.e. radio–loudness and flat spectrum) and γ–ray emission in AGN, but it is not readily apparent what other properties the γ–ray emitting sources have that distinguish them from other similar sources not detected in high energy γ–rays. It could be that:

① there is a *real spread* in the intrinsic properties of the blazar population, the γ–ray detected blazars being intrinsically louder than the rest of the population, which would be persistently γ–ray–quiet because conditions driving to high energy γ–ray emission do not exist in these sources.

② this may be due to *variability*, i.e. a source is detected only when it undergoes a flare. All blazars are similar and may become strong γ–ray emitters from time to time. The observed γ–ray/radio ratio would thus refer to flaring states, while the average level of each source would be lower.

③ the bias arises because some sources have the γ–ray emission that is beamed in a different direction or more narrowly than the synchrotron.

Since variability is a distinctive property of blazars and has been observed to occur also in γ–rays, often with extremely large amplitude (greater than a factor 10, e.g. 3C 279, Maraschi et al. 1994; PKS 0528+134, Mukherjee et al. 1996; 1622−297, Mattox et al. 1997) the *variability* alternative is likely although the problem remains open.

If this is the case we can hold the hypothesis that all blazars have similar γ–ray properties instead of distinguishing between γ–loud and γ–quiet sources.

On the other hand, some emission models make definite predictions about the γ–ray blazars representing a true subset of all blazars (see § 2.2 and § 2.7). ERC models predict a stronger Doppler boosting of the γ–ray flux $\propto \delta^{4+2\alpha}$ compared with the radio-to-optical synchrotron flux which is boosted only by the factor $\delta^{3+\alpha}$ (see § 2.3). With $\alpha = 1$, the prominence of the γ–ray component increases $\propto \delta^2$ implying that the most pronounced γ–ray blazars must be the ones with the largest Doppler factors (i.e. smallest viewing angles or largest bulk Lorentz factors). This prediction can be tested with radio observations.

We conclude that the average γ–ray luminosities computed here are necessarily overestimated. However we chose not to correct for this effect given the uncertainties. In particular the "bias factor" for different classes of blazars could be different if their γ–ray variability properties (amplitude and duty cycle) are (e.g. Ulrich et al. 1997).

BL Lacs vs. FSRQ

In this respect there is a last interesting comment to add concerning possible biases in the estimate of the the γ–ray loudness of EGRET sources. There is the possibility that data for BL Lacs and FSRQ are biased in opposite ways, respectively towards lower and higher values with respect to the "typical" peak flux level, due to the combination of differences in brightness and variability. The argument is the following: BL Lacs variability pattern is that of repeated short–lasting flares, whose flux level is moderate, requiring a fairly long integration time for detection. The measured flux is then the average over many rapid flares, interspersed with low level intervals leading to a decrease of the estimated source brightness, whose entity depends on the duty cycle of the source. On the contrary, FSRQ light curves show rather long trends and in general their flux in the EGRET bandpass is high enough to allow a "short" exposure time for detection. This enables us to measure the γ–rays in different brightness states, and eventually to really estimate the peak γ–ray level.

5.3 Results B: synchrotron peak frequency

We discussed in Chapter 2 the importance of the knowledge of the energy at which the synchrotron peak occurs, since it provides a powerful diagnostic for the physical

conditions in the emitting region.

How to tell the synchrotron peak position ? Polynomial fitting

In order to determine the position of the peak of the synchrotron component in individual objects with an objective procedure, we fitted the data points for each source (in a $\nu - \nu L_\nu$ diagram) with a third degree polynomial. This yields a complex SED profile, allowing an upturn which can better model the X–ray spectrum that can be dominated by the inverse Compton component, i.e. with data points not laying on the direct extrapolation from the lower energy spectrum.

In many cases there is evidence that the X–ray component, even in the soft *ROSAT* PSPC band, is due to the inverse Compton process (see Chapter 4 and e.g. Sambruna 1997; Comastri et al. 1997). Thus to impose that the X–ray point smoothly connects to the lower energy data, as would happen in a parabolic fit, could be misleading for a determination of the synchrotron peak frequency (see also Sambruna et al. 1996). We used a simple parabola when the cubic fit was not able to find a maximum, which typically happened when the peak occurs at energies higher than X–rays. In fact when the peak moves to high enough frequencies (typically beyond the IR band), the X–ray flux is completely dominated by the synchrotron emission, and the results given by the cubic and parabolic fits are fully consistent. In 8 cases neither the cubic nor the parabolic fit were able to determine a peak frequency/luminosity mainly due to the paucity of data points.

5.3.1 Synchrotron peak frequency *vs.* luminosity

The peak frequencies derived with the above procedure (defined as the frequencies of the maximum in the fitted polynomial function) are plotted in Fig. 5.4a,b,c versus the radio and γ–ray luminosities and versus the corresponding peak luminosities, as determined from the fits. Let us stress once again the *continuity* between the different samples. Considering the samples together strong correlations are present between these quantities, in the sense of $\nu_{\rm peak,sync}$ decreasing with increasing luminosity. The results of Kendall's τ statistical test (Press et al. 1992) show that the correlations are highly significant (Table 5.4).

redshift "subtraction"

Since on the one hand in flux limited samples spurious correlations can be introduced by the luminosity/redshift relation and on the other hand the correlations might be due to evolutionary effects genuinely related to redshift, we checked its role in two ways. We estimated the possible correlation of the relevant quantities with redshift, and performed partial correlation tests (by means of the "partial correlation" technique,

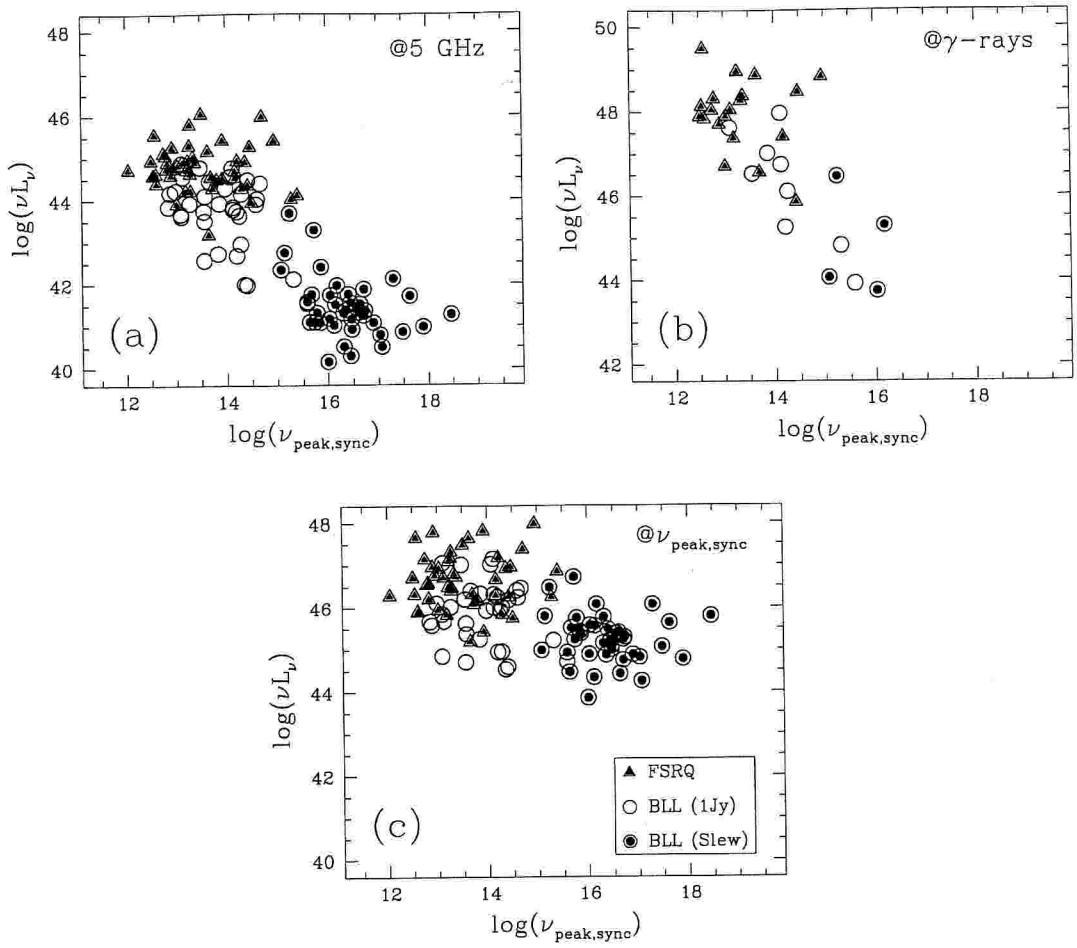

Figure 5.4: The peak frequency of the synchrotron component, $\nu_{\rm peak,sync}$, as derived with the polynomial fits, plotted against (a) the radio luminosity L_{5GHz}, (b) the γ–ray luminosity L_γ, and (c) the fitted peak luminosity of the synchrotron component, $L_{\rm peak,sync}$.

e.g. Padovani 1992) between two quantities subtracting out the common dependence on z. The results are reported in Table 5.4. In addition, in order to have an independent check on the redshift bias, we also considered the significance of the correlations restricting them to objects with $z < 0.5$.

The correlation between $\nu_{\rm peak,sync}$ and L_{5GHz} still holds after subtraction of the very strong dependence on redshift. The same is true for the relation between $\nu_{\rm peak,sync}$ and the γ–ray luminosity L_γ, although the significance is much smaller, due to the reduced number of sources. On the other hand the correlation between $\nu_{\rm peak,sync}$ and $L_{\rm peak,sync}$ is strongly weakened when subtracting the redshift effect.

Considering only the $z < 0.5$ interval the significance of the first two correlations persists and does not change when the redshift dependence is subtracted. These values can then be considered as irreducible, being the signature of a *true dependence* of

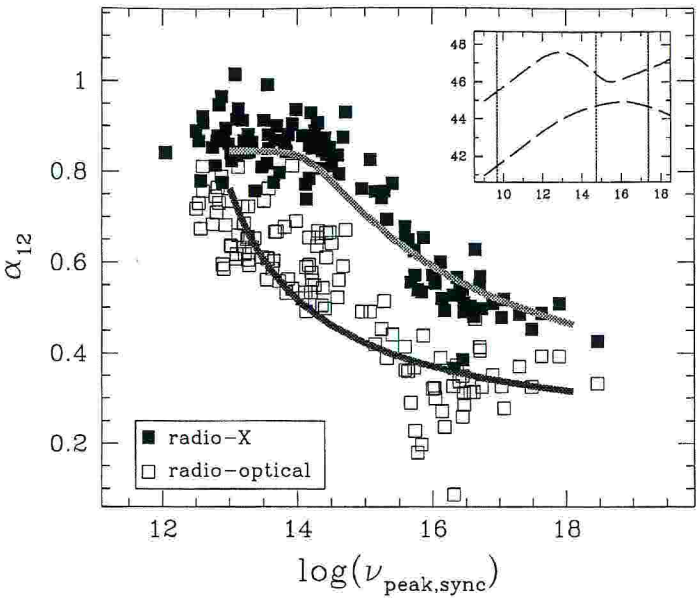

Figure 5.5: The broad band spectral indices α_{RO} and α_{RX} are plotted versus $\nu_{peak,sync}$. The curved lines overlayed to the data points represent the relations α_{RO}–$\nu_{peak,sync}$ and α_{RX}–$\nu_{peak,sync}$ obtained from a "synthetic" set of SEDs. Details on the adopted analytical parameterization are given in text, § 5.5. Two examples of typical SEDs are reported for reference in the inset: the top one peaking at $\nu \simeq 10^{13}$ Hz, with $\alpha_{RO} = 0.76$ and $\alpha_{RX} = 0.85$, the bottom one at $\nu \simeq 10^{16}$ Hz ($\alpha_{RO} = 0.35$ and $\alpha_{RX} = 0.56$). The three vertical lines mark the frequencies corresponding to 5 GHz, 5500 Å, and 1 keV, entering in the definitions of α_{RO} and α_{RX}.

$\nu_{peak,sync}$ on luminosity. This result can also be read as a check of the reliability of the partial correlation procedure. On the contrary the correlation $\nu_{peak,sync}$ *vs.* $L_{peak,sync}$ disappears at low redshifts, due to the narrow interval of values spanned by $L_{peak,sync}$, that varies less with the change of peak frequency than both radio and γ–ray luminosity do.

5.3.2 Synchrotron peak frequency *vs.* broad band spectral indices

The relations between the synchrotron peak frequency and each of the two point spectral indices α_{RO} and α_{RX} are shown in Fig. 5.5. Also these quantities are strongly correlated (see Table 5.4). In fact recent papers (e.g. Maraschi et al. 1995; Comastri et al. 1995; Comastri et al. 1997), suggested that the position of the synchrotron peak could be devised from the values of broad band spectral indices.

It would be very important to better assess the reliability/existence of a direct relationship between SED shape (i.e. synchrotron peak) and radio/optical/X–ray effective spectral indices, and in turn enable their use as predictive tools.

The power of these parameters resides in the fact that for present and future samples, which are going to be larger and larger, it will be difficult to have enough multi-

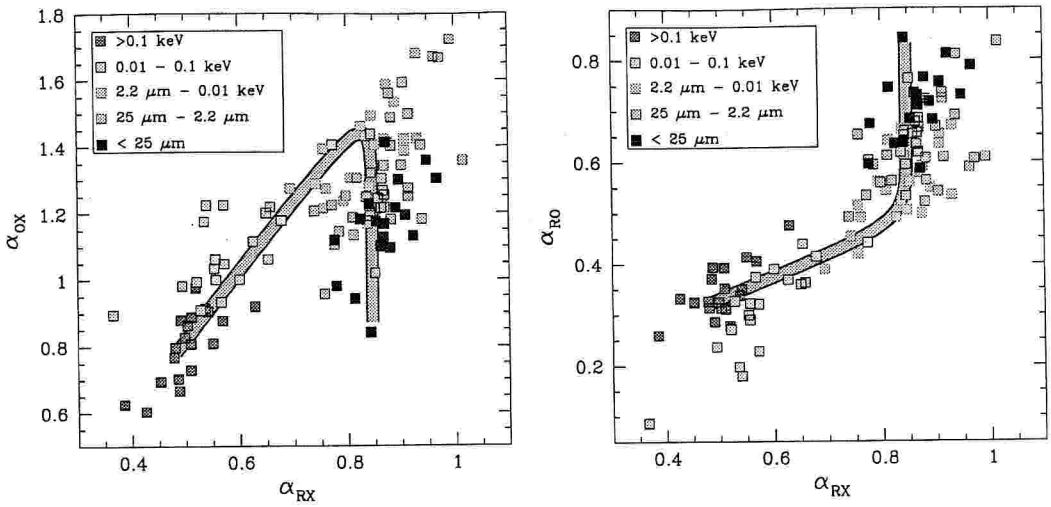

Figure 5.6: Color–color diagrams for the "total blazars sample" with color coding corresponding to the value of $\nu_{\rm peak,sync}$: (a) $\alpha_{\rm OX}$ *vs.* $\alpha_{\rm RX}$, (b) $\alpha_{\rm RO}$ *vs.* $\alpha_{\rm RX}$. The thick lines overlayed to the data points represent the relations $\alpha_{\rm RX}$–$\alpha_{\rm OX}$ and $\alpha_{\rm RX}$–$\alpha_{\rm OX}$ obtained from the "synthetic" SEDs.

frequency data to trace the radio–to–X–ray SED and tell where the synchrotron peak occurs, whilst it is very likely that the availability of the minimal set of radio/optical/X–ray fluxes will eventually improve. Actually most of the new samples whose selection is in progress[2] are derived from the cross-correlation of radio and X–ray catalogues/surveys, thanks to the fact that blazars are bright in both bands, and require optical follow–up for source identification.

We see in Fig. 5.5 that the knowledge of any of the two spectral indices is enough to guess the position of the peak of the synchrotron component, except for some ranges, namely $\nu_{\rm peak,sync} > 10^{16} - 10^{17}$ Hz for $\alpha_{\rm RO}$, and $\nu_{\rm peak,sync} < 10^{14}$ Hz for $\alpha_{\rm RX}$. These "failures" can be explained bearing in mind the typical shape of the blazar SEDs (see inset in Fig. 5.5): when the spectrum peaks at low frequencies, X–rays are typically dominated by the inverse Compton, flat spectrum, component whose luminosity level is strongly correlated with the radio one (see Fig. 1.4b, and Chap. 3, Fossati et al. 1997), and then the X–ray/radio ratio (i.e. $\alpha_{\rm RX}$) tends to a fixed value.

Conversely we can say that the Compton component begins to dominate the (*ROSAT*) X–ray band when $\alpha_{\rm RX} \simeq 0.75$, corresponding to $\nu_{\rm peak,sync} \lesssim 3 \times 10^{14}$ Hz. It is interesting to note that the adopted dividing threshold between LBL and HBL has been

[2]e.g. REX by Wolter and collaborators, Wolter et al. (1997); DXRBS by Padovani, Perlman and collaborators, Perlman et al. (1998); FIRST by Laurent-Muehleisen and collaborators, Laurent-Muehleisen (1996)

Table 5.4: CORRELATION PROBABILITIES FOR LUMINOSITIES AND BROAD BAND SPECTRAL INDICES[a]

x_1	x_2	x_1/x_2	x_1/z	x_2/z	x_1/x_2-z	x_1/x_2	x_1/z	x_2/z	x_1/x_2-z
(1)	(2)	(3)	(4)	(5)	(6)	(7)	(8)	(9)	(10)
		z unconstrained (# 109[b])				$z < 0.5$ (# 51[b])			
$\nu_{peak,sync}$	L_{5GHz}	1.2e-16	[1.1e-9]	[1.9e-31]	1.1e-11	1.3e-8	[—]	[4.0e-4]	9.2e-9
$\nu_{peak,sync}$	$L_{peak,sync}$	4.9e-8	[1.1e-9]	[9.5e-27]	6.5e-2	—	[—]	[1.2e-7]	—
$\nu_{peak,sync}$	α_{RO}	1.1e-23	[1.1e-9]	[7.7e-11]	4.7e-19	1.8e-7	[—]	[—]	2.9e-7
$\nu_{peak,sync}$	α_{RX}	4.2e-17	[1.1e-9]	[6.0e-5]	1.9e-14	4.1e-15	[—]	[—]	8.4e-15
Correlations involving γ–ray data									
EGRET sources included in our samples									
		z unconstrained (# 31)				$z < 0.5$ (# 11)			
$\nu_{peak,sync}$	L_{γ}	2.1e-3	[3.4e-2]	[1.5e-10]	1.8e-2	2.4e-2	[—]	[2.4e-3]	6.4e-2
L_{5GHz}	L_{γ}	6.0e-11	[5.5e-10]	[1.5e-10]	4.2e-5	3.9e-3	[5.2e-2]	[2.4e-3]	2.4e-2
$\nu_{peak,sync}$	$L_{\gamma}/L_{peak,sync}$	2.7e-5	[3.4e-2]	[1.5e-5]	2.2e-4	1.4e-3	[—]	[7.3e-1]	4.1e-3
$\nu_{peak,sync}$	$L_{\gamma}/L_{5500\text{Å}}$	2.5e-6	[3.4e-2]	[4.2e-5]	1.7e-5	2.4e-3	[—]	[—]	6.8e-3
sources in the whole EGRET sample									
		z unconstrained (# 60)				$z < 0.5$ (# 15)			
L_{5GHz}	L_{γ}	4.8e-15	[4.8e-15]	[1.8e-14]	2.4e-6	1.8e	[1.1e-2]	[1.4e-4]	4.1e-2

Notes to Table 5.4

(a) (1–2): quantities considered in the correlation; (3–10): significance of the "null–hypothesis", i.e. that the correlation is the result of pure chance, for the various quantities: in columns (3–6) for tests performed without any redshift constraint, while in (7–10) results for tests taking into account only sources with $z \gtrsim 0.5$. In (3),(7) the "face value" correlation between x_1 and x_2. In (4–5) and (8–9) the significance of the correlation of each quantity x_1 and x_2 with redshift. In (6) and (10) the "net" x_1/x_2 correlation remaining from (3) and (7) after subtraction of the redshift dependence of x_1 and x_2 via partial correlation algorithm. A dash is reported if the correlation is not significant (i.e. probability < 90 %.

(b) we considered only sources with at least a lower limit on redshift, and for which it has been possible to determine the "synchrotron" peak frequency by means of the polynomial fit.

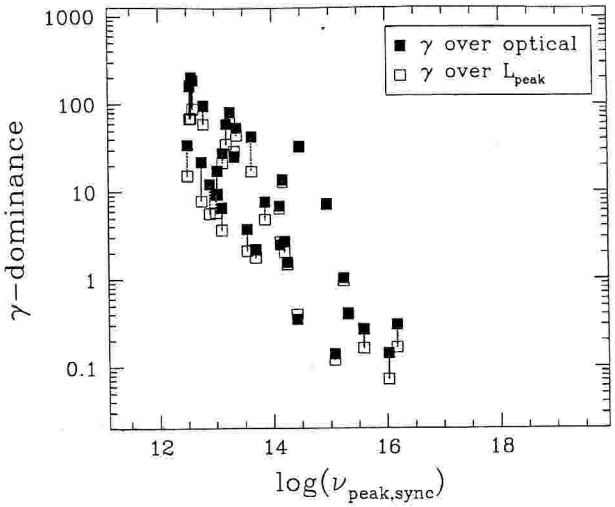

Figure 5.7: The γ–ray dominance (according to two definitions, see text § 5.3.3) versus the synchrotron peak frequency $\nu_{\rm peak,sync}$

set to this value from purely practical purposes, while in the light of the result above it assumes a more "physical" meaning: LBL sources have Compton–dominated soft–X–ray emission, while in HBL this is pure synchrotron (see also Padovani and Giommi 1995).

At the other end of the spectrum a problem arises when $\nu_{\rm peak,sync}$ moves at energies higher than that used to compute the broad band spectral index. The reason is that the ratio between, for instance, optical and radio luminosity is no longer sensitive to the peak moving further towards higher frequencies, because both the radio and optical bands lay on the same (rising) branch of the synchrotron "bump".

For comparison we draw in Fig. 5.5 the loci of $\alpha_{\rm RO}$–$\nu_{\rm peak,sync}$ and $\alpha_{\rm RX}$–$\nu_{\rm peak,sync}$ obtained from a set of SEDs of the kind reported in the inset, and that we are going to discuss in more detail in section 5.5 The parameterization describes the observed features very well.

In Figs. 5.6a,b we put together two broad band spectral indices, $\alpha_{\rm RX} - \alpha_{\rm RO}$ and $\alpha_{\rm RX} - \alpha_{\rm OX}$, trying to overcome the "degeneracy" just discussed, which is frustrating the use of these quantities to study SED properties. The sources have been plotted in five different colors according to the estimated synchrotron peak energy. Points follow a smooth continuous pattern across the diagram showing that the combination of two α's basically solve the problem giving a reasonable estimate of $\nu_{\rm peak,sync}$. The thick lines overlayed are the loci of points predicted on the basis of the already mentioned SED parameterization that we are going to introduce in § 5.5. The agreement is very good although not able to account for the whole scatter of points in the diagram.

5.3.3 Synchrotron peak frequency *vs.* γ–ray dominance

In Fig. 5.7 $\nu_{\rm peak,sync}$ is plotted against the γ–ray dominance parameter, here approximated with the ratio between the γ–ray and the synchrotron peak luminosities, which represents a lower limit estimate. A strong correlation (see Table 5.4) is present over four orders of magnitude in $\nu_{\rm peak,sync}$, in the sense of a decrease in the γ–ray dominance with an increase of the synchrotron peak frequency. In the same figure we plotted also the ratio between the γ–ray and optical luminosities, to check if the latter could eventually be a good indicator of the γ–ray dominance, with the advantage of being derived from two observational quantities. In fact there is little difference, at most a factor 3 for a quantity spanning more than three decades.

The γ–ray dominance parameter is interesting because it can be directly related to physical properties internal to the emitting blob, the ratio between radiation and magnetic energy density, and give a neat constraint, as detailed in Chapter 2.

5.4 Results C: Average SEDS

Having discussed extensively the possible biases introduced by the limited number of γ–ray detected sources in the complete samples we construct here the average SEDs for each sample.

Details of the averaging procedure

The averaging procedure has been performed on the logarithms of the luminosities at each frequency. Apart from the problems in the γ–ray range discussed above, the incompleteness of the data coverage at some frequencies could also introduce a bias in the average values. For instance in the Slew survey sample only 10/48 objects have a flux measured at 230 GHz, and they are the more luminous sources at 5 GHz. Averaging independently $L_{230\rm GHz}$ (for 10 objects) and $L_{5\rm GHz}$ (for 48 objects) we would obtain a ratio between the two luminosities higher than that derived considering only the subsample of 10 sources, and presumably higher than the actual one, too.

To reduce this effect we first normalized the monochromatic luminosities to the radio 5 GHz luminosity for each source. We then computed average ratios at each frequency ν^*, $\langle \log(L_{\nu^*}/L_{5\rm GHz}) \rangle_{sub}$, considering only the subsample of sources with a measured flux at ν^*, and on the other hand the average $L_{5\rm GHz}$ for all sources. Finally we used that ratio to compute the average monochromatic luminosity at ν^* for all sources

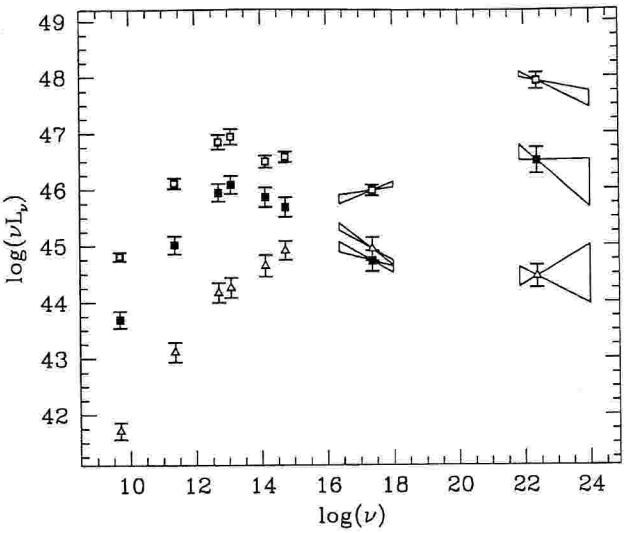

Figure 5.8: The average SEDs for each of the samples are shown. From top to bottom (referring to radio luminosity) Wall and Peacock FSRQs (empty boxes), 1 Jy BL Lac sample (filled boxes) and Slew survey BL Lac sample (triangles) . These latter two are in reversed order in X–ray band, the lowest spectrum being that of the 1 Jy sample.

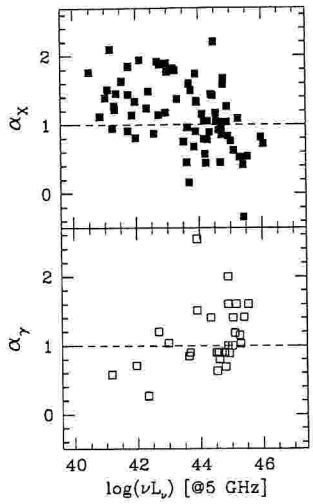

Figure 5.9: X–ray and γ–ray spectral indices plotted versus radio luminosity.

in the sample as:

$$\langle \log(L_{\nu^*}) \rangle_{all} = \langle \log(L_{5GHz}) \rangle_{all} + \langle \log(L_{\nu^*}/L_{5GHz}) \rangle_{sub}$$

In this way we basically averaged the spectral shape between ν^* and 5 GHz for the objects with available data at ν^* and assigned that spectral shape to the sample.

The X–ray and γ–ray spectral indices have been averaged with a simple mean, without weighting.

5.4.1 Average SEDs of XBL, RBL, FSRQ samples

The average broad band spectra for each of the three samples are shown in Fig. 5.8. The 6 sources common to the radio and the X–ray selected BL Lac samples are considered in both of them. Average luminosities entering Fig. 5.8 are reported in Table 5.5 together with the number of sources contributing at each frequency.

It is apparent from Fig. 5.8 that the three samples refer to objects with different average integrated luminosities and that the peak frequency of the power emitted between the radio and the X-ray band moves from the X-ray to the far infrared band going from the XBL to the FSRQ samples, as anticipated from the analysis of single objects in section 5.3. Correspondingly the γ–ray luminosities increase and the γ–ray

TABLE 5.5: AVERAGE LUMINOSITIES[a]

	Complete Samples			Total Blazar Sample ($\log(L_{5GHz})$ intervals)				
Band	Slew	1 Jy	W&P	<42	42–43	43–44	44–45	>45
(1)	(2)	(3)	(4)	(5)	(6)	(7)	(8)	(9)
5 GHz	41.71	43.69	44.81	41.24	42.47	43.71	44.54	45.39
	[48]	[34]	[50]	[38]	[10]	[17]	[44]	[17]
230 GHz	43.11	45.01	46.11	42.64	43.77	45.13	45.83	46.63
	[10]	[34]	[50]	[5]	[7]	[15]	[44]	[17]
60 μm	44.17	45.94	46.84	43.73	44.65	46.09	46.65	47.61
	[12]	[19]	[13]	[6]	[5]	[8]	[16]	[2]
25 μm	44.25	46.07	46.93	43.74	44.95	46.08	46.79	47.69
	[10]	[15]	[8]	[4]	[6]	[7]	[9]	[2]
K–band	44.64	45.86	46.49	44.42	45.04	45.96	46.27	47.21
	[23]	[31]	[28]	[13]	[10]	[15]	[32]	[6]
V–band	44.91	45.68	46.58	44.61	45.01	45.82	46.27	47.21
	[48]	[34]	[50]	[38]	[10]	[17]	[44]	[17]
1 keV	44.94	44.72	45.98	44.81	44.11	44.92	45.66	46.50
	[48]	[32]	[43]	[38]	[10]	[15]	[42]	[12]
100 MeV	44.45	46.50	47.93	44.24	44.79	46.67	47.71	48.68
	[7]	[8]	[20]	[3]	[5]	[9]	[33]	[12]
α_X	1.40 ± 0.07	1.25 ± 0.09	0.83 ± 0.08	1.37 ± 0.09	1.55 ± 0.15	1.16 ± 0.14	1.11 ± 0.08	0.57 ± 0.13
	[24]	[31]	[24]	[16]	[8]	[14]	[26]	[9]
α_γ	0.98 ± 0.32	1.26 ± 0.26	1.21 ± 0.09	0.64 ± 0.07	0.73 ± 0.47	1.37 ± 0.31	1.06 ± 0.13	1.30 ± 0.08
	[6]	[6]	[18]	[2]	[4]	[7]	[25]	[11]

Notes to Table 5.5

[a] Average luminosities, for each sample and for the total one (divided in bins of radio luminosity). In square brackets are reported the numbers of sources contributing at each datum.

References for Table 5.5:

(5 and 230 GHz): Becker et al. (1991); Bloom et al. (1994); Gear et al. (1986); Gear (1993b); Gear et al. (1994); Kühr et al. (1981); Kühr and Schmidt (1990); Perlman et al. (1996); Reuter et al. (1997); Steppe et al. (1988); Steppe et al. (1992); Steppe et al. (1993); Stevens et al. (1994); Stickel et al. (1991); Stickel et al. (1993); Stickel et al. (1994); Tornikoski et al. (1993); Tornikoski et al. (1996); Terasranta et al. (1992);

(IR–optical data): Allen et al. (1982); Ballard et al. (1990); Bersanelli et al. (1992); Bloom et al. (1994); Brindle et al. (1986); Brown et al. (1989); Elvis et al. (1994); Falomo et al. (1993); Falomo et al. (1993); Falomo et al. (1994); Gear et al. (1985); Gear et al. (1986); Gear (1993a); Glass (1979); Glass (1981); Holmes et al. (1984); Impey and Brand (1981); Impey and Brand (1982); Impey et al. (1982); Impey et al. (1984); Impey and Neugebauer (1988); Impey and Tapia (1988); Impey and Tapia (1990); Jannuzi et al. (1993); Jannuzi et al. (1994); Landau et al. (1986); Lepine et al. (1985); Litchfield et al. (1994); Lorenzetti et al. (1990); Mead et al. (1990); O'Dell et al. (1978); Pian et al. (1994); Sitko and Sitko (1991); Smith et al. (1987); Stevens et al. (1994); Wright et al. (1983);

(X–rays): Brinkmann et al. (1994); Brinkmann et al. (1995); Brunner et al. (1994); Comastri et al. (1995); Comastri et al. (1997); Lamer et al. (1996); Maraschi et al. (1995); Perlman et al. (1996); Perlman et al. (1996); Sambruna (1997); Urry et al. (1996);

(γ–rays): Bertsch et al. (1993); Catanese et al. (1997); Chiang et al. (1995); Dingus et al. (1996); Fichtel et al. (1994); Hartman et al. (1993); Lin et al. (1995); Lin et al. (1996); Madejski et al. (1996); Mattox et al. (1997); Mattox et al. (1997); Mattox et al. (1997); Mukherjee et al. (1995); Mukherjee et al. (1996); Nolan et al. (1996); Quinn et al. (1996); Radecke et al. (1995); Shrader et al. (1996); Sreekumar et al. (1996); Thompson et al. (1993); Thompson et al. (1995); Thompson et al. (1996); Vestrand et al. (1995); Von Montigny et al. (1995);

spectra steepen suggesting that also the peak frequency of the high energy emission moves to lower frequencies.

5.4.2 The total blazar sample

The overall similarity and regularity of the SEDs of the different samples as well as the continuity in the properties of the individual objects discussed in section 5.3 suggest a basic similarity of all blazars irrespective of their original classification and different appearance in a specific spectral band.

We therefore considered the merged total sample with the scope of finding the key parameter(s) governing the whole blazar phenomenology. Since luminosity appears to have an important role in that it correlates with the main spectral parameters we decided to bin the total blazar sample according to luminosity, irrespective of the original classification.

It may be desirable to use the total integrated luminosity which in all cases is basically the γ–ray one. However this latter is only available for a few objects. As a first and simpler approach we decided to overcome this problem using *radio power as indicator of the total bolometric luminosity*. On the basis of the empirical relationship that seems to hold between γ–ray and radio luminosity, we used the 5 GHz radio luminosity which is available for all objects. A correlation between γ–ray and radio luminosity has been claimed by many authors using different techniques (e.g. Dondi and Ghisellini 1995; Mattox et al. 1997). It is however still being debated whether it is true or it arises from selection effects, connected with the common redshift dependence of luminosities, and with the exclusion of upper limits, which could favour the appearance of a spurious correlation. It is worth mentioning that Mücke et al. (1997) using a technique designed to take into account both these effects did not find any significant correlation between radio and γ–ray data for a sample of 38 extragalactic EGRET sources.

why L_{5GHz}

radio–γ–ray correlation

We also checked the radio–γ correlation on both the 31 EGRET detected sources included in our samples and the larger "comparison sample" of 60 EGRET sources. In Table 5.4 we report the significance of the correlation, together with its value after subtracting the common redshift dependence through a partial correlation test, and its significance for samples restricted to $z < 0.5$. In all cases the radio and γ–ray luminosities correlate significantly.

In Figs. 5.9a,b α_X and α_γ for individual sources are plotted against the radio power, both showing a good correlation with it. In Chapter 4 we discussed the interesting consequences of the apparent anti–correlation between X–ray and γ–ray spectral indices,

α_X, α_γ vs. L_{5GHz}

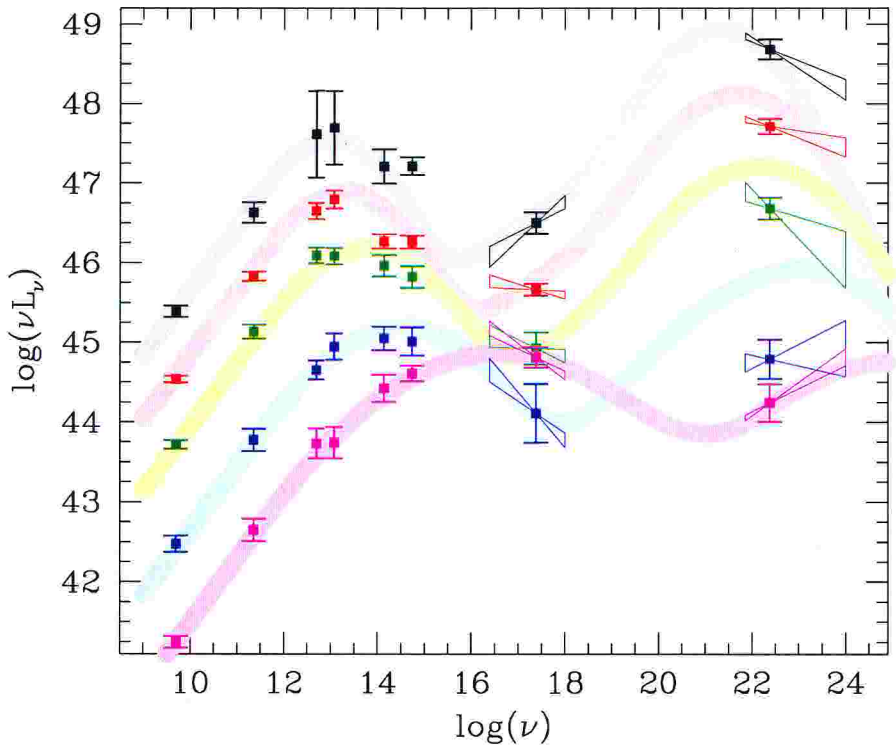

Figure 5.10: Average SEDs for the "total blazar sample" binned according to radio luminosity irrespective of the original classification. The overlayed curves are analytic approximations obtained according to the one–parameter–family definition described in the text.

without relating it to any "absolute" parameter, such as luminosity. Here again we see that these other spectral properties have a dependence on radio luminosity.

γ–ray in average SEDs

Since in some luminosity bins the number of γ–ray detected sources included in our sample is small, we used an indirect procedure to associate γ–ray fluxes and spectra to our average SEDs, taking advantage of the whole body of information regarding the γ–ray properties of blazars. Namely for each luminosity bin $\langle L_\gamma \rangle$ and $\langle \alpha_\gamma \rangle$ were computed from blazars in the general EGRET–detected sample (i.e. considering also the sources listed in Table 5.2) falling into the same L_{5GHz} bin. The basic assumption is the uniformity of the spectral properties, as discussed in section 5.2.

The resulting SEDs are shown in Fig. 5.10 and average luminosities, X–ray and γ–ray spectral indices, and number of sources are reported in Table 5.5. The most interesting result is that the trends pointed out for the three separate sub–classes of blazars (Fig. 5.8) hold for the total blazar sample, irrespective of the original classification of sources, when the radio luminosity is adopted as the key parameter characterizing each object.

5.5 Discussion

5.5.1 Blazars as a one parameter family

In Fig. 5.10 we superimposed to the averaged data a set of lines, whose main goal is to guide the eye. A full description of the parameterization can be found in Chapter 3 (§ 3.3.3, see also Appendix of Chapter 3) where it was introduced in the framework of the "unified bolometric" scenario to account for the source number densities of BL Lacs with different spectral properties (LBL and HBL).

synchrotron component

The radio–to–X–ray SED is approximated with a power law starting in the radio domain continuously connecting at $\nu \simeq 5{\times}10^{11}$ Hz with a parabolic branch, describing the synchrotron peak of the SED. In soft X–rays a rising power law, is summed to this curved "synchrotron" component to represent the onset of the inverse Compton component. The normalization of this second X–ray component is kept fixed relative to the radio one.

IC component

The analytic representation of the X–ray to γ–ray component is a parabola of the same width as the synchrotron one, and has been obtained assuming that:

- ✔ the ratio of the frequencies of the high and low energy peaks is constant
$$\nu_C/\nu_S \simeq 5 \times 10^8,$$
- ✔ the high energy (γ–ray) peak and radio luminosities have a fixed ratio,
$$\nu L_\nu|_\gamma / \nu L_\nu|_{5GHz} \simeq 3 \times 10^3.$$

$\nu_{peak} - L_{5GHz}$

Based on our findings (see Fig. 5.4a), we then assume that the peak frequency of the synchrotron spectral component is (inversely) related to radio luminosity. The simplest hypothesis of a straight unique relationship between $\nu_{peak,sync}$ and L_{5GHz} does not give a good result when compared with the average SEDs. We then allow for a different SED–shape *vs.* luminosity dependence for high and low luminosity objects, a distinction that turns out to roughly correspond also to that between objects with and without prominent emission lines. We adopted a "two–branch" relationship between $\nu_{peak,sync}$ and L_{5GHz} in the form of two power laws $\nu_{peak,sync} \propto L_{5GHz}^{-\eta}$, with $\eta = 0.6$ or $\eta = 1.8$ for $\log(L_{5GHz})$ higher or smaller than 42.5, respectively (compare to Fig. 5.4).

Given the extreme simplicity of the latter assumptions, it is remarkable that the phenomenological analytic model describes the run of the average SEDs reasonably well, actually very faithfully up to X–rays. The worst case refers to the second luminosity bin: the analytic model predicts a γ–ray luminosity larger than the computed bin average by a factor of 10 (but predicts the correct spectral shape). We note that only 5 γ–ray detected objects fall in this bin.

The results derived from the above analysis (see in particular Figs. 5.8–5.10) can then be summarized as follows:

① *two peaks* are present in all the SEDs. The first one (synchrotron) is anticorrelated with the source luminosity (see Figs. 5.4 and Table 5.4), moving from $\sim 10^{16} - 10^{17}$ Hz for less luminous sources to $\sim 10^{13} - 10^{14}$ Hz for the most luminous ones;

② the *X–ray spectrum* becomes harder while the *γ–ray spectrum* softens with increasing luminosity, indicating that the second (Compton) peak of the SEDs also moves to lower frequencies from $\sim 10^{24} - 10^{25}$ Hz for less luminous sources to $\sim 10^{21} - 10^{22}$ Hz for the most luminous ones (see also Fig. 5.9);

③ therefore *the frequencies of the two peaks are correlated*: the smaller the $\nu_{\rm peak,sync}$ the smaller the peak frequency of the high energy component; a comparison with the analytic curves shows that the data are *consistent* with a constant ratio between the two peak frequencies;

④ increasing L_{5GHz} increases the *γ–ray dominance*, i.e. the ratio of the power emitted in the inverse Compton and synchrotron components, estimated with the ratio of their respective peak luminosities (see also Fig. 5.7).

The fact that the trends present when comparing the different samples (e.g. Fig. 5.8), persist when the total blazar sample is considered and binned according to radio luminosity only, suggests that we deal with a *continuous spectral sequence* within the blazar family, rather than with separate spectral classes. In particular the "continuity" clearly applies also to the HBL – LBL subgroups: HBL have the lowest luminosities and the highest peak frequencies.

X-ray band

An interesting result apparent from the average SEDs is the variety and complexity of behaviour shown in the X–ray band. As expected the crossing between the synchrotron and inverse Compton components can occur below or above the X–ray band affecting the relation between the X–ray luminosity and that in other bands. A source can be brighter than another at 1 keV being dimmer in the rest of the radio–γ–ray spectrum except probably in the TeV range. This effect narrows the range of values spanned by L_{1keV} and explains why γ–ray detected sources do not select a particular range in the X–ray luminosity distributions (see Fig. 5.2b) while this happens for L_{5GHz} .

5.5.2 On the synchrotron and Compton peaks "distance"

The extreme "regularity" of the SEDs of blazars and in particular the trends discussed above must derive from the common underlying physical processes. Assuming the

simple case of a single (homogeneous) zone model the shape of the SED depends on the spectrum of the high energy electrons radiating via synchrotron and inverse Compton, the magnetic field and the nature of seed photons for the inverse Compton process, either SSC or ERC.

Here we briefly discuss the implications of the suggested trends for the two scenarios, in particular of the apparent constancy of the ratio of the synchrotron and Compton peak frequencies, ν_C / ν_S . The following relations hold (§ 2.3):

$$\text{SSC}: \quad \frac{\nu_C}{\nu_S} \propto \gamma^2_{\text{break}} \qquad\qquad \text{ERC}: \quad \frac{\nu_C}{\nu_S} \propto \frac{\Gamma\, \nu_{\text{ext}}}{B}$$

SSC Let us assume a constant bulk Lorentz factors in all blazars. Should the (homogeneous) SSC model be valid for all sources, it is easy to see that the (approximately) constant ratio between the high and low peak frequencies yields an (approximately) constant value for the energy of the particles radiating at the peaks. If the energy of the radiating particles is similar in all sources the different peak frequencies should result from a systematic variation in the magnetic field strength, HBLs having the highest, FSRQs the lowest random field intensity.

ERC Should instead the soft photons upscattered to the γ–ray range be produced outside the jet at a "typical" frequency ν_{ext} (the same for all sources) the condition of a constant ratio between the peak frequencies implies a constant value of the magnetic field. As a consequence the energy of the particles radiating at the peaks should vary along the spectral sequence being lower in FSRQs and higher in HBLs.

It could also be that there is a smooth transition between the SSC and ERC mechanisms depending on the physical conditions outside the jet. In all cases however the role of the luminosity, which phenomenologically appears dominant, does not find an immediate physical justification, although one could find plausible arguments to link it to the parameters mentioned above and in particular to the conditions surrounding the jet.

In the next Chapter we present model fits to the spectral energy distributions of 51 (γ–bright) individual objects, deriving the (model dependent) physical parameters for each source. These computations indeed suggest the idea that the blazar sequence follows from a transition from the SSC to the ERC scenario, LBLs being the intermediate objects. The computed radiation energy densities, which determine the amount of radiative cooling, increase with increasing source luminosity and may be responsible for the lower energy of the particles radiating at the peaks in higher luminosity sources.

The likely possibility that the external photon field involved in the ERC process is (or is related to) the radiation reprocessed as broad emission lines, seems to be at least

qualitatively in agreement with the observational evidence concerning the emission line luminosity in the suggested blazar sequence.

5.6 Summary

The main conclusion of this study of blazars SEDs is that despite the differences in the continuum shapes of different sub–classes of blazars, a unitary scheme is possible, whereby blazar continua can be described by a family of analytic curves with the source luminosity as the fundamental parameter. The "scheme" (admittedly empirical) determines both the frequency and luminosity of the peaks in the synchrotron and inverse Compton power distributions (and therefore also the γ–ray luminosity in the EGRET range) starting from the radio luminosity only. The main suggested trend is that with increasing luminosity both the synchrotron and the inverse Compton peaks move to lower frequencies and that the latter becomes energetically more dominant.

The "spectral sequence" finds a plausible interpretation in the framework of relativistic jet models radiating via the synchrotron and inverse Compton processes if the physical parameters (magnetic field and/or critical energy of the radiating electrons) vary with luminosity or if photons outside the jet become increasingly important as seed photons for the inverse Compton process in sources of larger power. The latter alternative is supported at least qualitatively by the increasing dominance of emission lines in higher luminosity objects.

Table 5.1: MULTI–FREQUENCY DATA FOR THE BLAZARS SAMPLE[a]

IAU Name	sample	z	F_{5GHz} (Jy)	F_{230GHz} (Jy)	$F_{60\mu m}$ (Jy)	$F_{25\mu m}$ (Jy)	F_K (mJy)	F_V (mJy)	F_{1keV} (μJy)	α_X	F_{100MeV} (nJy)	α_γ
(1)	(2)	(3)	(4)	(5)	(6)	(7)	(8)	(9)	(10)	(11)	(12)	(13)
0048−097	1Jy	...	1.650	0.618	...	...	7.060	1.903	0.889	1.79 ± 0.24	...	...
0118−272	1Jy	>0.557	0.732	0.289	...	...	10.199	1.710	0.278	1.74 ± 0.74	...	...
0133+476	wp	0.859	1.304	0.681	0.167	...	1.821	0.650	0.286	0.92 ± 0.39	...	...
0138−097	1Jy	>0.501	0.819	0.182	...	...	4.297	0.883	...	...	...	...
0145+138	Slew	0.125	0.005	...	...	...	6.536	0.255	5.596	...	...	...
0158+003	Slew	0.299	0.009	...	...	...	...	0.212	1.365	1.46 ± 0.27	...	...
0208−512	wp	1.003	1.342	1.359	...	...	...	0.850	0.627	1.04 ± 0.04	0.335	0.69 ± 0.05
0212+735	wp	2.370	0.453	0.319	...	...	...	0.849	0.051	-0.34 ± 0.59	...	...
0219+428	Slew	0.444	0.775	...	0.300	0.058	11.469	4.034	1.558	1.60 ± 0.17	0.094	0.90 ± 0.20
0229+200	Slew	0.139	0.044	...	...	...	...	5.515	3.141	...	...	...
0235+164	1Jy,Slew	0.940	1.438	1.134	0.218	...	12.607	2.969	1.700	1.59 ± 0.86	0.460	0.90 ± 0.20
0323+022	Slew	0.147	0.038	...	...	...	2.358	0.856	3.331	1.27 ± 0.09	...	...
0336−019	wp	0.852	1.171	0.827	0.335	...	1.036	0.245	0.253	...	0.875	...
0347−121	Slew	0.188	0.008	...	...	...	...	0.181	2.613	1.12 ± 0.09	...	...
0403−132	wp	0.571	1.606	0.348	...	...	1.593	0.688	0.362	0.78 ± 0.22	...	...
0405−123	wp	0.574	1.087	0.158	...	...	7.562	6.547	1.242	1.15 ± 0.17	...	...
0414+009	Slew	0.287	0.057	...	...	...	2.884	0.782	10.633	...	...	...
0420−014	wp	0.915	1.001	1.862	0.357	0.114	5.687	1.002	1.087	...	0.277	0.90 ± 0.30
0426−380	1Jy	>1.030	0.576	0.136	...	...	...	0.262	0.210	2.20 ± 1.25	...	...
0438−436	wp	2.852	1.072	0.248	...	...	...	0.212	0.103	0.72 ± 0.39	...	...
0440−003	wp	0.844	1.322	0.349	...	...	...	0.108	0.109	...	0.461	0.80 ± 0.20
0451−282	wp	2.559	0.434	0.145	...	...	...	0.268	...	...	...	...
0454+844	1Jy	0.112	1.250	0.772	0.137	0.100	4.987	1.079	0.030	0.87 ± 0.59	...	...

continued on next page

TABLE 5.1: CONTINUED

IAU Name	sample	z	F_{5GHz} (Jy)	F_{230GHz} (Jy)	$F_{60\mu m}$ (Jy)	$F_{25\mu m}$ (Jy)	F_K (mJy)	F_V (mJy)	F_{1keV} (μJy)	α_X	F_{100MeV} (nJy)	α_γ
(1)	(2)	(3)	(4)	(5)	(6)	(7)	(8)	(9)	(10)	(11)	(12)	(13)
0454−463	wp	0.858	1.037	0.290	...	...	...	0.527	0.267	...	0.162	0.90 ± 0.40
0502+675	Slew	...	0.028	...	...	...	...	0.744	3.903	...	...	...
0507−040	Slew	0.304	0.022	...	...	...	...	0.101	2.306	...	...	...
0528+134	wp	2.060	0.930	1.308	...	...	...	0.375	0.951	0.54 ± 0.29	1.738	1.60 ± 0.10
0537−441	1Jy	0.896	2.110	2.291	0.495	0.215	8.841	1.626	0.800	1.04 ± 0.33	0.241	1.00 ± 0.20
0548−322	Slew	0.069	0.161	...	0.124	...	6.289	1.337	9.558	0.95 ± 0.05	...	...
0605−085	wp	0.870	1.547	0.751	...	...	...	0.546	0.325	...	...	...
0637−752	wp	0.651	3.048	1.456	0.200	0.130	8.500	3.096	2.854	0.45 ± 0.48	...	...
0716+714	1Jy	?0.3	0.933	0.936	0.165	...	7.670	2.395	1.346	1.77 ± 0.09	0.139	1.04 ± 0.33
0735+178	1Jy,Slew	>0.424	1.590	1.085	0.261	0.143	14.774	1.783	0.248	1.34 ± 0.51	0.368	2.52 ± 0.83
0736+017	wp	0.191	1.593	1.041	0.148	0.076	5.054	1.462	1.720	1.82 ± 0.60	...	...
0737+746	Slew	0.315	0.019	...	...	...	...	0.598	1.083	0.91	...	...
0814+425	1Jy	0.258	2.615	0.402	...	...	1.531	0.162	0.041	0.16 ± 0.78	...	...
0820+225	1Jy	0.951	0.846	0.133	...	...	0.381	0.070	0.052	1.05 ± 0.47	...	...
0823+033	1Jy	0.506	0.976	0.916	...	...	3.958	0.869	...	...	...	...
0828+493	1Jy	0.548	0.665	0.409	...	...	1.271	0.138	0.035	0.68 ± 0.63	...	...
0834−201	wp	2.752	0.669	0.211	...	...	...	0.152	0.113	...	...	...
0836+710	wp	2.170	0.578	0.241	...	...	...	1.938	0.819	0.42 ± 0.04	0.315	1.41 ± 0.18
0851+202	1Jy,Slew	0.306	2.173	2.394	0.791	0.336	22.177	2.639	1.063	1.50 ± 0.17	0.187	...
0859−140	wp	1.327	0.767	0.367	...	...	1.377	1.405	0.487	...	...	...
0906+430	wp	0.670	0.924	0.337	...	...	1.306	0.210	0.088	0.57 ± 0.10	0.275	...
0923+392	wp	0.699	4.067	1.123	...	...	1.905	0.569	0.712	1.26 ± 0.13	...	...
0927+500	Slew	0.188	0.016	...	...	...	...	0.433	1.905	...	...	...

continued on next page

TABLE 5.1: CONTINUED

IAU Name	sample	z	F_{5GHz} (Jy)	F_{230GHz} (Jy)	$F_{60\mu m}$ (Jy)	$F_{25\mu m}$ (Jy)	F_K (mJy)	F_V (mJy)	F_{1keV} (μJy)	α_X	F_{100MeV} (nJy)	α_γ
(1)	(2)	(3)	(4)	(5)	(6)	(7)	(8)	(9)	(10)	(11)	(12)	(13)
0950+445	Slew	? 0.207	0.003	...	...	...	0.016	0.113	0.294	1.76 ± 0.25	...	...
0954+556	wp	0.909	0.936	0.329	...	...	...	0.405	0.112	1.17 ± 0.14	0.020	0.63 ± 0.23
0954+658	1Jy	0.367	1.068	0.469	...	0.109	7.598	1.835	0.158	0.96 ± 1.31	0.064	0.85 ± 0.24
1011+496	Slew	0.200	0.247	...	...	...	3.927	1.526	2.351	1.49 ± 0.08	...	...
1028+511	Slew	0.239	0.037	...	...	...	...	0.743	2.802	1.44 ± 0.05	...	...
1055+018	wp	0.888	1.519	1.301	...	...	5.055	0.558	0.201	0.93 ± 0.44	...	...
1101+384	Slew	0.031	0.705	0.323	0.178	0.134	50.558	16.796	37.333	2.10 ± 0.08	0.054	0.58 ± 0.22
1101−232	Slew	0.186	0.058	...	...	...	2.804	0.601	10.252	...	...	...
1118+424	Slew	0.124	0.032	...	...	...	...	0.542	3.896	...	...	...
1127−145	wp	1.187	2.376	0.506	...	...	...	1.060	0.659	...	0.794	1.15 ± 0.36
1133+704	Slew	0.046	0.264	...	0.285	...	9.241	4.084	2.681	1.51 ± 0.10	...	...
1144−379	1Jy	1.048	1.118	0.946	0.295	0.116	8.986	0.926	0.663	1.67 ± 0.38	...	...
1147+245	1Jy	...	0.833	0.380	0.168	...	10.205	1.307	0.047	1.18 ± 0.79	...	...
1148−001	wp	1.982	0.459	0.011	...	...	...	0.732	...	...	...	...
1212+078	Slew	0.136	0.085	...	...	...	...	1.269	0.747	...	...	...
1215+303	Slew	0.237	0.375	...	...	0.158	12.181	2.899	0.591	1.88 ± 0.08	...	...
1218+304	Slew	0.130	0.051	...	...	...	4.352	1.337	10.324	1.22 ± 0.03	...	...
1219+285	Slew	0.102	0.908	0.159	...	...	11.124	3.047	0.409	1.24 ± 0.16	0.010	0.27 ± 0.39
1226+023	wp	0.158	35.419	10.665	2.204	0.893	88.981	29.834	12.074	0.89 ± 0.05	0.234	1.40 ± 0.10
1239+069	Slew	0.150	0.009	...	...	...	...	0.057	0.806	...	...	...
1248−296	Slew	0.370	0.004	...	...	...	...	0.096	2.376	...	...	...
1253−055	wp	0.536	8.557	7.080	0.240	0.290	6.041	2.073	1.246	0.83 ± 0.04	1.612	0.89 ± 0.06
1255+244	Slew	0.141	0.007	...	...	...	...	2.420	10.184	...	...	...

continued on next page

TABLE 5.1: CONTINUED

IAU Name	sample	z	F_{5GHz} (Jy)	F_{230GHz} (Jy)	$F_{60\mu m}$ (Jy)	$F_{25\mu m}$ (Jy)	F_K (mJy)	F_V (mJy)	F_{1keV} (μJy)	α_X	F_{100MeV} (nJy)	α_γ
(1)	(2)	(3)	(4)	(5)	(6)	(7)	(8)	(9)	(10)	(11)	(12)	(13)
1308+326	1Jy,Slew	0.997	0.761	0.525	0.425	0.206	7.857	1.818	0.134	1.04 ± 0.33	...	...
1320+084	Slew	...	0.010	...	...	...	...	0.114	5.016	...	...	...
1332−295	Slew	0.513	0.008	...	...	...	...	0.076	0.360	1.14 ± 0.21	...	...
1402+042	Slew	? 0.344	0.016	0.018	...	...	2.217	0.571	0.874	1.85 ± 0.17	...	...
1418+546	1Jy	0.152	0.946	0.917	0.217	0.108	12.737	1.970	0.306	1.14 ± 0.19	...	...
1421+582	Slew	...	0.006	...	...	...	...	0.142	1.342	...	...	...
1424−418	wp	1.522	0.940	0.495	...	...	8.651	1.050	...	...	5.50	1.6 ± 0.4
1440+122	Slew	0.162	0.037	...	...	...	...	0.482	1.617	...	...	...
1504−166	wp	0.876	0.874	0.267	...	...	...	0.337	0.203	...	...	...
1508−055	wp	1.185	0.880	0.153	...	...	1.333	0.795	...	...	...	...
1510−089	wp	0.361	2.063	1.942	...	...	5.173	1.276	0.718	0.90 ± 0.16	0.269	1.51 ± 0.36
1514−241	1Jy	0.049	1.907	1.084	0.233	0.167	23.579	5.474	0.607	...	...	...
1517+656	Slew	...	0.033	...	...	...	...	1.445	3.410	...	...	...
1519−273	1Jy	...	1.958	0.336	...	...	1.049	0.217	0.417	1.37 ± 1.78	...	...
1533+535	Slew	...	0.008	...	...	...	...	0.307	1.457	...	...	...
1538+149	1Jy	0.605	1.452	0.319	0.080	...	2.485	0.485	0.092	1.05 ± 0.90	...	...
1544+820	Slew	...	0.036	...	...	...	...	0.640	2.596	...	...	...
1553+113	Slew	0.360	0.497	...	0.208	0.099	24.440	6.978	7.656	...	...	...
1610−771	wp	1.710	1.073	0.298	...	...	...	0.535	...	...	...	...
1611+343	wp	1.404	0.854	0.469	...	...	0.978	0.553	0.194	0.76 ± 0.06	0.317	1.00 ± 0.20
1633+382	wp	1.814	0.763	0.461	...	...	1.606	0.401	0.258	0.53 ± 0.08	0.739	1.03 ± 0.09
1641+399	wp	0.594	4.266	2.927	0.724	0.281	7.825	1.135	0.914	0.85 ± 0.23	...	...
1652+398	1Jy,Slew	0.034	1.383	0.313	0.105	0.066	41.250	11.040	8.475	1.63 ± 0.05	... [b]	...

continued on next page

TABLE 5.1: CONTINUED

IAU Name	sample	z	F_{5GHz} (Jy)	F_{230GHz} (Jy)	$F_{60\mu m}$ (Jy)	$F_{25\mu m}$ (Jy)	F_K (mJy)	F_V (mJy)	F_{1keV} (μJy)	α_X	F_{100MeV} (nJy)	α_γ
(1)	(2)	(3)	(4)	(5)	(6)	(7)	(8)	(9)	(10)	(11)	(12)	(13)
1727+502	Slew	0.055	0.152	...	...	...	3.737	1.668	3.707	1.39 ± 0.08	...	...
1741+196	Slew	0.083	0.209	...	...	...	...	0.845	3.079	...	...	...
1741−038	wp	1.046	1.455	0.806	...	...	...	0.753	2.213	...	0.921	2.00 ± 0.40
1749+096	1Jy	0.322	1.384	1.646	0.214	0.078	5.031	1.200	0.129	0.45 ± 1.43	...	...
1749+701	1Jy	0.770	1.023	0.217	...	...	...	1.079	0.193	1.44 ± 0.71	...	...
1803+784	1Jy	0.684	1.556	0.674	0.307	0.143	7.511	0.683	0.324	1.42 ± 0.45	...	...
1807+698	1Jy,Slew	0.051	1.646	0.822	0.273	0.154	27.842	5.099	0.317	0.81 ± 0.30	...	...
1823+568	1Jy	0.664	0.998	0.559	...	...	4.117	0.198	0.241	0.44 ± 0.38	...	...
1853+671	Slew	0.212	0.010	...	...	...	...	1.046	0.801	...	...	...
1928+738	wp	0.360	2.239	0.622	...	...	...	1.308	1.295	1.33 ± 0.19	...	...
1954−388	wp	0.630	1.091	1.179	...	...	5.950	1.113	0.353	...	...	...
1959+650	Slew	0.048	0.242	...	...	...	...	17.220	9.801	...	...	...
2005−489	1Jy	0.071	1.148	0.515	0.260	0.237	30.090	12.651	5.333	1.94 ± 0.06	0.117	...
2007+777	1Jy	0.342	0.939	0.630	...	...	...	0.819	0.158	0.75 ± 0.56	...	...
2052−474	wp	1.489	0.770	0.293	...	...	...	0.135	0.433	...	0.296	1.40 ± 0.40
2106−413	wp	1.055	0.921	0.578	...	...	...	0.053	0.312	...	...	...
2128−123	wp	0.501	1.233	0.413	0.080	...	3.280	3.167	1.917	...	...	...
2131−021	1Jy	0.557	1.362	0.385	...	...	1.029	0.145	0.051	1.05 ± 0.46	...	...
2134+004	wp	1.936	3.020	0.331	...	...	1.353	1.268	0.214	0.82 ± 0.42	...	...
2145+067	wp	0.990	1.844	1.734	...	...	...	1.417	0.392	...	...	...
2155−304	Slew	0.117	0.284	0.241	0.088	0.096	37.697	18.269	45.583	1.34 ± 0.03	0.124	0.71 ± 0.24
2200+420	1Jy	0.069	4.462	1.959	0.467	0.239	37.519	5.527	0.936	1.92 ± 2.46	0.338	1.20 ± 0.30
2203−188	wp	0.618	2.290	0.210	...	...	0.546	0.184	...	...	...	...

continued on next page

TABLE 5.1: CONTINUED

IAU Name	sample	z	F_{5GHz} (Jy)	F_{230GHz} (Jy)	$F_{60\mu m}$ (Jy)	$F_{25\mu m}$ (Jy)	F_K (mJy)	F_V (mJy)	F_{1keV} (μJy)	α_X	F_{100MeV} (nJy)	α_γ
(1)	(2)	(3)	(4)	(5)	(6)	(7)	(8)	(9)	(10)	(11)	(12)	(13)
2223−052	wp	1.404	1.445	3.346	0.841	0.347	10.821	1.615	0.292	1.09 ± 0.23	...	...
2230+114	wp	1.037	1.463	0.898	0.192	...	2.338	0.701	0.486	...	0.437	1.60 ± 0.20
2240−260	1Jy	0.774	0.581	0.129	...	...	1.890	0.295	0.062	0.79 ± 0.40	...	...
2243−123	wp	0.630	1.298	0.776	...	...	0.837	1.997	0.963	...	...	...
2245−328	wp	2.268	0.397	0.097	...	...	...	0.329	...	...	...	...
2251+158	wp	0.859	3.912	4.057	0.188	0.115	10.285	1.407	1.082	0.62 ± 0.04	0.699	1.18 ± 0.08
2254+074	1Jy	0.190	0.975	0.249	0.155	...	4.966	0.619	0.105	1.89 ± 0.61	...	...
2321+419	Slew	0.059	0.018	...	...	...	...	0.441	0.732	...	...	...
2326−477	wp	1.302	0.856	0.415	...	...	...	1.290	0.245	...	...	...
2343−151	Slew	0.226	0.007	...	...	...	...	0.073	0.853	...	...	...
2345−167	wp	0.576	2.032	0.916	0.093	...	1.156	0.314	0.216	...	...	...

Notes to Table 5.1

(a) (1) IAU name; (2) sample; (3) redshift; (4) flux @5 GHz; (5) flux @230 GHz; (6) flux @60 μm; (7) flux @25 μm; (8) flux @2.19 μm (K–band); (9) flux @5500 Å(V–band); (10) flux @1 keV; (11) X–ray spectral index; (12) flux @100 MeV; (13) γ–ray spectral index; For fluxes we report the average K–corrected values.

(b) source detected only by Whipple. The given value is the integrated flux measured at E > 300 GeV, in units of 10^{-11} photons cm^{-2} s^{-1}.

References for Table 5.1:

References for the data here reported are listed in the Notes to Table 5.5.

TABLE 5.2: BASIC DATA FOR 30 ADDITIONAL γ–RAY DETECTED SOURCES[a]

(1) IAU name	(2) z	(3) F_{5GHz} (Jy)	(4) F_{100MeV} (nJy)	(5) α_γ
0130−171	1.022	1.00	0.122	...
0202+149	1.202	2.40	0.383	1.5 ± 0.1
0234+285	1.213	2.36	0.296	1.7 ± 0.3
0446+112	1.207	1.22	0.470	0.8 ± 0.3
0454−234	1.009	2.2	0.143	...
0458−020	2.286	2.04	0.364	...
0506−612	1.093	2.1	0.062	...
0521−365	0.055	9.7	0.139	1.16 ± 0.36
0804+499	1.433	2.05	0.322	1.72 ± 0.38
0805−077	1.837	1.04	0.404	1.4 ± 0.6
0827+243	0.939	0.67	0.226	1.21 ± 0.47
0829+046	0.18	1.65	0.132	...
0917+449	2.18	1.03	0.075	0.98 ± 0.25
1156+295	0.729	1.65	1.727	1.21 ± 0.52
1222+216	0.435	0.81	0.278	1.50 ± 0.21
1229−021	1.045	1.1	0.250	1.92 ± 0.44
1313−333	1.210	1.47	0.098	0.8 ± 0.3
1317+520	1.060	0.66	0.079	...
1331+170	2.084	0.713	0.091	...
1406−076	1.494	1.08	1.013	1.03 ± 0.12
1604+159	0.357	0.50	0.260	0.99 ± 0.50
1606+106	1.227	1.78	0.312	1.20 ± 0.30
1622−297	0.815	1.92	2.416	1.2 ± 0.1
1622−253	0.786	2.2	0.336	1.3 ± 0.2
1730−130	0.902	6.9	0.258	1.39 ± 0.27
1739+522	1.375	1.98	0.236	1.23 ± 0.38
1933−400	0.966	1.48	0.158	1.4 ± 0.2
2032+107	0.601	0.77	0.192	1.5 ± 0.3
2344+514	0.044	0.215	0.8[b]	...
2356+196	1.066	0.70	0.311	...

Notes to Table 5.2

(a) included in our samples : (1): IAU name; (2): redshift; (3): radio flux at 5 GHz; (4): γ–ray flux at 100 MeV; (5): EGRET spectral index

(b) source detected only by Whipple. The given value is the integrated flux measured at E > 300 GeV, in units of 10^{-11} photons cm^{-2} s^{-1}.

References for Table 5.2:

References for the data here reported are listed in the Notes to Table 5.5.

CHAPTER 6

PHYSICAL MODELING

After the observational results derived in Chapter 5, we consider models to explore the regularities in the SED properties directly dealing with physical parameters. The goal is to determine trends and correlations among *physical quantities* which can shed light on the relationship among different sub–classes of blazars and ultimately on the processes at work in these objects.

Here we examine two of the leading pictures, namely the pure SSC and the ERC models, applying them to all sources with sufficient available data to constrain the models parameters.

Through a search in the literature the multiwavelength overall spectra of 51 γ–loud blazars have been assembled. Even if the vast majority of the data are not simultaneous and the sample is not complete in any respect, they provide a useful template of the SED of different classes of γ–loud blazars. While the non–simultaneity of the data (except for a few sources) precludes from deriving strong conclusions about specific objects, their large number allows us to study trends in the physical parameters of the models and possible correlations among them and with the observed spectral characteristics of different sub–classes of blazars.

6.1 The sample

We considered all blazars for which sufficient information could be found so that the location of both the synchrotron and inverse Compton peaks and the luminosity of each source could be estimated. In this view two pieces of information are essential:

① either detection *and* estimate of the γ–ray spectral slope in the EGRET band *or* detection by the Whipple telescope;

② measured (or lower limit on) redshift.

The resulting 51 sources are listed in Table 6.1 (all Tables are at the end of the Chapter), together with their redshift, classification and the list of references relative to the data plotted in Fig. 6.1a–f. The sample includes 14 BL Lac objects and 37 FSRQ. According to the adopted definition for HBL/LBL (see § 1.2.2), there are 10 LBL and 4 HBL. Among FSRQs, 16 are HPQ (highly polarized: optical polarization >3 per cent), 16 are LPQ (lowly polarized), while for the remaining 5, labelled NP, polarization measurements were not found.

Note that in our list there are the two sources detected by ground based Cherenkov telescope (Whipple, and HEGRA) in the TeV band, but not by EGRET in the GeV band: the two HBL objects Mkn 501 (1652+398) (Quinn et al. 1996) and 1ES 2344+514 (Catanese et al. 1998).

In Fig. 6.1a–f, the overall SEDs of all the blazars listed in Table 6.1 are plotted. Frequencies and luminosities are in the rest frame of the source. Fluxes have been de-reddened using the absorption values A_V reported in the NED database.

6.2 The models

6.2.1 General assumptions

The emitting region is assumed to be a sphere, with a homogeneous and tangled magnetic field. Throughout the source relativistic electrons are continuously injected at a rate $Q'(\gamma)$ [cm^{-3} s^{-1}], corresponding to a luminosity $L'_{\rm inj}$ and a compactness

$$\ell'_{\rm inj} \equiv \frac{L'_{\rm inj}\,\sigma_{\rm T}}{R\,m_{\rm e}c^3} \tag{6.1}$$

This power is assumed to be entirely converted into radiation. The injected particles are distributed in energy as a power–law of slope s [$Q'(\gamma) = Q'_0\,\gamma^{-s}$], between $\gamma_{\rm min}$ and $\gamma_{\rm max}$.

For simplicity we always assume $\theta_{\rm obs} \sim 1/\Gamma$, resulting in $\delta \sim \Gamma$. In the following to distinguish quantities measured in the blob comoving frame and in the observer frame we adopt the same convention used in Chapter 2: primed variables for values in the blob frame, e.g. frequency, luminosity, energy density, compactness, with the exception of electron energy/Lorentz factors and magnetic field.

We consider a *stationary situation*, that is we determine the particle equilibrium distribution and the spectrum of the emitted radiation self–consistently, assuming that the timescale over which the particles reach equilibrium is shorter than the injection one. We *neglect particle escape* and *adiabatic expansion*.

6.2.2 The particle distribution

The equilibrium particle distribution $N(\gamma)$ (cm^{-3}) is determined by the stationary solution of the continuity equation:

$$N'(\gamma) \;=\; \frac{\int_{\gamma}^{\gamma_{\rm max}} (Q'(\gamma) + P'(\gamma))\, d\gamma}{\dot{\gamma}} \tag{6.2}$$

where $P'(\gamma)$ is the rate of electron–positron pair production. The only important mechanism for pair production is photon–photon collisions, the rate of which is calculated according to the prescriptions given in e.g. Ghisellini (1989).

Electron cooling

$\dot{\gamma}$ takes into account the following cooling mechanisms (see § 2):

synchrotron emission

inverse Compton emission

Klein–Nishina

Since the radiation spectrum extends to high energies, the scattering process has to be calculated by means of the Klein–Nishina cross section. For simplicity, we approximate it with a step function equal to the Thomson cross section for frequencies $x \equiv h\nu/(m_{\rm e}c^2) \leq (3/4)/\gamma$, and zero otherwise. This implies that the radiation energy density effectively involved in the inverse Compton cooling depends on the electron energy

$$U'_{\rm rad}(\gamma) \;=\; m_{\rm e}c^2 \int_0^{3/(4\gamma)} U'(x)\, dx \tag{6.3}$$

The continuity equation is solved numerically, with an iterative approach, as described in Ghisellini (1989). The numerical treatment is necessary because of the high non–linearity of the processes involved: $N'(\gamma)$ depends on the radiation spectrum (because of the inverse Compton cooling term and the pair production rate), which in turn is determined by $N'(\gamma)$.

Steady state electron spectrum

When the Klein–Nishina and pair production effects can be neglected, the solution of equation 6.2 is trivial. These are the different cases, depending on the slope s of the injected electron spectrum:

$s > 2$ it is a broken power law: $N'(\gamma) \propto \gamma^{-2}$ up to $\gamma_{\rm min}$ and $N'(\gamma) \propto \gamma^{-s-1}$ above. In this case $\gamma_{\rm min}$ can be identified with the crucial parameter $\gamma_{\rm peak}$, i.e. the Lorentz factor of the electrons emitting at the peaks of the synchrotron and inverse Compton components;

$1 < s < 2$ we have the same solutions for $N'(\gamma)$, but in this case $\gamma_{\rm min} < \gamma_{\rm peak} < \gamma_{\rm max}$, since the spectral index of the radiation emitted by particles above $\gamma_{\rm min}$ is flatter than unity;

$s < 1$ the lower limit of the integral in equation 6.2 becomes unimportant, yielding $N'(\gamma) \propto \gamma^{-2}$ in the entire energy range, except for γ close to $\gamma_{\rm max}$.

Note that the assumption of constant radius and no escape tends to overestimate the particle distribution at the lowest energies, where these effects are potentially more important than radiative cooling (if the overall compactness is much less than unity). This has no effect on the synchrotron spectrum, which is self–absorbed at low frequencies, and has no effect on the observable SSC spectrum, mainly made by high energy electrons. In the case of the ERC model, instead, the X–ray spectrum is made by the sum of the ERC and SSC components, and therefore the X-ray flux and spectrum can depend on the details of the low energy particle distribution if the ERC component dominates. Then in these cases the calculated X–ray spectrum could be flatter than what derived here.

6.2.3 Target photons

The radiation energy density, $U'_{\rm rad}(\gamma)$, in the emitting blob includes the contribution from the radiation both produced internally (by synchrotron, self–Compton emission and ERC emission) and externally to the blob:

$$U'_{\rm rad} = U'_{\rm sync} + U'_{\rm ext} + U'_{\rm SSC} + U'_{\rm ERC} \simeq U'_{\rm sync} + U'_{\rm ext} \qquad (6.4)$$

The approximate equality with the rightmost term is based on the fact that in the hypothesized conditions second order Compton scattering is not important. The external photon field is again assumed to be distributed as a (diluted) blackbody, peaking at a frequency $x_{\rm ext} \equiv h\nu_{\rm ext}/(m_{\rm e}c^2)$ between 5×10^{-5} and 2×10^{-4}, in the rest frame of

the blob, corresponding to $\lambda \simeq 1200 - 5000$ Å for $\delta = 10$. The exact value depends on the radiation mechanism responsible for the external field and the bulk Lorentz factor of the blob. The assumption of a blackbody spectral distribution is merely for ease of calculation. For instance, in the case of external radiation dominated by the broad emission line photons, an observer in the comoving frame of the blob would see a complex spectrum, not isotropic (blueshifted in the forward direction and redshifted in the opposite one): even a single, monochromatic line would be transformed into a peaked, but extended, spectrum.

Consequently, a peaked distribution can approximate the case of externally produced photons distributed in lines, independently of the origin of the photoionizing continuum. On the other hand, this assumption can mimic the effect of an external scattering medium only if the illuminating continuum is narrowly distributed in frequency (e.g. radiation produced by an accretion disk), but it is not satisfactory for a scattering medium illuminated by the jet (which produces a more extended spectrum).

For a direct comparison with the value of the compactness in injected electrons, $\ell'_{\rm inj}$, we assume that also the external radiation can be characterized by an "effective compactness" $\ell'_{\rm ext}$, defined as:

$$\ell'_{\rm ext} = \frac{\sigma_{\rm T}\, R\, U'_{\rm ext}}{m_{\rm e} c^2} \tag{6.5}$$

where $U'_{\rm ext}$ is therefore amplified by a factor Γ^2 with respect to the same quantity measured in the frame of the observer (§ 2.2).

As already mentioned, this external field is not isotropic in the comoving frame (see Dermer 1995). However both for simplicity and because of the uncertainty in the origin and therefore in the angular distribution of the external radiation, we assume an isotropic pattern for $\ell'_{\rm ext}$ (in the comoving frame). With this approximation also the inverse Compton radiation is isotropically distributed in this frame, and subject to the same Lorentz transformation as the synchrotron and self–Compton emission.

The uncertainty related to the latter assumption can be estimated comparing the two extreme cases of the Compton flux emitted assuming (in the comoving frame) an isotropic seed photon distribution and the case of soft photons distributed only along the jet axis. Assume for simplicity that in both cases the seed photons are monochromatic, at the frequency ν_0. The total power emitted by an electron of energy $\gamma_{\rm e}\, m_{\rm e} c^2$ is:

$$P' = \sigma_{\rm T}\, c\, U'_{\rm rad} \left[\gamma_{\rm e}^2 \int (1 - \beta_{\rm e} \cos\phi)^2 \frac{d\Omega}{4\pi} - 1 \right]$$

(see e.g. Rybicki and Lightman 1979), where ϕ is the angle between the incoming photon and the electron velocity vector and $U'_{\rm rad}$ is the energy density of the seed photons. The viewing angle $\phi = 1/\Gamma$ corresponds in the blob frame to the aberrated angle $\phi' = 90°$: at this angle, the power received in the isotropic case is $P'_{\rm iso} \simeq \frac{4}{3}\gamma_{\rm e}^2\sigma_{\rm T}\, c\, U'_{\rm rad}$, while the power received in the monodirectional case ($\phi' = 90°$)[1] is $P'_{\rm mono} \simeq \frac{1}{2}\gamma_{\rm e}^2\sigma_{\rm T}\, c\, U'_{\rm rad}$. The ratio $P'_{\rm mono}/P'_{\rm iso}$ for large $\gamma_{\rm e}$ is therefore equal to 3/8. The corresponding ratio between the scattered frequencies is equal to 3/2.

6.2.4 Observational constraints

We require that the model parameters, besides giving a good description of the broad band SED, also satisfy additional constraints.

① The minimum variability timescale must be as short as a day, or a fraction of a day, as commonly observed for the optical–UV and γ–ray emission of blazars (e.g. Ulrich et al. 1997). This corresponds to demand:

$$R \lesssim 2.6 \cdot 10^{16} \left(\frac{t_{\rm var}}{1\ {\rm day}}\right) \frac{\delta_1}{1+z} \quad [{\rm cm}] \tag{6.6}$$

② The Doppler factor is constrained not to exceed a value of 20–25, to be consistent with the observed superluminal speeds (e.g. Vermeulen and Cohen 1994).

③ A third requirement, which is not imposed a priori but has to be satisfied in all cases, concerns the amount of pair production. As discussed in Ghisellini and Madau (1996), the γ–ray emitting region *must* be *thin* to the high energy radiation, otherwise it inevitably leads to overproduction of X–rays. Since the importance of the pair production process is measured by the compactness, the transparency requirement translates into an upper limit to the allowed values of $\ell'_{\rm inj} \lesssim 1$ (see Dondi and Ghisellini 1995).

Summarizing, for the *pure SSC* model 7 input parameters are required, namely:

$$R, \quad B, \quad \Gamma, \quad \ell'_{\rm inj}, \quad s, \quad \gamma_{\rm min}, \quad \gamma_{\rm max}$$

If the inverse Compton scattering on external photons is included, two more parameters are required $\ell'_{\rm ext}$ and $x_{\rm ext}$ (i.e. a total of 9).

[1] the value of the angle between electron and photon, in the blob frame which is relevant for this geometry is 90°. In fact, the observer at $\theta \simeq 1/\Gamma$ is receiving the radiation emitted by electrons which are moving/emitting at 90° with respect to the direction of motion of the blob, and then with respect of the direction from which are coming the aberrated external photons.

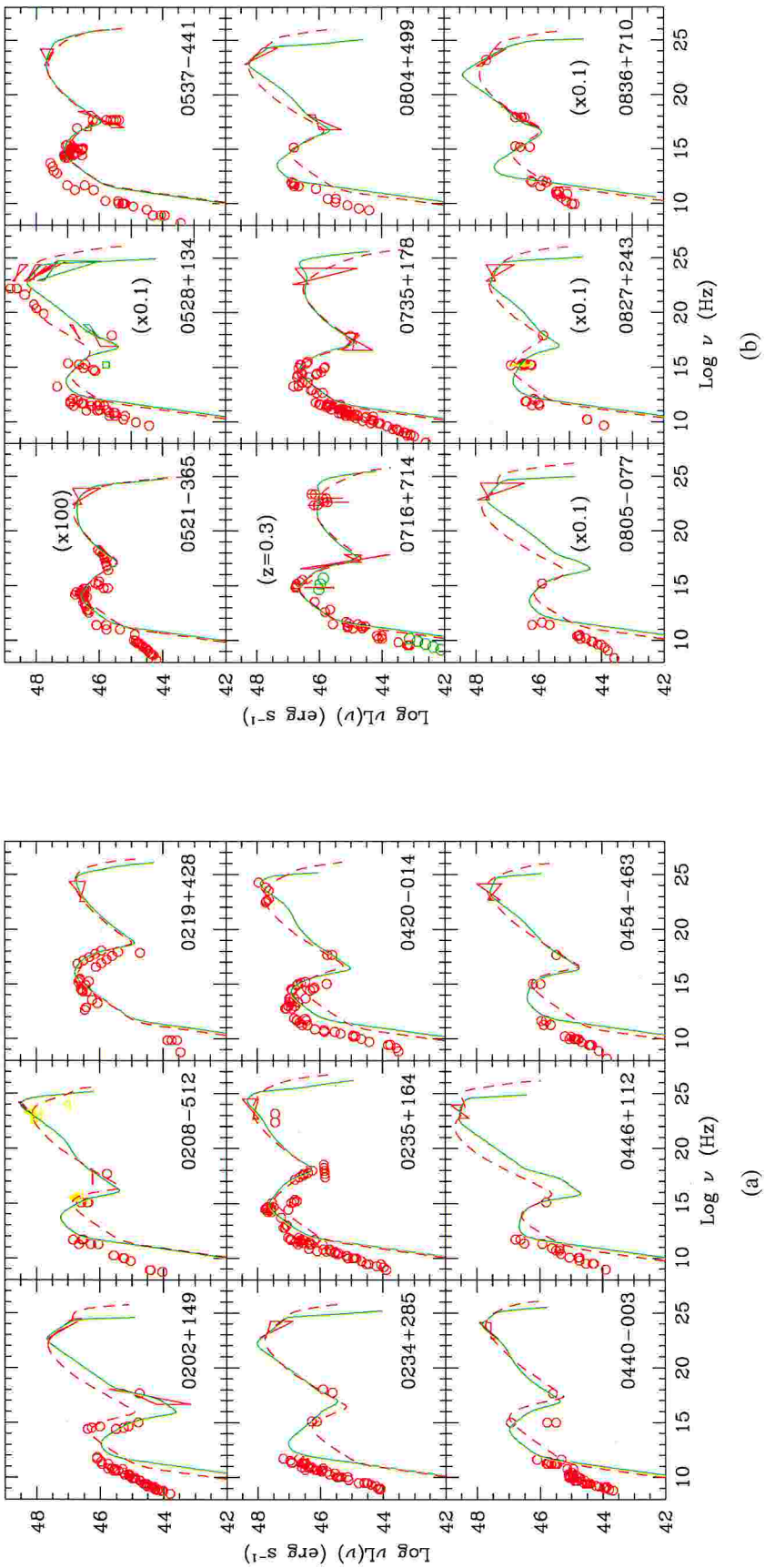

Figure 6.1: (a,b): Spectral energy distributions (in νL_ν) of the 51 γ−ray loud sources. The broad band spectra have been assembled from data in the literature (the complete list of references is given in Table 6.1). In parenthesis the rescaling factors used for graphical purpose are indicated. SED from the SSC and ERC models are superposed to the data, as dashed (red) and solid (green) line, respectively. The model parameters are reported in Table 6.2.

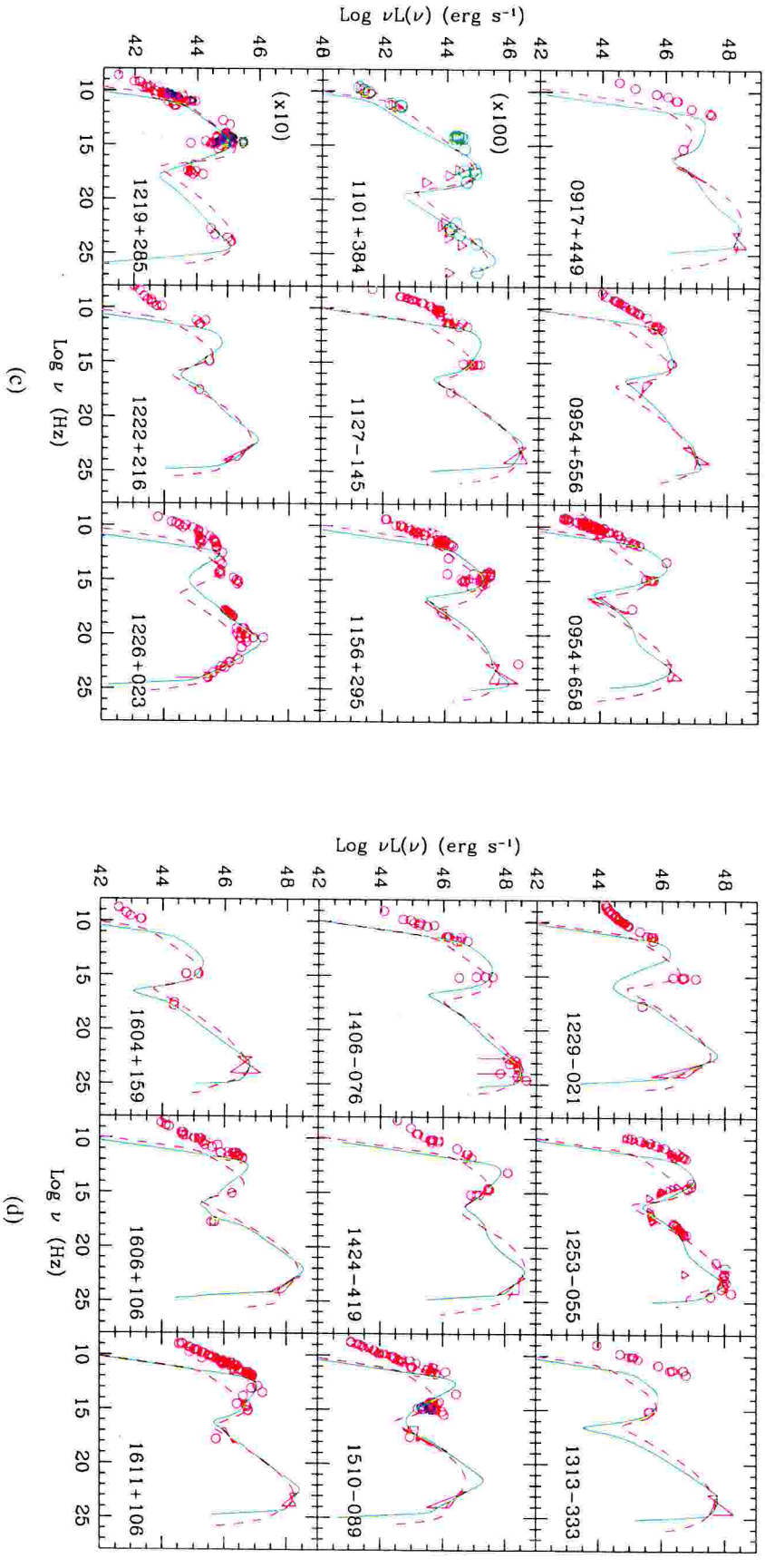

Figure 6.1: (c,d): same as Fig. 6.1a

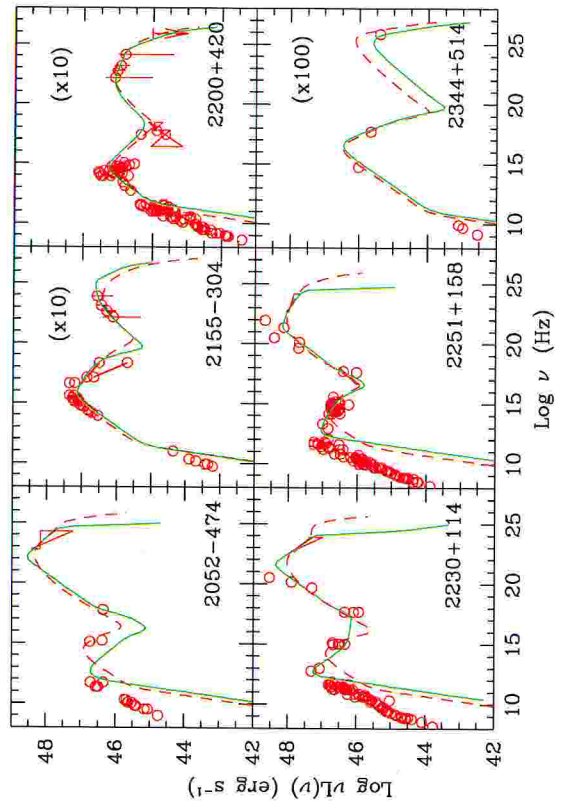

(f)

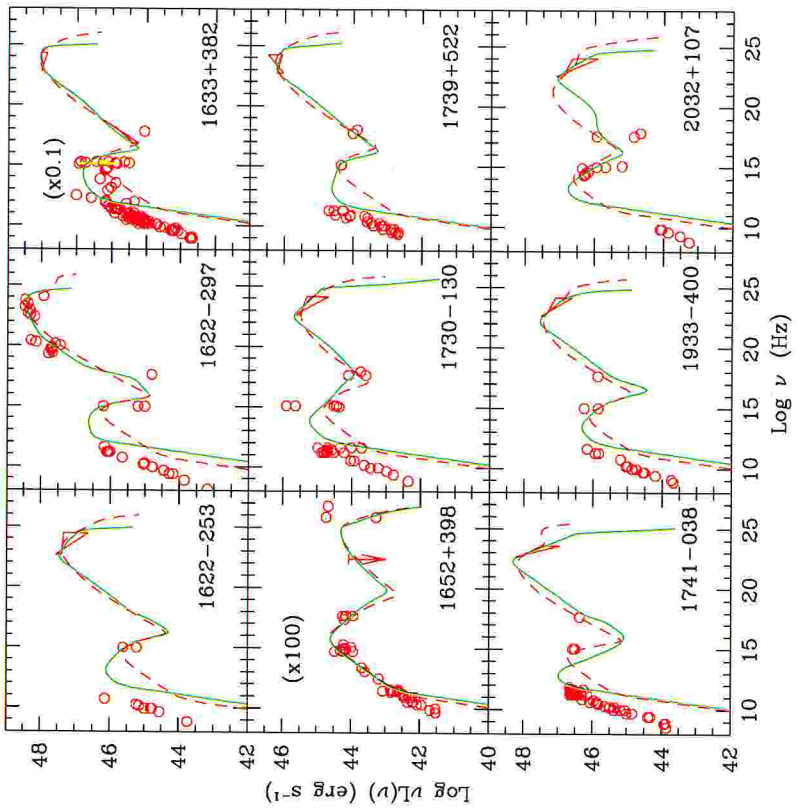

(e)

Figure 6.1: (e,f): same as Fig. 6.1a

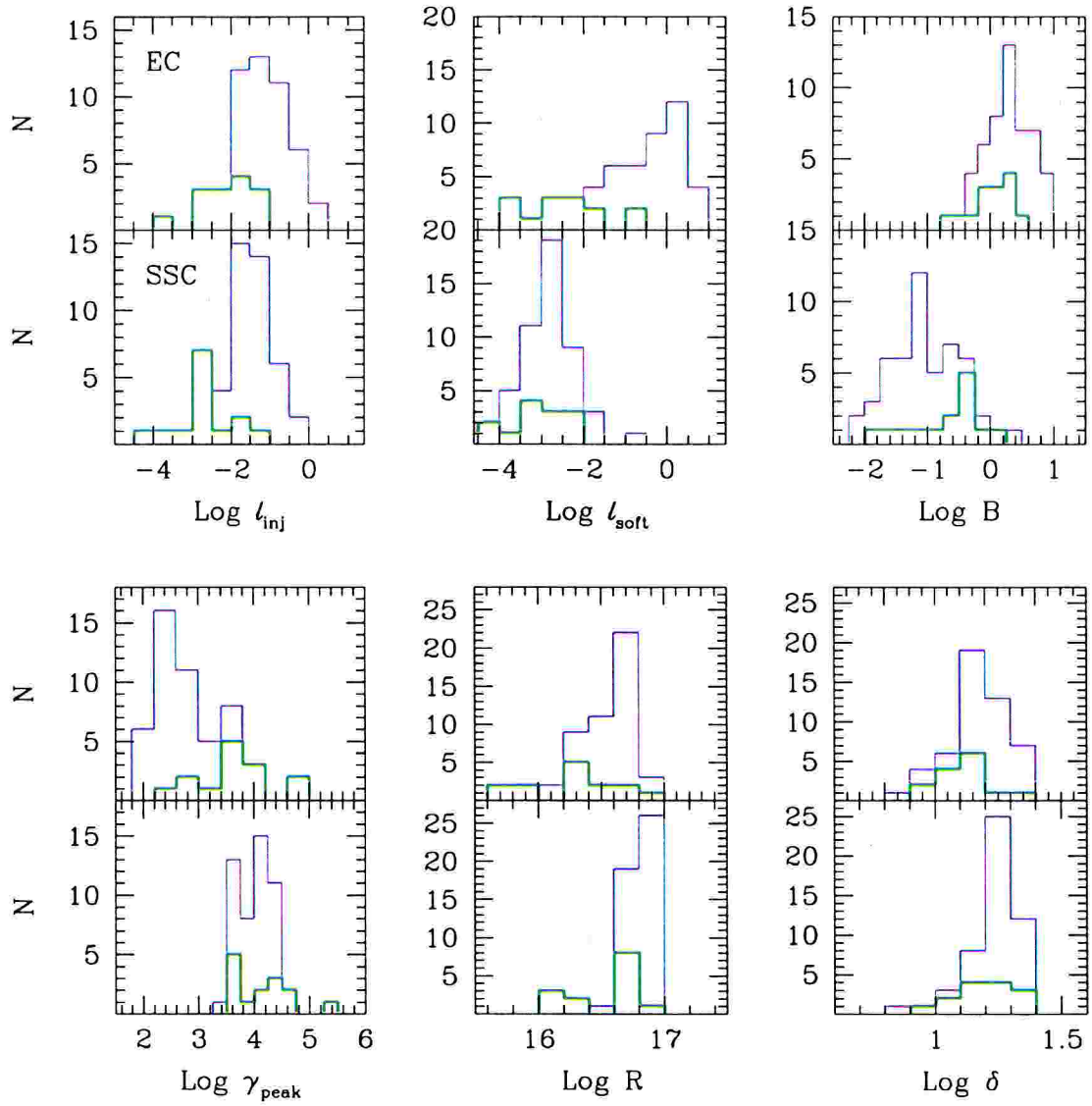

Figure 6.2: The histograms show the distributions of the parameters of the fits for the ERC (upper panels) and the SSC (lower panels) models for all sources. Green lines represent BL Lac objects. Please note that all the quantities refer to the blob comoving frame even though compactnesses are not primed. $\ell_{\rm soft} \equiv \ell_{\rm ext}$ in the case of the ERC model and $\ell_{\rm soft} \equiv \ell_{\rm sync}$ (compactness of the synchrotron radiation) in the case of the SSC model

However, if the slope of the injected electron distribution is steep ($s > 2$), which is the case for most sources, the exact value of $\gamma_{\rm max}$ becomes energetically unimportant and is practically irrelevant in the comparison with spectral data. Furthermore, if the external radiation is constituted of broad line photons, the value of $x_{\rm ext}$ is constrained in a very narrow energy range.

In conclusion, even if there are formally nine free input parameters, $\gamma_{\rm max}$ is relatively unimportant, $x_{\rm ext}$ is tightly limited and constraints apply to the possible values of R, δ and $\ell'_{\rm inj}$.

6.2.5 Uniqueness of fits

Given the number of free parameters, a key question concerns the uniqueness of the "fits".

From an observational point of view, we have already mentioned (§ 2)the most critical quantities, which determine the global spectral shape, namely the energy and luminosity of the two spectral peaks, ν_S, ν_C, L_S, L_C. Furthermore, the optical–to–X–rays and the X–ray–to–γ–ray spectral indices and the three limits discussed above (on R, δ, ℓ'_{inj}) also constrain the parameters.

SSC

In particular , as shown in Chapter 2 (and e.g. Ghisellini et al. 1996), in the SSC scenario all the parameters are strongly constrained by the frequencies of the synchrotron and the self–Compton peaks, and by the corresponding powers. These allow to uniquely determine B, δ and ℓ'_{inj}. R and ℓ'_{inj} have then to satisfy the above constraints.

ERC

In the ERC scenario, the further free parameter ℓ'_{ext} could be in principle be constrained by the observed soft photon component (e.g. emission line intensities). Although we choose not to assume a priori the origin of the external soft photon field, however this should at least contain the contribution of photons produced in the broad line region. The addition of ℓ'_{ext} as a free parameter makes the choice of δ not unique.

Independently of our assumption of selecting values of δ consistent with the observed superluminal speeds, one might therefore examine the consequences of allowing arbitrary values of δ. In principle, one can obtain good fits with, e.g. $\delta \simeq 100$ and small values of ℓ'_{inj} ($\propto \delta^{-4}$). But since $\ell'_{ext} \propto \Gamma^2 \simeq \delta^2$, the external photons become important as targets in collisions with very high energy γ–rays, with the result of overproducing X–rays. Assuming instead a small value of ℓ'_{ext} corresponds to limit the broad line radiation to an implausibly small contribution. We therefore conclude that also the ERC model is well constrained.

The main source of uncertainty on the model parameters is given by the incomplete and poor spectral coverage of several sources, which does not allow to determine with accuracy the observational constraints, most critically the peak of the synchrotron emission. Another source of uncertainty regards the presence of other spectral components. Our single–zone and homogeneous models cannot reproduce the spectrum at frequencies below the far IR, since at these frequencies the model spectrum is self–absorbed. Other emitting regions, of greater dimensions, are necessary to fit the radio band. If these also emit in the IR and optical bands, they could contribute to the synchrotron spectrum, possibly shifting its peak at a frequency different from the one corresponding to the γ–ray emitting region.

fit procedure

As far as the actual fitting procedure is concerned, it should be pointed out that we try to reproduce collections of data that rarely are simultaneous, for sources whose variability is a defining property. Note also that the spectral coverage differs widely from object to object. On the one hand this makes it difficult to determine a method to estimate the goodness of "fit" other than the visual inspection (with all its limits). On the other hand, as mentioned in the introduction, the main goal of our study is not to model specific blazars, but to unveil possible trends using a large number of sources. In this sense, although the model parameters relative to a specific source are not 'objectively' found (as it would be for a best fit determined through a statistical χ^2 test) nevertheless they represent a reasonable description of the spectral properties of each of the blazar in the sample.

6.3 Results

The spectral distributions derived from the SSC and ERC models which better describe the SEDs are superposed to the data in Fig. 6.1a–f. On the basis of these "fits" *both* models can be acceptable for basically all sources. The input parameters for all the fits are reported in Table 6.2.

6.3.1 ERC *vs.* SSC

magnetic field

The most remarkable difference between the two sets of parameters (SSC *vs.* ERC) is the relatively smaller value of the magnetic field in the SSC model. This has to be expected, since in order to reproduce the large ratios of inverse Compton to synchrotron luminosities, the SSC model requires a small magnetic energy density, while this constraint is relaxed in the ERC scenario (see also § 2.5.3).

Although at first sight it seems difficult to discriminate between the two models, at least for FSRQ the parameters derived in the SSC scenario argue in favour of the ERC model. In fact, let us consider the typical quantities required by the SSC model: $\delta \simeq 20$, $\ell'_{\rm inj} \simeq 0.03$, $B \simeq 0.05$ G, $R \simeq 10^{17}$ cm. These imply a compactness in synchrotron radiation $\ell'_{\rm sync} \simeq 3 \times 10^{-3}$. Inverse Compton scattering on broad line photons is unimportant if the external radiation energy density $U'_{\rm ext}$ is less than the synchrotron one, i.e.:

$$\mathrm{L_{ext}} < \frac{1}{\delta^2} \frac{m_{\rm e} c^3 \, \ell'_{\rm sync}}{\sigma_{\rm T} R} R^2_{\rm ext} \simeq 3 \times 10^{42} \, R^2_{\rm ext,18} \quad [\mathrm{erg\ s^{-1}}] \tag{6.7}$$

where the above typical parameters have been used. This limit on $\mathrm{L_{ext}}$ is certainly not observationally satisfied in FSRQ for which certainly there is a contribution from the

emission of the BLR, and for instance, easily $L_{MgII} \gtrsim 10^{43}$erg s^{-1} (e.g. Celotti et al. 1997; Scarpa and Falomo 1997). For BL Lacs the situation is ambiguous. While the absence of observable emission lines in most BL Lacs suggests that the SSC process can dominate on the ERC one, (weak) broad emission lines have been occasionally observed in some LBL (e.g. BL Lac itself, Vermeulen et al. 1995; OJ 287 Sitko and Junkkarinen 1985; PKS 0537–441, Stickel et al. 1993; Scarpa and Falomo 1997), sometimes exceeding the above limit. And indeed in some cases the inclusion of an external radiation component yields a "better" broad band fit.

Therefore in the following the discussion is *focused on the results of the ERC scenario*. For HBL the different parameters derived in the SSC and ERC models can be considered an indication of the allowed range of values and, in particular, the external radiation (e.g. emission line luminosity) required by the ERC fit can be taken as an upper limit.

Parameters distributions

BL Lac vs. FSRQ

Fig. 6.2 shows the distributions of values of the model parameters for the ERC (upper panels) and the SSC (lower panels) models. The thick solid lines correspond to the results for BL Lacs. In the ERC case, BL Lac objects almost always form the left tail of the distributions, being characterized by smaller compactness, magnetic field and slightly smaller degree of beaming. On the contrary, comparable dimensions R and greater value of γ_{peak} are required by the ERC fits of BL Lacs with respect to FSRQ. In the SSC case the required γ_{peak} is limited in a narrow range, without a clear distinction between BL Lacs and FSRQ, while BL Lacs are characterized by a larger average value of the magnetic field.

As a consequence of the constraints imposed on the Doppler factor and the variability timescales, the distributions of δ and R span less than one order of magnitude each, with $R \simeq 10^{16} - 10^{17}$ cm. On the contrary the other (intrinsic) quantities are spread over much larger ranges of values, with the external photon compactness covering the wider interval of about 5 decades. Note that given the high values of the Doppler factors derived from the fits, the assumption $\theta \simeq 1/\Gamma$ is satisfied. The only exception is 0521–365, which only requires $\delta \simeq 1.4$.

electron distribution

The injected particle energy distribution is highly different from source to sources (see Table 6.2), in shape, compactness and (rather low) maximum energy $\gamma_{max} m_e c^2$, thus not requiring a very finely tuned injection/acceleration mechanism.

6.3.2 Correlations

The most interesting quantities to investigate links among adopted and derived model parameters is the Lorentz factor at the break of the electron distribution $\gamma_{\rm peak}$, which largely determines the shape of the SED.

The other important parameters controlling the SED are the Compton dominance L_C/L_S, the power (or the corresponding compactness $\ell'_{\rm inj}$) injected in the form of electrons (which in our model corresponds to the radiated power), and the power in the external photon component, $\ell'_{\rm ext}$. The results of linear correlations involving these quantities are shown in Figs. 6.3a,b, and 6.4, and their statistical significance is reported in Table 6.3.

Let us consider the results of the correlations:

$\gamma_{\rm peak}$ Strong correlations are present between $\gamma_{\rm peak}$ and $\ell'_{\rm ext}$, $\ell'_{\rm inj}$ and the energy densities in radiation $U'_{\rm rad}$ and magnetic field $U'_{\rm B}$, both for the whole sample and for the FSRQ sub–sample. In particular, a very strong linear correlation is found between $\gamma_{\rm peak}$ and the total energy density, with a dependence $\gamma_{\rm peak} \propto (U'_{\rm rad} + U'_{\rm B})^{-0.6}$. The same trend appears from the correlation of $\gamma_{\rm peak}$ with $\ell'_{\rm ext} + \ell'_{\rm inj}$. It should be pointed out that these correlations are not, or at most only partly, induced by an observational selection effect: there would not be bias against detecting sources with either high values of $\gamma_{\rm peak}$ and $(U'_{\rm rad} + U'_{\rm B})$ or viceversa. Furthermore the significance of the correlations (i.e. their small spread) can be taken as a posteriori indication of the tightness of the observational constraints imposed on the model parameters. Note that HBL, LBL and quasars are located along a sequence.

L_C/L_S The Compton dominance correlates with $\gamma_{\rm peak}$, $\ell'_{\rm ext}$, $\ell'_{\rm inj}$, and $\nu^{\rm obs}_{\rm peak}$, the latter being the *observed* peak frequency of the modeled synchrotron emission. It also correlates with the observed (beamed) power $L^{\rm obs}_{\rm inj} = \delta^4 L'_{\rm inj}$, while only a marginal correlation exists between L_C/L_S and the magnetic field intensity. The statistical significance of all these correlations is higher when considering the entire blazar sample, while weakens when the subsamples of BL Lacs and FSRQ are considered separately. Again, note that in all cases BL Lacs are "separated" from FSRQ, with HBL at the extremes and some LBL smoothly overlapping with FSRQ.

$\ell'_{\rm ext} - \ell'_{\rm inj}$ A significant linear correlation is present when FSRQ are considered, while (most) BL Lacs show a relative deficiency in the external photon component with respect to this trend (see Fig. 6.4).

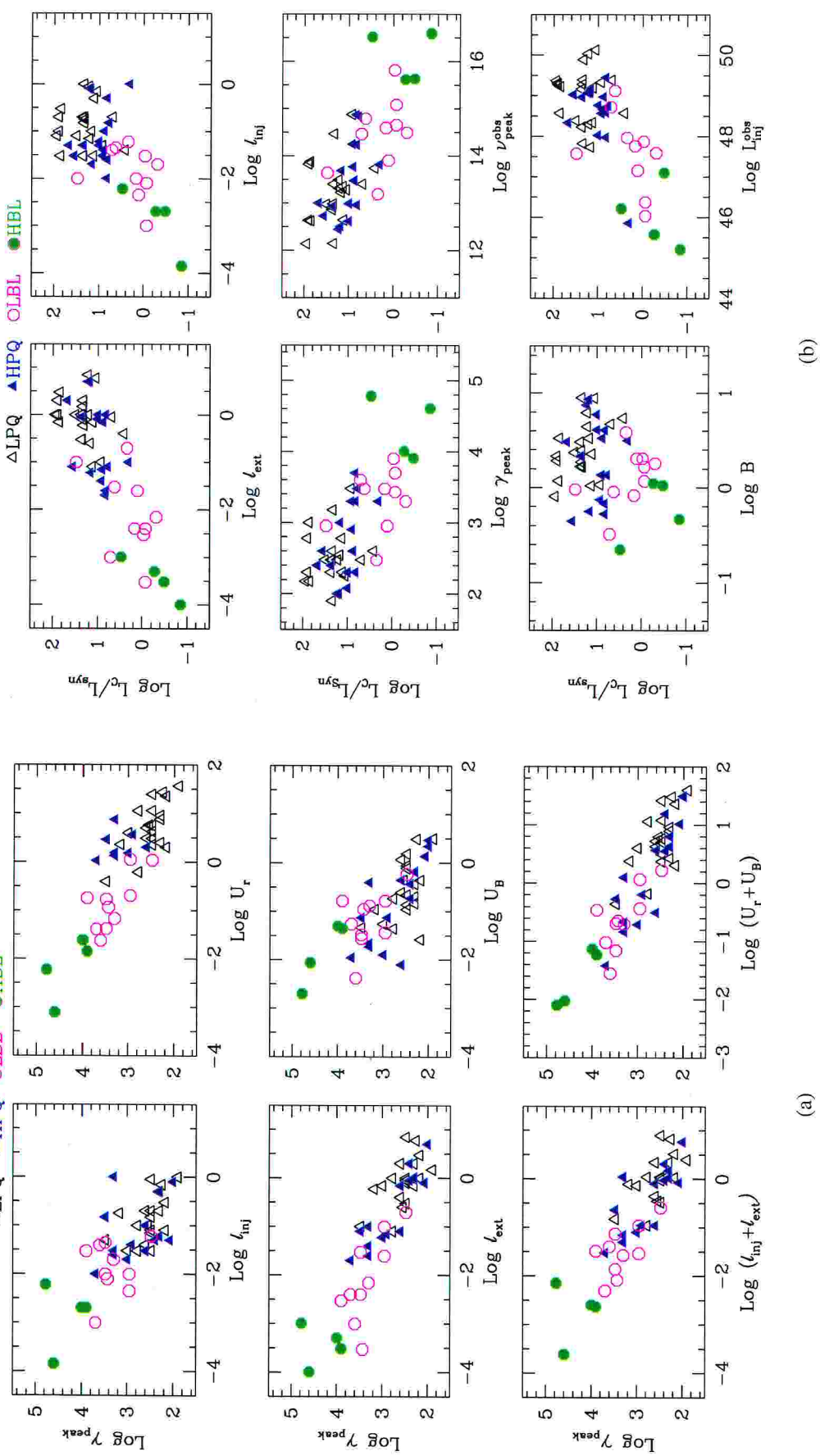

Figure 6.3: (a) $\gamma_{\rm peak}$ and (b) the Compton dominance $L_{\rm C}/L_{\rm S}$, as derived from the ERC model, are plotted versus some other (both intrinsic and "observable") relevant parameters. As in Fig. 6.2, please note that compactnesses and energy densities refer to the blob comoving frame, even though not primed. The statistical significance of the correlations is reported in Table 6.3.

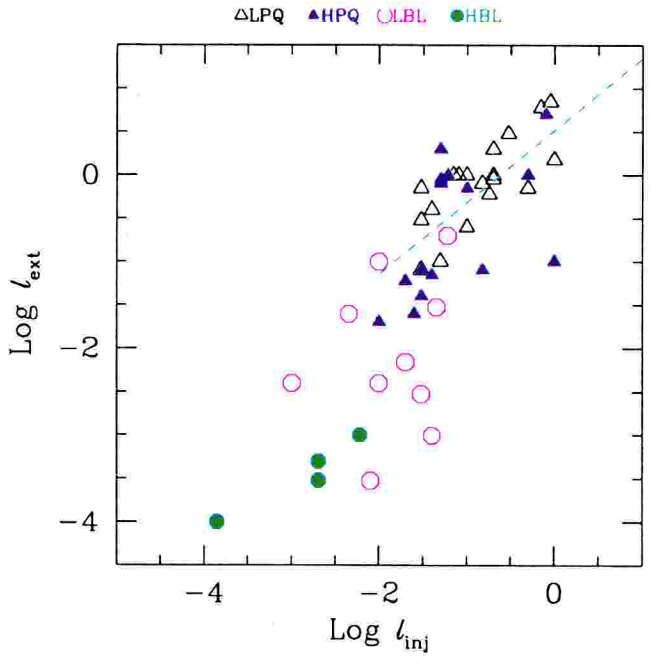

Figure 6.4: The relation between the compactnesses in external photons ℓ_{ext} and injected power ℓ_{inj}, in the blob comoving frame. The line represents the best–fit linear correlation for FSRQ only (see Table 6.3.

PCA

To further investigate the correlations among the various quantities described above, we performed a Principal Component Analysis (PCA). Briefly, the PCA is a method to describe a multidimensional ensemble of correlated parameters, by defining a new coordinate system in which each successive coordinate direction defined by the eigenvectors, accounts for as much of the remaining variance in the data is possible. PCA reduces the number of relevant components and the remaining should represent more basic parameters than the original ones. (see e.g. Boroson and Green 1992 for an application). We choose to present the PCA done with the 6 most important parameters of the fits: ℓ'_{inj}, ℓ'_{ext}, δ, γ_{peak}, B and R.

The results of the analysis are presented in Table 6.4, which lists the most significant eigenvectors in terms of their projection upon the original 6 quantities. At the top of each column the percentage variance accounted for by the eigenvectors is given.

The first eigenvector accounts for about 45% of the total variance and is dominated by the contribution of the two compactnesses and the magnetic field energy density which anti–correlate (see above) with γ_{peak}. This eigenvector could be associated with the total power of the source. The largest contribution to the second eigenvector comes from δ, R and γ_{peak}, while the only relevant projection on the third one is due to γ_{peak}.

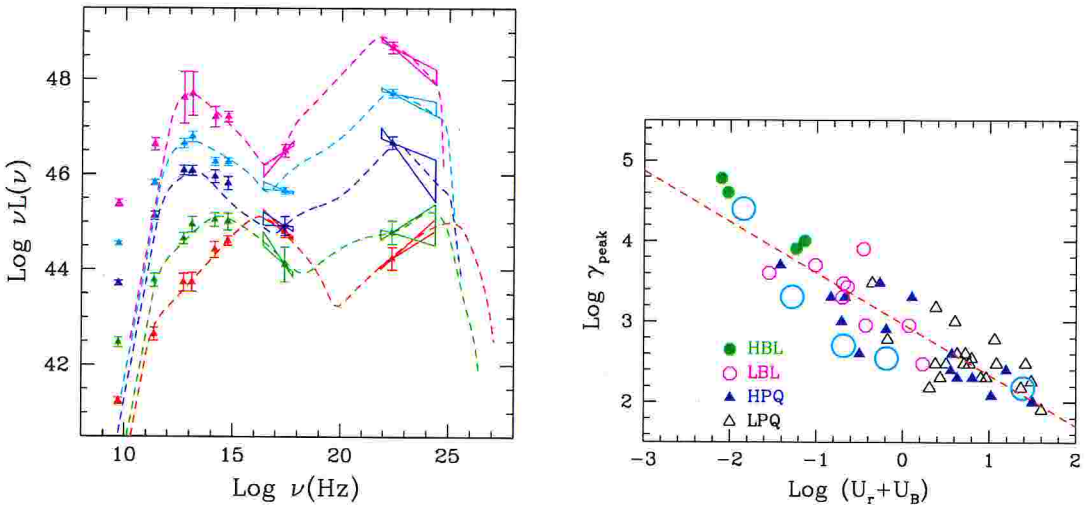

(a) (b)

Figure 6.5: (a) Fits with the ERC model of the average SEDs derived in Chapter 5. (b) $\gamma_{\rm peak}$ *vs.* $(U'_{\rm rad} + U'_{\rm B})$ (as in Fig. 6.3) with added five big circles corresponding to the parameters of the fit to the average SEDs, which are in complete agreement with the parameters determined for the γ–ray loud sources examined in this Chapter. Parameters values are reported in Table 6.5,

Given that the Doppler factor δ and the blob dimension R are not completely independent quantities (see § 6.2.4), the PCA analysis points to $\gamma_{\rm peak}$, $\ell'_{\rm inj}$ and $\ell'_{\rm ext}$ as fundamental variables in explaining the formation of the blazar SED, and confirms the results found through the linear regression analysis.

6.3.3 Fit to average Blazars SEDs

Evidence for continuity in the observed spectral properties of BL Lacs and FSRQ has been presented in previous Chapter studying complete samples of sub–classes of blazars in different energy bands. Diagrams and quantities derived in Chapter 5 from either data or their analytical representation of the SEDs turn out to be similar to and consistent with those found through model fitting.

In Fig. 6.5a, the ERC model considered here is applied to the average SEDs derived in Chapter 5 by binning, according to the radio luminosity, both BL Lacs and FSRQ merged in a "total blazars sample". The parameters of these fits are reported in Table 6.5, while the corresponding $\gamma_{\rm peak}$'s and comoving total energy densities are plotted as big circles in Fig. 6.5b. The fact that the model fits the average SEDs derived from complete blazars samples, with similar parameters and trends as for the γ–ray blazars, gives us confidence that our results are valid for all blazars.

6.3.4 Ratio of synchrotron and Compton peak energies[2]

In Chapter 5 we found that the ratio of the frequency of the Compton (ν_C) to the synchrotron (ν_S) peak is compatible with being approximately constant. The results obtained here applying physical models to γ–bright sources are in agreement with these findings, despite the relatively wide range spanned in some case by model parameters.

In fact in the ERC scenario (and in the Thomson regime of the inverse Compton process), ν_C/ν_S is independent of γ_{peak} and the narrow range of values of B found in the ERC model can account for the approximate constant ratio of ν_C/ν_S, although γ_{peak} varies $\simeq 3$ decades.

On the contrary for the SSC model, it is γ_{peak} which is found in a narrow interval, i.e. less than 2 decades, again supporting the idea that ν_C/ν_S tends to be constant.

6.4 Summary

We examined and reproduced the broad band spectral properties of a sample of 51 γ–ray loud blazars, in terms of synchrotron and inverse Compton emission from a homogeneous (one–zone) model. This gives a reasonable good description of the observations at frequencies greater than typically $\sim 10^{11}$ Hz. The radio emission is expected to be produced by less compact regions on larger jet scales.

On the basis of the "fits", it is difficult to determine whether the seed field for the inverse Compton scattering is mostly provided by synchrotron or external photons. However, as pointed out by Sikora et al. (1994), the presence of broad emission lines, together with the found values of δ, make photons produced externally to the emitting jet unavoidably important. For this reason we consider the parameters derived in the ERC scenario as the most likely for all FSRQ and some BL Lacs.

Strong correlations have been found among the physical parameters derived from the ERC model.

γ_{peak} *vs.* U'_{tot}

Of particular physical interest is the strong correlation between the energy of electrons emitting at the peak of the observed spectra and the total energy density present in the emitting region, $\gamma_{peak} \propto (U'_{rad} + U'_B)^{-0.6}$. One way to explain this is to assume that γ_{peak} is the result of a competition between the radiative cooling and the (re–)acceleration process, i.e. $\dot{\gamma}_{acc}(\gamma_{peak}) \simeq \dot{\gamma}_{cool}(\gamma_{peak})$. The typical emitting electron

[2] We recall that holds:

$$\text{SSC}: \quad \frac{\nu_C}{\nu_S} \propto \gamma^2_{break} \qquad\qquad \text{ERC}: \quad \frac{\nu_C}{\nu_S} \propto \frac{\delta\, \nu_{ext}}{B}$$

would in this case be quickly accelerated up to the energy where cooling is important, while only a few particles would be accelerated at higher energies.

The found correlation would then imply that the (re–)acceleration process is almost independent of both the energy density in the region (both in radiation and in magnetic field) and the energy of the particles, since $\dot{\gamma}_{\rm cool}(\gamma_{\rm peak}) \propto \gamma^2_{\rm peak}(U'_{\rm rad} + U'_{\rm B}) \sim$ const.

In addition, the injected particle distribution does not require characteristic shape and/or maximum energy.

$\gamma_{\rm peak}$ *vs.* $\frac{\rm L_C}{\rm L_S}$

We found another strong correlation between $\gamma_{\rm peak}$ and the Compton dominance $\rm L_C/L_S$. This confirms and quantifies, from a different perspective, the observational trends pointed out in Chapter 5 (and Fossati et al. 1998) on the relation between the dominance of the Compton/γ–ray emission and the energy of the peaks of the two spectral components for complete samples of blazars. On the other hand, it suggests that this link can be simply interpreted as the consequence of a change in the radiation energy density of the external field. An increase in the latter in fact leads to an increase in the particle Compton cooling and therefore both to a decrease in $\gamma_{\rm peak}$ and a relative increase in the γ–ray luminosity. Once again we stress that different sub–classes of blazars are located in different areas of this correlation.

As expected from the above correlations $\gamma_{\rm peak}$ is also (inversely) related to the power injected in the form of relativistic emitting particles.

TABLE 6.1: LIST OF SOURCES INCLUDED IN THE γ–RAY BRIGHT SAMPLE

Source	Other name	z	Class.	Refs. for data
(1)	(2)	(3)	(4)	(5)
0202+149	4C 15.05	0.833	HPQ	B85, BM94, C97, IT90, K81, NED, St92, St96, vM95
0208−512	PKS	1.003	HPQ	Be93, C97, IT88, NED, Sta96, To96
0219+428	3C 66A	0.444	LBL	C97, Di96, G86, NED, Pi93, Si91, T95, WW90
0234−285	CTD 20	1.213	HPQ	B95, BM91, E87, K81, NED, P82, St93, T92, vM95
0235+164	AO	0.940	LBL	BM94, E87, G94, H93, K81, Ma96 NED, Pi93, S94, Si91, To96, WW90
0420−014	PKS	0.915	HPQ	BM94, Ch89, Co95, E87, IN88, K81, Li94, NED, Ra97, R95, S94, Si91, Sm88, To96, WW90
0440−003	NRAO 190	0.844	HPQ	Bo90, K81, NED, St88, T95, To93, To96, W87, WP85
0446+112	PKS	1.207	NP	NED, St88, T95, To96, W92
0454−463	PKS	0.858	LPQ	B94, Fr83, IT90, K81, NED, To96, vM95, W91, WP85
0521−365	PKS	0.055	HPQ	C97, IN88, NED, Pi93, Pi94, Pi96, T95, To96
0528+134	OG 147	2.07	LPQ	B85, BM94, Co77, Co96, E87, IT90, Mc95, Mu96, NED, Po96, R82, R97, Sa97, V92, WP85
0537−441	PKS	0.896	LBL	Be92, C97, IN88, K81, L96, Ma85, NED, Pi93, Sa94, WP85, WW90
0716+714	S5	>0.3	LBL	BM94, C94, E87, G97, IN88, K81, L95, NED, St92, W96
0735+178	PKS	>0.424	LBL	C97, E87, G94, IN88, NED, N96, Pi93, Si91, To96, WW90
0804+499	0J 508	1.433	HPQ	BM94, C97, NED, St94, vM95
0805−077	PKS	1.837	NP	K81, NED, St93, T95
0827+243	OJ 248	2.05	LPQ	B95, BM94, NED, Ra97, To96, V97, vM95
0836+710	4C 71.07	2.172	LPQ	BM94, C97, E92, E87, K81, NED, Ra97, T93, W90, W92, WP85
0917+449	S4	2.18	LPQ	BM94, C97, E87, NED, St93, T95
0954+556	4C55.17	0.901	HPQ	BM94, C97, G94, K81, NED, Sr96

continued on next page

TABLE 6.1: CONTINUED

Source	Other name	z	Class.	Refs. for data
(1)	(2)	(3)	(4)	(5)
0954+658	S4	0.368	LBL	C97, G94, IN88, K81, L86, Mu95, NED, St88
1101+384	Mkn 421	0.031	HBL	Ma95, Ma96b
1127−145	PKS	1.187	LPQ	A85, B94, Bo90, E87, IT90, K81, NED, Sr96, To96
1156+295	4C 29.45	0.729	HPQ	BM94, E87, G94, IN88, Le85, Li94, LT96, NED, Pi93, Ra97, S94, Sa94, Si91, To96, V97, vM95, We95
1219+285	ON 231	0.102	LBL	BM91, C97, E92, E87, IN88, Lo90, NED, Pi93, Si91, To97, vM95, WW90
1222+216	4C 21.35	0.435	LPQ	B95, NED, Sr96, To96
1226+023	3C 273	0.158	LPQ	Al85, C83, G94, IN88, K81, L83, Mc95, NED, R86, Sh94, T90
1229−021	PKS	1.045	LPQ	K81, NED, P88, Ra97, Sr96, St88, St94, To96, Wi94
1253−055	3C 279	0.538	HPQ	Ma94
1313−333	PKS	1.210	NP	N96, NED, St88, St92, St94, To96
1406−076	PKS	1.494	LPQ	NED, St88, To93, To96, W95
1424−418	PKS	1.522	HPQ	G81, IN88, NED, To96, T96
1510−089	PKS	0.361	HPQ	C97, E87, G81, G94, IN88, K81, L86 LT97, NED, Pi93, Ra97, Sa94, Si91, Sm88, Sr96, St93, To96, V97, WP85
1604+159	4C15.54	0.357	LBL	GAM95, IN88, Le85, NED, Sr96
1606+106	4C 10.45	1.227	LPQ	B95, Bi87, BM94, E87, IT90, K81, NED, To96, vM95
1611+343	DA 406	1.404	LPQ	C97, E87, G94, K81, NED, Ra97, vM95
1622−253	PKS	0.786	LPQ	N96, NED, St94
1622−297	PKS	0.815	LPQ	K81, M97, NED, St93
1633+382	4C 38.41	1.814	LPQ	BM91, BM94, Bo90, C97, IN88, K81, M93, Ra97, V92, V97, WP85
1652+398	Mkn 501	0.055	HBL	B97, BM91, C97, G94, IN88, L91, Pi93, Q96, Sa94, St88, W92, WW90
1730−130	NRAO 530	0.902	NP	B94, BM91, E87, N96, NED, St88, St93, To96, W88
1739+522	4C 51.37	1.375	HPQ	B95, BM91, K81, NED, St88, St93, St94, V92, vM95
1741−038	OT-68	1.054	HPQ	B94, E87, G94, K81, NED, St88, St92, St93, St94, To96, vM95

continued on next page

TABLE 6.1: CONTINUED

Source	Other name	z	Class.	Refs. for data
(1)	(2)	(3)	(4)	(5)
1933−400	PKS	0.966	NP	B94, Di96, K81, NED, St94, To96
2032+107	PKS	0.601	LBL	Di96, GAM95, NED, WW90
2052−474	PKS	0.071	LPQ	B94, IT90, K81, NED, To96, vM95
2155−304	PKS	0.117	HBL	U97, V96
2200+420	BL Lac	0.069	LBL	BM94, Ca97, E87, IN88, NED, P96, Pi93, S94, St93, To96, U96
2230+114	CTA 102	1.037	HPQ	B94, BM94, E87, F94, IN88, K81, Le85, Mc95, N93, Ne96, Ra97, St93, T89, To96, W92, Wi94
2251+158	3C 454.3	0.859	HPQ	Be92, BM91, BM94, C97, E87, G94, Ha93, IN88, K81, Le85, Mc95, Ne96, NED, Pi93, Ra97, S94, Sm88
2344+514	1ES	0.044	HBL	Ca98, NED, P96

Notes to Table 6.1

(a) Meaning of columns: (1),(2) Source names; (3) redshift; (4) classification: HPQ and LPQ stand for highly and lowly polarized quasars, while NP indicates sources with no polarization measure; HBL, LBL and IBL refer to high, low and intermediate frequency BL Lacs, respectively; (5) references to the data.

REFERENCES FOR DATA USED IN THE SEDS OF OBJECTS IN TABLE 6.1

A85:	Adam (1985)
Al85:	Aller et al. (1985)
B85:	Bregman et al. (1985)
B94:	Brinkmann et al. (1994)
B95:	Brinkmann et al. (1995)
B97:	Breslin et al. (1997)
Be92:	Bersanelli et al. (1992)
Be93:	Bertsch et al. (1993)
Bi87:	Biermann et al. (1987)
BM91:	Bloom and Marscher (1991)
BM94:	Bloom et al. (1994)
Bo90:	Bozyan et al. (1990);
C83:	Clegg et al. (1983)
C94:	Cappi et al. (1994)
C97:	Comastri et al. (1997)
Ca97:	Catanese et al. (1997)
Ca98:	Catanese et al. (1998)
Ch89:	Chini et al. (1989)
Co77:	Condon et al. (1977)
Co95:	Condon et al. (1995)
Co96:	Collmar (1996)
Di96:	Dingus et al. (1996)
E92:	Elvis et al. (1992)
E87:	Edelson (1987)
F94:	Falomo et al. (1994)
Fr83:	Fricke et al. (1983)
GAM95:	Giommi et al. (1995)
G81:	Glass (1981)
G86:	Ghisellini et al. (1986)
G94:	Gear et al. (1994)
G97:	Ghisellini et al. (1997)
H93:	Hunter et al. (1993)
Ha93:	Hartman et al. (1993)
IN88:	Impey and Neugebauer (1988)
IT88:	Impey and Tapia (1988)
IT90:	Impey and Tapia (1990)
K81:	Kühr et al. (1981)
L83:	Landau et al. (1983)
L86:	Landau et al. (1986)
L91:	Lawrence et al. (1991)
L95:	Lin et al. (1995)
L96:	Lin et al. (1996)
Le85:	Ledden and O'Dell (1985)
Li94:	Litchfield et al. (1994)
Lo90:	Lorenzetti et al. (1990)
LT97:	Lawson and Turner (1997)
M93:	Mattox et al. (1993)
M97:	Mattox et al. (1997)
Ma85:	Maraschi et al. (1985)
Ma94:	Maraschi et al. (1994)
Ma95:	Macomb et al. (1995)
Ma96:	Madejski et al. (1996)
Ma96b:	Macomb et al. (1996)
Mc95:	McNaron-Brown et al. (1995)
Mu95:	Mukherjee et al. (1995)
Mu96:	Mukherjee et al. (1996)
N93:	Nolan et al. (1993)
N96:	Nolan et al. (1996)
Ne96:	Netzer et al. (1996)
P82:	Perley (1982)
P88:	Pica et al. (1988)
P96:	Perlman et al. (1996)
Pi93:	Pian and Treves (1993)
Pi94:	Pian et al. (1994)
Pi96:	Pian et al. (1996)
Po96:	Pohl et al. (1996)
Q96:	Quinn et al. (1996)
R82:	Rieke et al. (1982)
R86:	Robson et al. (1986)
R95:	Radecke et al. (1995)
R97:	Reuter et al. (1997)
Ra97:	Raiteri et al. (1998)
S94:	Stevens et al. (1994)
Sa94:	Sambruna et al. (1994)
Sa97:	Sambruna et al. (1997)
Sh94:	Schoenfelder (1994)
Si91:	Sitko and Sitko (1991)
Sm88:	Smith et al. (1988)
Sr96:	Sreekumar et al. (1996)
St88:	Steppe et al. (1988)
St92:	Steppe et al. (1992)
St93:	Steppe et al. (1993)
St94:	Stickel et al. (1994)
St96:	Stickel et al. (1996)
Sta96:	Stacy et al. (1996)
T89:	Terasranta et al. (1989)
T90:	Turner et al. (1990)
T92:	Terasranta et al. (1992)
T93:	Thompson et al. (1993)
T95:	Thompson et al. (1995)
T96:	Thompson et al. (1996)
To93:	(Tornikoski et al. 1993)
To96:	Tornikoski et al. (1996)
To98:	(Tosti et al. 1998)
U96:	Urry et al. (1996)
U97:	Urry et al. (1997)
V92:	Valtaoja et al. (1992)
V96:	Vestrand et al. (1995)
V97:	Villata et al. (1997)
vM95:	Von Montigny et al. (1995)
W87:	Worrall et al. (1987)
W88:	Webb et al. (1988)
W90:	Wagner et al. (1990)
W91:	Wright et al. (1991)
W92:	Wiren et al. (1992)
W95:	Wagner et al. (1995)
W96:	Wagner et al. (1996)
We95:	Webb et al. (1995)
Wi94:	Wilkes et al. (1994)
WP85:	Wall and Peacock (1985)
WW90:	Worrall and Wilkes (1990)

TABLE 6.2: INPUT PARAMETERS FOR THE ERC AND SSC MODELS[a]

Source	$R/10^{15}$	ℓ_{inj}	ℓ_{ext}	γ_{max}	γ_{peak}	s	B	δ
(1)	(2)	(3)	(4)	(5)	(6)	(7)	(8)	(9)
0202+149	30	0.05	2	3.0e3	2.5e2	3.0	3.040	14
	80	0.01	–	4.0e4	1.0e4	3.3	0.026	18
0208−512	70	0.02	0.06	7.0e3	1.0e3	3.8	0.563	23
	50	0.08	–	3.0e4	1.5e4	2.0	0.106	16
0219+428	20	0.03	3e-3	1.0e5	8.0e3	2.4	2.040	13.5
	40	0.01	–	2.0e5	1.0e4	2.4	0.590	15
0234−285	40	0.06	1	1.0e4	2.0e2	2.9	4.080	16
	50	0.08	–	6.0e4	1.0e4	3.0	0.067	13
0235+164	50	0.05	0.03	8.0e4	3.0e3	3.0	0.912	20
	60	0.02	–	3.0e5	1.0e4	2.9	0.215	21
0420−014	50	0.03	0.04	1.0e4	2.0e3	3.5	0.745	16
	80	0.01	–	8.0e4	1.5e4	3.0	0.034	20
0440−003	50	0.025	0.025	2.0e4	2.0e3	3.0	0.680	17
	70	0.01	–	8.0e4	2.0e4	3.0	0.106	20
0446+112	50	0.08	1	4.0e3	1.5e2	2.0	0.810	20
	90	0.08	–	1.0e5	1.0e4	3.5	0.011	20
0454−463	30	0.03	0.08	8.0e3	6.0e2	2.1	1.050	16
	80	7e-3	–	8.0e4	3.0e4	2.5	0.018	20
0521−365	50	1.00	0.10	5.0e4	2.0e3	2.5	3.141	1.4
	50	0.60	–	7.0e4	3.5e3	2.7	2.580	1.6
0528+134	65	0.90	7	6.0e3	3.0e2	2.6	6.198	15
	60	0.60	–	8.0e4	3.0e3	3.0	0.215	19
0537−441	70	0.04	1e-3	7.0e4	4.0e3	2.2	0.325	15
	50	0.05	–	1.0e5	4.0e3	2.5	0.430	15
0716+714	30	0.02	7e-3	3.0e4	2.0e3	2.6	1.813	11.5
	50	3e-3	–	5.0e4	4.0e3	2.7	0.460	15
0735+178	40	0.01	4e-3	3.0e4	3.0e3	3.0	0.833	14
	50	3e-3	–	4.0e4	5.0e3	3.3	0.408	17
0804+499	50	0.10	0.70	8.0e3	4.0e2	3.1	3.333	15
	70	0.06	–	8.0e4	1.0e4	3.4	0.073	17
0805−077	40	0.20	2	6.0e3	4.0e2	2.5	2.483	17
	90	0.09	–	1.0e5	9.0e3	3.7	0.037	20
0827+234	50	0.20	0.90	8.0e3	3.0e2	2.3	4.711	16
	70	0.20	–	8.0e4	5.0e3	2.7	0.563	16

continued on next page

TABLE 6.2: CONTINUED

Source	$R/10^{15}$	ℓ_{inj}	ℓ_{ext}	γ_{max}	γ_{peak}	s	B	δ
(1)	(2)	(3)	(4)	(5)	(6)	(7)	(8)	(9)
0836+710	50	0.70	6.00	7.0e3	1.8e2	3.1	8.814	18
	70	0.30	–	5.0e4	4.0e3	3.0	0.282	17
0917+449	30	0.50	8	6.0e3	2.0e2	2.1	2.267	13
	90	0.03	–	1.0e5	4.0e3	2.3	0.025	23
0954+556	50	0.01	0.02	1.5e4	5.0e3	1.7	0.527	15
	70	4e-3	–	7.0e4	1.0e4	0.0	0.056	17
0954+658	30	4.5e-3	0.025	6.0e3	9.0e2	3.6	2.040	13
	60	7e-4	–	7.0e4	2.0e4	2.0	0.025	18
1101+384	5	6e-3	1e-3	8.0e5	6.0e4	2.0	0.222	11
	10	2e-3	–	8.0e5	2.0e5	1.2	0.093	12
1127−145	60	0.15	0.80	8.0e3	3.0e2	2.3	1.862	15.5
	70	0.10	–	8.0e4	1.5e4	2.3	0.048	17
1156+295	20	0.15	0.08	1.0e4	3.0e3	2.4	1.360	15
	70	0.02	–	8.0e4	9.0e3	2.0	0.252	18
1219+285	20	1.e-3	4.e-3	1.0e5	5.0e3	4.2	1.178	11
	70	5.e-5	–	7.0e4	4.0e4	0.0	0.036	20
1222+216	10	0.10	0.25	8.0e3	3.5e2	2.9	3.333	11
	40	0.02	–	4.0e4	9.0e3	3.2	0.068	11
1226+023	10	1.00	1.50	1.0e4	8.0e1	3.2	8.900	6.5
	40	0.06	–	3.0e4	3.5e3	3.2	0.456	7
1229−021	40	0.08	1.00	8.0e3	3.0e2	3.8	2.356	12
	50	0.03	–	2.0e4	1.0e4	4.0	0.105	16
1253−055[b]	30	0.04	0.07	7.0e3	8.0e2	3.2	1.360	18
	80	0.04	–	2.0e4	2.0e4	–	0.059	15
1313−333	40	0.03	0.70	9.0e3	1.0e3	1.9	1.180	17
	70	0.01	–	1.0e5	3.0e4	1.0	0.009	20
1406−076	60	0.05	0.10	1.0e4	3.0e3	1.5	1.080	21
	70	0.08	–	6.0e4	1.5e4	2.3	0.206	18
1424−418	30	0.50	1.00	6.0e3	2.0e2	2.7	4.060	15
	90	0.07	–	1.0e5	5.0e3	3.0	0.093	20
1510−089	20	0.05	0.80	1.0e4	1.2e2	3.3	5.890	13
	30	4e-3	–	3.0e4	4.0e3	2.2	0.061	18
1604+159	20	0.01	0.10	1.0e4	9.0e2	2.1	0.960	15
	50	2e-3	–	7.0e4	3.0e4	2.1	0.011	18
1606+106	30	0.30	3.00	5.0e3	1.5e2	3.0	3.330	15
	70	0.06	–	3.0e4	1.0e4	3.0	0.028	18

continued on next page

TABLE 6.2: CONTINUED

Source	$R/10^{15}$	ℓ_{inj}	ℓ_{ext}	γ_{max}	γ_{peak}	s	B	δ
(1)	(2)	(3)	(4)	(5)	(6)	(7)	(8)	(9)
1611+343	30	0.20	1.00	5.0e3	2.0e2	2.6	3.041	16
	50	0.20	–	6.0e4	1.3e4	3.3	0.105	13.5
1622−253	30	0.03	0.30	6.0e3	3.0e2	2.5	1.670	15
	70	0.01	–	8.0e4	2.0e4	2.3	0.013	16
1622−297	20	0.10	1.00	2.5e3	6.0e2	1.5	2.150	23
	80	0.03	–	5.0e4	3.0e4	2.1	0.007	21
1633+382	60	0.18	0.60	6.0e3	1.5e3	1.5	1.667	21
	80	0.20	–	7.0e4	2.0e4	2.0	0.052	19
1652+398	5	2e-3	5e-4	8.0e5	1.0e4	2.8	1.110	10
	10	1e-3	–	8.0e5	2.0e4	3.0	0.497	10
1730−130	30	0.04	0.40	3.0e4	4.0e2	2.8	5.440	17
	60	0.02	–	6.0e4	6.0e3	2.4	0.192	16
1739+522	60	0.03	0.08	1.0e4	4.0e2	2.2	0.450	20
	70	0.04	–	1.0e5	2.0e4	2.1	0.019	19
1741−038	60	0.05	0.90	8.0e3	2.5e2	3.8	2.150	17
	60	0.05	–	2.0e4	1.0e4	3.0	0.048	17.5
1933−400	20	0.07	1.00	6.0e3	3.0e2	2.6	4.410	14
	50	0.03	–	5.0e4	8.0e3	2.9	0.060	14
2032+107	20	0.06	0.20	6.0e3	3.0e2	3.0	3.850	12
	50	5e-3	–	5.0e4	4.0e3	3.3	0.118	20
2052−474	50	0.20	2.00	7.0e3	2.0e2	2.8	1.920	15
	70	0.10	–	5.0e4	8.0e3	2.9	0.073	16
2155−304	20	2e-3	3e-4	4.0e5	8.0e3	2.4	1.050	17
	20	2e-3	–	1.0e6	7.0e3	2.6	1.216	18
2200+420	8	8e-3	3e-4	3.0e5	2.7e3	2.8	1.670	10
	20	2e-3	–	3.0e5	5.0e3	2.8	0.430	11
2230+114	40	0.80	5.00	1.0e4	1.0e2	3.1	8.600	10
	70	0.03	–	3.0e4	6.0e3	2.9	0.077	18
2251+158	40	0.80	5.00	6.0e3	1.0e2	2.3	7.450	10
	70	0.04	–	6.0e4	4.0e3	2.2	0.073	18
2344+512	8	1.4e-4	1e-4	7.0e5	4.0e4	3.7	0.470	14
	10	2e-4	–	8.0e5	4.5e4	3.5	0.220	13

Notes to Table 6.2

[a] The input parameters for the ERC and SSC models are reported in the first and second line for each source, respectively. (1) Source name; (2) region size in units of 10^{15} cm; (3,4) compactnesses in injected particles and external radiation field; (5) maximum energy of the injected particles; (6) energy of the peak of the stationary electron distribution; (7) spectral index of the injected particles; (8) magnetic field intensity (in Gauss); (9) relativistic Doppler factor.

[b] The SSC model for 1253−055 requires monoenergetic injection.

TABLE 6.3: LINEAR CORRELATIONS BETWEEN ERC MODEL PARAMETERS[a]

		$\gamma_{\rm peak}$					
y	x	N	m	q	r	$\mathcal{P}$	Objects
(1)	(2)	(3)	(4)	(5)	(6)	(7)	(8)
$\log \gamma_{\rm peak}$	$\log(U_{\rm rad}+U_{\rm B})$	51	-0.63 ± 0.04	2.97 ± 0.04	0.902	$7.2 \cdot 10^{-10}$	All
		37	-0.50 ± 0.06	2.88 ± 0.05	0.812	$2.5 \cdot 10^{-9}$	Only FSRQ
		14	-0.80 ± 0.12	2.88 ± 0.14	0.886	$2.4 \cdot 10^{-5}$	Only BL Lacs
$\log \gamma_{\rm peak}$	$\log U'_{\rm B}$	51	-0.64 ± 0.09	2.33 ± 0.10	0.735	$2.3 \cdot 10^{-9}$	All
		37	-0.43 ± 0.08	2.33 ± 0.08	0.676	$4.5 \cdot 10^{-6}$	Only FSRQ
		14	-0.67 ± 0.19	2.70 ± 0.28	0.719	$3.7 \cdot 10^{-3}$	Only BL Lacs
$\log \gamma_{\rm peak}$	$\log U'_{\rm rad}$	51	-0.56 ± 0.04	2.89 ± 0.04	0.911	$1.2 \cdot 10^{-10}$	All
		37	-0.50 ± 0.06	2.85 ± 0.05	0.818	$7.9 \cdot 10^{-11}$	Only FSRQ
		14	-0.64 ± 0.10	2.82 ± 0.15	0.875	$4.0 \cdot 10^{-5}$	Only BL Lacs
$\log \gamma_{\rm peak}$	$\log \ell'_{\rm ext}$	51	-0.48 ± 0.04	2.47 ± 0.05	0.890	$7.1 \cdot 10^{-10}$	All
		37	-0.54 ± 0.07	2.47 ± 0.05	0.799	$1.6 \cdot 10^{-9}$	Only FSRQ
		14	-0.49 ± 0.11	2.39 ± 0.29	0.794	$7.0 \cdot 10^{-4}$	Only BL Lacs
$\log \gamma_{\rm peak}$	$\log \ell'_{\rm inj}$	51	-0.61 ± 0.08	2.11 ± 0.12	0.735	$3.4 \cdot 10^{-9}$	All
		37	-0.41 ± 0.12	2.23 ± 0.14	0.491	$2.0 \cdot 10^{-3}$	Only FSRQ
		14	-0.48 ± 0.21	2.59 ± 0.48	0.566	$3.5 \cdot 10^{-2}$	Only BL Lacs
$\log \gamma_{\rm peak}$	$\log(\ell'_{\rm inj}+\ell'_{\rm ext})$	51	-0.58 ± 0.05	2.54 ± 0.06	0.871	$1.7 \cdot 10^{-10}$	All
		37	-0.55 ± 0.09	2.54 ± 0.05	0.740	$1.7 \cdot 10^{-7}$	Only FSRQ
		14	-0.61 ± 0.14	2.49 ± 0.29	0.776	$1.1 \cdot 10^{-3}$	Only BL Lacs
$\log \gamma_{\rm peak}$	$\log {\rm L_C}/{\rm L_S}$	51	-0.70 ± 0.11	3.53 ± 0.12	0.690	$2.2 \cdot 10^{-8}$	All
		37	-0.44 ± 0.18	3.15 ± 0.23	0.381	$2.0 \cdot 10^{-2}$	Only FSRQ
		14	-0.46 ± 0.28	3.67 ± 0.16	0.427	$1.3 \cdot 10^{-1}$	Only BL Lacs

continued on next page

TABLE 6.3: CONTINUED

y	x	N	m	q	r	$\mathcal{P}$	Objects
(1)	(2)	(3)	(4)	(5)	(6)	(7)	(8)
L_C/L_S							
$\log L_C/L_S$	$\log \ell'_{inj}$	51	0.49 ± 0.09	1.54 ± 0.14	0.601	$2.3 \cdot 10^{-6}$	All
		37	0.02 ± 0.12	1.18 ± 0.13	0.027	$8.7 \cdot 10^{-1}$	Only FSRQ
		14	0.47 ± 0.18	1.15 ± 0.41	0.599	$2.4 \cdot 10^{-2}$	Only BL Lacs
$\log L_C/L_S$	$\log \ell'_{ext}$	51	0.42 ± 0.05	1.28 ± 0.07	0.797	$2.2 \cdot 10^{-9}$	All
		37	0.25 ± 0.09	1.27 ± 0.07	0.426	$8.6 \cdot 10^{-3}$	Only FSRQ
		14	0.38 ± 0.13	1.07 ± 0.34	0.649	$1.2 \cdot 10^{-2}$	Only BL Lacs
$\log L_C/L_S$	$\log(\ell'_{inj} + \ell'_{ext})$	51	0.50 ± 0.06	1.22 ± 0.07	0.771	$6.7 \cdot 10^{-10}$	All
		37	0.20 ± 0.10	1.23 ± 0.07	0.311	$6.1 \cdot 10^{-2}$	Only FSRQ
		14	0.55 ± 0.14	1.15 ± 0.28	0.749	$2.0 \cdot 10^{-3}$	Only BL Lacs
$\log L_C/L_S$	$\log L^{obs}_{inj}$	51	0.40 ± 0.06	-18.44 ± 2.81	0.702	$8.7 \cdot 10^{-9}$	All
		37	0.17 ± 0.08	-7.28 ± 4.03	0.335	$4.2 \cdot 10^{-2}$	Only FSRQ
		14	0.29 ± 0.12	-13.44 ± 5.61	0.573	$3.2 \cdot 10^{-2}$	Only BL Lacs
$\log L_C/L_S$	$\log \nu^{obs}_{peak}$	51	-0.45 ± 0.06	11.57 ± 1.40	0.736	$1.4 \cdot 10^{-9}$	All
		37	-0.25 ± 0.08	6.92 ± 1.93	0.449	$5.3 \cdot 10^{-3}$	Only FSRQ
		14	-0.31 ± 0.14	7.88 ± 3.45	0.544	$4.4 \cdot 10^{-2}$	Only BL Lacs
$\log L_C/L_S$	$\log B$	51	0.37 ± 0.24	0.81 ± 0.11	0.217	$1.3 \cdot 10^{-1}$	All
		37	-0.15 ± 0.19	1.26 ± 0.09	0.132	$4.3 \cdot 10^{-1}$	Only FSRQ
		14	-0.25 ± 0.50	0.14 ± 0.16	0.145	$6.2 \cdot 10^{-1}$	Only BL Lacs
more correlations							
$\log \ell'_{ext}$	$\log \ell'_{inj}$	51	1.28 ± 0.13	0.76 ± 0.19	0.822	$6.3 \cdot 10^{-10}$	All
		37	0.83 ± 0.16	0.52 ± 0.17	0.671	$5.5 \cdot 10^{-6}$	Only FSRQ
		14	0.82 ± 0.31	-0.71 ± 0.71	0.605	$2.2 \cdot 10^{-2}$	Only BL Lacs
$\log U'_B$	$\log U'_{rad}$	51	0.57 ± 0.06	-0.86 ± 0.06	0.812	$1.2 \cdot 10^{-10}$	All
		37	0.82 ± 0.08	-1.05 ± 0.07	0.857	$5.7 \cdot 10^{-10}$	Only FSRQ
		14	0.54 ± 0.16	-0.69 ± 0.24	0.693	$6.0 \cdot 10^{-3}$	Only BL Lacs

Notes to Table 6.3

(a) Meaning of columns: (1), (2), (4), (5) parameters of the linear correlation of the form $y = mx + q$, with associated formal errors; (3) number of objects; (6) correlation coefficient; (7) probability of a random distribution; (8) sources considered.

TABLE 6.4: RESULTS OF THE PRINCIPAL COMPONENT ANALYSIS[a]

Variable	EV_1	EV_2	EV_3	EV_4	EV_5	EV_6
%	44.55	27.08	13.17	9.0	3.52	2.66
δ	−0.2408	−0.5922	−0.3525	0.5140	0.1872	−0.4098
$\ell'_{\rm inj}$	0.5608	0.0623	−0.0525	−0.3317	0.0915	−0.7486
$\ell'_{\rm ext}$	0.5242	−0.1578	−0.3110	0.2645	−0.7031	0.1982
$\gamma_{\rm peak}$	−0.2086	0.4119	−0.8594	−0.2063	0.0652	0.0376
$U'_{\rm B}$	0.5510	0.0746	−0.1082	0.3196	0.6654	0.3663
R	0.0748	−0.6673	−0.1611	−0.6412	0.1234	0.3111

Notes to Table 6.4

(a) EV stands for eigenvector. The first row of the table lists the percentage of the correlation accounted for by the different eigenvectors.

TABLE 6.5: ERC MODEL PARAMETERS FOR THE FIT TO THE AVERAGE SED[a]

$\log L_{\rm 5GHz}$	$R/10^{15}$	$\ell'_{\rm inj}$	$\ell'_{\rm ext}$	$\gamma_{\rm max}$	$\gamma_{\rm peak}$	s	B	δ
(1)	(2)	(3)	(4)	(5)	(6)	(7)	(8)	(9)
< 42	10	7e-4	1e-5	1.0e6	2.5e4	3.0	0.441	15
$42 - 43$	10	1e-3	1e-3	2.0e5	2.0e3	2.8	0.745	15
$43 - 44$	30	5e-3	2e-2	3.0e4	5.0e2	3.0	1.075	15
$44 - 45$	40	5e-2	0.1	1.5e4	3.5e2	2.5	1.178	15
> 45	50	5e-1	5.0	6.0e3	1.5e2	2.8	6.082	15

Notes to Table 6.5

(a) The input parameters for the ERC model reproducing the average SEDs. Meaning of columns: (1) Radio luminosity bin; (2) region size in units of 10^{15} cm; (3,4) comoving compactnesses in injected particles and external radiation field; (5) maximum energy of the injected particles; (6) energy of the break in the stationary electron distribution which corresponds to the synchrotron peak in the SED; (7) spectral index of the injected particles; (8) magnetic field intensity (in Gauss). In the fits the relativistic Doppler factor (column 9) has been fixed at the value δ=15.

CHAPTER 7

CONCLUSIONS AND PROSPECTS

7.1 The blazar unification

The main result of the research work presented in this thesis is the proposal of a new consistent unifying framework, within which the complex variety of "flavours", in which blazars observationally come, is interpreted in terms of a continuous sequence, determined by a key physical parameter.

This unification picture relies upon the idea of an intrinsic relationship among phenomenologically different classes of blazars, and in particular on the evidence for a well defined sequence in the properties of HBL, LBL and FSRQ with increasing importance of an external radiation field. The observed spectral properties of HBL, LBL, FSRQ can be therefore accounted for by e.g. the increasing role of broad emission line radiation (see Chapter 6, Fig. 6.5a,b and Table 6.5). This in fact dictates the peak energy of the emitting particle distribution and hence the shape of the spectra, thus determining the classification of an object into one of the blazar flavours. The fundamental physical processes occurring in and outside the relativistic jet are instead the same. This is indicated by the correlation between $\ell'_{\rm ext}$ and $\ell'_{\rm inj}$ (Fig. 6.4).

This proposed blazar unifying sequence can be therefore summarized as follows (see the schematic sketch in Fig. 7.1):

① HBL are sources characterized by the lowest intrinsic power and the weakest external radiation field (no or weak emission lines). Consequently the cooling is less dramatic and particles can be present with energies high enough to produce synchrotron emission extending to soft X–ray energies and TeV radiation through the SSC process. Being the inverse Compton cooling small, the Compton dominance is expected to be small.

② LBL are intrinsically more powerful than HBL and in some cases the external field can be responsible for most of the cooling. The stronger cooling limits the emitting particle energy implying that the synchrotron and inverse Compton emission peak at lower frequencies, in the optical and GeV bands, respectively, with a larger Compton dominance parameter.

③ FSRQ represent the most powerful blazars, where the contribution from the external radiation to the cooling is the largest. The emission by synchrotron and ERC cannot extend at frequencies higher than the IR and MeV–GeV bands and the γ–ray radiation completely dominates the radiative output. Within this class, there is an hint of a further subdivision between low and high polarization objects, with a tendency for LPQ to be more extreme (lower values of $\gamma_{\rm peak}$ and larger values of $(U'_{\rm rad} + U'_{\rm B})$, $\ell'_{\rm inj}$ and so on).

The correlations among the different quantities ensure that the knowledge of one of them allows to estimate the entire spectral energy distribution, and also the probable classification of the object.

This is of course of great relevance for the study at high energies of those blazars not detected so far in the γ–ray band and the consequences on their variability patterns and duty cycles. Finally, the above findings have to be taken into account when considering the absorption of high energy radiation by the infrared diffuse background fields as well as the estimates on the blazar contribution to the γ–ray background.

Within this frame, the blazar sequence would therefore manifest itself in several observational properties, including the total source power, the luminosity in emission lines, the extended radio power, the dominance of γ–rays over the other spectral components and the broad band shape of the SED (see Fig. 7.1). We therefore provide evidence for the unification of all radio–loud sources and suggest a deeper physical understanding for it, based on the total power generated in the very central engine of these spectacular sources.

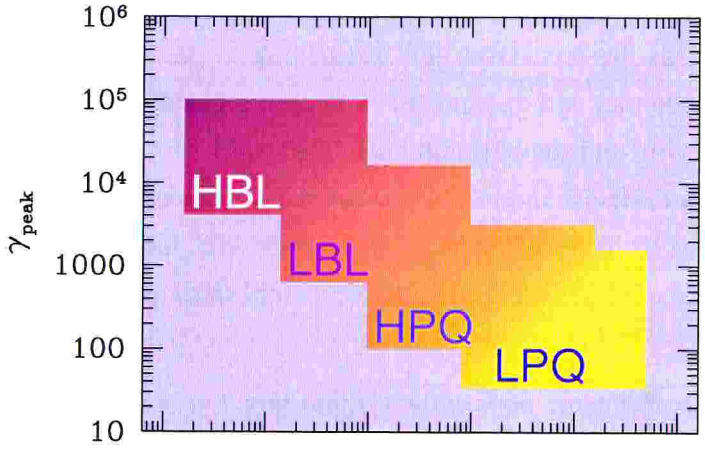

Figure 7.1: Schematic representation of the proposed unifying scheme: the sequence HBL, LBL, FSRQ (further distinguished in HPQ, LPQ on the basis of their optical polarization) corresponds to an increase in the external radiation field, the total energy density and the injected power. These in turn result in a decrease of $\gamma_{\rm peak}$ and an increase in the Compton dominance.

7.2 Consequences

The proposed framework has consequences still to be explored, concerning different aspects of blazar phenomenology not (yet) included in its formulation. In particular the following issues:

- The key question about the *ultimate physical difference* among blazars, which are now regarded as following a sequence in terms of source power and/or of "external" diffuse radiation field.
  It is crucial (and possible) to check the consistency of the sequence in the compactness of the diffuse radiation field with observational data. The best candidate for this component is the emission coming from the broad line region, which could be traced by the observed broad line luminosity. An extremely interesting step is thus to study the emission line properties of all blazars, although this task could be troublesome for HBLs. Relatively little attention has been paid so far to this subject, and a desirable goal is to determine whether or not there is an actual relationship between the highly anisotropic radiation, associated with the relativistic jet, and properties of broad emission lines, working in one direction or the other (jet emission properties are influenced by the BLR, or rather the jet affects the BLR). In this respect a very important task would be to perform simultaneous observations of emission lines and high energy continuum variability.
  On the other hand, the BLR emission is an indirect signature of a nuclear quasi–

thermal component, likely linked to the power released in an accretion disk, which eventually feeds the relativistic jet. According to our, and previous, studies a link emerges between jet and disk power: a puzzling question is then what is the mechanism underlying and regulating their relationship.
It is necessary to devise models in which it would be natural for sources with weaker emission lines to have different jet properties, e.g. down to the level of showing different types of shocks (e.g. transverse *vs.* oblique) as apparent from VLBI polarization maps.

- ◇ Whether *γ–loud blazars constitute a different sub–class*, intrinsically peculiar with respect to a γ–quiet population, or if their selection is affected by instrument sensitivity and/or source variability.
  Preliminary findings derived from the study of a large blazar sample, show that γ–loud(/detected) sources do not differ with respect to the whole sample in terms of redshift distributions, power, and SED shape.

Many other points need to be taken into account in order to determine that the proposed new unifying picture is robust.

7.2.1 Blazars and the γ–ray sky

From the observational point of view, the peculiarity of the model we developed, residing in the association of a specific spectral shape with each luminosity, has interesting consequences on the predictions of the γ–ray properties of blazars. We can at least identify a couple of main issues:

- ◇ the prediction of the contribution of blazars to the *diffuse extragalactic γ–ray background*;
- ◇ the *detectability of blazars in the TeV band*, that in turn could have feedbacks on studies of the diffuse extragalactic radiation in the infrared band. A peculiar prediction of this model is the intrinsic absence of high luminosity sources emitting in the TeV band, as objects peaking at such high frequency should be intrinsically of low luminosity.

It is particularly interesting to work out some simple estimates of the γ–ray properties of blazars. Using the simple scheme of SED parameterization introduced in Chapters 3 and 5, we can compute the luminosities in the EGRET (30 MeV – 3 GeV) and Whipple (0.3 – 10 TeV) bands. These are plotted in Fig. 7.2 (bottom panel) together with their ratio with the radio and X–ray luminosities (top and middle panel, respectively).

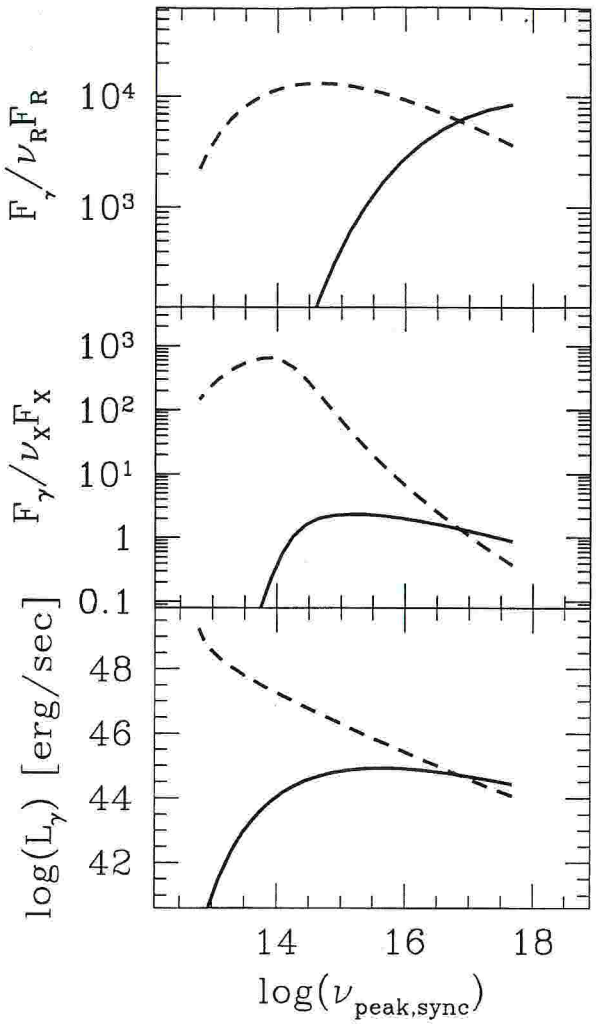

Figure 7.2: The predicted relations with $\nu_{peak,sync}$ of the following quantities: the ratio of the EGRET (dashed line) and Whipple (solid line) fluxes (luminosities) with the radio one (top panel); the ratio of the EGRET and Whipple fluxes (luminosities) with the X–ray one (middle panel); EGRET and Whipple absolute luminosities (bottom panel). The γ–ray luminosities are integrated in a band approximately corresponding to that of EGRET or Whipple telescopes, 30 MeV–3 GeV and 0.3–10 TeV, respectively.

It is easy to recognize that for a given radio flux, sources with $\nu_{peak,sync}$ around 10^{14} Hz have the largest relative flux in the EGRET band, because the peak of the Compton component falls right there (Fig. 7.2, top panel). For higher values of $\nu_{peak,sync}$ the γ–ray peak moves to higher energies too and the contribution in the EGRET band is reduced. For sufficiently high $\nu_{peak,sync}$ the γ–ray peak reaches the TeV band where it becomes detectable.

Qualitatively the same general behaviour is present also in the ratios between EGRET/Whipple fluxes and the X–ray one (Fig. 7.2, middle panel). There are however a couple of significant differences: firstly the EGRET/X–ray ratio profile, while still peaking around 10^{14} Hz, is sharper than in the EGRET/radio case; secondly, the

TeV relative flux distribution is broader and skewed towards lower values of the synchrotron peak frequency. Thus, for a given X–ray flux (as would be the case in a flux limited X–ray selected sample) only those sources falling in the restricted interval $\nu_{\rm peak,sync} \sim 10^{13} - 10^{15}$ Hz would have a flux in the EGRET band high enough to be detectable. On the other hand, for the TeV band it turns out that the chance of being observable is not confined to very extreme HBLs, with X-ray synchrotron peaks, but also intermediate BL Lacs could reach a comparable TeV flux.

Since $\nu_{\rm peak,sync}$ is directly related to both $\alpha_{\rm RO}$ and $\alpha_{\rm RX}$ we can understand now the tendency (section 5.2) of γ–ray detected sources in the Slew survey to have larger values of $\alpha_{\rm RO}$ and $\alpha_{\rm RX}$. Moreover, due to the fact that in the Slew sample LBLs are only a small fraction, the above discussion explains also the lower EGRET detection rate with respect to other blazar samples.

These considerations are based on luminosity ratios only. The proposed scenario relates the shape of the continuum to the total source power. It thus follows that predictions of this unifying scheme on both the detectability of blazars at γ–ray energies (in view of more sensitive γ–ray detectors, e.g. GLAST, improved Cherenkov telescopes, etc.), and their contribution to the γ–ray diffuse background depend on the combined effects of the SED shape, the luminosity functions and possibly evolution (see e.g. Stecker et al. 1996).

In particular, an interesting and testable prediction of the scheme is the *absence of high luminosity sources with synchrotron peaks in the X-ray range and strong associated TeV emission.*

7.2.2 Unification of all Radio-Loud AGNs

Two parallel unified schemes are currently believed to link blazars with galaxies of comparable isotropic radio power: on one hand there are quasar–like blazars and luminous radio-galaxies (FR II), on the other hand BL Lacs and FR I radio-galaxies. The observed range of properties is attributed to orientation effects resulting by a combination of anisotropic emission (relativistic beaming) and obscuration.

BL Lacs–FR I

There is a general consensus that FR I radio galaxies are the parent population of BL Lacs. To begin with, the two classes are statistically matched in properties expected to be aspect independent, such as the radio lobe emission, the host galaxies appearance, and the cluster environment (e.g. Perlman and Stocke 1993; Smith et al. 1995). Furthermore it was shown that the observed radio luminosity function of BL Lacs can be modeled starting from that of the (randomly oriented) FR I galaxies, if the characteristic $\Gamma \simeq 10 - 20$ (Urry et al. 1991; Maraschi and Rovetti 1994). This means

that a FR I radio galaxy would be classified as a BL Lac if its jet is observed within a critical angle $\theta \lesssim 15°$.

FSRQ–FR II

A parallel unification holds between powerful radio galaxies, i.e. FR II, and FSRQ. Even in this case, several statistical properties related to radio jets and lobes are in accord with simple predictions of the unified schemes (e.g. Padovani and Urry 1992; Maraschi and Rovetti 1994). Additional supporting evidence comes from statistical studies that are based on supposedly orientation independent properties, e.g. emission lines (Heckman et al. 1991; Heckman et al. 1992; Hes et al. 1993).

FR I–FR II

On the other hand, it has been suggested that FR I and FR II radio galaxies are fundamentally different (Heckman et al. 1994; Baum et al. 1995), and therefore these two unification schemes have evolved separately considering radio-moderate (FR I) and radio-powerful (FR II) galaxies.

However, in some jet propagation scenarios (e.g. Gopal-Krishna 1991; De Young 1993; Bicknell 1994) the FR I/FR II dichotomy may be bridged, thereby opening the possibility of merging the two unification scenarios into a single paradigm.

In fact, after a long debate the prevailing view is that both FR I and FR II radio galaxies contain relativistic jets which can be decelerated, giving rise to the FR I morphology depending on the jet kinetic power and the pressure of the ambient medium. It is indeed possible that the main differences (e.g. in morphology) are due to differences in the initial power of the jet as it is formed, and to the interaction with the ambient matter, with FR I jets comparably weaker and possibly suffering of entrainment (Bicknell 1995; Bicknell and Dopita 1997).

A couple of important questions are then still open to discussion and can be considered in a new light in the unification scenario proposed in this thesis.

- ◇ What is the relationship between FR I and FR II radio galaxies ?
  The relationship between the –so far– separate unifying schemes for high and low luminosity sources is not well established for what concerns the not–beamed representatives, i.e. radio galaxies, that actually are the great majority of sources.
  Our unifying scheme for blazars would imply that the parent populations of radio–loud AGNs should be essentially similar, following a trend of increasing power mirroring that holding for the beamed population: all radio-galaxies would be linked along a power sequence, too.
- ◇ To which extent is the unification picture between radio galaxies and their putative beamed counterpart true and do they constitute a single population ?
  The two scenarios for low– and high–luminosity radio sources are quite convinc-

ing and well sustained by observational findings, although there are a number of open issues. For low-luminosity sources there is not (yet) a stringent observational requirement for the presence of obscuring material (torus ?), and this could be an important difference with respect to high–luminosity sources.

Answering these problems would provide further important insights on the fundamental questions about jets, their formation and propagation, and the AGN central engine, shedding light on the physical relationships between AGN, their hosts and the environment.

At this stage we can only stress that the scenario in which the intrinsic jet power regulates, in a continuous sequence, the observational properties from the weaker HBL, through LBL, to the most powerful FSRQs, fits in very nicely with the unification of FR I and FR II type radio galaxies as proposed by Bicknell (1995).
The *whole radio–loud AGN population could be unified* in a two parameter space, one being the intrinsic jet power, the other the viewing angle. An interesting point for future discussion is whether a *third parameter* associated with the luminosity of an accretion disk is necessary or is already implicitly and uniquely linked to the jet power.

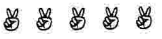

Acknowledgments

The first "special" thought is for Cecilia, and I am going to keep it for myself.....
Those, lucky, who know her could tell how special she is, and know how important she has been, and is, for me.

The second "special" thought, but actually deserving an *ex–aequo*, is for my parents, so different one each other, so important both. Only one point worries me: sometimes I have the feeling, that they are overestimating their "curly–hair" son, but maybe this simply has to do with being parents. However, they often find the way to "reassure me".

The first "normal" thought is for Laura Maraschi, who has been a constant reference for me during these years. Together with Laura, my deeper thanks go to Annalisa Celotti and Gabriele Ghisellini, who have also been my supervisors. They all are striking researchers, and I am grateful to them for the scientific discussions, for the way they tried to teach me how to tackle the problems, and for the constant effortto correct me and my defects. I am a stubborn and I easily waste my time pursuing minor goals. They know how it could be difficult to deal with me. But I mostly thank Laura, Annalisa and Gabriele for being such bright and available persons and for the many many times they supported and encouraged me, trying to convince me that what we were doing was good. Eventually they succeeded....almost.

A special thank to Annalisa, for being a friend, of mine and in particular of Cecilia. Annalisa has been very important during this last year, started with the tough period of post–doc applications. She has been one of the most influential and forming persons for me.

I then would like to thank Prof. Dennis Sciama, head of the Astrophysical sector at SISSA, a delightful man and scientist. I only regret that his lectures, always amazing, have been only a few. I really wish to have the chance to meet him again.

I am indebted with Aldo Treves, my tutor and supervisor and the beginning of my period in Trieste (he is now in Como): he helped and tried to stimulate me, a hard task sometimes.

A special mention is worth for Meg Urry, at STScI. I thank her for her kindness, the help she provided me, the very nice (not–only–scientific) discussions we had during my short "fly–by" in Baltimore, and the support for the "fly–by" itself. We only recently had the chance to think something together, and the discussion have been very fruitful and enlightening.

There are three more persons who have been important in various ways, more or less related with post–docs: Antonella at CfA, Rita and PSU, and Prof. Jayanth Banavar at PSU. Thank you.

Of the people with whom I "worked" a few are left. I would like to thank Lucio Chiappetti and Gianpiero Tagliaferri, who initiated me to the oddities of data analysis, and Silvano Molendi, who already at the time of the early stages of the work for the Laurea Thesis has been helpful, and taught me a lot on data analysis, too.

Last but not least Andrea Comastri: what could I say of Andrea ? He is a surprising father of a family, with the famous crazy "bambine" (I've never meet them, but he made me love them too), an exciting researcher, an extremely nice and funny guy, an excellent Local Organizing Committee. Thank you for the good time we had together.

There is then Francesco Haardt, bridging between friend and co–worker. He is a brilliant man, 360 degrees. He tried to teach me how to do this job, and how to deal with people doing this job. I am grateful to Francesco for being bizarre, as I like to be sometimes, and for being one of the column of the "Capanno". We even succeeded to work together: it took us ten times the time needed by any other person, but we have made pretty nice things, and having a lot of fun. Pippol !!

With Francesco, I thank all the people who passed by, or better still lived at the "Capanno" during these years: Monica, Alberto "ùord", Alberto "scarpa–di–palissandro" Vecchio, Lucio "Sepp–Rufus" Mayer, Simona "Ghizza", Alessandro "Saudade" Gardini, "La Pierpa", "Il Monfo", Fabrizio "Ta–Old"...

And then Trieste. First, and by far, "Giallone", and Betta. They are special, under many aspects, and I owe them a lot (how to forget "spring rolls" and Calvin & Hobbes). Giallo has been able to live with me, two long years at the "grunge flat", and to bear me, with my laziness and my difficult temper. With Giallo I shared everything in Trieste, and a lot also out of this tiny corner of the world.

Many more friends made nice this period in Trieste, and enriched my life. With most of them I spent three or even four years of "high" and "low" in life, and successes and disappointments. I want to thank first Daniele, who has often been an example for me, and with whom I lived the tough period of the writing of the thesis, with

mutual support. There are then the sweet Elis, the hyper(–everything) Marco, Lorenzo and Antonella, Chiara5, Matteo, Valentina, Cristiano (l'"omone"), Paola with Stefano (an amazing story–teller and our favourite *harbour master*), il Conte Marengo, Laura, Claudio Teb.

And more, Marco Chiabergé and Jani, and all of those who passed by the chaotic room 103, whose official occupants have been Silvia, Martok and Francesca, but basically everybody in SISSA came here at least once. I should have put a guestbook !

Finally I thank all the *People at SISSA*, scientific and administrative staff, but especially the unlucky of the basement, Luisa, Marina, Davide, Dario, Roberto, and Fabio, for making our "electronic–alter–ego" live every day, often week ends, and Franco, the factotum.

That's all, and that's a lot,

THANK YOU !

Bibliography

Adam G., 1985, A&AS, **61**, 225.

Aharonian F., et al., 1997, A&A, **327**, L5.

Allen D. A., Ward M. J. and Hyland A. R., 1982, MNRAS, **199**, 969.

Aller H. D., Aller M. F., Latimer G. E. and Hodge P. E., 1985, ApJS, **59**, 513.

Ballard K. R., Mead A. R. G., Brand P. W. J. L. and Hough J. H., 1990, MNRAS, **243**, 640.

Baum S. A., Zirbel E. L. and O'Dea C. P., 1995, ApJ, **451**, 88.

Becker R. H., White R. L. and Edwards A. L., 1991, ApJS, **75**, 1.

Bednarek W., 1993, ApJ, **402**, L29.

Bednarek W., 1998, A&A, **336**, 123.

Bersanelli M., Bouchet P., Falomo R. and Tanzi E. G., 1992, AJ, **104**, 28.

Bertsch D. L., et al., 1993, ApJ, **405**, L21.

Bicknell G. V., 1994, ApJ, **422**, 542.

Bicknell G. V., 1995, ApJS, **101**, 29.

Bicknell G. V. and Dopita M. A., 1997, In Proc. of the Workshop on *Relativistic Jets in AGNs,* eds. M. Ostrowski, M. Sikora, G. Madejski, M. Begelman, Cracow (Poland), May 1997, pp. 1.

Biermann P. L., 1995, Space Science Reviews, **74**, 385.

Biermann P. L., Kühr H., Snyder W. A. and Zensus J. A., 1987, A&A, **185**, 9.

Blandford R. D., 1993, In AIP Conf. Proc. 280, *Compton Gamma Ray Observatory* Symp., eds. M. Friedlander, N. Gehrels, D. J. Macomb (New York:AIP), pp. 533.

Blandford R. D. and Konigl A., 1979, ApJ, **232**, 34.

Blandford R. D. and Levinson A., 1995, ApJ, **441**, 79.

Blandford R. D. and Rees M. J., 1978, In *Proc. of Pittsburgh Conference on BL Lac Objects,* Pittsburgh (PA), April 24–26, 1978. (A79-30026 11-90) Pittsburgh (PA), University of Pittsburgh, NATO-supported research, pp. 328.

Blom J. J., et al., 1995, A&A, **298**, L33.

Bloom S. D. and Marscher A. P., 1991, ApJ, **366**, 16.

Bloom S. D. and Marscher A. P., 1996, ApJ, **461**, 657.

Bloom S. D., Marscher A. P., Gear W. K., Terasranta H., Valtaoja E., Aller H. D. and Aller M. F., 1994, AJ, **108**, 398.

Boroson T. A. and Green R. F., 1992, ApJS, **80**, 109.

Bozyan E. P., Hemenway P. D. and Argue A. N., 1990, AJ, **99**, 1421.

Bradbury S. M., et al., 1997, A&A, **320**, L5.

Bregman J. N., Glassgold A. E., Huggins P. J. and Kinney A. L., 1985, ApJ, **291**, 505.

Breslin A. C., et al., 1997, IAU Circ., **6592**, 1.

Brindle C., Hough J. H., Bailey J. A., Axon D. J. and Hyland A. R., 1986, MNRAS, **221**, 739.

Brinkmann W., Siebert J. and Boller T., 1994, A&A, **281**, 355.

Brinkmann W., Siebert J., Reich W., Fuerst E., Reich P., Voges W., Trümper J. and Wielebinski R., 1995, A&AS, **109**, 147.

Brown L. M. J., et al., 1989, ApJ, **340**, 129.

Browne I. W. A. and Marchã M. J. M., 1993, MNRAS, **261**, 795.

Brunner H., Lamer G., Worrall D. M. and Staubert R., 1994, A&A, **287**, 436.

Cappi M., Comastri A., Molendi S., Palumbo G. C. C., Della Ceca R. and Maccacaro T., 1994, MNRAS, **271**, 438.

Catanese M., et al., 1997, ApJ, **480**, 562.

Catanese M., et al., 1998, ApJ, **501**, 616.

Celotti A., 1997, In Proc. of the Workshop on *Relativistic Jets in AGNs,* eds. M. Ostrowski, M. Sikora, G. Madejski, M. Begelman, Cracow (Poland), May 1997, pp. 270.

Celotti A., Maraschi L., Ghisellini G., Caccianiga A. and Maccacaro T., 1993, ApJ, **416**, 118.

Celotti A., Padovani P. and Ghisellini G., 1997, MNRAS, **286**, 415.

Chiang J., Fichtel C. E., Von Montigny C., Nolan P. L. and Petrosian V., 1995, ApJ, **452**, 156.

Chini R., Biermann P. L., Kreysa E. and Gemuend H. P., 1989, A&A, **221**, L3.

Clegg P. E., et al., 1983, ApJ, **273**, 58.

Collier S. J., et al., 1998, ApJ, **500**, 162.

Collmar W., 1996, In Proc. of the Heidelberg Workshop on *Gamma Ray Emitting AGNs*, eds. J.G. Kirk, M. Camenzind, C. von Montigny, S. Wagner, pp. 9.

Comastri A., Fossati G., Ghisellini G. and Molendi S., 1997, ApJ, **480**, 534.

Comastri A., Molendi S. and Ghisellini G., 1995, MNRAS, **277**, 297.

Condon J. J., Anderson E. and Broderick J. J., 1995, AJ, **109**, 2318.

Condon J. J., Hicks P. D. and Jauncey D. L., 1977, AJ, **82**, 692.

Dar A. and Laor A., 1997, ApJ, **478**, L5.

De Jager O. C., Stecker F. W. and Salamon M. H., 1994, Nature, **369**, 294.

De Vries H. W., Thaddeus P. and Heithausen A., 1987, ApJ, **319**, 723.

De Young D. S., 1993, ApJ, **405**, L13.

Dermer C. D., 1995, ApJ, **446**, L63.

Dermer C. D. and Schlickeiser R., 1993, ApJ, **416**, 458.

Dermer C. D., Schlickeiser R. and Mastichiadis A., 1992, A&A, **256**, L27.

Dickey J. M. and Lockman F. J., 1990, ARA&A, **28**, 215.

Dingus B. L., et al., 1996, ApJ, **467**, 589.

Dondi L. and Ghisellini G., 1995, MNRAS, **273**, 583.

Edelson R. A., 1987, AJ, **94**, 1150.

Elvis M., Plummer D., Schachter J. and Fabbiano G., 1992, ApJS, **80**, 257.

Elvis M., Wilkes B. J. and Lockman F. J., 1989, AJ, **97**, 777.

Elvis M., et al., 1994, ApJS, **95**, 1.

Falcke H., Malkan M. A. and Biermann P. L., 1995, A&A, **298**, 375.

Falomo R., Bersanelli M., Bouchet P. and Tanzi E. G., 1993, AJ, **106**, 11.

Falomo R., Scarpa R. and Bersanelli M., 1994, ApJS, **93**, 125.

Falomo R., Treves A., Chiapetti L., Maraschi L., Pian E. and Tanzi E. G., 1993, ApJ, **402**, 532.

Fanaroff B. L. and Riley J. M., 1974, MNRAS, **167**, 31.

Feigelson E. D. and Nelson P. I., 1985, ApJ, **293**, 192.

Fichtel C. E., et al., 1994, ApJS, **94**, 551.

Fossati G., Celotti A., Ghisellini G. and Maraschi L., 1997, MNRAS, **289**, 136.

Fossati G., Celotti A., Ghisellini G., Maraschi L. and Comastri A., 1998, MNRAS, **299**, 433.

Fossati G., et al., 1998, in preparation.

Fossati G., Maraschi L., Rovetti F. and Treves A., 1996, In *Roentgenstrahlung from the Universe,* eds. H.U. Zimmermann, J. Trümper, H. Yorke, Wurzburg, September 1995, MPE Report 263, pp. 447.

Fricke K. J., Kollatschny W. and Witzel A., 1983, A&A, **117**, 60.

Gabuzda D. C., Mullan C. M., Cawthorne T. V., Wardle J. F. C. and Roberts D. H., 1994, ApJ, **435**, 140.

Gear W. K., 1993a, MNRAS, **264**, 919.

Gear W. K., 1993b, MNRAS, **264**, L21.

Gear W. K., et al., 1985, ApJ, **291**, 511.

Gear W. K., et al., 1986, ApJ, **304**, 295.

Gear W. K., et al., 1994, MNRAS, **267**, 167.

Ghisellini G., 1989, *Non thermal radiative processes in compact sources*, Ph. D. thesis, International School for Advanced Studies, Trieste, Italy.

Ghisellini G., Celotti A., Fossati G., Maraschi L. and Comastri A., 1998, in press.

Ghisellini G. and Madau P., 1996, MNRAS, **280**, 67.

Ghisellini G. and Maraschi L., 1989, ApJ, **340**, 181.

Ghisellini G., Maraschi L. and Dondi L., 1996, A&AS, **120**, 503.

Ghisellini G., Maraschi L. and Treves A., 1985, A&A, **146**, 204.

Ghisellini G., Maraschi L., Treves A. and Tanzi E. G., 1986, ApJ, **310**, 317.

Ghisellini G., Padovani P., Celotti A. and Maraschi L., 1993, ApJ, **407**, 65.

Ghisellini G., et al., 1998 *The blazar PKS 0528+134: new results from BeppoSAX observations,* , in preparation.

Ghisellini G., et al., 1997, A&A, **327**, 61.

Giommi P., Ansari S. G. and Micol A., 1995, A&AS, **109**, 267.

Giommi P. and Padovani P., 1994, MNRAS, **268**, L51.

Glass I. S., 1979, MNRAS, **186**, 29P.

Glass I. S., 1981, MNRAS, **194**, 795.

Gopal-Krishna, 1991, A&A, **248**, 415.

Gregory P. C. and Condon J. J., 1991, ApJS, **75**, 1011.

Hartman R. C., et al., 1993, ApJ, **407**, L41.

Hartman R. C., et al., 1996, ApJ, **461**, 698.

Hasinger G., Turner T., George I. and Boese G., 1992, Legacy No. 2.

Heckman T. M., Chambers K. C. and Postman M., 1992, ApJ, **391**, 39.

Heckman T. M., Lehnert M. D., Miley G. K. and Van Breugel W., 1991, ApJ, **381**, 373.

Heckman T. M., O'Dea C. P., Baum S. A. and Laurikainen E., 1994, ApJ, **428**, 65.

Hes R., Barthel P. D. and Fosbury R. A. E., 1993, Nature, **362**, 326.

Hewitt A. and Burbidge G., 1993, ApJS, **87**, 451.

Holmes P. A., Brand P. W. J. L., Impey C. D. and Williams P. M., 1984, MNRAS, **210**, 961.

Hunter S. D., et al., 1993, A&A, **272**, 59.

Impey C., 1996, AJ, **112**, 2667.

Impey C. D. and Brand P. W. J. L., 1981, Nature, **292**, 814.

Impey C. D. and Brand P. W. J. L., 1982, MNRAS, **201**, 849.

Impey C. D., Brand P. W. J. L., Wolstencroft R. D. and Williams P. M., 1982, MNRAS, **200**, 19.

Impey C. D., Brand P. W. J. L., Wolstencroft R. D. and Williams P. M., 1984, MNRAS, **209**, 245.

Impey C. D. and Neugebauer G., 1988, AJ, **95**, 307.

Impey C. D. and Tapia S., 1988, ApJ, **333**, 666.

Impey C. D. and Tapia S., 1990, ApJ, **354**, 124.

Inoue S. and Takahara F., 1996, ApJ, **463**, 555.

Jannuzi B. T., Smith P. S. and Elston R., 1993, ApJS, **85**, 265.

Jannuzi B. T., Smith P. S. and Elston R., 1994, ApJ, **428**, 130.

Jones T. W., O'Dell S. L. and Stein W. A., 1974a, ApJ, **188**, 353.

Jones T. W., O'Dell S. L. and Stein W. A., 1974b, ApJ, **192**, 261.

Kanbach G., 1996, In Proc. of the Heidelberg Workshop on *Gamma Ray Emitting AGNs,* eds. J.G. Kirk, M. Camenzind, C. von Montigny, S. Wagner, pp. 1.

Kendall M. and Stuart A., 1979, *The advanced theory of statistics. Vol.2: Inference and relationship*. London: Griffin, 1979, 4th ed.

Kirk J. G., 1997, In Proc. of the Workshop on *Relativistic Jets in AGNs,* eds. M. Ostrowski, M. Sikora, G. Madejski, M. Begelman, Cracow (Poland), May 1997, pp. 145.

Kollgaard R. I., 1994, Vistas in Astronomy, **38**, 29.

Kollgaard R. I., Palma C., Laurent-Muehleisen S. A. and Feigelson E. D., 1996, ApJ, **465**, 115.

Kollgaard R. I., Wardle J. F. C., Roberts D. H. and Gabuzda D. C., 1992, AJ, **104**, 1687.

Königl A., 1981, ApJ, **243**, 700.

Krennrich F., et al., 1997, ApJ, **481**, 758.

Kubo H., 1997, Ph. D. thesis, University of Tokio, Tokio, Japan.

Kühr H. and Schmidt G. D., 1990, AJ, **99**, 1.

Kühr H., Witzel A., Pauliny-Toth I. I. K. and Nauber U., 1981, A&AS, **45**, 367.

Lamer G., Brunner H. and Staubert R., 1996, A&A, **311**, 384.

Lampton M., Margon B. and Bowyer S., 1976, ApJ, **208**, 177.

Landau R., et al., 1986, ApJ, **308**, 78.

Landau R., Jones T. W., Epstein E. E., Neugebauer G., Soifer B. T., Werner M. W., Puschell J. J. and Balonek T. J., 1983, ApJ, **268**, 68.

Laurent-Muehleisen S. A., 1996, *A New Sample of BL Lacertae Objects and Implications for Unified Schemes*, Ph. D. thesis, Pennsylvania State University, State College (PA).

Lavalley M., Isobe T. and Feigelson E., 1992, In ASP Conf. Ser. 25: *Astronomical Data Analysis Software and Systems I,* eds. D.M. Worrall, C. Biemesderfer, J. Barnes, Volume 1, pp. 245.

Lawrence A., Rowan-Robinson M., Efstathiou A., Ward M. J., Elvis M., Smith M. G., Duncan W. D. and Robson E. I., 1991, MNRAS, **248**, 91.

Lawson A. J. and Turner M. J. L., 1997, MNRAS, **288**, 920.

Ledden J. E. and O'Dell S. L., 1985, ApJ, **298**, 630.

Lepine J. R. D., Braz M. A. and Epchtein N., 1985, A&A, **149**, 351.

Levinson A. and Blandford R., 1995, ApJ, **449**, 86.

Lin Y. C., et al., 1995, ApJ, **442**, 96.

Lin Y. C., et al., 1996, ApJS, **105**, 331.

Lin Y. C., et al., 1997, ApJ, **476**, L11.

Lind K. R. and Blandford R. D., 1985, ApJ, **295**, 358.

Liszt H., 1994, ApJ, **429**, 638.

Liszt H. S. and Wilson R. W., 1993, ApJ, **403**, 663.

Litchfield S. J., Robson E. I. and Stevens J. A., 1994, MNRAS, **270**, 341.

Lockman F. J. and Savage B. D., 1995, ApJS, **97**, 1.

Lorenzetti D., Spinoglio L., Massaro E. and Perola G. C., 1990, A&A, **235**, 35.

Maccacaro T., Gioia I. M., Wolter A., Zamorani G. and Stocke J. T., 1988, ApJ, **326**, 680.

Macomb D. J., et al., 1995, ApJ, **449**, L99.

Macomb D. J., et al., 1996, ApJ, **459**, L111.

Madejski G., Takahashi T., Tashiro M., Kubo H., Hartman R., Kallman T. and Sikora M., 1996, ApJ, **459**, 156.

Mannheim K., 1993, A&A, **269**, 67.

Mannheim K. and Biermann P. L., 1989, A&A, **221**, 211.

Mannheim K. and Biermann P. L., 1992, A&A, **253**, L21.

Maoz D., et al., 1993, ApJ, **409**, 28.

Maraschi L., Fossati G., Tagliaferri G. and Treves A., 1995, ApJ, **443**, 578.

Maraschi L., Ghisellini G. and Celotti A., 1992, ApJ, **397**, L5.

Maraschi L., Ghisellini G., Tanzi E. G. and Treves A., 1986, ApJ, **310**, 325.

Maraschi L., et al., 1994, ApJ, **435**, L91.

Maraschi L. and Rovetti F., 1994, ApJ, **436**, 79.

Maraschi L., Treves A., Schwartz D. A. and Tanzi E. G., 1985, ApJ, **294**, 615.

Marscher A. P. and Gear W. K., 1985, ApJ, **298**, 114.

Marscher A. P. and Travis J. P., 1996, A&AS, **120**, 537.

Mastichiadis A. and Kirk J. G., 1997, A&A, **320**, 19.

Mattox J. R., et al., 1993, ApJ, **410**, 609.

Mattox J. R., Schachter J., Molnar L., Hartman R. C. and Patnaik A. R., 1997, ApJ, **481**, 95.

Mattox J. R., Wagner S., McGlynn T. A., Malkan M., Schachter J. F. and Sreekumar P., 1995, IAU Circ., **6161**, 2.

Mattox J. R., Wagner S. J., Malkan M., McGlynn T. A., Schachter J. F., Grove J. E., Johnson W. N. and Kurfess J. D., 1997, ApJ, **476**, 692.

McNaron-Brown K., et al., 1995, ApJ, **451**, 575.

Mead A. R. G., Ballard K. R., Brand P. W. J. L., Hough J. H., Brindle C. and Bailey J. A., 1990, A&AS, **83**, 183.

Morris S. L., Stocke J. T., Gioia I. M., Schild R. E., Wolter A., Maccacaro T. and Della Ceca R., 1991, ApJ, **380**, 49.

Morrison R. and McCammon D., 1983, ApJ, **270**, 119.

Mücke A., et al., 1997, A&A, **320**, 33.

Mukherjee R., et al., 1995, ApJ, **445**, 189.

Mukherjee R., et al., 1996, ApJ, **470**, 831.

Mukherjee R., et al., 1997, ApJ, **490**, 116.

Murphy D. W., Browne I. W. A. and Perley R. A., 1993, MNRAS, **264**, 298.

Murphy E. M., Lockman F. J., Laor A. and Elvis M., 1996, ApJS, **105**, 369.

Netzer H., et al., 1996, MNRAS, **279**, 429.

Nolan P. L., et al., 1993, ApJ, **414**, 82.

Nolan P. L., et al., 1996, ApJ, **459**, 100.

O'Dell S. L., Puschell J. J., Stein W. A. and Warner J. W., 1978, ApJS, **38**, 267.

Padovani P., 1992, A&A, **256**, 399.

Padovani P. and Giommi P., 1995, ApJ, **444**, 567.

Padovani P. and Giommi P., 1996, MNRAS, **279**, 526.

Padovani P. and Urry C. M., 1992, ApJ, **387**, 449.

Pearson T. J. and Readhead A. C. S., 1988, ApJ, **328**, 114.

Perley R. A., 1982, AJ, **87**, 859.

Perlman E. S., Padovani P., Giommi P., Sambruna R., Jones L. R., Tzioumis A. and Reynolds J., 1998, AJ, **115**, 1253.

Perlman E. S. and Stocke J. T., 1993, ApJ, **406**, 430.

Perlman E. S., et al., 1996, ApJS, **104**, 251.

Perlman E. S., Stocke J. T., Wang Q. D. and Morris S. L., 1996, ApJ, **456**, 451.

Petry D., et al., 1996, A&A, **311**, L13.

Pfeffermann E. and Briel U. G., 1986, In *X-ray instrumentation in astronomy,* Proceedings of the Meeting, Cannes, France, December 2-4, 1985 (Bellingham, WA, Society of Photo-Optical Instrumentation Engineers), Volume 597, pp. 208.

Pfeffermann E., et al., 1987, In Proc. of the meeting of the Society for Photo–Optical Instrumentation Engineers (SPIE), Berlin, West Germany, Dec. 1986.

Pian E., Falomo R., Ghisellini G., Maraschi L., Sambruna R. M., Scarpa R. and Treves A., 1996, ApJ, **459**, 169.

Pian E., Falomo R., Scarpa R. and Treves A., 1994, ApJ, **432**, 547.

Pian E. and Treves A., 1993, ApJ, **416**, 130.

Pica A. J., Smith A. G., Webb J. R., Leacock R. J., Clements S. and Gombola P. P., 1988, AJ, **96**, 1215.

Pohl M., Reich W., Schlickeiser R., Reich P. and Ungerechts H., 1996, A&AS, **120**, C529.

Press W., Teukolsky S., Vetterling W. and Flannery B., 1992, *Numerical Recipes, the art of scientific computing* second edition. Cambridge University Press.

Preston R. A., Morabito D. D., Williams J. G., Faulkner J., Jauncey D. L. and Nicolson G., 1985, AJ, **90**, 1599.

Protheroe R. J., Bhat C. L., Fleury P., Lorenz E., Teshima M. and Weekes T. C., 1997, In Highlight Session on Markarian 501 at the *25th International Cosmic Ray Conference,* Durban, 1997.

Punch M., et al., 1992, Nature, **358**, 477.

Quinn J., et al., 1996, ApJ, **456**, L83.

Radecke H. D., et al., 1995, ApJ, **438**, 659.

Raiteri C. M., Ghisellini G., Villata M., De Francesco G., Lanteri L., Chiaberge M., Peila A. and Antico G., 1998, A&AS, **127**, 445.

Reuter H. P., et al., 1997, AA&AS, **122**, 271.

Rieke G. H. and Lebofsky M. J., 1985, ApJ, **288**, 618.

Rieke G. H., Wisniewski W. Z. and Lebofsky M. J., 1982, ApJ, **263**, 73.

Robson E. I., Gear W. K., Brown L. M. J., Courvoisier T. J. L. and Smith M. G., 1986, Nature, **323**, 134.

Rusk R. and Seaquist E. R., 1985, AJ, **90**, 30.

Rybicki G. B. and Lightman A. P., 1979, *Radiative Processes in Astrophysics,* John Wiley & Sons, (New York): John Wiley & Sons.

Sambruna R. M., 1997, ApJ, **487**, 536.

Sambruna R. M., Barr P., Giommi P., Maraschi L., Tagliaferri G. and Treves A., 1994, ApJS, **95**, 371.

Sambruna R. M., Maraschi L. and Urry C. M., 1996, ApJ, **463**, 444.

Sambruna R. M., Urry C. M., Ghisellini G. and Maraschi L., 1995, ApJ, **449**, 567.

Sambruna R. M., et al., 1997, ApJ, **474**, 639.

Samuelson F. W., et al., 1998, ApJ, **501**, L17.

Scarpa R. and Falomo R., 1997, A&A, **325**, 109.

Schoenfelder V., 1994, ApJS, **92**, 593.

Shafer R., Haberl F., Arnaud K. and Tennant A., 1991, In *XSPEC User's Guide,* ESA TM–09, Noordwijk, The Netherlands.

Shrader C. R., Hartman R. C. and Webb J. R., 1996, A&AS, **120**, 599.

Shrader C. R., et al., 1994, AJ, **107**, 904.

Sikora M., Begelman M. C. and Rees M. J., 1994, ApJ, **421**, 153.

Sikora M., Madejski G., Moderski R. and Poutanen J., 1997, ApJ, **484**, 108.

Sikora M., Madejski G. M. and Begelman M. C., 1997, In Proc. of the Workshop on *Relativistic Jets in AGNs*, eds. M. Ostrowski, M. Sikora, G. Madejski, M. Begelman, Cracow (Poland), May 1997, pp. 287.

Sikora M., Sol H., Begelman M. C. and Madejski G. M., 1996, MNRAS, **280**, 781.

Sitko M. L. and Junkkarinen V. T., 1985, PASP, **97**, 1158.

Sitko M. L. and Sitko A. K., 1991, PASP, **103**, 160.

Smith E. P., O'Dea C. P. and Baum S. A., 1995, ApJ, **441**, 113.

Smith P. S., Balonek T. J., Elston R. and Heckert P. A., 1987, ApJS, **64**, 459.

Smith P. S., Elston R., Berriman G., Allen R. G. and Balonek T. J., 1988, ApJ, **326**, L39.

Sreekumar P., et al., 1996, ApJ, **464**, 628.

Stacy J. G., Vestrand W. T., Sreekumar P., Bonnell J., Kubo H. and Hartman R. C., 1996, A&AS, **120**, C549.

Stecker F. W. and De Jager O. C., 1998, A&A, **334**, L85.

Stecker F. W., De Jager O. C. and Salamon M. H., 1996, ApJ, **473**, L75.

Steppe H., Liechti S., Mauersberger R., Koempe C., Brunswig W. and Ruiz-Moreno M., 1992, A&AS, **96**, 441.

Steppe H., et al., 1993, A&AS, **102**, 611.

Steppe H., Salter C. J., Chini R., Kreysa E., Brunswig W. and Lobato Perez J., 1988, A&AS, **75**, 317.

Stevens J. A., Litchfield S. J., Robson E. I., Hughes D. H., Gear W. K., Terasranta H., Valtaoja E. and Tornikoski M., 1994, ApJ, **437**, 91.

Stickel M., Fried J. W. and Kühr H., 1993, A&AS, **98**, 393.

Stickel M., Fried J. W., Kühr H., Padovani P. and Urry C. M., 1991, ApJ, **374**, 431.

Stickel M. and Kühr H., 1996, A&AS, **115**, 1.

Stickel M. and Kühr H., 1994, A&AS, **103**, 349.

Stickel M., Meisenheimer K. and Kühr H., 1994, A&AS, **105**, 211.

Stickel M., Rieke G. H., Kühr H. and Rieke M. J., 1996, ApJ, **468**, 556.

Stocke J. T., Liebert J., Schmidt G., Gioia I. M., Maccacaro T., Schild R. E., Maccagni D. and Arp H. C., 1985, ApJ, **298**, 619.

Strong A. W., et al., 1988, A&A, **207**, 1.

Takahashi T., et al., 1996, ApJ, **470**, L89.

Terasranta H., et al., 1992, A&AS, **94**, 121.

Thompson D. J., et al., 1993, ApJ, **410**, 87.

Thompson D. J., et al., 1993, ApJ, **415**, L13.

Thompson D. J., et al., 1995, ApJS, **101**, 259.

Thompson D. J., et al., 1996, ApJS, **107**, 227.

Tornikoski M., et al., 1996, A&AS, **116**, 157.

Tornikoski M., Valtaoja E., Terasranta H., Lainela M., Bramwell M. and Botti L. C. L., 1993, AJ, **105**, 1680.

Tosti G., et al., 1998, A&AS, **130**, 109.

Treves A., Belloni T., Falomo R., Fink H., Maraschi L., Sambruna R. M., Tagliaferri G. and Zimmermann H. U., 1993, ApJ, **406**, 447.

Trümper J., 1982, Advances in Space Research, **2**, 241.

Turner M. J. L., et al., 1990, MNRAS, **244**, 310.

Ulrich M.-H., Maraschi L. and Megan C., 1997, ARA&A, **35**, 445.

Urry C. M. and Padovani P., 1991, ApJ, **371**, 60.

Urry C. M. and Padovani P., 1995, PASP, **107**, 803.

Urry C. M., Padovani P. and Stickel M., 1991, ApJ, **382**, 501.

Urry C. M., Sambruna R. M., Worrall D. M., Kollgaard R. I., Feigelson E. D., Perlman E. S. and Stocke J. T., 1996, ApJ, **463**, 424.

Urry C. M. and Shafer R. A., 1984, ApJ, **280**, 569.

Urry C. M., et al., 1997, ApJ, **486**, 799.

Vagnetti F., Cavaliere A. and Giallongo E., 1991, ApJ, **368**, 366.

Vagnetti F. and Spera R., 1994, ApJ, **436**, 611.

Valtaoja E., Lahteenmaki A. and Terasranta H., 1992, A&AS, **95**, 73.

Vermeulen R. C. and Cohen M. H., 1994, ApJ, **430**, 467.

Vermeulen R. C., Ogle P. M., Tran H. D., Browne I. W. A., Cohen M. H., Readhead A. C. S., Taylor G. B. and Goodrich R. W., 1995, ApJ, **452**, L5.

Veron-Cetty M. P. and Veron P., 1993, ESO Scientific Report, **13**, 1.

Vestrand W. T., Stacy J. G. and Sreekumar P., 1995, ApJ, **454**, L93.

Villata M., et al., 1997, A&AS, **121**, 119.

Von Montigny C., et al., 1997, ApJ, **483**, 161.

Von Montigny C., et al., 1995, ApJ, **440**, 525.

Wagner S., Sanchez-Pons F., Quirrenbach A. and Witzel A., 1990, A&A, **235**, L1.

Wagner S. J., et al., 1995, ApJ, **454**, L97.

Wagner S. J. and Witzel A., 1995, ARA&A, **33**, 163.

Wagner S. J., et al., 1996, AJ, **111**, 2187.

Wall J. V. and Peacock J. A., 1985, MNRAS, **216**, 173.

Wang J., Luo Q. and Xie G., 1996, ApJ, **457**, L65.

Webb J. R., Barnello T., Robson I. and Hartman R. C., 1995, IAU Circ., **6168**, 1.

Webb J. R., Smith A. G., Leacock R. J., Fitzgibbons G. L., Gombola P. P. and Shepherd D. W., 1988, AJ, **95**, 374.

Weekes T. C., et al., 1996, A&AS, **120**, 603.

Wehrle A. E., et al., 1998, ApJ, **497**, 178.

White R. L. and Becker R. H., 1992, ApJS, **79**, 331.

Wilkes B. J., Tananbaum H., Worrall D. M., Avni Y., Oey M. S. and Flanagan J., 1994, ApJS, **92**, 53.

Wiren S., Valtaoja E., Terasranta H. and Kotilainen J., 1992, AJ, **104**, 1009.

Wolter A., Caccianiga A., Della Ceca R. and Maccacaro T., 1994, ApJ, **433**, 29.

Wolter A., et al., 1997, MNRAS, **284**, 225.

Worrall D. M., Tananbaum H., Giommi P. and Zamorani G., 1987, ApJ, **313**, 596.

Worrall D. M. and Wilkes B. J., 1990, ApJ, **360**, 396.

Wright A. E., Ables J. G. and Allen D. A., 1983, MNRAS, **205**, 793.

Wright A. E., Griffith M. R., Burke B. F. and Ekers R. D., 1994, ApJS, **91**, 111.

Wright A. E., Wark R. M., Troup E., Otrupcek R., Jennings D., Hunt A. and Cooke D. J., 1991, MNRAS, **251**, 330.

Wurtz R. E., 1994, *The host galaxies and galaxy clustering environments of BL Lacertae objects*, Ph. D. thesis, University of Colorado at Boulder.

Zhang Y. F., Marscher A. P., Aller H. D., Aller M. F., Terasranta H. and Valtaoja E., 1994, ApJ, **432**, 91.

Zimmermann H., Belloni T., Izzo C., Kahabka P. and Schwentker O., 1993, In *EXSAS User's Guide,* MPE Report 244.